UNIVERSITY OF CALIFORNIA, SAN DIEGO

Multiscale Modeling of a Red Blood Cell and its Fluid-Structure Interaction

A dissertation submitted in partial satisfaction of the
requirements for the degree
Doctor of Philosophy

in

Structural Engineering

by

Zhangli Peng

Committee in charge:

Professor Qiang Zhu, Chair
Professor Robert Asaro
Professor Joel Conte
Professor Eric Lauga
Professor Vlado Lubarda
Professor Keiko Nomura

2011

The Dissertation of Zhangli Peng is approved, and it is acceptable in quality and form for publication on microfilm and electronically:

_____

_____

_____

_____

_____

_____
Chair

University of California, San Diego

2011

DEDICATION

To my parents

EPIGRAPH

Seek and you will find.
—Matthew 7:7

TABLE OF CONTENTS

LIST OF FIGURES

LIST OF TABLES

L_f, L_u	the contour lengths for folded and unfolded domains
x_f, x_u	the projected extensions of folded and unfolded domains
$\Delta\Delta x^*$	the difference between the activation length of the unfolding process and that of the refolding process.
$F_{1/2}$	the force corresponding to the state when half of the domains are unfolded
k_B	the Boltzmann constant
T	the temperature
p_f, p_u	the persistence lengths of each domain in folded and unfolded states
$x_{f\to u}$	the activation length
$k_{f\to u}$	the rate of transition
$\beta_0, \beta_1, \beta_2, \beta_3$	Euler parameters
$\mathbf{\Lambda}$	the diagonal component of the Oseen hydrodynamic tensor
κ_c	the bending modulus of the bilayer
σ	the existing tension in the lipid bilayer
$\boldsymbol{\sigma}$	the Cauchy stress in Voigt notation
$\mathbf{X}, \mathbf{X}'$	the positive vectors
t	time
Δt	the time step
$\zeta(\mathbf{X}', t)$	the random thermal fluctuation force
$F^{(c)}(\mathbf{X}, t)$	the force by the tension of spectrins
$F^{(p)}(\mathbf{X}, t)$	the repulsive force between the bilayer and the actin
$F^{(s)}(\mathbf{X}, t)$	the repulsive force between spectrins and the bilayer
$f_{iZ}(t)$	the Z-component of the stretching force inside the i^{th} Sp
$\mathbf{X}^{(c)}$	the location of the SCs
δ	the Dirac delta-function or Kronecker's delta
$\mathbf{k}$	the Fourier mode vector
k	the shear rate
$\mathbf{f}^{(s)}, \mathbf{f}^{(b)}, \mathbf{f}^{(\zeta)}$	forces on the actin due to spectrin, bilayer, Brownian fluctuation
$\mathbf{M}^{(s)}, \mathbf{M}^{(b)}, \mathbf{M}^{(\zeta)}$	moments on the actin due to spectrin, bilayer, Brownian fluctuation
D_x, D_y, D_z	the drag coefficients
D_{Mx}, D_{My}, D_{Mz}	the rotational drag coefficients
Re	the Reynolds number
ρ	the density of the surrounding fluid or the protein density of the cytoskeleton
A_0	the projected area of a JC without deformation
A	the deformed projected area of a JC

P	the probability of unfolding
$\mathbf{C}$	the transformation matrix or the damping matrix
α	a measure of area deformation
β	a measure of shear deformation
K_b	the area modulus of the lipid bilayer
$\mathbf{\Theta}$	the Cauchy stress tensor
∇	the spatial gradient operator
Γ^D	the Dirichlet boundary
Γ^N	the Neumann boundary
$\mathbf{n}$	the normal vector to the surface
$\mathbf{x}, \mathbf{u}, \mathbf{v}$	position, displacement and velocity vectors
$\boldsymbol{\omega}$	the angular velocity
$\dot{\gamma}$	the strain rate
$\mathbf{F}$	deformation gradient
h	the thickness of the membrane or the vertical displacement of the bilayer
$\mathbf{N}$	the shape function
ξ, η, ζ	isoparametric coordinates
R_p, R_s	the micropipette inner radius and the radius of the spherical part
ΔV	the volume change of the cell
ΔP	the internal pressure due to the volume change
λ_1, λ_2	principal in-plane stretches
$\mathbf{f}_{jc}$	the interaction force on a JC
f_0	the resultant force applied on the tether
R_t	the radius of the cylindrical tether
Ω	the computational domain
η_1, η_2, η_f	fluid dynamic viscosities
Λ	the fluid viscosity contrast ratio
$\boldsymbol{\tau}^{bs}$	the bilayer-skeleton interaction force
$\mathbf{t}$	surface tractions
μ, K	the membrane shear modulus and area modulus
$\bar{\mathbf{x}}$	the position vector of the shell reference surface
$\mathbf{x}'$	the position vector of the shell fiber direction
$\bar{\mathbf{u}}$	the displacement vector of the shell reference surface
$\mathbf{u}'$	the displacement vector of the shell fiber direction
$\mathbf{e}^{\ell}$	the lamina coordinate base
$\bar{T}, \bar{T}_0$	the isotropic tension and the prestress of the cytoskeleton
$\mathbf{G}, \mathbf{T}$	Green's functions for velocity and stress
$\mathbf{b}$	the left Cauchy-Green deformation tensor
$\mathbf{B}$	the displacement-strain matrix in FEM
$\mathbf{L}$	the connectivity matrix in FEM
G	the transverse shear stiffness or normalized shear rate
D_T, b_T	the translational diffusivity and mobility of a protein

ACKNOWLEDGEMENTS

First of all, I am very grateful to have Professor Qiang Zhu as my advisor. During my Ph.D. study, Professor Qiang Zhu gave me unlimited guidance, encouragement, understanding, and patience. He introduced me to the exciting fields of cellular biomechanics and renewable energy harvesting, which are both at the frontier of the current scientific adventure. He offered me great training opportunities to write papers for prestigious journals, and create proposals for National Institutes of Health (NIH). He helped me extensively on improving my presentation skills, and supported me to attend famous conferences held by Biophysical Society, American Physical Society (APS) and National Science Foundation (NSF). He gave me significant freedom on choosing my research topics and courses, and arranging my time. Furthermore, I would like to thank him for supporting me significantly in my job search, and being so considerate to help me graduate sooner.

Secondly, I would like thank Professor Robert Asaro for his great guidances and invaluable advices. He introduced me to the interesting research on the micromechanics of nacre and the crystal plasticity. He shared a lot of experiences on careers with me and supported me in my job search.

I am also thankful to our collaborators, Professor Amy Sung, Dr. Carlos Vera, and Professor Pedro Cabrales from the Department of Bioengineering in UCSD. Professor Amy Sung and Dr. Carlos Vera carried out a lot of micropipette experiments on red blood cells, which are very helpful for validating my numerical simulations in this dissertation. Professor Sung also invited me to her group study where I learned a lot on the molecular biology of red blood cells. Professor Pedro Cabrales is so patient to show me their amazing *in vivo* experiments on hamsters.

I also would like to thank my committee members, Professor Joel Conte, Professor Vlado Lubarda, Professor Eric Lauga, and Professor Keiko Nomura for their great advices, suggestions and encouragements. Especially, Professor Lubarda shared with me his beautiful theory on membrane viscoelasticity and Professor Lauga taught me a lot on fluid mechanics.

I would like to thank my colleagues Kourosh Shoele, Jiddu Bezares and Sara Salehyar for their friendships and helps. Kourosh gave me many great suggestions.

Jiddu put significant efforts on experiments of nacres, red blood cells and yeast cells. He also read this dissertation carefully and provided numerous suggestions and corrections. I am also grateful to all the Structural Engineering staff, especially Daryl Rysdyk for helping me solve computer problems and Debra Bomar for helping me prepare various documents.

I would like to thank Professor David Benson and Professor Yuri Bazilevs for their patience in teaching me finite element methods for solid and fluid, respectively. I would like to thank Professor Yijun Liu from the University of Cincinnati for offering me the NSF fellowship to attend the NSF workshop on the Boundary Element Method. I am also thankful to Professor Juan Carlos del Alamo from Mechanical Engineering for teaching me cellular mechanics.

Last but certainly not least, I would like to thank my parents for their tremendous supports. My gratitude is extended to all the friends in the UCSD Chinese Student Fellowship for their love.

I would like to acknowledge the funding support from the National Heart, Lung, and Blood Institute under award number R01HL092793, which made the research presented in this dissertation possible.

Chapter 2 and Chapter 3, in part, are a reprint of the material as it appears in 'Multiscale modeling of erythrocyte membranes', *Physical Review E*, **81**: 031904, 2010. Zhangli Peng, Robert J. Asaro and Qiang Zhu, 2010. The dissertation author was the primary investigator and author of this paper.

Chapter 4 and Chapter 5, in part, have been submitted for publication of the material as it may appear in 'Molecular-detailed modeling of erythrocytes in Stokes flow', *Journal of Fluid Mechanics*, 2011. Zhangli Peng, Robert J. Asaro and Qiang Zhu, 2011. The dissertation author was the primary investigator and author of this paper.

VITA

2004	Bachelor of Science in Civil Engineering, Tongji University, China
2006	Master of Science in Structural Engineering, Zhejiang University, China
2011	Doctor of Philosophy in Structural Engineering, University of California, San Diego

HONORS & AWARDS

NSF Fellowship, NSF Boundary Element Method Workshop, 2010

Best Poster Award, NSF Boundary Element Method Workshop, 2010

PUBLICATIONS

Macromolecular structure of the organic framework of nacre in haliotis rufescens: visco-elastic response
Jiddu Bezares, Zhangli Peng, Robert J. Asaro, and Qiang Zhu. (In preparation)

Molecular-detailed modeling of erythrocytes in Stokes flow
Zhangli Peng, Robert J. Asaro, and Qiang Zhu. (Submitted to Journal of Fluid Mechanics)

Multiscale modeling of erythrocyte membranes
Zhangli Peng, Robert J. Asaro, and Qiang Zhu, *Physical Review E*, 81: 031904, 2010. pdf

Energy harvesting through flow-induced oscillations of a foil
Zhangli Peng and Qiang Zhu, *Physics of Fluids*, 21: 123602, 2009.

Mode coupling and flow energy harvesting by a flapping foil
Qiang Zhu and Zhangli Peng, *Physics of Fluids*, 21: 033601, 2009.

A new tensegrity module -"Torus"
Xingfei Yuan, Zhangli Peng and Shilin Dong, Baojun Zhao, *Advances in Structural Engineering*, 11: 243-251, 2008.

Study and application of tensegrity torus
Xingfei Yuan, Zhangli Peng, Shilin Dong, *China Civil Engineering Journal*, 41:8-13, 2008.

Load-carrying capacity of welded hollow spherical joints subject to combined planar tri-directional axial force and bending moment
Xingfei Yuan, Zhangli Peng and Shilin Dong, *Journal of Zhejiang University (Engineering Science)*, 41:1436-1442, 2007.

Tensegrity Torus
Zhangli Peng, Xingfei Yuan, and Shilin Dong, *Spatial Structures*, 13:60-64, 2007.

TEACHING EXPERIENCE

TA, *Nonlinear Finite Element Method and Isogeometric Analysis* (SE276C/MAE232C), Spring 2010 (graduate course, instructor Professor David Benson)

TA, *Mechanical Vibration* (SE101C/MAE130C), Fall 2008 (undergraduate course, instructor Professor Qiang Zhu)

PRESENTATIONS

Talk, The 54th Annual Meeting of the Biophysical Society, San Francisco, 2010.

Talk, The 63rd Annual Meeting of the APS/DFD, Long Beach, 2010.

Talk, Departmental Seminar of Structural Engineering, UC San Diego, 2010.

Talk, Jacobs Innovators Forum of Jacob Engineering School, UC San Diego, 2011.

Talk, All Graduate Symposium, UC San Diego, 2010.

Poster, NSF Boundary Element Method Workshop, University of Akron, Ohio, 2010.

Poster, Research Expo of Jacob Engineering School, UC San Diego, 2010.

Poster, Research Expo of Jacob Engineering School, UC San Diego, 2009.

ABSTRACT OF THE DISSERTATION

Multiscale Modeling of a Red Blood Cell and its Fluid-Structure Interaction

by

Zhangli Peng
Doctor of Philosophy in Structural Engineering
University of California San Diego, 2011
Professor Qiang Zhu, Chair

We develop a three-level multiscale approach of the red blood cell (RBC) membrane and couple this approach with a boundary element method (BEM) for the surrounding Stokes flow to simulate the mechanical behavior of a RBC under various *in vitro* and *in vivo* conditions.

Our multiscale approach of this membrane includes three models: in the whole cell level (Level III), a finite element method (FEM) is employed to model the lipid bilayer and the cytoskeleton as two distinct layers of shells with sliding-only interaction. The mechanical properties of the cytoskeleton are obtained from a coarse-grained molecular dynamics model (Level II) of the junctional complex. The spectrin, a major protein of the cytoskeleton, is simulated using a molecular-based constitutive model (Level I), including its domain folding/unfolding reactions. A BEM of the surrounding Stokes flow is coupled with the FEM model of the membrane through a staggered coupling algorithm.

Using this method, we first predict the resting shapes of healthy and diseased RBCs.

Secondly, we simulate three quasi-static experiments of the micropipette aspiration, the optical tweezer stretching, and the flow channel stretching. Detailed distributions of the bilayer-skeleton interaction force that may cause their dissociation and lead to phenomena such as vesiculation are predicted. Specifically, our model

predicts a correlation between the occurrence of spectrin unfolding and increase in the mechanical load upon individual bilayer-skeleton pinning points in micropipette aspirations. A simulation of the necking process after bilayer-skeleton dissociation is also conducted.

Thirdly, we study RBC dynamics in capillary flow and find that the skeleton density is large near the vessel wall, and the maximum bilayer-skeleton interaction force occurs at the trailing edge.

Finally, we investigate the tumbling, tank-treading, and swinging motions of RBCs in shear flow. The dependencies of tank-treading frequency on the blood plasma viscosity and the membrane viscosity we found match well with the existing experimental and computational data. The simulation results show that during tank-treading there is almost no protein density variation of the skeleton due to the significant bilayer-skeleton friction. The distributions of shear deformation, bilayer-skeleton interaction forces are also predicted.

Chapter 1

Introduction: Structure vs. Function

The investigation of the molecular structure vs. physiological functions of cells is at the frontier of today's scientific adventure (Discher *et al.*, 2009; Lim *et al.*, 2006). Among all types of cells, erythrocyte (red blood cell, or RBC) possesses one of the simplest and best characterized molecular structure as well as several critical physiological functions. In the following, the molecular structure of red blood cells and their physiological functions are presented.

1.1 The molecular structure of red blood cells

Without a nucleus, a mature RBC contains a liquid cytosol enclosed within a highly flexible yet surprisingly strong cell membrane. This composite membrane, consisting of a lipid bilayer supported from inside by a cytoskeleton as shown in Fig. 1.1a, is essential to the structural integrity, the stability and the beautiful biconcave shape of the RBC.

The lipid bilayer is a thin membrane made of two layers of lipid molecules. It is a two-dimensional liquid with almost zero shear stiffness and a thickness of 4 nm.

The cytoskeleton is a protein network. It is composed of several major proteins: α and β spectrin (Sp), ankyrin, band 3, protein 4.1, protein 4.2, and actin, as well as some minor proteins such as myosin, tropomyosin (TM), and tropomodulin

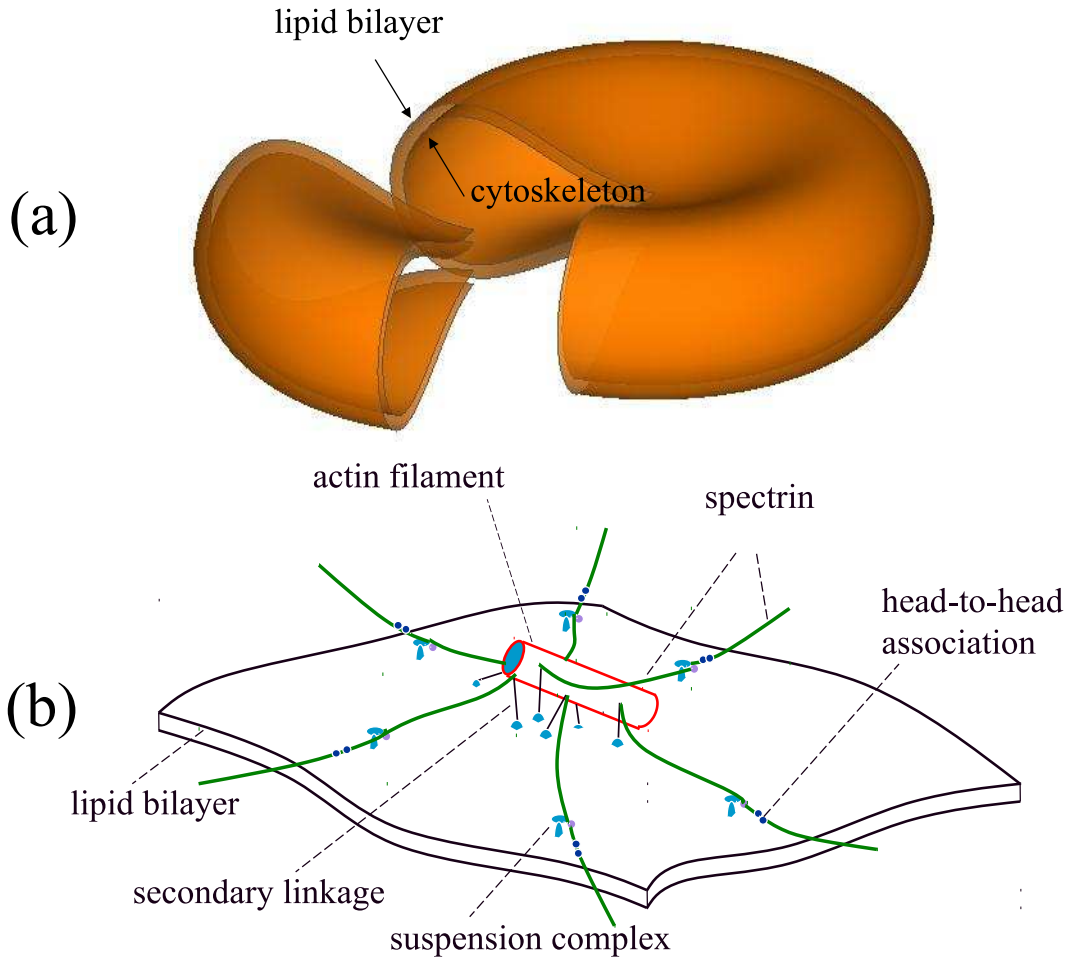

Figure 1.1: (a) Red blood cell membrane consisting of the lipid bilayer and the cytoskeleton. (b) Molecular-detailed structure of the junctional complex (JC).

(E-Tmod). Structurally, the cytoskeleton is organized into approximately 33,000 repeating units called junctional complexes (JCs) as shown in Fig. 1.1b. As revealed by transmission electron microscopy (TEM), each JC is viewed as a small "spoked" but edge-free hexagon, with 6 long $\alpha\beta$ spectrin dimers radiating from a central short actin protofilament. Spectrins behavior like cables or strings, and actin protofilaments are like cylinders. These repeating units connect with each other through the head-to-head association of Sp dimers from two neighboring units (Cohen *et al.*, 1980). The basic molecular architecture of a JC, and its connectivity with the lipid bilayer, is shown in Fig. 1.1b.

Besides the junctional complex (JC), there is also another basic unit in the cytoskeleton called suspension complex. Suspension complexes (SCs) function as the primary connections between the protein network (the cytoskeleton) and the lipid bilayer (Bruce *et al.*, 2003). A SC consists mainly of band 3 (a transmembrane protein), ankyrin, and protein 4.2 (Bennett and Stenbuck, 1979). The secondary linkage between the protein network to the lipid bilayer involves the actin (Chang and Low, 2001), protein 4.1 and the glycophorin C, another transmembrane protein with a single transmembrane domain (Reid *et al.*, 1990).

1.2 The physiological functions of red blood cells

1.2.1 The primary physiological function

The primary physiological function of erythrocytes (red blood cells, or RBCs) is to deliver oxygen to the tissues through blood flow. Its cytoplasm is rich in hemoglobin, an iron-containing biomolecule that can bind oxygen and is responsible for the blood's red color. Red blood cells take up oxygen in the lungs and release it while squeezing through the body's capillaries. Capillaries are tiny blood vessels. Hemoglobin in the erythrocytes also carries some of the waste product carbon dioxide back from the tissues; most waste carbon dioxide, however, is transported back to the pulmonary capillaries of the lungs as bicarbonate dissolved in the blood plasma.

The diameter of a red blood cell is around 7.8 μm (Fung, 1993) and the diameter of a capillary which RBCs pass through may be as small as 3 μm. During this

process, the red blood cell routinely undergoes large deformations and even structural remodeling. These deformations are determined by the molecular structure of its membrane as well as its interaction with the surrounding tissues and fluids.

1.2.2 Secondary physiological functions

Red blood cells also have several secondary physiological functions.

They can release ATP (adenosine triphosphate) which causes the vessel walls to relax and dilate so as to promote normal blood flow, when they undergo shear stress in blood vessels (Wan *et al.*, 2008). When their hemoglobin molecules are deoxygenated, erythrocytes release S-nitrosothiols which also acts to dilate vessels (Diesen *et al.*, 2008), thus directing more blood to areas of the body depleted of oxygen.

It has been recently demonstrated that erythrocytes can also synthesize nitric oxide (NO) enzymatically, using L-arginine as substrate, just like endothelial cells (Kleinbongard *et al.*, 2009). Endothelial cells are cells that line up the interior surface of blood vessels, forming an interface between circulating blood in the lumen and the rest of the vessel wall. Exposure of erythrocytes to physiological levels of shear stress activates nitric oxide (NO) synthase and export of nitric oxide, which may contribute to the regulation of vascular tonus (Ulker *et al.*, 2009), which is the continuous and passive partial contraction of the arterioles (a small diameter blood vessel in the microcirculation that extends and branches out from an artery and leads to capillaries).

Erythrocytes can also produce hydrogen sulfide, a signalling gas that acts to relax vessel walls. It is believed that the cardioprotective effects of garlic are due to erythrocytes converting its sulfur compounds into hydrogen sulfide (Benavides *et al.*, 2007).

The erythrocyte also plays an important role in the body's immune response. When lysed by pathogens such as bacteria, their hemoglobin releases free radicals which break down the pathogen's cell wall and membrane, and kill it (Jiang *et al.*, 2007).

1.3 Motivations

To explore the relationships between the molecular structure of the RBC and its physiological functions as described above, this dissertation presents a multiscale modeling of a RBC and its fluid-structure interaction, and focuses on the mechanical aspect of these structure-function relationships. Specifically, there are several general motivations for the research on red blood cell biomechanics.

1.3.1 Red blood cell diseases and dysfunctions

First, there are more than 1 billion people (1 in 6 humans in the world) are affected by red cell abnormalities as a result of natural selection driven by severe forms of malaria (Mohandas and Gallagher, 2008), which makes them the most common of inherited disorders.

Many of these abnormalities are related to the altered mechanical properties of the red blood cell membrane. It is crucial to understand these abnormalities from a mechanical point of view before we can make significant steps in treatments of these diseases. For example, the mechanical properties, structural stability, and occurrence of mechanically induced structural remodeling and phase transitions of RBCs are affected by a number of genetic defects. Typical defects include: (a) Southeast Asian ovalocytosis (SAO) (Palek and Lambert (1990); Jarolim *et al.* (1991); Liu *et al.* (1995); Sarabia *et al.* (1993); Liu *et al.* (1990); Liu *et al.* (1995); (b) Hereditary spherocytosis (HS) (Savvides *et al.* (1993); Palek and Lambert (1993); Liu *et al.* (1990); Waugh and Agre (1988)); (c) Hereditary pyropoikilocytosis (HPP) (Liu *et al.* (1990); Waugh (1983)); and (d) Hereditary elliptocytosis (HE) (Liu *et al.* (1983); Waugh (1983)). These mutations affect the intra-protein and inter-protein interactions in the skeleton as well as the skeleton-bilayer connectivity, and lead to variations in the mechanical properties of the cell and its malfunction.

Besides these genetic defects of membrane proteins, in malaria and sickle cell disease, the mechanical properties of red blood cells are changed dramatically as well. Malaria is a parasitic disease that involves high fevers, shaking chills, flu-like symptoms, and anemia. The sickle cell disease is a blood disorder characterized by red blood cells that assume an abnormal, rigid, sickle shape because of a mutation in

the hemoglobin gene. A detailed review of these diseases from a mechanical point of view can be found in Diez-Silva *et al.* (2010).

Even for a healthy red blood cell, its structural integrity is known to be altered by mechanical loads. In natural conditions, during its life span of approximately four months, a RBC circulates around the circulatory system. During this process the cell sustains large dynamic deformation owing to the combined effect of the fluid loading and confinement within capillaries and the slits of venous sinuses such as in the spleen (Mebius and Kraal, 2004). The loading associated with such deformation may affect the structural integrity of the cell (especially for those cells with molecular defects), as manifested in structural remodeling, structural failure and cell dysfunction.

The possibility of flow-induced cell damage is more pronounced within artificially-created flow fields inside mechanical circulatory support apparatus (for example within artificial blood pumps). It has been reported that flow with high shear rates and strong turbulence inside artificial heart valves can destroy these cells, causing blood hemolysis (see for example Deutsch *et al.*, 2006).

1.3.2 Model system for general cellular mechanics

The second motivation for red blood cell biomechanics research is that the red blood cell can be studied as a model system for general cellular mechanics since it possesses one of the simplest and best characterized molecular architectures.

The red blood cell has no nucleus and its cytoskeleton is on a two-dimensional surface. Most proteins in the RBC cytoskeleton have been extensively studied, *e.g.* spectrin (Rief *et al.*, 1997; Law *et al.*, 2003) and ankyrin (Lee *et al.*, 2006), and these proteins are organized in a very regular geometry as shown in Fig. 1.1b. However, a general animal cell usually has a nucleus, many organelles and a three-dimensional cytoskeleton consisting of actin filaments, intermediate filaments and microtubules. For most of these cells, the intracellular architecture is very complicated. Neither the exact geometry nor the connectivities between proteins are very clear. In addition, cells such as white blood cells and endothelial cells can actively generate forces and migrate by the growth of actin filaments and the contractility of myosin proteins. The motility behavior makes it harder to study these cells, while red blood cells are

almost passive. Owing to the simplicity of RBC and the large amount of data of its molecular architecture, it serves as an ideal model system for structure vs. response and fluid-structure interactions of living cells.

The biomechanical studies on red blood cells greatly facilitated the general cellular mechanics (Fung, 1993). For example, significant advances were made in understanding the mechanical properties of the lipid bilayer through red blood cell research (Seifert, 1997). Furthemore, many cells have a cortical cytoskeleton made of actin filaments. The investigation of the bilayer-skeleton interaction, which is the focus of this dissertation, may shed insights on the interaction between the lipid bilayer and the cortical cytoskeleton for general cells.

Finally, a lot of cells circulate around the circulatory system through blood flow, *e.g.,* white blood cells and cancer cells. The fluid-structure interaction model of red blood cells may help understand the circulation of these cells in many aspects.

1.3.3 Biomimetic applications

The red blood cell has a very strong yet flexible membrane structure. It can pass through a capillary with a much smaller diameter. As mentioned before, the diameter of a red blood cell is around 7.8 μm (Fung, 1993) and the diameter of a capillary through which RBCs pass may be as small as 3 μm. Furthermore, red blood cells need to squeeze through these capillaries about half a million times in their lifetime.

This remarkable mechanical performance may inspire many biomimetic applications. For example, Skelton and de Oliveira (2009) showed that the red blood cell cytoskeleton may be organized based on an architectural concept of tensegrity, which is a conjunction of the two words *tension* and *integrity*. Tensegrity is a type of structure with an integrity based on a balance between tension and compression components. In a tensegrity structure the compressive members are connected to each other by tensile members. For example, I made a tensegrity torus consisting of cables and bars shown in Fig. 1.2 (see Peng *et al.* (2007); Yuan *et al.* (2008)). The biologist Don Ingber at Harvard proposed tensegrity models of other cell cytoskeletons (see for example Wang *et al.* (1997)). It was found that the mechanical behavior in living

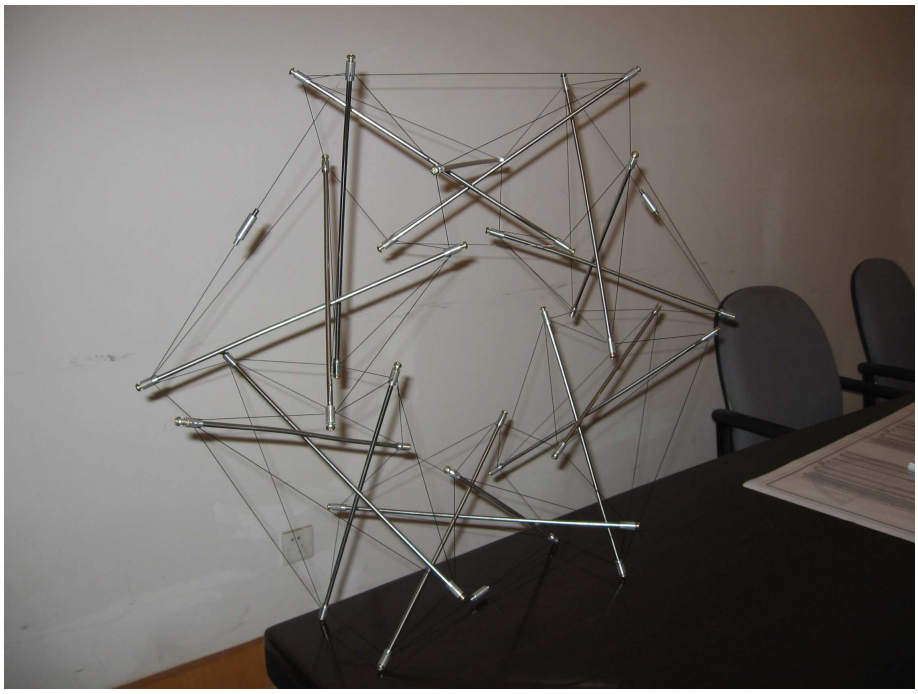

(a)

(b)

Figure 1.2: (a) Tensegrity torus (Peng *et al.*, 2007). (b) Local connections.

animal cells is consistent with the tensegrity model. We may be able to build high performance artificial structures with special features by learning from the molecular structures of red blood cells and other cells.

1.4 Canonical experiments on red blood cells

Before the existing studies are reviewed, I would like to briefly describe several important and canonical experiments conducted on red blood cells to determine their mechanical properties. Since these experiments will be studied and simulated extensively in this dissertation, it is desirable to introduce them first in this chapter.

1.4.1 Micropipette aspiration

Micropipette aspiration is one of the most useful experiments for determining the mechanical properties of cells (Lim *et al.*, 2006). It is also one of the earliest methods used to study red blood cells (Jay, 1973; Jay and Canham, 1973). In this experiment, a tiny glass pipette (tube) with a diameter around 2-5 μm is prepared. By connecting it to a pressure system (*e.g.,* a U-tube system), a negative pressure is applied to aspirate (suck) the cell into the micropipette as shown in Fig. 1.3a. The predicted shape from our simulation is also shown in 1.3b. The contour shows the skeleton density variation, which will be explained in Chapter 3.

By applying this technique on red blood cells and labeling the membrane proteins using fluorescence imaging, several important phenomena can be observed, including the relationship between aspiraton length and pressure, skeleton density variation, vesiculation and necking. Utilizing fluorescence imaging, membrane proteins (*e.g.* spectrins, band 3 and ankyrin) are labeled with different fluorescent markers. Based on the intensity of the fluorescence image, the protein density variation can be measured (Discher *et al.*, 1994). In vesiculation, a small portion of the lipid bilayer will separate (detach) from the cytoskeleton and form a lipid vesicle when the negative pressure is extremely large. Before this vesiculation, a necking usually happens for the tongue of the cell aspirated into the pipette.

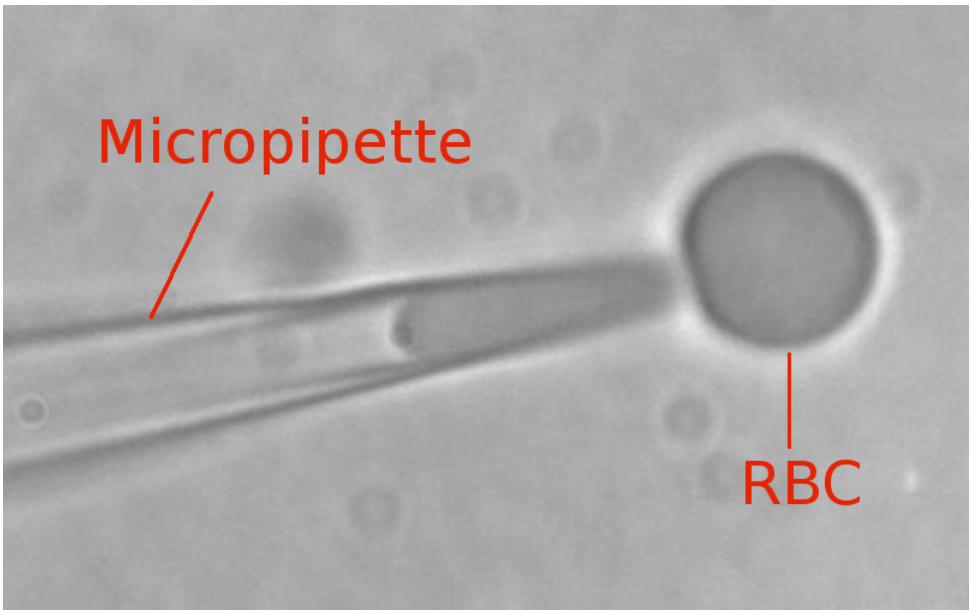

(a)

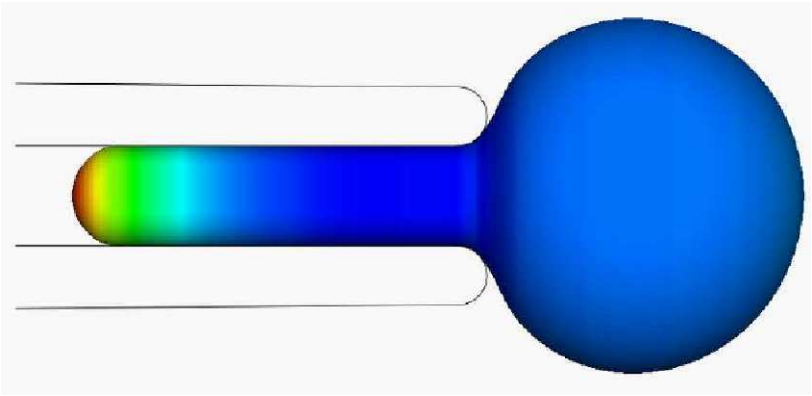

(b)

Figure 1.3: (a) Micropipette aspiration experiment (Courtesy of Dr. Carlos Vera, Bioengineering, UC San Diego). (b) Simulation of micropipette aspiration.

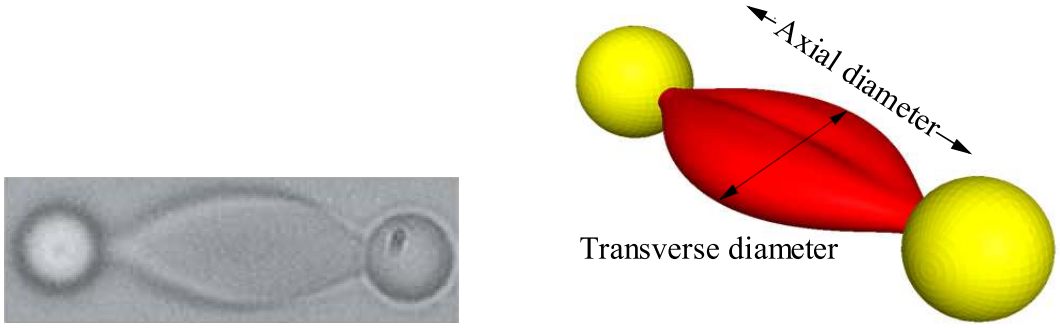

(a) (b)

Figure 1.4: (a) Optical tweezer stretching of a red blood cell (Reprinted from Dao *et al.* (2006), with kind permission from Elsevier. Courtesy of Dr. Ming Dao, Mechanical Engineering, MIT). (b) Simulation of optical tweezer stretching.

1.4.2 Optical tweezer stretching

Optical tweezers are scientific instruments that use a highly-focused laser beam to provide an attractive or repulsive force (typically on the order of piconewtons), depending on the refractive index mismatch to physically hold and move microscopic dielectric objects. In the optical tweezer stretching of red blood cells, an erythrocyte is stretched by two attached beads at two ends. The motion of two beads is optically controlled by laser beams as shown in Fig. 1.4. As reported by Dao *et al.* (2006), the stretching force is applied by two silica beads, which are attached at the opposite ends of the cell over a small oval region with a diameter of 1$\sim$2 μm. Using this technique, the quasi-static and dynamic mechanical properties of healthy and diseased red blood cells can be extracted.

1.4.3 Flow channel stretching

Flow channel stretching experiments have been developed to examine the response of cells attached to a substrate under shear stresses exerted by an incoming flow. This is also called flow channel shearing. In order to distinguish it from the experiment by imposing shear flow on red blood cells using a rheometer, in this dissertation this experiment will be referred to as flow channel stretching . In a typical flow channel stretching setup, erythrocytes are allowed to sediment inside a channel consisting of two parallel plates. The substrate is coated with bovine serum albumin

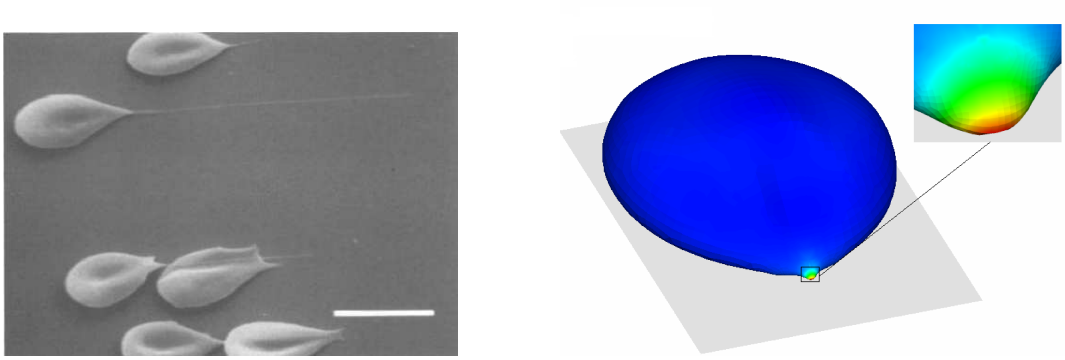

(a) (b)

Figure 1.5: (a) Flow channel stretching of a red blood cell (Reprinted from Waugh and Bauserman (1995), with kind permission from Springer Science+Business Media. Courtesy of Dr. Richard E. Waugh, Biomedical Engineering, University of Rochester). (b) Simulation of flow channel stretching.

(BSA) so that most cells do not adhere to the bottom with large attaching areas. When external flows are introduced the cells deform while one (in some cases more than one) point remains attached to the substrate. As shown in Fig. 1.5a (Waugh and Bauserman, 1995), long membrane strands (tethers) may appear when the fluidic shear surpasses a threshold value ($\sim$1.5 dyn/cm^2, or 0.15 pN/μm^2) (Hochmuth, 1973). A simulation of this experiment is shown in Fig. 1.5b.

1.4.4 Microfluidic experiments of tube flow and shear flow

There are two major microfluidic experiments on red blood cells. For example, red blood cells can be pumped to pass through small flow channels made of glass tubes to mimick capillary flow, in which the tube is usually larger than the glass tube in micropipette experiment as shown in Fig. 1.6a (Pozrikidis, 2003a; Pries and Secomb, 2008). The other important microfluidic experiment is to impose a shearing flow on the red blood cells using rheometers (Abkarian *et al.*, 2007; Fischer, 2004) as illustrated in Fig. 1.6b (Pozrikidis, 2003a), in which the red blood cells are suspended in a free space. It is different from the flow channel stretching experiment, in which some small regions of the red blood cells are attached to the subtrate. Fig. 1.6b shows a time sequence of the cell images. The time direction is from top left to top right, then from bottom left to bottom right. A bead is attached to the RBC membrane

and circulates around the cell in a tank-treading motion. A comprehensive review of microfluidic experiments on red blood cells can be found in Abkarian *et al.* (2008).

1.5 Existing studies

Due to its important physiological functions and structural simplicity, the mechanics of the red blood cell has been extensively studied during the past fifty years. Existing studies fall into three categories: (I) those concentrating on the macroscopic response of the complete cell, including experimental investigations using micropipettes (see for example Waugh and Evans, 1979; Discher *et al.*, 1994), optical tweezers (Henon, 1999; Sleep *et al.*, 1999; Dao *et al.*, 2003), optical magnetic twisting cytometry (Puig-De-Morales-Marinkovic *et al.*, 2007), full-field laser interferometry techniques (Park *et al.*, 2009), as well as numerical models of complete cells without considering effects of surrounding fluids (Discher *et al.*, 1998; Dao *et al.*, 2006; Li *et al.*, 2007; Kabaso *et al.*, 2010); (II) those focusing on the mechanical response and constitutive properties of single molecules or interconnectivity between molecules, for example that of spectrin (Rief *et al.*, 1997; Law *et al.*, 2003) or of ankryn (Lee *et al.*, 2006), by using atomic force microscopy (AFM) or molecular-dynamics (MD) simulations; (III) those focusing on fluid-structure interactions, including *in vitro* experiments using flow channels (Hochmuth, 1973; Berk and Hochmuth, 1992), microfluidic tools (see for example Fischer, 2004; Abkarian *et al.*, 2007), as well as various analytical and numerical studies (see for example Pozrikidis, 2003a, 2010). Since the primary goal of this dissertation focuses on the whole cell behavior, more detailed reviews are given on categories I and III as follows.

1.5.1 Macroscopic response of the complete cell

In earlier studies, Evans and Fung (1972) measured the biconcave geometry of red blood cells very precisely. An insightful theoretical consideration of the membrane equilibrium was given in the book by Fung (1993). Evans and Skalak (1980) established an elasticity theory of the red blood cell membrane. Despite extensive investigations in the past few decades, there are still many remaining questions about

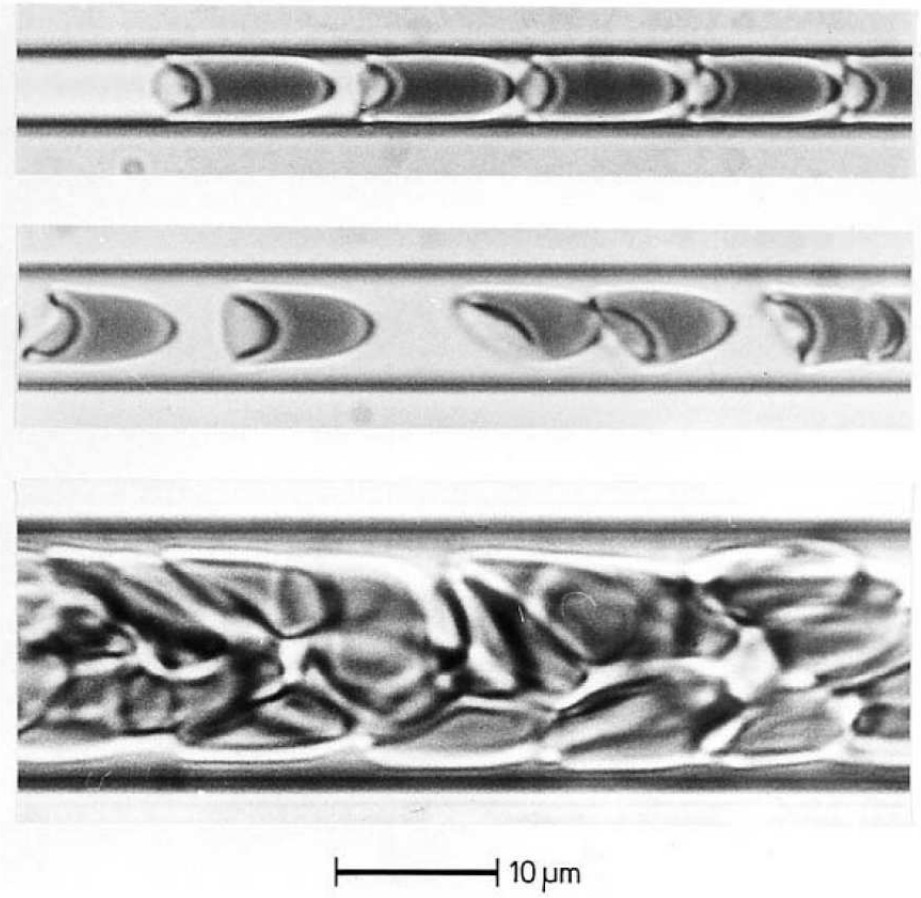

(a)

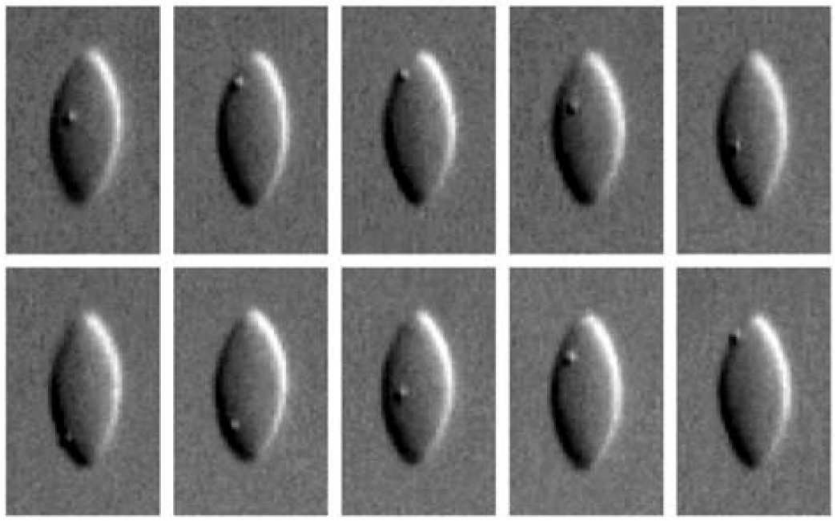

(b)

Figure 1.6: (a) Red blood cells in glass tubes (Reprinted from Pozrikidis (2003a), with kind permission from CRC PRESS LLC. Courtesy of Dr. Axel R. Pries, Free University of Berlin, Germany). (b) A red blood cell in shear flow (Reprinted from Pozrikidis (2003a), with kind permission from CRC PRESS LLC. Courtesy of Dr. Thomas M. Fischer, RWTH-Aachen, Germany).

the mechanics of erythrocytes. For example, it is still not fully understood what determines its resting biconcave shape (this is the first of eight mysteries about RBCs proposed by Hoffman (2001)). Herein a pivotal issue is the effect of the protein skeleton upon cell shape. Although a stomatocyte-discocyte-echinocyte sequence was obtained numerically based on the bilayer-coupled hypothesis (Lim *et al.*, 2002) and the stabilizing function of the skeleton in maintaining the biconcave shape was explored by Khairy *et al.* (2008), the relaxed stress-free reference shape of the skeleton remains controversial. Indeed, if a spherically relaxed skeleton is assumed, to obtain the biconcave shape the elasticity of the skeleton must be significantly reduced (Li *et al.*, 2005). Otherwise, nonspherical (*e.g.* biconcave (Zarda *et al.*, 1977) or oblate (Lim *et al.*, 2002; Khairy *et al.*, 2008)) relaxed shapes must be assumed. These are beyond the state-of-the-art knowledge about RBCs.

Moreover, much is unknown about the response of cells undergoing large deformations. One remaining issue is the strength of the skeleton-bilayer linkage (Hwang and Waugh, 1997). Under sufficiently large dissociation forces this linkage may rupture, causing cell remodelings such as vesiculation. The current understanding is based upon the adhesion energy theory by Hochmuth and Marcus (2002). Being essentially phenomenological, this theory does not offer much insight into the molecular origin of the lipid-skeleton dissociation. In large deformations, the effects of spectrin unfolding (Zhu and Asaro, 2008) and dissociation of spectrin head-to-head connections (Li *et al.*, 2007) upon the mechanical behavior of the cell are also unexplored.

1.5.2 Fluid-structure interaction of red blood cells

Regarding the fluid-structure interaction of RBCs, the asymptotic theories by Barthès-Biesel (1980) and Barthès-Biesel and Rallison (1981) showed the influence of interfacial elasticity on the small deformation of a capsule consisting of a thin elastic solid skin, enclosing a Newtonian incompressible liquid, and the rheology of dilute suspensions of capsules. Keller and Skalak (1982) studied the motion of a tank-treading ellipsoidal particle in a shear flow using an analytical approach. Secomb *et al.* (1986) applied lubrication theory to investigate the motion of axisymmetric RBCs in narrow capillaries (also see Halpern and Secomb, 1992). Skotheim and

Secomb (2007) obtained the complete phase diagram from tumbling to tank-treading motions for red blood cells in shear flow. Following these analytical studies, various numerical models were developed to study large deformation and non-axisymmetric cases of capsules in Stokes flows, including the boundary element methods developed by Pozrikidis (1990), Zhou and Pozrikidis (1990), Ramanujan and Pozrikidis (1998), Pozrikidis (2001), Pozrikidis (2003b), Pozrikidis (2005a), Lac *et al.* (2004), Kessler *et al.* (2004), Zhao *et al.* (2010), the immersed boundary methods by Eggleton and Popel (1998), Bagchi (2007), Zhang *et al.* (2008), Le (2010), and multiparticle collision dynamics method by Noguchi and Gompper (2005) and McWhirter *et al.* (2009). The RBC membrane is considered as a uniform continuum media in these models, and the detailed molecular structure was neglected.

1.5.3 Existing multiscale models

Recently multiscale models have been developed to study the static and dynamic response of RBCs (see for example Fedosov *et al.*, 2010a,b). These models, however, do not explicitly address the detailed internal connectivity of the cell (*e.g.* the connectivity between the protein skeleton and the lipid bilayer), making them inappropriate to use in simulations involving structural remodeling caused by large deformations. Also, important molecular-level processes such as protein unfolding were not considered due to the absence of models for molecular connectivity. Controversies arise due to the lack of detailed modeling of internal connectivity. For example, it is still not clear whether density of the cytoskeleton will change significantly during tank-treading motions. According to the model by Dodson and Dimitrakopoulos (2010), considerable area dilation of the cytoskeleton is possible. This is in contradiction with Fischer (1992), who found that during tank treading there was not enough time for bilayer-skeleton slip to happen.

1.6 Dissertation outline

Due to the limitations of existing computational models described above, this dissertation presents a new three-level multiscale model of the red blood cell mem-

brane, in which the lipid bilayer and the cytoskeleton are modeled as two distinct layers and the detailed molecular structures are considered as well.

The rest of this dissertation is organized as follows. A three-level quasi-static multiscale model is described in Chapter 2, that includes the spectrin model (Level I), the junctional complex model (Level II) and the complete cell finite element model (Level III). The continuum-based shell element and the master-slave penalty contact algorithm are formulated in details. In Chapter 3, the resting shape problem and the quasi-static experiments including optical tweezer stretching, micropipette aspiration and flow channel stretching are investigated. In Chapter 4, we extend the quasi-static multiscale model of the RBC membrane presented in Chapter 2 to a dynamic version by including the fluid-structure interaction and the membrane viscoelasticity. The fluid-bilayer interaction problem is solved by coupling the finite element method (FEM) and the boundary element method (BEM), and the corresponding cytoskeleton dynamics is also presented. In Chapter 5, red blood cell dynamics, including the deformation of a RBC in tube flow, and the tumbling, tank-treading and swinging motions of a RBC in shear flow, are studied. A final summary and future directions are provided in Chapter 6.

Chapter 2

Three-level Quasi-static Multiscale Modeling Approach

In this chapter, we describe the three-level quasi-static multiscale modeling approach of the red blood cell membrane. A dynamic version of this approach will be presented in Chapter 4. A quasi-static process is a thermodynamic process that happens infinitely slowly. However, no real process is quasi-static. If the experiments are performed at very slow rates, such as with micropipette aspiration and optical tweezer stretching, which will be described in Chapter 3, they can be treated approximately as quasi-static processes. In these experiments,the concern is with the final configuration of the deformed cell. In the beginning of this chapter, detailed background on inter- and intra-protein interactions within the red blood cell cytoskeleton is reviewed. The spectrin model (Level I), the junctional complex model (Level II) and the complete cell finite element model (Level III) are then formulated in details respectively. We also derive the mathematical formulation of the continuum-based shell element (Hughes-Liu shell element) at the complete cell level, and describe the master-slave penalty contact algorithm to calculate the bilayer-skeleton interaction and the interaction between the lipid bilayer and analytical surfaces, *e.g.,* the micropipette surface.

2.1 Background on inter- and intra-protein interactions within the red blood cell cytoskeleton

A red blood cell possesses a thin skeletal network coupled with a lipid bilayer. The network is composed primarily of flexible spectrin (Sp) dimers (a dimer is a macromolecular complex formed by two, usually non-covalently bound, macromolecules like proteins or nucleic acids), and relatively rigid actin protofilaments, and structurally organized into approximately 33,000 junctional complexes (JCs). As shown in Fig. 2.1, each JC contains a central piece of actin protofilament as well as (up to) six Sp dimers. Horizontally, the JCs are linked *via* the Sp dimer/tetramer reaction (*i.e.* the head-to-head association that connects two dimers into a tetramer). Vertically, this membrane skeleton is mainly connected to the lipid bilayer at pinning points called suspension complexes (SCs). Each SC consists of ankyrin, protein 4.2, and band 3. Band 3 is a transmembrane protein. In addition, the actin protofilaments are also connected to the lipid bilayer through protein 4.1 and glycophorin C (another transmembrane protein). This linkage is usually referred to as the secondary connection. Both band 3 and glycophorin C can drift within the lipid bilayer, rendering horizontal mobility of the skeleton-bilayer connection. Inter- and intra-protein reactions are essential to the structural integrity and mechanical response of the cell (Mohandas and Evans, 1994).

It has been illustrated that in the erythrocyte membrane there exists a dynamic equilibrium as a result of dynamic balances between associated and dissociated states of many inter-protein and protein-to-lipid linkages. These balances can be disturbed by mechanical loads. The connections that may rupture under mechanical loads include: the head-to-head association between Sp dimers that link the neighboring JCs (DeSilva *et al.*, 1992; An *et al.*, 2002), the band 3–ankyrin "bridge" that is the connection between the SC and the lipid bilayer (Anong *et al.*, 2006), the protein 4.1–band 3 connection (An *et al.*, 1996), and the band 3–lipid bilayer connection (Butler *et al.*, 2008). These dissociations dramatically change the mechanical properties of the membrane, causing structural instability and even permanently damaging the cell. For example, as shown in micropipette aspirations and flow channel experiments, the rupture of the band 3–lipid linkage causes detachment of the skeleton from the lipid

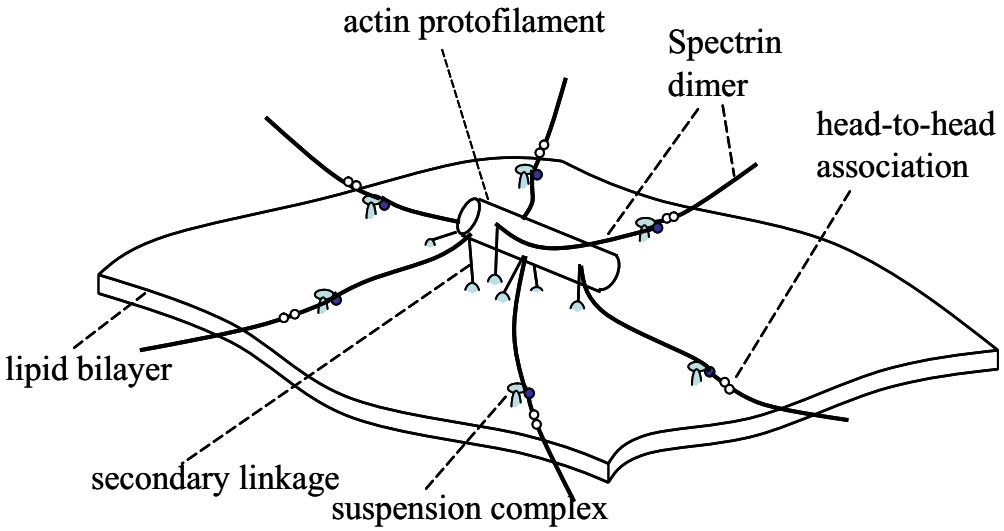

Figure 2.1: Schematic of a junctional complex (JC).

bilayer, leading to creation of vesicles (vesiculation) or tethers (Knowles *et al.*, 1997; Butler *et al.*, 2008). A vesicle is an entity formed by part of the cell membrane which contains no protein skeleton. Vesiculation is associated with membrane loss, with changes in the shape and physiology of the cell.

To understand conditions related with these cell remodeling processes, numerical models are required to correlate cell deformation to mechanical loads on these connections. Since cell deformation and mechanical forces on these connections occur at different length scales, it is desirable to develop a multiscale approach with models at different length scales to explore their relationships. In the following, our three-level multiscale approach motivated by this purpose will be presented.

2.2 Information-passing multiscale approach

The quasi-static multiscale approach consists of three models characterized by different length scales. These are referred to models at Levels I, II, and III. At the complete cell level (Level III as shown in Fig. 2.2a) the membrane is modeled as two distinct layers of continuum shells using the finite element method, in which the skeleton-bilayer interactions are depicted as a slide in the lateral (*i.e.* in-plane) direction (caused by the mobility of the skeleton-bilayer pinning points) and a normal

interaction force. The constitutive laws of the inner layer (the protein skeleton) are obtained from a molecular-detailed model of the junctional complex (Level II as shown in Fig. 2.2b). The mechanical properties of the Sp, including its domain folding/unfolding reactions, are obtained with a molecular-based thermally activated constitutive model (Level I as shown in Fig. 2.2c). These three models are coupled through an information-passing multiscale algorithm, in which predictions of Level I and Level II models are employed as constitutive laws in the Level II and Level III models, respectively. The information-passing multiscale methods are also called hierarchical multiscale methods (Fish, 2010). In these methods, the response of a representative volume or surface element at the fine-scale is first computed over a range of expected inputs, and then a stress-strain law is extracted. They are different from the concurrent multiscale methods, in which the fine-scale model is embedded in the coarse-scale model and is directly and intimately coupled to it (Fish, 2010).

In the following, these three models are described in detail, respectively.

2.3 Level I: Spectrin (Sp) model

Multidomain proteins such as spectrin (Sp) can undergo overstretching due to unfolding of domains or multiple repeats (Rief *et al.*, 1999; Lee and Discher, 2001; Law *et al.*, 2003; Paramore and Voth, 2006; Rief *et al.*, 1997) (*ref.* Fig. 2.2c). As illustrated in AFM experiments, the transient force-extension curve of Sp stretching displays a trademark sawtooth pattern related to unfolding of the domains (Rief *et al.*, 1999). Each peak in this curve corresponds to the unfolding of one or more than one domains (Law *et al.*, 2003). The exact characteristic of this curve is dependent on the rate of extension. With an infinitely slow extension rate, the quasi-static (equilibrium) force-extension curve contains a strain-stiffening part before the first unfolding event. Afterwards, a distinctive plateau appears, where the extension force remains almost a constant due to the successive unfolding of domains.

Based on this description, a quasi-static/dynamic model of a Sp was developed by Zhu and Asaro (2008). Using this model, Zhu and Asaro (2008) have quantitatively reproduced the experimentally-measured force-extension relation of a Sp. It has also been demonstrated that the calculated shear modulus near the natural configuration

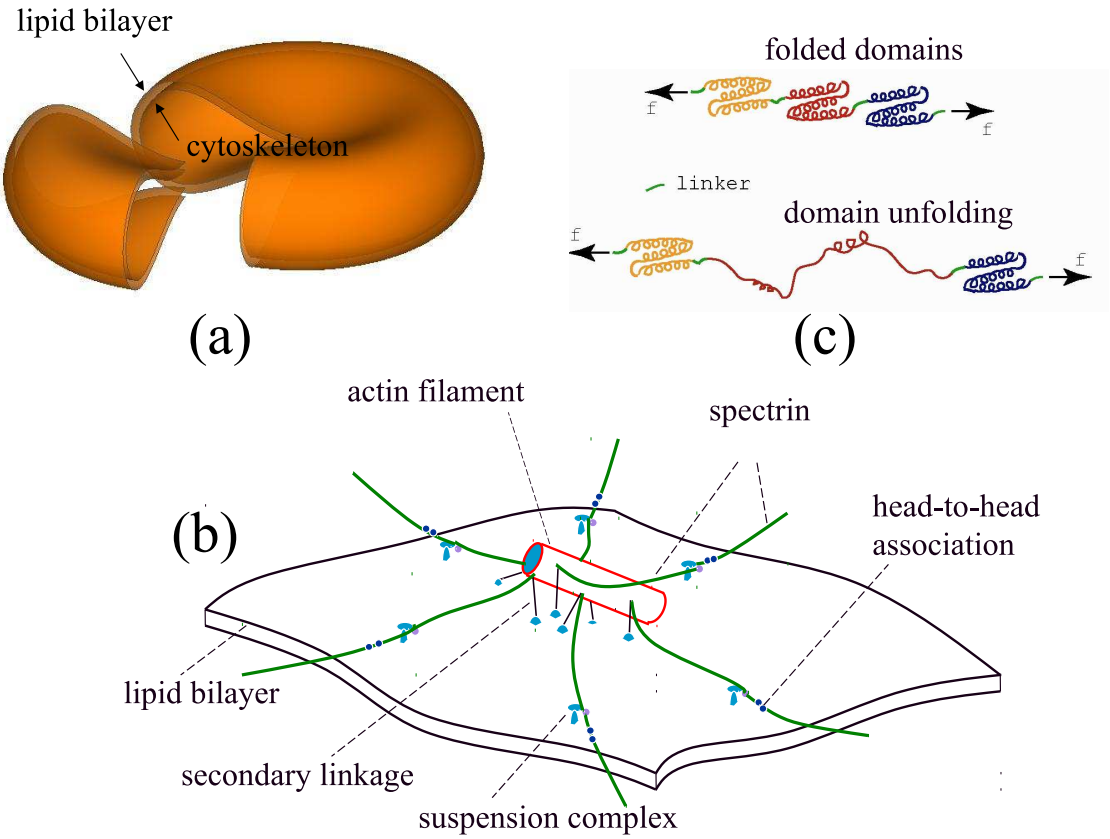

Figure 2.2: Multiscale models of an erythrocyte: (a) the double-layer continuum shell model, (b) the molecular-detailed JC model, and (c) the constitutive model of a Sp including the folding/unfolding reactions. (b) and (c) are modified from Zhu and Asaro (2008).

is consistent with those found in previous studies (around 5-10 μN/m).

2.3.1 Quasi-static response

In the quasi-static model of spectrin, Zhu and Asaro (2008) consider a Sp with N domains stretched by a force F. When there is N_f folded domains and N_u unfolded domains in a Sp (note that $N = N_u + N_f$), the projected end-to-end distance x (*i.e.* the end-to-end distance projected to the direction of F) is given as $x = N_f x_f + N_u x_u$, where x_f and x_u are the projected extensions of folded and unfolded domains, respectively. Let $\phi_u = N_u/N$, we have

$$\frac{x}{NL_f} = (1-\phi_u)\frac{x_f}{L_f} + \phi_u \frac{x_u}{L_u}\left(\frac{L_u}{L_f}\right), \tag{2.1}$$

where L_f and L_u are the contour lengths for folded and unfolded domains, respectively. The contour length of a polymer chain (a big molecule consisting of many similar smaller molecules) is its length at maximum physically possible extension.

In the equilibrium state, by considering the balance between the unfolding and the folding processes *via* the Arrhenius rate relation (the Arrhenius equation is a simple, but remarkably accurate, formula for the temperature dependence of the reaction rate constant, and therefore, rate of a chemical reaction), ϕ_u is expressed as

$$\phi_u = \frac{\exp\left(\frac{(F-F_{1/2})\Delta\Delta x^*}{k_B T}\right)}{1+\exp\left(\frac{(F-F_{1/2})\Delta\Delta x^*}{k_B T}\right)}, \tag{2.2}$$

where $\Delta\Delta x^* = \Delta x_{f\to u} - \Delta x_{u\to f}$, the difference between the activation length of the unfolding process and that of the refolding process. $F_{1/2}$ is the force F corresponding to the state when half of the domains are unfolded. k_B is the Boltzmann constant, and T is the temperature (assumed to be 300K in our simulations).

x_f/L_f and x_u/L_u can be evaluated *via* the freely joint chain model (see for example Weiner (1983)) as,

$$\frac{x_i}{L_i} = \coth\left(\frac{2Fp_i}{k_B T}\right) - \frac{k_B T}{2Fp_i},\ i = f, u, \tag{2.3}$$

where p_f and p_u are the persistence lengthes of each domain in folded and unfolded states, respectively. The persistence length is a basic mechanical property quantifying the bending stiffness of a long polymer. The persistence length is defined as

$$p_i = \frac{\kappa_i}{k_B T},\ i = f, u. \tag{2.4}$$

where κ_i is the bending stiffness of the polymer. The larger the persistence length is, the stiffer the polymer is.

x_f/L_f and x_u/L_u can be also evaluated *via* the worm-like chain (WLC) model (Discher *et al.*, 1998; Li *et al.*, 2005) as

$$F = \frac{k_B T}{p_i}\left(\frac{1}{4(1 - x_i/L_i)^2} - \frac{1}{4} + \frac{x_i}{L_i}\right),\ i = f, u. \tag{2.5}$$

The freely joint chain model and the worm-like chain (WLC) model are two most commonly used models in polymer physics to describe the behavior of semi-flexible polymers. In the following formulations and simulations, we will use the worm-like chain (WLC) model.

Based upon the molecular architecture of Sp as well as comparisons with experiments by Rief *et al.* (1999), we took: $N = 19$, $L_f = 5.3$ nm, $L_u = 39$ nm, $p_f = 8$ nm, $p_u = 0.8$ nm, $\Delta\Delta x^* = 12.6$ nm, and $F_{1/2} = 5$ nm.

2.3.2 Dynamic response

For dynamics responses of spectrins, a Monte Carlos method was used by Zhu and Asaro (2008) to study the potential influence of rate-dependent domain unfolding-refolding. Zhu and Asaro (2008) developed a simple numerical algorithm to include the kinetics of unfolding, and simulated the Atomic Force Microscopy (AFM) experiments of Rief *et al.* (1997, 1999) and Law *et al.* (2003). A constant rate of stretching is imposed in this algorithm. We compute the spectrin force based on Eqns. 2.1 to 2.5 after each time step. The probaility of unfolding is calculcated as

$$P(F) = k_{f\to u}(0)\exp(F\Delta x_{f\to u}/k_B T)\Delta t, \tag{2.6}$$

where $x_{f\to u}$ is the activation length and $k_{f\to u}$ is the rate of transition as defined in Zhu and Asaro (2008).

Based on this probability function, we poll each folded domain to determine if it should be unfolded at the new time or not. The steps of this algorithm are summarized as follows:

1. Initialize the stretching rate $\dot{x} = \partial x/\partial t$, Δt, $\Delta x_{f\to u}$, and set $x = 0$,
2. $x = x + \dot{x}\Delta t$,
3. Compute force, F, based on Eqns. 2.1 to 2.5,
4. Calculate probability P *via* Eq. 2.6,
5. Poll each folded domain for unfolding (n_b unfolds found?)
   (a) Update $\phi_u = \phi_u + n_b/N$,
   (b) Recalculate F, based on Eqns. 2.1 to 2.5,
   (c) Save (F, x), go to Step 2.

Using this model, Zhu and Asaro (2008) have quantitatively reproduced the experimentally-measured force-extension relation of a Sp.

After obtaining the force-extension relation of a Sp, it is passed to our next level model of junctional complex as the constitutive law of the spectrins.

2.4 Level II: Junctional Complex (JC) model

Our model of a JC is based upon the three-dimensional description of a single JC unit by Sung and Vera (2003) (also see Vera *et al.* (2005)) and implemented within the mechanical model of Zhu *et al.* (2007) and Zhu and Asaro (2008). According to this depiction (Fig. 2.1), in a JC the protofilament functions as a mechanical axis, anchoring 3 pairs of Sp. Each Sp pair is arranged in a back-to-back fashion.

The dynamic and quasi-static responses of individual and multiple JCs interacting with the lipid bilayer have been studied *via* a hybrid scheme that simulated the response to thermal fluctuations and applied displacements or stresses Zhu *et al.*

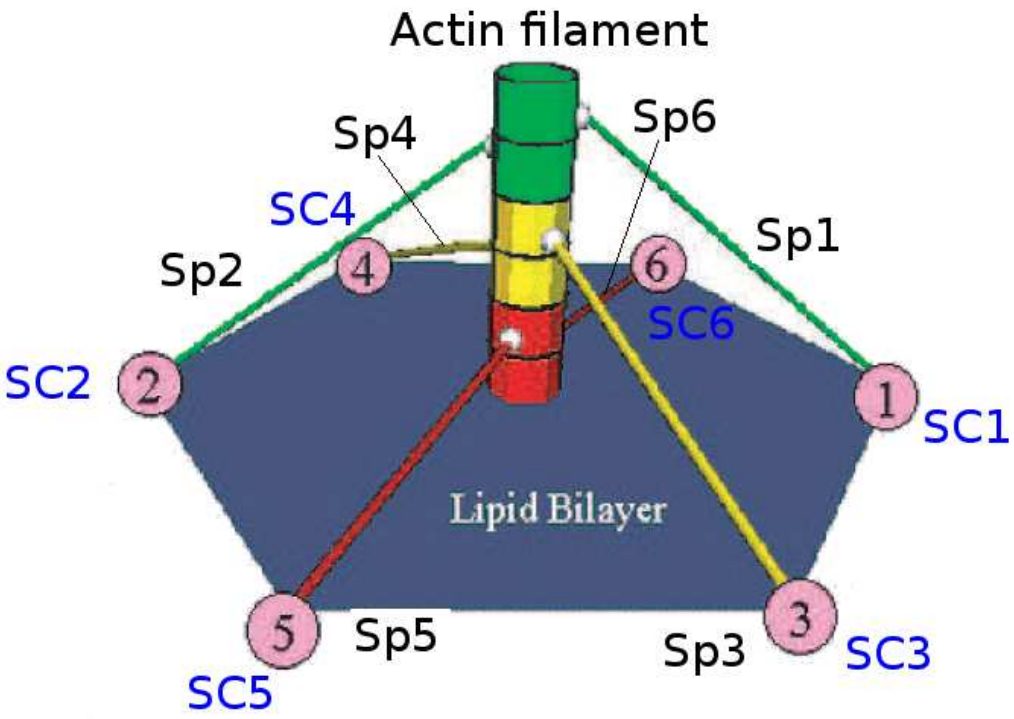

Figure 2.3: Topology of a spoked hexagon (JC) in the erythrocyte membrane skeleton - a three-dimensional view showing a protofilament with 6 pairs of G actin associated with 6 Sp. Each Sp may connect to a SC in the lipid bilayer, forming a small hexagon without physical edges. (Modified from Zhu *et al.* (2007)).

(2007); Zhu and Asaro (2008). From such simulations constitutive properties for JC units and JC assemblies are extracted, yielding shear and area moduli.

2.4.1 Physical model of the junctional complex

Vera *et al.* (2005) studied the 3-D nanomechanics of a junctional complex (JC) in red blood cells. They found the exact geometry of JC, including the structure of the actin filament and the attachment sites between the spectrin and actin filament. An actin protofilament is composed of 12-13 G-actins (globular actins) arranged in a helical fashion. Because the persistence length of the actin protofilament is about 100 times larger than its actual length in the RBC cytoskeleton, it is modeled as a rigid cylinder.

A local Lagrangian Cartesian coordinate system (x, y, z) is built within this actin filament modeled as a cylinder as shown in Fig. 2.3. The origin of this coordinate system is at the center of the actin, x is parallel to the actin, and both y and z are perpendicular to x.

Another global fixed Eulerian coordinate system (X, Y, Z) is built within the lipid bilayer, which is defined that the undisturbed lipid bilayer lies with in the $X-Y$ plane and Z points toward the JC.

An arbitrary vector $\mathbf{v}$ can be represented in either as (v_X, v_Y, v_Z) in the Eulerian system or the Lagrangian system as (v_x, v_y, v_z). The transformation between these two systems is

$$\begin{bmatrix} v_x \\ v_y \\ v_z \end{bmatrix} = \mathbf{C} \cdot \begin{bmatrix} v_X \\ v_Y \\ v_Z \end{bmatrix}, \tag{2.7}$$

where

$$\mathbf{C} = \begin{bmatrix} \beta_0^2 + \beta_1^2 - \beta_2^2 - \beta_3^2 & 2(\beta_1\beta_2 + \beta_0\beta_3) & 2(\beta_1\beta_3 - \beta_0\beta_2) \\ 2(\beta_1\beta_2 - \beta_0\beta_3) & \beta_0^2 - \beta_1^2 + \beta_2^2 - \beta_3^2 & 2(\beta_2\beta_3 - \beta_0\beta_1) \\ 2(\beta_1\beta_3 + \beta_0\beta_2) & 2(\beta_2\beta_3 - \beta_0\beta_1) & \beta_0^2 - \beta_1^2 - \beta_2^2 + \beta_3^2 \end{bmatrix}, \tag{2.8}$$

is the transformation matrix, where $\beta_0, \beta_1, \beta_2, \beta_3$ are Euler parameters, also called unit quaternions, which represent rotations in three dimensions through the use of the four numbers.

The Sp-actin attachment sites and the locations of SCs (*ref* Fig. 2.3) are shown in Tables 2.1 and 2.2, respectively.

2.4.2 Fourier Space Brownian Dynamics (FSBD) of the lipid bilayer

Based on the Langevin equation, Zhu *et al.* (2007) used Fourier Space Brownian Dynamics (FSBD) to model the lipid bilayer, stemming from the work by Lin and Brown (2005). In statistical physics, a Langevin equation (Langevin, 1908) is a stochastic differential equation describing the time evolution of a subset of the degrees

Table 2.1: Sp-actin attachment sites in the local Lagrangian Cartesian coordinate system (x, y, z)

Spectrins	Sp-actin attachment sites
Sp_1	(12.38,0,4.5)
Sp_2	(9.63,-1.08,-4.37)
Sp_3	(1.38,3.70,2.56)
Sp_4	(-1.38,-4.21,-1.60)
Sp_5	(-9.63,4.21,-1.60)
Sp_6	(-12.38,-3.70,2.56)

Table 2.2: SC sites in the global Eulerian coordinate system (X, Y, Z)

SC	SC sites in the lipid bilayer
SC_1	(0,30,0)
SC_2	(0,-30,0)
SC_3	(26,15,0)
SC_4	(-26,-15,0)
SC_5	(26,-15,0)
SC_6	(-26,15,0)

of freedom. These degrees of freedom typically are collective (macroscopic) variables changing only slowly in comparison to the other (microscopic) variables of the system. The nonlocal Langevin equation for a lipid bilayer with uniform tension σ is written as,

$$\frac{\partial h(\mathbf{X},t)}{\partial t} = \iint d\mathbf{X}'\mathbf{\Lambda}(\mathbf{X}-\mathbf{X}')[-\kappa_c \bigtriangledown^4 h(\mathbf{X}',t) + \sigma \bigtriangledown^2 h(\mathbf{X}',t) + F(\mathbf{X}',t) + \zeta(\mathbf{X}',t)], \tag{2.9}$$

where h is the vertical position of the bilayer. $\mathbf{\Lambda}(\mathbf{X}-\mathbf{X}') = 1/8\pi\eta_f|\mathbf{X}-\mathbf{X}'|$ is the diagonal component of the Oseen hydrodynamic tensor, η_f is the dynamic viscosity of the surrounding fluid, and κ_c the bending modulus of the bilayer. σ is the existing tension. $F(\mathbf{X}',t)$ and $\zeta(\mathbf{X}',t)$ are the interaction force (Z direction) and the random thermal fluctuation force respectively.

The interaction force (Z direction) can be divided into the following three

parts as,

$$F(\mathbf{X},t) = F^{(c)}(\mathbf{X},t) + F^{(p)}(\mathbf{X},t) + F^{(s)}(\mathbf{X},t), \tag{2.10}$$

where $F^{(c)}(\mathbf{X},t)$ is the force due to the tension of spectrins, $F^{(p)}(\mathbf{X},t)$ the repulsive force between the bilayer and the actin, $F^{(s)}(\mathbf{X},t)$ the repulsive force between spectrins and the bilayer.

$$F^{(c)}(\mathbf{X},t) = \sum_{i=1}^{6} \frac{f_{iZ}(t)}{\pi(l/4)^2} \exp\left(-\left|\frac{\mathbf{X}-\mathbf{X}^{(c)}}{c_1/4}\right|^2\right), \tag{2.11}$$

where $f_{iZ}(t)$ is the Z-component of the stretching force inside the i^{th} Sp, which is evaluated based on the spectrin model (Level I). c_1 is a localization parameter. $\mathbf{X}^{(c)}$ is the location of the SCs as shown in Table 2.2. l is the length of the spectrin.

$$F^{(p)}(\mathbf{X},t) = -\gamma \sum_{\alpha=1}^{N_p} s_\alpha \exp\left(-\frac{Z_\alpha^{(p)} - h(\mathbf{X},t)}{c_2} - \left|\frac{\mathbf{X}-\mathbf{X}^{(c)}}{c_1/4}\right|^2\right), \tag{2.12}$$

where γ is the magnitude of interaction and $c_2 = 0.2nm$ is its steepness. $F^{(p)}(\mathbf{X},t)$ is the short-range repulsive interaction force between the actin and the bilayer. The actin protofilament is divided into N_p elements. $(\mathbf{X}_\alpha^{(p)}, Z_\alpha^{(p)})$ is the center of each element with area $s_\alpha(\alpha = 1, ..., N_p)$.

$$F^{(s)}(\mathbf{X},t) = \eta \sum_{i=1}^{6} \exp\left(-\frac{Z_{Pi} - h(\mathbf{X},t)}{c_2} - \frac{1}{A_i^2 + B_i^2}\left[\frac{A_iX + B_iY + C_i}{c_1/4}\right]^2\right). \tag{2.13}$$

where η is a constant characterizing the magnitude of the repulsive interaction. $A_iX + B_iY + C_i = 0$ is a straight line of the projection of i^{th} spectrin on the mean plane of lipid bilayer ($Z = 0$).

Detailed descriptions of these three kinds of interaction forces can be found in Zhu *et al.* (2007).

Zhu *et al.* (2007) modeled the random thermal fluctuation force $\zeta(\mathbf{X},t)$ as a Gaussian variable with zero mean

$$\langle \zeta(\mathbf{X},t) \rangle = 0, \tag{2.14}$$

and a variance.

$$\langle \zeta(\mathbf{X},t)\zeta(\mathbf{X}',t)\rangle = 2k_BT\Lambda^{-1}(\mathbf{X}-\mathbf{X}')\delta(t-t'), \tag{2.15}$$

where k_B is Boltzmann's constant, T temperature and δ the Dirac delta-function.

Numerically, an efficient Fourier spectral algorithm is used to solve the above equations. For a doubly periodic function $f(\mathbf{X})$, the Fourier transform and reverse Fourier transform are

$$\tilde{f}(\mathbf{k}) = \iint_{L\times L} f(\mathbf{X})\exp(-i\mathbf{k}\cdot\mathbf{X})d\mathbf{X}, \tag{2.16}$$

$$f(\mathbf{X}) = \frac{1}{L^2}\iint_{L\times L} \tilde{f}(\mathbf{k})\exp(i\mathbf{k}\cdot\mathbf{X})d\mathbf{k}. \tag{2.17}$$

where $\mathbf{k} = (2m\pi/L, 2n\pi/L)$ with $m,n = -N/2, ..., N/2-1$ are $N\times N$ Fourier modes. In Fourier space Eq. 2.9 becomes

$$\frac{\partial\tilde{h}(\mathbf{k},t)}{\partial t} = \Lambda(\mathbf{k})\left[-(\kappa_c k^4+\sigma k^2)\tilde{h}(\mathbf{k},t) + \tilde{F}(\mathbf{k},t) + \tilde{\zeta}(\mathbf{k},t)\right], \tag{2.18}$$

where $k = |\mathbf{k}|$ and $\Lambda(\mathbf{k}) = 1/4\eta_f k$. The modes of Eq. 2.18 are decoupled and Eq. 2.18 can be integrated by

$$\tilde{h}(\mathbf{k},t+\Delta t) = \tilde{h}(\mathbf{k},t) + \Delta t\Lambda(\mathbf{k})\left[-(\kappa_c k^4+\sigma k^2)\tilde{h}(\mathbf{k},t) + \tilde{F}(\mathbf{k},t)\right] + R(\mathbf{k},\Delta t), \tag{2.19}$$

where $R(\mathbf{k},\Delta t)$ is the Brownian random term. The computational cost of this algorithm is only proportional to $N^2\log N^2$.

2.4.3 Dynamics of the actin protofilament

Since at this length scale, the inertial force is negligible, the motion of the actin protofilament can be described by the micro-hydrodynamics in the Stokes regime. The

linear and angular velocities are calculated as

$$v_i = \frac{f_i^{(s)} + f_i^{(b)} + f_i^{(\zeta)}}{D_i}, \tag{2.20}$$

$$\omega_i = \frac{M_i^{(s)} + M_i^{(b)} + M_i^{(\zeta)}}{D_{Mi}}, \tag{2.21}$$

$$i = x, y, z, \tag{2.22}$$

where $f_i^{(s)}, f_i^{(b)}, f_i^{(\zeta)}$ are forces on the actin due to spectrin, bilayer, Brownian fluctuation, respectively. $M_i^{(s)}, M_i^{(b)}, M_i^{(\zeta)}$ are corresponding moments. D_x is the tangential drag coefficient and $D_y = D_z$ are the normal drag coefficients. D_{Mx}, D_{My}, D_{Mz} are corresponding rotational coefficients.

The normal and tangential drag coefficients per unit length are

$$K_N = \frac{4\pi\eta_f}{\ln(2q/a) + 1/2}, \tag{2.23}$$

$$K_T = \frac{2\pi\eta_f}{\ln(2q/a)}, \tag{2.24}$$

where q is a length scale that measures the correlation length along the length of the actin, and $a = 4.5nm$ is the actin radius. Following Lamb's theory of two-dimensional Stokes flow around a circular cylinder, the normal drag coefficient is given as

$$K_N = \frac{4\pi\eta_f}{2 - \ln(Re)}, \tag{2.25}$$

where $Re = 2a\rho\sqrt{v_y^2 + v_z^2}/\eta_f$ is the Reynolds number. ρ is the density of the surrounding fluid. q is obtained by comparing Eq. 2.25 with Eq. 2.23 . Then we calculate the drag coefficients as

$$D_x = bK_T, \tag{2.26}$$

$$D_y = bK_N, \tag{2.27}$$

$$D_z = bK_N, \tag{2.28}$$

where $b = 35.75nm$ is the length of the actin filament, and

$$D_{Mx} = a^2 D_x, \tag{2.29}$$

$$D_{My} = \frac{b^2 D_y}{12}, \tag{2.30}$$

$$D_{Mz} = \frac{b^2 D_z}{12}. \tag{2.31}$$

Detailed evaluation of forces and moments $f_i^{(s)}, f_i^{(b)}, f_i^{(\zeta)}$ and $M_i^{(s)}, M_i^{(b)}, M_i^{(\zeta)}$ can be found in Zhu *et al.* (2007).

The Euler parameters of the actin protofilament orientation are then determined through

$$\begin{aligned} \frac{d}{dt}\begin{bmatrix} X_0 \\ Y_0 \\ Z_0 \end{bmatrix} &= \begin{bmatrix} v_X \\ v_Y \\ v_Z \end{bmatrix} = \mathbf{C}^{-1} \cdot \begin{bmatrix} v_x \\ v_y \\ v_z \end{bmatrix}, \\ \frac{d}{dt}\begin{bmatrix} \beta_0 \\ \beta_1 \\ \beta_2 \\ \beta_3 \end{bmatrix} &= \frac{1}{2}\begin{bmatrix} \beta_0 & -\beta_1 & -\beta_2 & -\beta_3 \\ \beta_1 & \beta_0 & -\beta_3 & \beta_2 \\ \beta_2 & \beta_3 & \beta_0 & -\beta_1 \\ \beta_3 & -\beta_2 & \beta_1 & \beta_0 \end{bmatrix} \cdot \begin{bmatrix} 0 \\ \omega_x \\ \omega_y \\ \omega_z \end{bmatrix}. \end{aligned} \tag{2.32}$$

Eq. 2.32 is integrated in time using the central difference method.

2.5 Level III: Complete cell model

Following Evans and Skalak (1980), we calculate the shear and area moduli of a JC undergoing finite deformations based upon the strain energy Φ stored in the Sp. In this approach, an arbitrary in-plane deformation is achieved by stretching in two orthogonal axes, axis 1 and axis 2, with stretching ratios λ_1 and λ_2 ($\lambda_1 \geq \lambda_2$). Two

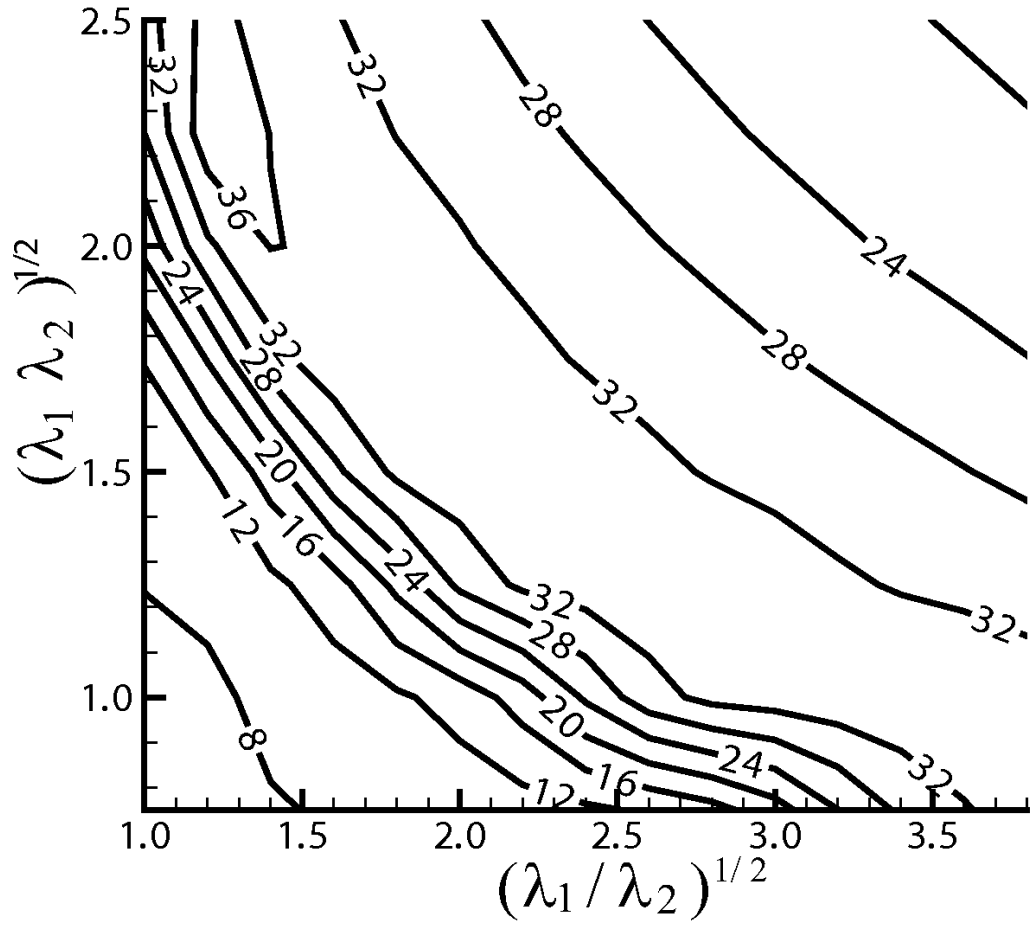

Figure 2.4: Shear modulus (μN/m) of the protein skeleton as predicted by the single-JC model containing the constitutive model of Sp.

independent deformation parameters are also defined as

$$\alpha = \lambda_1\lambda_2 - 1, \tag{2.33}$$

$$\beta = (\lambda_1^2 + \lambda_2^2)/(2\lambda_1\lambda_2) - 1. \tag{2.34}$$

It is seen that α represents area change, and β a change of aspect ratio or eccentricity, which is a measure of shear deformation.

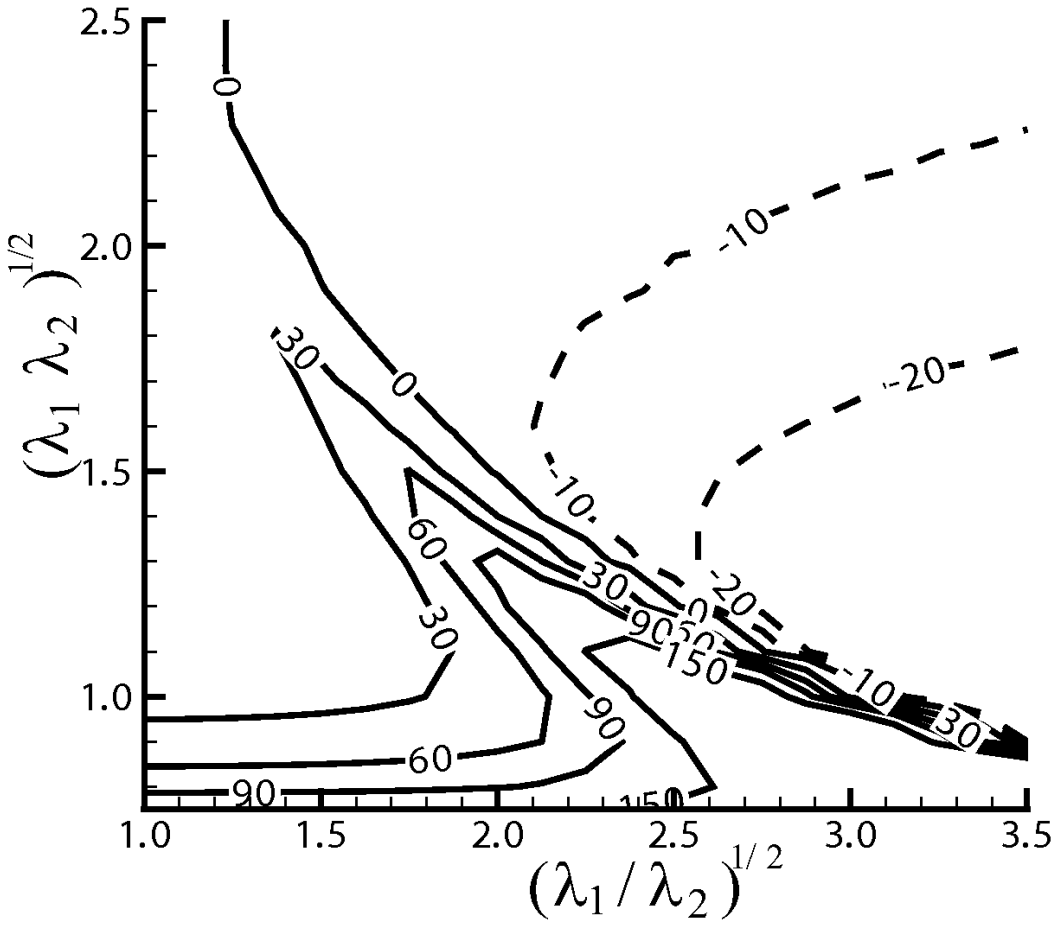

Figure 2.5: Area modulus (μN/m) of the protein skeleton as predicted by the single-JC model containing the constitutive model of Sp.

2.5.1 Shear stiffness

The shear modulus of the skeleton, μ_s, is then given as

$$\mu_s = \frac{1}{A_0}\frac{\partial \Phi}{\partial \beta}\Big|_{\alpha}, \tag{2.35}$$

where A_0 is the projected area of a JC without deformation (*i.e.* the area of the hexagon formed by the six SCs). α is a constant that corresponds to anisotropic deformation. The potential energy stored inside each Sp dimer is calculated by integrating its internal tension times the extension, starting from the natural state. Φ is then evaluated by summing up the total potential energy in the six dimers.

2.5.2 Isotropic tension and area stiffness

To obtain area stiffness, we first evaluate the isotropic tension $\bar{T}$ in an equibiaxial deformation (β = constant). We have (see Evans and Skalak (1980))

$$\bar{T} = \frac{1}{A_0}\frac{\partial \Phi}{\partial \alpha}\Big|_{\beta} - C/A^2, \tag{2.36}$$

where the second term corresponds to a steric effect in the form suggested by Discher *et al.* (1998) (see also Dao *et al.* (2006)), *i.e.* the compression of the network causes a repulsive force due to interactions among components of the protein skeleton. A_0 and A are the initial projected area of a JC and the deformed area of a JC, respectively. The value of C is determined by assuming that the tension $\bar{T}$ vanishes at the natural configuration. Applying this isotropic tension, the area modulus K_s is given as

$$K_s = \frac{\partial \bar{T}}{\partial \alpha}. \tag{2.37}$$

Using the single-JC model we performed simulations of the quasi-static and ensemble-averaged response of a JC undergoing in-plane deformation. Thermal fluctuations, which may have potential impact on local dynamic responses and cause phenomena such as mode switching Zhu *et al.* (2007), are not included in this simulation. The shear and area moduli of the protein skeleton are extracted by using Eqns. 2.35-2.37. We obtain that in its natural configuration ($\lambda_1 = \lambda_2 = 1$), the

protein skeleton has a shear modulus $\mu_s \sim 6$ μN/m, and an area modulus $K_s \sim 12$ μN/m. Both predictions are consistent with experimental measurements and model simulations reported in the literature. For a more general case, in Fig. 2.4 and Fig. 2.5 we plot μ_s and K_s of a JC undergoing general in-plane stretching (including both shear deformation and area variation) characterized by the two principle stretching ratios λ_1 and λ_2. In our calculations we use $\sqrt{\lambda_1/\lambda_2}$ and $\sqrt{\lambda_1\lambda_2}$ as metrics to measure shear and area deformations in general cases.

The shear modulus (Fig. 2.4) clearly displays a strain-induced unstiffening feature: for fixed projected area ($\sqrt{\lambda_1\lambda_2}$ = constant) it reaches a peak value with increasing shear ($\sqrt{\lambda_1/\lambda_2}$); afterwards it starts to decay (albeit moderately). The threshold of unstiffening decreases with increasing $\sqrt{\lambda_1\lambda_2}$. This phenomenon is related to Sp unfolding and may be corroborated theoretically as discussed in Zhu and Asaro (2008). Corresponding to the unstiffening of μ_s, slightly negative area modulus appears (as shown in dashed lines in Fig. 2.5). This is again inferred theoretically: the tension inside a Sp approaches a constant with the unfolding of its domains; thus the internal pressure of the network decays as the area increases, leading to negative area stiffness. This is reminiscent of the negative bulk stiffness as reported in composite materials, which is often related to post-buckling behavior or phase transition (Wang and Lakes, 2004). A more detailed explanation of the occurrence of negative area stiffness is provided in Appendix A. It is also necessary to point out that the occurrence of negative area stiffness is directly related to the quasi-static assumption – any finite deformation rate will eliminate it. Moreover, it has been found that the occurrence of negative area stiffness often generates numerical instability. For these reasons in the following finite element simulations we use a small yet positive area stiffness which is 10% the value at the initial state, if the negative area stiffness occurs.

The lipid bilayer consists of an (almost) incompressible fluid-like membrane. It therefore possesses a large area modulus and a quite small shear modulus. For numerical stability we take μ_b, the shear stiffness of the lipid bilayer, to be a finite value 10^{-3} μN/m, which is about three orders of magnitude smaller than that of the protein skeleton. The area stiffness of the bilayer is taken to be $K_b \doteq 5 \times 10^5$ μN/m (Mohandas and Evans, 1994). This value is sufficiently large to guarantee small area

variations so that its exact value has negligible effect on the result (the area variation of the lipid bilayer is less than 3% in all of our simulations).

2.5.3 Constitutive model

We relate the in-plane components of Cauchy stress $\mathbf{\Theta}$ in the finite element method with the deformation *via* the constitutive law provided by Evans and Skalak (1980). For the inner layer (skeleton network), we use

$$\Theta_{ij}h = \bar{T}\delta_{ij} + \frac{\mu_s}{J^2}\left(b_{ij} - \frac{b_{11}+b_{22}}{2}\delta_{ij}\right), \qquad i,j = 1,2. \tag{2.38}$$

$$J = \begin{vmatrix} F^\ell_{11} & F^\ell_{12} \\ F^\ell_{21} & F^\ell_{22} \end{vmatrix}, \tag{2.39}$$

is the in-plane Jacobian, and

$$F^\ell_{ij} = \frac{\partial y^\ell_i}{\partial x^\ell_j}, \tag{2.40}$$

are the deformation gradients (Asaro and Lubarda, 2006).

$$b^\ell_{ij} = \sum_{k=1}^{2} F^\ell_{ik}F^\ell_{jk}, \tag{2.41}$$

are components of the in-plane left Cauchy-Green deformation tensor. $\bar{T}$ and μ_s are the isotropic tension and the shear modulus, which are defined in Eqs. (2.35) and (2.36). h is the thickness of the shell. δ_{ij} is the Kronecker delta.

For the outer layer (lipid bilayer), since it is nearly incompressible, we use

$$\Theta_{ij}h = K_b(J-1)\delta_{ij} + \frac{\mu_b}{J^2}\left(b_{ij} - \frac{b_{11}+b_{22}}{2}\delta_{ij}\right), \qquad i,j = 1,2, \tag{2.42}$$

where $K_b = 5 \times 10^5$ pN/μm is the area modulus of the outer layer. Although the outer layer is a fluidic and its shear modulus is nearly zero, for numerical stability we choose a small but nonzero value. In practice this value is chosen to be three orders of magnitude smaller than the shear modulus of the inner layer. Through sensitivity tests it has been shown that its actual value has no influence upon the results.

2.6 Finite element method for the complete cell model (Level III)

At the top level of our multiscale model, the cell membrane is represented by two coupled continuous layers (ref. Fig. 2.2a). Numerically, we employ the finite element method and simulate each of these layers as congregations of shell elements. The development of this finite element model is summarized below.

2.6.1 Finite element representation of a thin shell

We model both the outer layer (the lipid bilayer) and the inner layer (the protein skeleton) by using Hughes-Liu shell elements. The choice of this method rather than alternatives (*e.g.* the Belytschko-Tsay shell elements) is based upon the fact that the Hughes-Liu shell element is suitable for problems with arbitrarily large strain, which is a characteristic of erythrocyte deformations. On the other hand, although the C^1-conforming thin shell elements may be more accurate (Cirak *et al.*, 2000; Feng and Klug, 2006; Ma and Klug, 2008; Benson *et al.*, 2010; Le, 2010) to model the lipid bilayer, for simplicity and numerical robustness, in our current study we choose the C^0 explicit Hughes-Liu elements (Hughes and Liu, 1981a).

In the following, the Hughes-Liu shell element formulation, including the general 3D version and the axisymmetric version, is briefly reviewed. We will first introduce the geometry and kinematics of the shell element, and then give the governing equations for general solid continua. After that, we will discretize the weak form of the governing equations for general solid continua, and apply shell assumptions. This procedure is called degenerating a solid brick element to a shell element, because the shell kinematic constraints are applied at the level of finite element discretization rather than the level of governing equations. Detailed formulation can be found in Hughes and Liu (1981a) and Hughes and Liu (1981b). Modifications to accommodate our specific physical problem are given here as well.

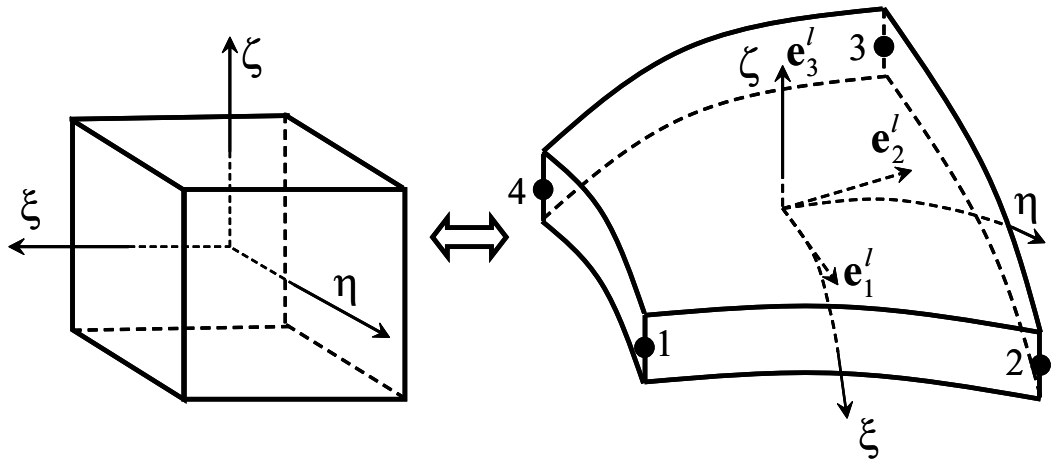

Figure 2.6: 3D iso-parametric mapping from a bi-unit cube to the physical shell element domain.

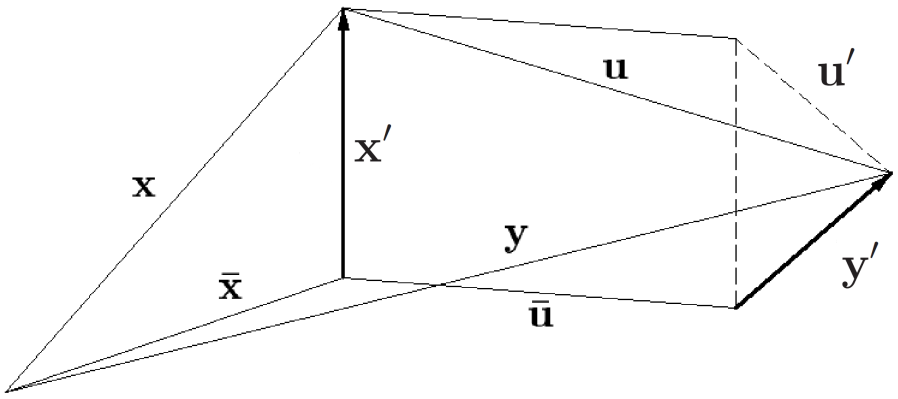

Figure 2.7: Displacements and position vectors of the deformed configuration

2.6.2 Geometry

The Hughes-Liu shell element method involves an isoparametric coordinate system (ξ, η, ζ) and a global Cartesian coordinate system with unit direction vectors $\mathbf{e}_1$, $\mathbf{e}_2$, and $\mathbf{e}_3$. A local lamina Cartesian coordinate system with unit direction vectors $\mathbf{e}_1^\ell$, $\mathbf{e}_2^\ell$, and $\mathbf{e}_3^\ell$ is also used, which will be defined later. In the global coordinate system, the initial configuration is represented by $\mathbf{x}$, and the deformed configuration is denoted by $\mathbf{y}$. Hereafter we use bold capital symbols to represent tensors or multi-column matrices, and bold lower-case symbols to represent vectors or single-column matrices.

A bi-unit cube within the (ξ, η, ζ) space is mapped to the geometry of a shell element $\mathbf{x}$ based on the iso-parametric representation as shown in Fig. 2.6. In the physical space, the lines corresponding to constant ξ and η (*i.e.* the lines in ζ direction) are called *fibers*. The surfaces of constant ζ are called *laminae*. Four nodes are chosen at $\zeta = 0$, the middle lamina ($\zeta = 0$) which is called the *reference surface*. With the bilinear in-plane interpolation, $\mathbf{x}$ of a shell element is given as

$$\mathbf{x}(\xi, \eta, \zeta) = \bar{\mathbf{x}}(\xi, \eta) + \mathbf{x}'(\xi, \eta, \zeta), \tag{2.43}$$

where

$$\bar{\mathbf{x}}(\xi, \eta) = \sum_{a=1}^{4} N^{(a)}(\xi, \eta)\bar{\mathbf{x}}^{(a)}, \tag{2.44}$$

and

$$\mathbf{x}'(\xi, \eta, \zeta) = \sum_{a=1}^{4} N^{(a)}(\xi, \eta)\mathbf{x}'^{(a)}(\zeta). \tag{2.45}$$

$\bar{\mathbf{x}}$ denotes the position vector of a point at the reference surface. $\mathbf{x}'$ is the point vector which starts from $\bar{\mathbf{x}}$ and points towards the fiber direction. $a = 1, 2, 3, 4$ correspond to the four nodes shown in Fig. 2.6. The superscript '(a)' denotes quantities at node 'a'. For example, $\bar{\mathbf{x}}^{(1)}$ and $\mathbf{x}'^{(1)}$ are the position and the point vectors at node '1', respectively. $N^{(a)}$ are the shape (interpolation) functions at node 'a', which are given

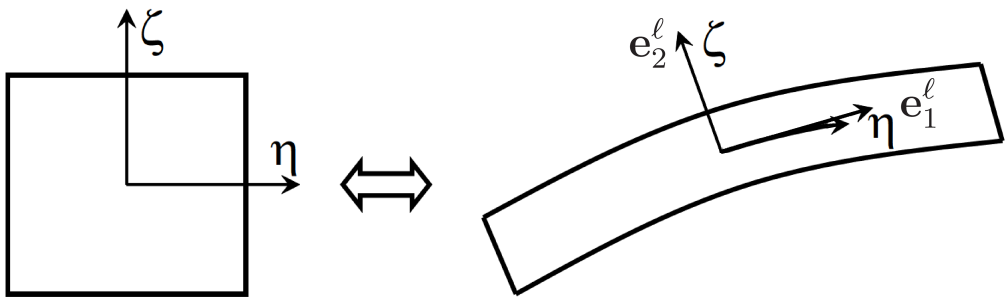

Figure 2.8: Axisymmetric isoparametric mapping from a square to the physical shell element domain.

as

$$\begin{aligned} N^{(1)} &= \frac{1}{4}(1-\xi)(1-\eta), \\ N^{(2)} &= \frac{1}{4}(1+\xi)(1-\eta), \\ N^{(3)} &= \frac{1}{4}(1+\xi)(1+\eta), \\ N^{(4)} &= \frac{1}{4}(1-\xi)(1+\eta). \end{aligned} \tag{2.46}$$

In our formulation, we consider the thicknesses h of both layers to be constants. Correspondingly, at node 'a' we also define a unit point vector $\hat{\mathbf{x}}'^{(a)}$ so that

$$\mathbf{x}'^{(a)}(\zeta) = \frac{h}{2}\zeta\hat{\mathbf{x}}'^{(a)}. \tag{2.47}$$

In some special cases, *e.g.* aspiration of an erythrocyte into a cylindrical micropipette from its dimple region, the configuration is axisymmetric so that axisymmetric shell elements can be employed to reduce the computational effort (Fig. 2.8). Similar to the 3D elements, the geometry of an axisymmetric shell element is described upon a unit square within the (η, ζ) space (ζ corresponding to the fiber direction) as

$$\mathbf{x}(\eta, \zeta) = \bar{\mathbf{x}}(\eta) + \mathbf{x}'(\eta, \zeta), \tag{2.48}$$

where

$$\bar{\mathbf{x}}(\eta) = \sum_{a=1}^{2} N^{(a)}(\eta)\bar{\mathbf{x}}^{(a)}, \tag{2.49}$$

$$\mathbf{x}'(\eta,\zeta) = \sum_{a=1}^{2} N^{(a)}(\eta)\mathbf{x}'^{(a)}(\zeta), \tag{2.50}$$

and

$$N^{(1)} = \frac{1}{2}(1-\eta),$$

$$N^{(2)} = \frac{1}{2}(1+\eta), \tag{2.51}$$

$$\mathbf{x}'^{(a)}(\zeta) = \frac{h}{2}\zeta\hat{\mathbf{x}}'^{(a)}. \tag{2.52}$$

2.6.3 Kinematics

Similar to the geometry description, we decompose the displacement $\mathbf{u}$ into two parts, the displacement of the reference surface and the displacement of the fiber directions. In 3D cases, we have

$$\mathbf{u}(\xi,\eta,\zeta) = \bar{\mathbf{u}}(\xi,\eta) + \mathbf{u}'(\xi,\eta,\zeta), \tag{2.53}$$

where

$$\bar{\mathbf{u}}(\xi,\eta) = \sum_{a=1}^{4} N^{(a)}(\xi,\eta)\bar{\mathbf{u}}^{(a)}, \tag{2.54}$$

$$\mathbf{u}'(\xi,\eta,\zeta) = \sum_{a=1}^{4} N^{(a)}(\xi,\eta)\mathbf{u}'^{(a)}(\zeta), \tag{2.55}$$

and

$$\mathbf{u}'^{(a)}(\zeta) = \frac{h}{2}\zeta\hat{\mathbf{u}}'^{(a)}. \tag{2.56}$$

In axisymmetric cases, we have

$$\mathbf{u}(\eta,\zeta) = \bar{\mathbf{u}}(\eta) + \mathbf{u}'(\eta,\zeta), \tag{2.57}$$

where

$$\bar{\mathbf{u}}(\eta) = \sum_{a=1}^{2} N^{(a)}(\eta)\bar{\mathbf{u}}^{(a)}, \tag{2.58}$$

$$\mathbf{u}'(\eta,\zeta) = \sum_{a=1}^{2} N^{(a)}(\eta)\mathbf{u}'^{(a)}(\zeta), \tag{2.59}$$

and

$$\mathbf{u}'^{(a)}(\zeta) = \frac{h}{2}\zeta\hat{\mathbf{u}}'^{(a)}. \tag{2.60}$$

Clearly, the deformed geometry $\mathbf{y} = \mathbf{x} + \mathbf{u}$. We also have

$$\mathbf{y} = \bar{\mathbf{y}} + \mathbf{y}', \tag{2.61}$$

where

$$\begin{aligned} \bar{\mathbf{y}} &= \bar{\mathbf{x}} + \bar{\mathbf{u}}, \\ \mathbf{y}' &= \mathbf{x}' + \mathbf{u}'. \end{aligned} \tag{2.62}$$

These relations are shown in Fig. 2.7.

2.6.4 Lamina coordinate system

In order to formulate the constitutive equations in an appropriate way, we build a lamina reference system with three directional vectors $\mathbf{e}_1^\ell, \mathbf{e}_2^\ell$ as shown in Fig. 2.6, and $\mathbf{e}_3^\ell$ defined as

$$\mathbf{e}_1^\ell = \mathbf{y}_{,\xi} / \left|\mathbf{y}_{,\xi}\right|, \tag{2.63}$$

$$\mathbf{e}_3^\ell = \mathbf{e}_1^\ell \times \mathbf{y}_{,\eta} / \left|\mathbf{e}_1^\ell \times \mathbf{y}_{,\eta}\right|, \tag{2.64}$$

and

$$\mathbf{e}_2^\ell = \mathbf{e}_3^\ell \times \mathbf{e}_1^\ell, \tag{2.65}$$

where $\mathbf{y}_{,\xi}$ and $\mathbf{y}_{,\eta}$ denote the partial derivatives of $\mathbf{y}$ with respect to ξ and η, respectively. The transformation matrix $\mathbf{Q}$ from the global coordinate system to the lamina

coordinate system is given as

$$\mathbf{Q} = \left[\mathbf{e}_1^\ell \;\; \mathbf{e}_2^\ell \;\; \mathbf{e}_3^\ell\right]^T. \tag{2.66}$$

The inverse transformation is achieved by $\mathbf{Q}^T$.

For axisymmetric cases, the lamina coordinate system is established as follows

$$\mathbf{e}_1^\ell = \begin{bmatrix} e_{11}^\ell \\ e_{12}^\ell \end{bmatrix} = \mathbf{y}_{,\eta} / \left|\mathbf{y}_{,\eta}\right|, \tag{2.67}$$

$$\mathbf{e}_2^\ell = e_{11}^\ell \mathbf{e}_2 - e_{12}^\ell \mathbf{e}_1. \tag{2.68}$$

Note that the out-of-plane direction in the axisymmetric cases is $\mathbf{e}_2^\ell$ instead of $\mathbf{e}_3^\ell$ as shown in Fig. 2.8. It is different from the 3D cases.

Correspondingly, the transformation matrix is

$$\mathbf{Q} = \left[\mathbf{e}_1^\ell \;\; \mathbf{e}_2^\ell\right]^T. \tag{2.69}$$

2.6.5 Governing equations

For a nonlinear solid mechanics problem in small length scales (*i.e.* the inertial effect is negligible), the momentum equation with updated Lagrangian description can be stated as follows,

$$c\frac{\partial \mathbf{u}}{\partial t} - \nabla \cdot \boldsymbol{\Theta} = \mathbf{0}. \tag{2.70}$$

The boundary conditions are

$$\begin{cases} \mathbf{u} = \mathbf{g} \quad \text{on} \quad \Gamma^D \\ \boldsymbol{\Theta} \cdot \mathbf{n} = \mathbf{f}^{ext} \quad \text{on} \quad \Gamma^{ext,N} \\ \boldsymbol{\Theta} \cdot \mathbf{n} = \mathbf{f}^{cnt} \quad \text{on} \quad \Gamma^{cnt,N} \end{cases} \tag{2.71}$$

c is the viscous damping coefficient. $\boldsymbol{\Theta}$ is the Cauchy stress. ∇ is the spatial gradient operator with respect to $\mathbf{y}$. Γ^D is the Dirichlet part of the boundary. $\Gamma^{ext,N}$ is the Neumann part of the boundary where external forces are applied. $\Gamma^{cnt,N}$ is the Neumann part of the boundary where contact interaction forces are applied. $\mathbf{n}$ is the normal vector to the surface. $\mathbf{f}^{ext}$ represents the external forces (*e.g.* the pressure force

inside a micropipette). $\mathbf{f}^{cnt}$ is the contact force between the two layers, and between the outer layer and boundaries (*e.g.* micropipettes). $\mathbf{g}$ is the specified displacements on the boundary. Generally speaking, c, $\boldsymbol{\Theta}$, $\mathbf{f}^{ext}$, $\mathbf{f}^{cnt}$ and $\mathbf{g}$ are functions of $\mathbf{u}$, $\mathbf{v}$ and t, where $\mathbf{v} = \partial\mathbf{u}/\partial t$ is the velocity.

Let Ω denote the physical space occupied by the shell in its current configuration, $V = V(\Omega)$ the trial function space for displacements, and $W = W(\Omega)$ the test function space for the momentum equations. By using the principle of virtual power (Belytschko *et al.*, 2000), the variational form (weak form) of Eq. (2.70) is stated as: finding $\mathbf{u} \in V$ such that for $\forall \delta\mathbf{v} \in W$,

$$\iiint_{\Omega} \delta\mathbf{v} \cdot c\frac{\partial \mathbf{u}}{\partial t} d\Omega + \iiint_{\Omega} \nabla\delta\mathbf{v} : \boldsymbol{\Theta} d\Omega = \iint_{\Gamma^{ext,N}} \delta\mathbf{v} \cdot \mathbf{f}^{ext} d\Gamma + \iint_{\Gamma^{cnt,N}} \delta\mathbf{v} \cdot \mathbf{f}^{cnt} d\Gamma. \quad (2.72)$$

The assumption that the two layers are shells instead of general solid leads to a number of conditions, including: (1) The fibers remain straight; (2) The normal stress vanishes (*i.e.* plane stress condition); (3)The momentum in the fiber direction is neglected. The first condition is already applied in the aforementioned geometry and kinematics implementations. The second condition will be applied in the constitutive equations. The third condition is implied in the assumption of constant thickness.

2.6.6 Spatial discretization and temporal integration

We apply the geometry and kinematics of shell element to the weak form equation (Eq. (4.10)) to get the finite element discretization. For convenience, we rewrite the Cauchy stress $\boldsymbol{\Theta}$, which is a tensor, as a vector $\boldsymbol{\sigma}$ by using the Voigt notation. In 3D cases, the nonzero components of $\boldsymbol{\Theta}$ are included in $\boldsymbol{\sigma}$ and expressed within the lamina coordinate system as

$$\boldsymbol{\sigma}^{\ell} = \begin{bmatrix} \Theta^{\ell}_{11} \\ \Theta^{\ell}_{12} \\ \Theta^{\ell}_{22} \\ \Theta^{\ell}_{23} \\ \Theta^{\ell}_{31} \end{bmatrix}, \quad (2.73)$$

where the superscript 'ℓ' denotes quantities measured in the lamina coordinate system. $\Theta^{\ell}_{33} = 0$ due to the plane stress condition.

For axisymmetric cases, we have

$$\boldsymbol{\sigma}^{\ell} = \begin{bmatrix} \Theta^{\ell}_{11} \\ \Theta^{\ell}_{12} \\ \Theta^{\ell}_{33} \end{bmatrix}. \tag{2.74}$$

Note that the out-of-plane direction in the axisymmetric cases is $\mathbf{e}^{\ell}_2$ instead of $\mathbf{e}^{\ell}_3$ as shown in Fig. 2.8. $\Theta^{\ell}_{22} = 0$ due to the plane stress condition. It is different from the 3D cases.

The finite-element approximation is formulated based upon Ω, the configuration at the last time step. We divide Ω into element domains Ω_e, and its boundary Γ into element boundaries Γ_e $(e = 1, \cdots, n_e)$. At each element, we employ the Galerkin approximation as

$$\begin{aligned} \mathbf{u} &= \mathbf{N}\mathbf{u}_e \\ \delta\mathbf{u} &= \mathbf{N}\delta\mathbf{u}_e. \end{aligned} \tag{2.75}$$

The subscript 'e' represents quantities in element e. $\mathbf{N}$ is a matrix consisting of shape functions. The element displacement vector $\mathbf{u}_e$ assembles the displacement vectors of all the nodes within an element expressed in the global coordinate system,

and $\delta\mathbf{u}_e$ is the corresponding part for $\delta\mathbf{u}$. For 3D cases, they are given as

$$\mathbf{u}_e = \begin{bmatrix} \bar{u}_1^{(1)} \\ \bar{u}_2^{(1)} \\ \bar{u}_3^{(1)} \\ \hat{u}_1'^{(1)} \\ \hat{u}_2'^{(1)} \\ \hat{u}_3'^{(1)} \\ \vdots \\ \bar{u}_1^{(4)} \\ \bar{u}_2^{(4)} \\ \bar{u}_3^{(4)} \\ \hat{u}_1'^{(4)} \\ \hat{u}_2'^{(4)} \\ \hat{u}_3'^{(4)} \end{bmatrix}, \quad \delta\mathbf{u}_e = \begin{bmatrix} \delta\bar{u}_1^{(1)} \\ \delta\bar{u}_2^{(1)} \\ \delta\bar{u}_3^{(1)} \\ \delta\hat{u}_1'^{(1)} \\ \delta\hat{u}_2'^{(1)} \\ \delta\hat{u}_3'^{(1)} \\ \vdots \\ \delta\bar{u}_1^{(4)} \\ \delta\bar{u}_2^{(4)} \\ \delta\bar{u}_3^{(4)} \\ \delta\hat{u}_1'^{(4)} \\ \delta\hat{u}_2'^{(4)} \\ \delta\hat{u}_3'^{(4)} \end{bmatrix}, \quad \mathbf{N}^T = \begin{bmatrix} N^{(1)} & 0 & 0 \\ 0 & N^{(1)} & 0 \\ 0 & 0 & N^{(1)} \\ \frac{h}{2}\zeta N^{(1)} & 0 & 0 \\ 0 & \frac{h}{2}\zeta N^{(1)} & 0 \\ 0 & 0 & \frac{h}{2}\zeta N^{(1)} \\ \vdots & \vdots & \vdots \\ N^{(4)} & 0 & 0 \\ 0 & N^{(4)} & 0 \\ 0 & 0 & N^{(4)} \\ \frac{h}{2}\zeta N^{(4)} & 0 & 0 \\ 0 & \frac{h}{2}\zeta N^{(4)} & 0 \\ 0 & 0 & \frac{h}{2}\zeta N^{(4)} \end{bmatrix}. \tag{2.76}$$

Since

$$\frac{\partial\hat{\mathbf{u}}'^{(a)}}{\partial t} = \boldsymbol{\omega}^{(a)} \times \hat{\mathbf{u}}'^{(a)} = \boldsymbol{\Lambda}^{(a)}\boldsymbol{\omega}^{(a)}, \tag{2.77}$$

where $\boldsymbol{\omega}^{(a)}$ is the angular velocity at node a, and

$$\boldsymbol{\Lambda}^{(a)} = \begin{bmatrix} 0 & \hat{u}_3'^{(a)} & -\hat{u}_2'^{(a)} \\ -\hat{u}_3'^{(a)} & 0 & \hat{u}_1'^{(a)} \\ \hat{u}_2'^{(a)} & -\hat{u}_1'^{(a)} & 0 \end{bmatrix}, \tag{2.78}$$

the velocity of a general point in the shell can be expressed as

$$\mathbf{v} = \frac{\partial\mathbf{u}}{\partial t} = \mathbf{N}\frac{\partial\mathbf{u}_e}{\partial t} = \mathbf{N}\mathbf{T}_e\mathbf{v}_e, \tag{2.79}$$

and

$$\delta\mathbf{v} = \mathbf{N}\mathbf{T}_e\delta\mathbf{v}_e, \tag{2.80}$$

where

$$\mathbf{v}_e = \begin{bmatrix} \bar{v}_1^{(1)} \\ \bar{v}_2^{(1)} \\ \bar{v}_3^{(1)} \\ \omega_1^{(1)} \\ \omega_2^{(1)} \\ \omega_3^{(1)} \\ \vdots \\ \bar{v}_1^{(4)} \\ \bar{v}_2^{(4)} \\ \bar{v}_3^{(4)} \\ \omega_1^{(4)} \\ \omega_2^{(4)} \\ \omega_3^{(4)} \end{bmatrix}, \quad \delta\mathbf{v}_e = \begin{bmatrix} \delta\bar{v}_1^{(1)} \\ \delta\bar{v}_2^{(1)} \\ \delta\bar{v}_3^{(1)} \\ \delta\omega_1^{(1)} \\ \delta\omega_2^{(1)} \\ \delta\omega_3^{(1)} \\ \vdots \\ \delta\bar{v}_1^{(4)} \\ \delta\bar{v}_2^{(4)} \\ \delta\bar{v}_3^{(4)} \\ \delta\omega_1^{(4)} \\ \delta\omega_2^{(4)} \\ \delta\omega_3^{(4)} \end{bmatrix}, \tag{2.81}$$

$$\mathbf{T}_e = \begin{bmatrix} \mathbf{I} & \mathbf{\Lambda}^{(1)} & \mathbf{I} & \mathbf{\Lambda}^{(2)} & \mathbf{I} & \mathbf{\Lambda}^{(3)} & \mathbf{I} & \mathbf{\Lambda}^{(4)} \end{bmatrix}, \tag{2.82}$$

and $\bar{\mathbf{v}} = \partial\bar{\mathbf{u}}/\partial t$.

By substituting Eq. (2.79) and (2.80) into Eq. (2.72) and making the finite element discretization, we get

$$\begin{aligned} &\sum_{e=1}^{n_e} \left(\delta\mathbf{v}_e^T \mathbf{T}_e^T \iiint_{\Omega_e} c\mathbf{N}^T\mathbf{N} d\Omega \mathbf{T}_e \frac{\partial \mathbf{v}_e}{\partial t} \right) + \sum_{e=1}^{n_e} \delta\mathbf{v}_e^T \mathbf{T}_e^T \iiint_{\Omega_e} \mathbf{\Phi}^T \mathbf{B}^T \boldsymbol{\sigma}^\ell d\Omega \\ &= \sum_{e=1}^{n_e} \delta\mathbf{v}_e^T \mathbf{T}_e^T \iint_{\Gamma_e^{ext,N}} \mathbf{N}^T \mathbf{f}^{ext} d\Gamma + \sum_{e=1}^{n_e} \delta\mathbf{v}_e^T \mathbf{T}_e^T \iint_{\Gamma_e^{cnt,N}} \mathbf{N}^T \mathbf{f}^{cnt} d\Gamma. \end{aligned} \tag{2.83}$$

$\mathbf{\Phi}$ is a transformation matrix from global coordinate system to lamina coordinate system so that

$$\mathbf{v}_e^\ell = \mathbf{\Phi}\mathbf{v}_e. \tag{2.84}$$

It is clear that in terms of the transformation matrix $\mathbf{Q}$ defined in §2.6.4, $\mathbf{\Phi}$ is a 24×24 matrix with diagonal sub-matrices $\mathbf{Q}$. In axisymmetric cases, the definitions of $\mathbf{v}_e$ and $\mathbf{\Phi}$ are similar.

$\mathbf{B}$ is the strain-displacement matrix which relates the local strain rate to the

vector $\partial \mathbf{u}_e^\ell / \partial t$ in the lamina coordinate system, *i.e.*

$$\dot{\boldsymbol{\gamma}}^\ell = \nabla_\gamma (\partial \mathbf{u}^\ell / \partial t) = \nabla_\gamma \mathbf{N}\, \partial \mathbf{u}_e^\ell / \partial t = \mathbf{B}\, \partial \mathbf{u}_e^\ell / \partial t, \tag{2.85}$$

where $\dot{\boldsymbol{\gamma}}^\ell$ is the strain rate vector and ∇_γ is a gradient operator related to strain rate. In 3D cases, we have

$$\dot{\boldsymbol{\gamma}}^\ell = \begin{bmatrix} \dot{\gamma}_{11}^\ell \\ 2\dot{\gamma}_{12}^\ell \\ \dot{\gamma}_{22}^\ell \\ 2\dot{\gamma}_{23}^\ell \\ 2\dot{\gamma}_{31}^\ell \end{bmatrix}, \nabla_\gamma(\cdot) = \begin{bmatrix} \frac{\partial(\cdot)_1}{\partial \mathbf{y}_1^\ell} \\ \frac{\partial(\cdot)_1}{\partial \mathbf{y}_2^\ell} + \frac{\partial(\cdot)_2}{\partial \mathbf{y}_1^\ell} \\ \frac{\partial(\cdot)_2}{\partial \mathbf{y}_2^\ell} \\ \frac{\partial(\cdot)_2}{\partial \mathbf{y}_3^\ell} + \frac{\partial(\cdot)_3}{\partial \mathbf{y}_2^\ell} \\ \frac{\partial(\cdot)_1}{\partial \mathbf{y}_3^\ell} + \frac{\partial(\cdot)_3}{\partial \mathbf{y}_1^\ell} \end{bmatrix}, \tag{2.86}$$

and

$$\mathbf{B} = \begin{bmatrix} \mathbf{B}^{(1)} & \mathbf{B}^{(2)} & \mathbf{B}^{(3)} & \mathbf{B}^{(4)} \end{bmatrix}, \tag{2.87}$$

where

$$\mathbf{B}^{(a)} = \begin{bmatrix} B_1^{(a)} & 0 & 0 & B_4^{(a)} & 0 & 0 \\ B_2^{(a)} & B_1^{(a)} & 0 & B_5^{(a)} & B_4^{(a)} & 0 \\ 0 & B_2^{(a)} & 0 & 0 & B_5^{(a)} & 0 \\ 0 & B_3^{(a)} & B_2^{(a)} & 0 & B_6^{(a)} & B_5^{(a)} \\ B_3^{(a)} & 0 & B_1^{(a)} & B_6^{(a)} & 0 & B_4^{(a)} \end{bmatrix}, \tag{2.88}$$

$$B_i^{(a)} = \begin{cases} N_{,i}^{(a)} & i = 1,2,3 \\ \frac{h}{2}\left(N^{(a)}\zeta\right)_{,i-3} & i = 4,5,6 \end{cases}. \tag{2.89}$$

The subscript '$,i$' denotes derivatives with respect to y_i^ℓ.

$$\frac{\partial N^{(a)}}{\partial y_i^\ell} = \frac{\partial N^{(a)}}{\partial \xi}\frac{\partial \xi}{\partial y_i^\ell} + \frac{\partial N^{(a)}}{\partial \eta}\frac{\partial \eta}{\partial y_i^\ell} + \frac{\partial N^{(a)}}{\partial \zeta}\frac{\partial \zeta}{\partial y_i^\ell}, \tag{2.90}$$

and

$$\begin{bmatrix} \frac{\partial \xi}{\partial y_1^\ell} & \frac{\partial \xi}{\partial y_2^\ell} & \frac{\partial \xi}{\partial y_3^\ell} \\ \frac{\partial \eta}{\partial y_1^\ell} & \frac{\partial \eta}{\partial y_2^\ell} & \frac{\partial \eta}{\partial y_3^\ell} \\ \frac{\partial \zeta}{\partial y_1^\ell} & \frac{\partial \zeta}{\partial y_2^\ell} & \frac{\partial \zeta}{\partial y_3^\ell} \end{bmatrix} = \begin{bmatrix} y_{1,\xi}^\ell & y_{1,\eta}^\ell & y_{1,\zeta}^\ell \\ y_{2,\xi}^\ell & y_{2,\eta}^\ell & y_{2,\zeta}^\ell \\ y_{3,\xi}^\ell & y_{3,\eta}^\ell & y_{3,\zeta}^\ell \end{bmatrix}^{-1}. \tag{2.91}$$

In axisymmetric cases, we have

$$\mathbf{B}^{(a)} = \begin{bmatrix} B_1^{(a)} & 0 & B_4^{(a)} & 0 \\ B_2^{(a)} & B_1^{(a)} & B_5^{(a)} & B_4^{(a)} \\ Q_{11}B_3 & Q_{21}B_3^{(a)} & Q_{11}B_6^{(a)} & Q_{21}B_6^{(a)} \end{bmatrix}, \tag{2.92}$$

where Q_{11}, Q_{21} are components of the transformation matrix $\mathbf{Q}$, and

$$B_i^{(a)} = \begin{cases} N_{,i}^{(a)} & i = 1, 2 \\ N^{(a)}/r & i = 3 \\ \frac{h}{2}\left(N^{(a)}\zeta\right)_{,i-3} & i = 4, 5 \\ \frac{h}{2}N^{(a)}\zeta/r & i = 6 \end{cases} \tag{2.93}$$

r is the radial coordinate. If $\mathbf{e}_2$ is chosen as the axisymmetric axis, then $r = |y_1|$.

The element vectors $\mathbf{u}_e$, $\delta\mathbf{u}_e$, $\mathbf{v}_e$ and $\delta\mathbf{v}_e$ are related to the global vectors $\mathbf{u}_g$, $\delta\mathbf{u}_g$, $\mathbf{v}_g$ and $\delta\mathbf{v}_g$ respectively by

$$\mathbf{u}_e = \mathbf{L}_e\mathbf{u}_g, \delta\mathbf{u}_e = \mathbf{L}_e\delta\mathbf{u}_g, \mathbf{v}_e = \mathbf{L}_e\mathbf{v}_g, \delta\mathbf{v}_e = \mathbf{L}_e\delta\mathbf{v}_g, \tag{2.94}$$

where $\mathbf{L}_e$ is the connectivity matrix, which consists of the integers 0 and 1. For the example shown in Figure 2.9, the connectivity matrices can be obtained as:

$$\mathbf{L}_1 = \begin{bmatrix} \mathbf{I}_6 & 0 & 0 & 0 & 0 & 0 \\ 0 & \mathbf{I}_6 & 0 & 0 & 0 & 0 \\ 0 & 0 & 0 & 0 & \mathbf{I}_6 & 0 \\ 0 & 0 & 0 & 0 & 0 & \mathbf{I}_6 \end{bmatrix}, \mathbf{L}_2 = \begin{bmatrix} 0 & \mathbf{I}_6 & 0 & 0 & 0 & 0 \\ 0 & 0 & \mathbf{I}_6 & 0 & 0 & 0 \\ 0 & 0 & 0 & \mathbf{I}_6 & 0 & 0 \\ 0 & 0 & 0 & 0 & \mathbf{I}_6 & 0 \end{bmatrix}, \tag{2.95}$$

where $\mathbf{I}_6$ is a 6×6 identity matrix.

Collecting $\delta\mathbf{v}_g^T$ in Eq. (2.83) , we obtain

$$\begin{aligned} &\delta\mathbf{v}_g^T \left[\sum_{e=1}^{n_e}\left(\mathbf{L}_e^T\mathbf{T}_e^T \iiint_{\Omega_e} c\mathbf{N}^T\mathbf{N}d\Omega\,\mathbf{T}_e\mathbf{L}_e\right)\cdot\mathbf{v}_g + \sum_{e=1}^{n_e}\left(\mathbf{L}_e^T\mathbf{T}_e^T \iiint_{\Omega_e} \mathbf{\Phi}^T\mathbf{B}^T\boldsymbol{\sigma}^\ell d\Omega\right)\right] \\ &= \delta\mathbf{v}_g^T \left[\sum_{e=1}^{n_e}\left(\mathbf{L}_e^T\mathbf{T}_e^T \iint_{\Gamma_e^{ext,N}} \mathbf{N}^T\mathbf{f}^{ext}d\Gamma\right) + \sum_{e=1}^{n_e}\left(\mathbf{L}_e^T\mathbf{T}_e^T \iint_{\Gamma_e^{cnt,N}} \mathbf{N}^T\mathbf{f}^{cnt}d\Gamma\right)\right]. \end{aligned} \tag{2.96}$$

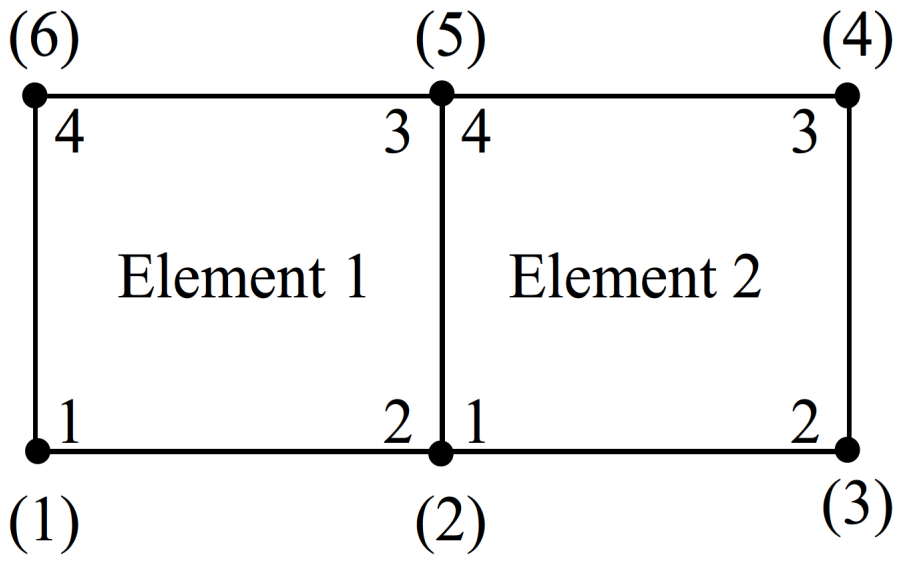

Figure 2.9: A simple example for connectivity matrix. 1,2,3,4 denote local nodal index and (1),(2),(3),(4),(5),(6) denote global nodal index.

Eliminating $\delta \mathbf{v}_g^T$, we get

$$\sum_{e=1}^{n_e} \left(\mathbf{L}_e^T \mathbf{T}_e^T \iiint_{\Omega_e} c \mathbf{N}^T \mathbf{N} d\Omega \, \mathbf{T}_e \mathbf{L}_e \right) \mathbf{v}_g + \sum_{e=1}^{n_e} \left(\mathbf{L}_e^T \mathbf{T}_e^T \iiint_{\Omega_e} \mathbf{\Phi}^T \mathbf{B}^T \boldsymbol{\sigma}^\ell d\Omega \right)$$
$$= \sum_{e=1}^{n_e} \left(\mathbf{L}_e^T \mathbf{T}_e^T \iint_{\Gamma_e^{ext,N}} \mathbf{N}^T \mathbf{f}^{ext} d\Gamma \right) + \sum_{e=1}^{n_e} \left(\mathbf{L}_e^T \mathbf{T}_e^T \iint_{\Gamma_e^{cnt,N}} \mathbf{N}^T \mathbf{f}^{cnt} d\Gamma \right). \quad (2.97)$$

In matrix form, these equations can be rewritten as

$$\mathbf{C}\mathbf{v}_g + \mathbf{f}_g^{int} = \mathbf{f}_g^{ext} + \mathbf{f}_g^{cnt}, \quad (2.98)$$

Overall, there are n_{node} nodes in the shell (due to overlapping of nodes in neighboring elements, $n_{node} < 4n_e$). Each node contributes six components to the displacement vector, three of them representing position changes and the other three orientation changes. Therefore, altogether $\mathbf{v}_g$ contains $6n_{node}$ components.

$$\mathbf{C} = \sum_{e=1}^{n_e} \left(\mathbf{L}_e^T \mathbf{T}_e^T \iiint_{\Omega_e} c \mathbf{N}^T \mathbf{N} d\Omega \, \mathbf{T}_e \mathbf{L}_e \right), \quad (2.99)$$

is the assembled damping matrix. In Chapter 2 and Chapter 3, we concentrate upon quasi-static cases so that $\mathbf{C}$ is a numerical parameter which affects the

convergence *via* dynamic relaxation but not the final result. In Chapter 4, a boundary element method (BEM) will be developed to model the damping effect from the surrounding fluid to simulate the real dynamic process. $\mathbf{f}_g^{ext}$ and $\mathbf{f}_g^{cnt}$ are the global external force vector and the global contact force vector, respectively.

$$\mathbf{f}_g^{int} = \sum_{e=1}^{n_e} \left(\mathbf{L}_e^T \mathbf{T}_e^T \iiint_{\Omega_e} \mathbf{\Phi}^T \mathbf{B}^T \boldsymbol{\sigma}^\ell d\Omega \right) = \sum_{e=1}^{n_e} (\mathbf{L}_e^T \mathbf{T}_e^T \mathbf{f}^{(e)int}),$$

is the global internal force vector, which comes from elastic stiffness. In 3D cases, $\mathbf{f}^{(e)int}$ is given as

$$\mathbf{f}^{(e)int} = \int_{-1}^{+1} \int_{-1}^{+1} \int_{-1}^{+1} \mathbf{\Phi}^T \mathbf{B}^T \boldsymbol{\sigma}^\ell j d\xi d\eta d\zeta, \tag{2.100}$$

and

$$j = \begin{vmatrix} y_{1,\xi}^\ell & y_{1,\eta}^\ell & y_{1,\zeta}^\ell \\ y_{2,\xi}^\ell & y_{2,\eta}^\ell & y_{2,\zeta}^\ell \\ y_{3,\xi}^\ell & y_{3,\eta}^\ell & y_{3,\zeta}^\ell \end{vmatrix}, \tag{2.101}$$

where y_1^ℓ, y_2^ℓ, and y_3^ℓ are the components of $\mathbf{y}^\ell$ in $\mathbf{e}_1^\ell$, $\mathbf{e}_2^\ell$, and $\mathbf{e}_3^\ell$ directions, respectively.

In axisymmetric cases, we have

$$\mathbf{f}^{(e)int} = \int_{-1}^{+1} \int_{-1}^{+1} \mathbf{\Phi}^T \mathbf{B}^T \boldsymbol{\sigma}^\ell j d\eta d\zeta, \tag{2.102}$$

where

$$j = r \cdot \begin{vmatrix} y_{1,\eta}^\ell & y_{1,\zeta}^\ell \\ y_{2,\eta}^\ell & y_{2,\zeta}^\ell \end{vmatrix}. \tag{2.103}$$

The integrations are carried out numerically by using Gaussian quadratures. One-point reduced integration at $(\xi = 0, \eta = 0)$ with hourglass control is used in each lamina to avoid locking (Belytschko *et al.*, 2000). Three-points integration is used in the thickness direction.

To integrate Eq. (2.98) from time step n to time step $n+1$, we first compute

$$\mathbf{v}_{g,n} = \mathbf{C}^{-1} \left(\mathbf{f}_{g,n}^{ext} + \mathbf{f}_{g,n}^{cnt} - \mathbf{f}_{g,n}^{int} \right). \tag{2.104}$$

The displacement of reference surface $\bar{\mathbf{u}}_g$ at node 'a' is then updated by using explicit

Euler algorithm as

$$\bar{\mathbf{u}}_{g,n+1}^{(a)} = \bar{\mathbf{u}}_{g,n}^{(a)} + \Delta t \bar{\mathbf{v}}_{g,n}^{(a)}, \tag{2.105}$$

where Δt is the time step. For the direction displacement part $\mathbf{u}'_g$, we employ the Hughes-Winget formula (Hughes and Winget, 1980) to update it as

$$\mathbf{u}_{g,n+1}^{\prime(a)} = \mathbf{R}^{(a)} \mathbf{u}_{g,n}^{\prime(a)}, \tag{2.106}$$

where

$$\mathbf{R}^{(a)} = \left(\mathbf{I} - \frac{1}{2}\mathbf{\Omega}^{(a)}\right)^{-1} \left(\mathbf{I} + \frac{1}{2}\mathbf{\Omega}^{(a)}\right), \tag{2.107}$$

$$\mathbf{\Omega}^{(a)} = \begin{bmatrix} 0 & -\omega_3^{(a)}\Delta t & \omega_2^{(a)}\Delta t \\ \omega_3^{(a)}\Delta t & 0 & -\omega_1^{(a)}\Delta t \\ -\omega_2^{(a)}\Delta t & \omega_1^{(a)}\Delta t & 0 \end{bmatrix}, \tag{2.108}$$

and $\omega_i^{(a)}$ is the angular velocity component in $\mathbf{v}_{g,n}$ for node 'a' in i direction.

2.6.7 Constitutive equations

To close our finite element formulations, we relate the in-plane components of stress $\mathbf{\Theta}$ with the deformation *via* the constitutive law provided by Evans and Skalak (1980) as shown in Eqns. 2.38 and 2.42 in §2.5.3. The stress-strain relation for axisymmetric cases is similar.

Furthermore, we update the transverse shear stresses Θ_{23}^{ℓ} and Θ_{31}^{ℓ} by using the linear elastic model expressed as

$$\dot{\Theta}_{23}^{\ell} h = G\dot{\gamma}_{23}^{\ell}, \quad \dot{\Theta}_{31}^{\ell} h = G\dot{\gamma}_{31}^{\ell}, \tag{2.109}$$

where $\dot{\gamma}_{23}^{\ell}$ and $\dot{\gamma}_{31}^{\ell}$ are the relevant strain rates obtained from Eq. (2.85). $G = \kappa\mu$ is the transverse shear stiffness. κ is the correction coefficient that results from matching the transverse shear energy to that of a three-dimensional structure in pure bending. For a linear orthotropic elastic material, $\kappa = \frac{5}{6}$. In our model, since both the inner layer and the outer layer are very thin, the transverse shear should be negligibly small. We find that as long as the transverse shear stiffness is sufficiently large (*e.g.* $\kappa \geq 1$), its actual value has no influence on the results.

2.6.8 Bending stiffness

Considering a shell with thickness h described by Evans and Skalak (1980), its bending stiffness k_c and area modulus K are related by

$$k_c = \int_{-\frac{h}{2}}^{+\frac{h}{2}} y^2 \frac{K}{h}\, dy = \frac{Kh^2}{12}. \tag{2.110}$$

For the lipid bilayer, we use $h = 2.2$ nm and $K = K_b = 5 \times 10^5$ pN/μm (see §2.5), then $k_c = 2 \times 10^{-19}$ J. This is the same as the value used in Mohandas and Evans (1994). It is also within the range of reported bending stiffness (from 4×10^{-14} to 3×10^{-13} μNm) (Mohandas and Evans, 1994; Discher *et al.*, 1998; Lin and Brown, 2005; Hwang and Waugh, 1997; Marcelli *et al.*, 2005; Bo and Waugh., 1989). The discrepancy between the bilayer thickness used herein and its actual value (5 nm) is attributed to the fact that in our study the bilayer is simplified as a continuous (but anisotropic) shell without considering its detailed molecular architecture.

The bending stiffness of the protein skeleton is negligibly small (experiments show that the persistence length of a Sp is only around $O(1)$ nm (Rief *et al.*, 1999), indicating that it has a small bending stiffness). It is found that if its thickness h is chosen to be comparable to that of the bilayer (in our simulations we choose $h = 2$ nm), this characteristics can be duplicated in our model. For example, with small deformations a typical value of the area modulus of the skeleton is around 20 pN/μm, leading to a bending stiffness of 6.67×10^{-24} J, which is five orders smaller than that of the lipid bilayer.

2.6.9 Bilayer spontaneous curvature and skeleton in-plane prestress

The lipid bilayer may possess a spontaneous curvature as illustrated in Fig. 2.10 (see also Seifert (1997); Seifert *et al.* (1991)). To account for the in-plane prestress and the spontaneous curvature of the two layers, we replace the deformation gradient tensor $\mathbf{F}^\ell$, defined as

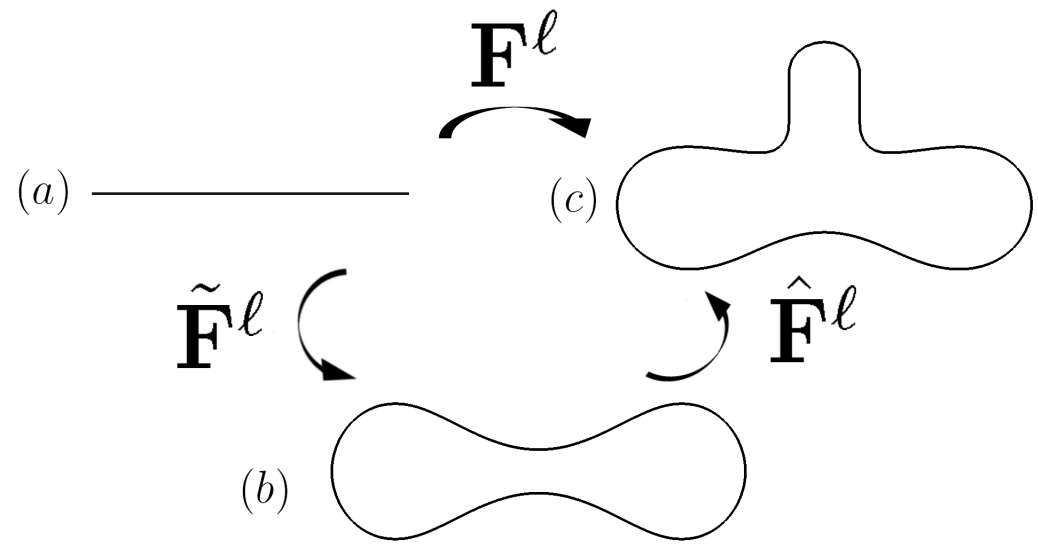

Figure 2.10: (a) Spontaneous configuration. (b) Initial configuration. (c) Deformed configuration.

$$\mathbf{F}^\ell = \begin{bmatrix} F_{11}^\ell & F_{12}^\ell & F_{13}^\ell \\ F_{21}^\ell & F_{22}^\ell & F_{23}^\ell \\ F_{31}^\ell & F_{32}^\ell & F_{33}^\ell \end{bmatrix}, \tag{2.111}$$

with $\hat{\mathbf{F}}^\ell\tilde{\mathbf{F}}^\ell$, where $\tilde{\mathbf{F}}^\ell$ is the initial deformation gradient caused by in-plane prestress and/or spontaneous curvature, and $\hat{\mathbf{F}}^\ell$ is the deformation caused by external loading.

In its free state the lipid bilayer may possess a spontaneous curvature C_0, referring to the curvature a free membrane patch cut from a vesicle would acquire spontaneously (Helfrich, 1973). On the other hand, to date there exists no widely accepted value of C_0. In most of our simulations, we consider the spontaneous configuration to be flat so that $C_0 = 0$, except predicting the resting shape of red blood cells. The initial deformation gradient caused by the spontaneous curvature is then calculated as

$$\tilde{\mathbf{F}}^\ell = \frac{\partial \mathbf{x}^\ell}{\partial \mathbf{x}_0^\ell} = \frac{\partial(\bar{\mathbf{x}}^\ell + \mathbf{x}'^\ell)}{\partial(\bar{\mathbf{x}}^\ell + \mathbf{x}_0'^\ell)}, \tag{2.112}$$

where $\mathbf{x}'^\ell$ is the director of the initial configuration and $\mathbf{x}_0'^\ell = \begin{bmatrix} 0 & 0 & \zeta h/2 \end{bmatrix}^T$ is the direction of the spontaneous configuration. For example, if the shell is spherical, the

initial stretches will be $\lambda_1 = \lambda_2 = (R + h/2)/R$ on the outer surface (pretensioned) and $\lambda_1 = \lambda_2 = (R - h/2)/R$ on the inner surface (precompressed), where R is the radius and h is the thickness. Consequently the initial deformation gradient

$$\tilde{\mathbf{F}}^{\ell} = \begin{bmatrix} \lambda_1 & 0 & 0 \\ 0 & \lambda_2 & 0 \\ 0 & 0 & 1 \end{bmatrix}. \tag{2.113}$$

Besides the spontaneous curvature, the area difference elasticity (ADE) theory based on the bilayer-couple hypothesis (Lim *et al.*, 2002) can be also incorporated in the spontaneous curvature model using the finite element method, which is described in Appendix B. But for simplicity, the area difference elasticity (ADE) theory is not considered in our following simulations.

For the protein skeleton, in the literature two possible initial states have been suggested, pre-compressed (Boal, 1994) or pre-stretched (Svoboda *et al.*, 1992). Following Discher *et al.* (1998), two different scenarios of prestress are considered. In the first scenario the skeleton has no initial tension inside it (stress-free case with $\bar{T}_0 = 0$). In this case p_f=5.625 nm, L_f=6.257 nm. In the second scenario the skeleton is prestressed with nonzero $\bar{T}_0$. Here we use p_f=11.118 nm, L_f=6.388 nm. Note that all these parameters are from Discher *et al.* (1998). Two different levels of prestress are considered, $T_0 = -15$ pN/μm (following Discher *et al.* (1998)) and $T_0 = -30$ pN/μm (which provides best comparison with experiments), which will be shown in Chapter 3.

2.6.10 Interaction between bilayer and skeleton

The interaction between the outer layer and the inner layer in the vertical direction is modeled as uniformly distributed penalty springs. Tangentially, the two layers are allowed to slide viscously against each other. In Chapter 4, the exact magnitude of the viscous drag in the tangential direction rendered by the mobility of the transmembrane proteins band 3 and glycophorin C will be formulated, but for quasi-static processes, it is irrelevant since we consider quasi-static cases through dynamic relaxation. A master-slave penalty contact formulation is employed (Malone

and Johnson, 1994). The outer layer is treated as the master surface and the nodes on the master surface are called master nodes, while the inner layer is considered as the slave surface and the nodes on the slave surface are called slave nodes. All the slave nodes are projected to the master surface, and the distances between the slave nodes and master surface are calculated. The contact stress depends linearly upon these distances with a penalty stiffness. The contact force, defined as the contact stress times element area, is distributed to the slave nodes and master nodes. The penalty stiffness is tested numerically so that it is sufficiently large to enforce the contact constraint accurately, and small enough so that it does not introduce numerical instability during time integration. In addition, we ignore the thicknesses of the shells in this contact algorithm and consider the reference surfaces of the shell elements as the contact surfaces.

In the following, the detailed formulations for these master-slave penalty contact algorithms are presented for both 3D and axisymmetric cases.

3D case

In 3D cases, each shell element on the master surface is divided into four triangles by adding a virtual node A at the center of the element $BCDF$ as shown in Fig. 2.11. Then for each triangle, the following algorithm is applied to calculate the projection point K and contact force as shown in Fig. 2.12.

The plane of the master segment (triangle ABC) can be written as

$$ax_1 + bx_2 + cx_3 + d = 0, \tag{2.114}$$

where

$$d = -(ax_1^A + bx_2^A + cx_3^A), \tag{2.115}$$

where x_i^A is the coordinate component of point A at direction i.

$$\mathbf{n} = (a, b, c) = \frac{\mathbf{AB} \otimes \mathbf{AC}}{|\mathbf{AB} \otimes \mathbf{AC}|}, \tag{2.116}$$

is the normal to the plane ABC, where $\otimes$ denotes the cross product of vectors.

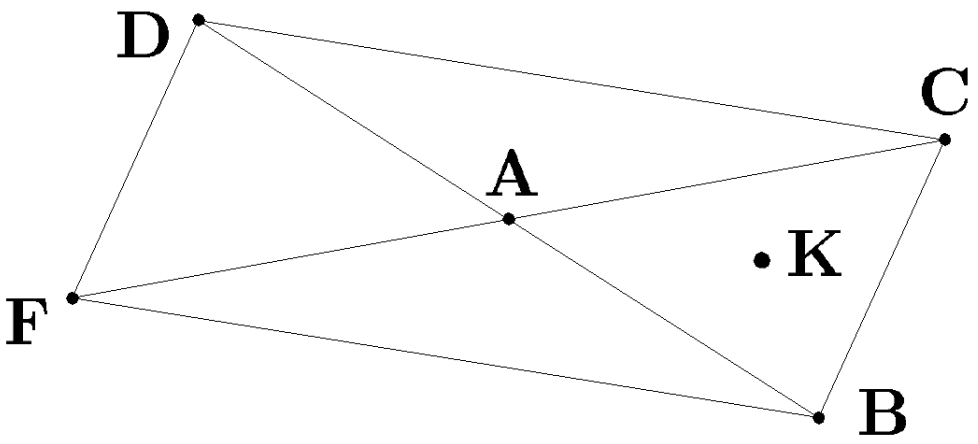

Figure 2.11: Break a quadrilateral shell element into four triangles.

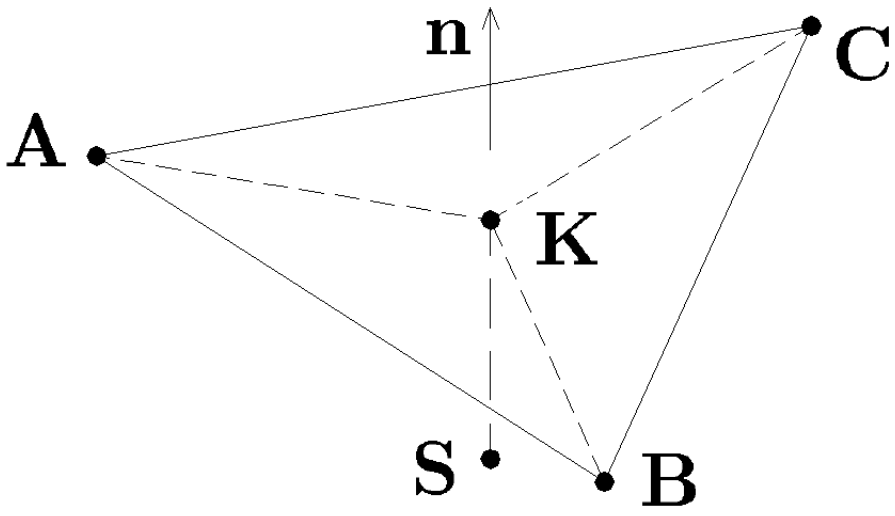

Figure 2.12: Slave node S contacts with the master segment ABC

The projection point K is given as

$$x_i^K = x_i^S + n_i\varphi, \tag{2.117}$$

where

$$\varphi = \frac{-(ax_1^S + bx_2^S + cx_3^S + d)}{an_1 + bn_2 + cn_3}, \tag{2.118}$$

where x_i^S are coordinates of the slave node S.

The distance between the slave node and the master surface is calculated as

$$\delta = |\mathbf{x}^K - \mathbf{x}^S|. \tag{2.119}$$

Then we can get the contact force as

$$\mathbf{F}^S = k(\mathbf{x}^K - \mathbf{x}^S)A^S, \tag{2.120}$$

where A^S is the nodal area of the node S and k is the penalty stiffness.

Finally, the contact force is also distributed to the master nodes of the quadrilateral element as

$$\mathbf{F}^a = \mathbf{N}_a(\xi, \eta)\mathbf{F}^S, \tag{2.121}$$

where $\mathbf{N}_a(\xi, \eta)$ are the shape functions, and the isoparametric coordinates ξ, η are obtained through, *e.g.,*

$$\begin{aligned} \xi &= 1.0 - \frac{area(BCK)}{area(BCF)}, \\ \eta &= -1.0 + \frac{area(BKF)}{area(BCF)}, \end{aligned} \tag{2.122}$$

where $area(BCK)$ denotes the area of triangle BCK. More detailed formulations can be found in Malone and Johnson (1994). Furthermore, damping is added in both normal and tangential directions in the contact algorithm for stability and robustness.

For our simulation, usually we use the same mesh for both the cytoskeleton and the lipid bilayer. In the beginning of the simulation, it is very easy to assign the master-slave pairs. Also because they are sliding only (no dissociation), the global search is not needed. For the local search, we identify the closest master node to the

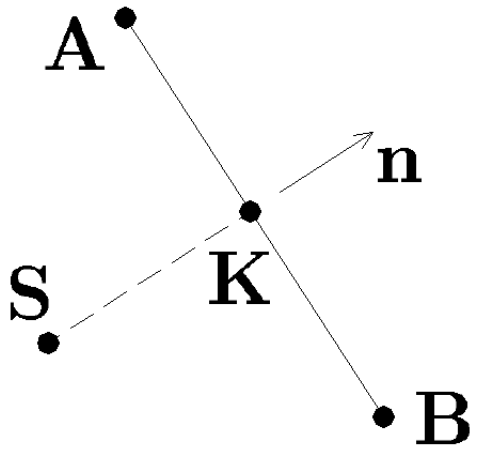

Figure 2.13: Slave node K contacts with segment AB.

slave node first, then search the elements connected to this master node.

Axisymmetric case

The axisymmetric problem is simplified as calculating the distance between the slave node S and the master line segment AB. First, the normal is calculated by

$$\mathbf{n} = \mathbf{AB} \otimes \mathbf{e}_3, \tag{2.123}$$

where $\mathbf{e}_3 = (0, 0, 1)^T$. d is obtained by

$$d = -(n_1 x_1^A + n_2 x_2^A). \tag{2.124}$$

Then, the contact distance is calculated by

$$\varphi = \frac{n_1 x_1^S + n_2 x_2^S + d}{n_1^2 + n_2^2}. \tag{2.125}$$

The projection point K is given as

$$x_i^K = x_i^S + n_i \varphi. \tag{2.126}$$

The distance between the slave node and the master surface is calculated as

$$\delta = |\mathbf{x}^K - \mathbf{x}^S|. \tag{2.127}$$

Then we can get the contact force as

$$\mathbf{F}^S = k(\mathbf{x}^K - \mathbf{x}^S)A^S, \tag{2.128}$$

where A^S is the nodal area of the node S.

Finally, the contact force is also distributed to the master nodes as

$$\mathbf{F}^a = \mathbf{N}_a(\eta)\mathbf{F}^S, \tag{2.129}$$

where η is obtained *via*

$$\eta = -1.0 + 0.5\frac{|\mathbf{AK}|}{|\mathbf{AB}|}. \tag{2.130}$$

2.6.11 Interaction between the bilayer and rigid walls

A similar master-slave penalty contact algorithm is applied for the interaction between the outer layer and analytical surfaces, *e.g.,* the micropipette inner surface in micropipette aspiration experiment and the subtrate plane in the flow channel experiment. In the case of the interaction between the lipid bilayer and analytical surfaces, the analytical surfaces are considered as master surfaces. The contact algorithm is illustrated in the following.

Micropipette aspiration

The micropipette aspiration experiment is introduced in §1.4.1 in Chapter 1. The micropipette inner surface is modeled as a rigid analytical surface and considered as the master surface, while the outer layer of the cell is considered as the slave surface. The micropipette internal surface is divided into a spherical part and a cylindrical part as shown in Fig. 2.14. x_1 is chosed as in the axial direction of the pipette.

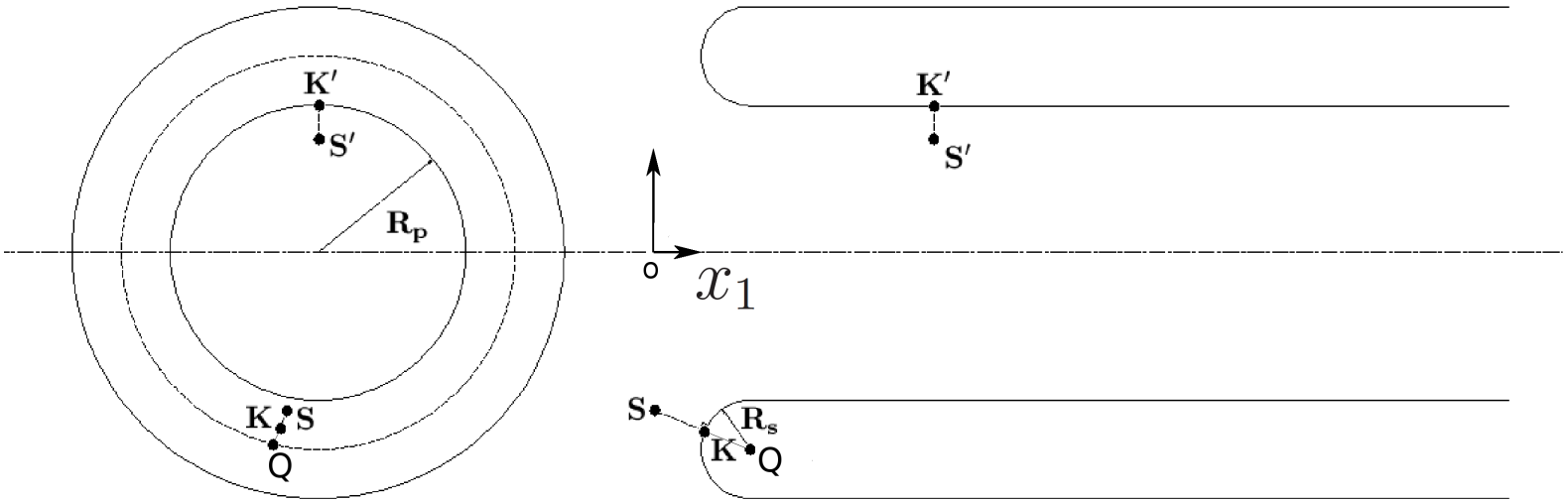

Figure 2.14: The contact algorithm for the interaction between the lipid bilayer and the pipette inner surface.

For the spherical part, the point Q is given by

$$x_1^Q = x_{en}, \tag{2.131}$$

$$x_2^Q = \frac{x_2^S}{\sqrt{(x_2^S)^2 + (x_3^S)^2}}(R_p + R_s), \tag{2.132}$$

$$x_3^Q = \frac{x_3^S}{\sqrt{(x_2^S)^2 + (x_3^S)^2}}(R_p + R_s), \tag{2.133}$$

where x_{en} is the coordinate in x_1 direction where cylindrical part starts, which is a constant, and R_p, R_s are the micropipette inner radius and the radius of the spherical part.

Then, the projection point K is given by

$$\mathbf{x}^K = \mathbf{x}^Q + \frac{\mathbf{x}^S - \mathbf{x}^Q}{|\mathbf{x}^S - \mathbf{x}^Q|}R_s. \tag{2.134}$$

The distance between the slave node and the master surface is calculated as

$$\delta = |\mathbf{x}^K - \mathbf{x}^S|. \tag{2.135}$$

Then we can get the contact force as

$$\mathbf{F}^S = k(\mathbf{x}^K - \mathbf{x}^S)A^S, \tag{2.136}$$

where A^S is the nodal area of the node S.

For the cylindrical part, the projection point K' is given as

$$x_1^{K'} = x_1^{S'} \tag{2.137}$$

$$x_2^{K'} = \frac{x_2^{S'}}{\sqrt{(x_2^{S'})^2 + (x_3^{S'})^2}}R_p \tag{2.138}$$

$$x_3^{K'} = \frac{x_3^{S'}}{\sqrt{(x_2^{S'})^2 + (x_3^{S'})^2}}R_p \tag{2.139}$$

The contact distance is calculated as

$$\delta = |\mathbf{x}^{K'} - \mathbf{x}^{S'}|. \tag{2.140}$$

Then we can get the contact force as

$$\mathbf{F}^{S'} = k(\mathbf{x}^{K'} - \mathbf{x}^{S'})A^{S'}, \tag{2.141}$$

where $A^{S'}$ is the nodal area of the node S'.

Flow channel stretching experiment

The flow channel stretching experiment was introduced in §1.4.3 in Chapter 1. The substrate rigid plate in the flow channel experiment is put at $z = 0$. The projection point K is given by

$$x_1^K = x_1^S \tag{2.142}$$

$$x_2^K = x_2^S \tag{2.143}$$

$$x_3^K = 0 \tag{2.144}$$

The distance between the slave node and the master surface is calculated as

$$\delta = |\mathbf{x}^K - \mathbf{x}^S|. \tag{2.145}$$

Then we can get the contact force as

$$\mathbf{F}^S = k(\mathbf{x}^K - \mathbf{x}^S)A^S, \tag{2.146}$$

where A^S is the nodal area of the node S.

2.6.12 Cell volume conservation

The internal volume of the cell is conserved through the following penalty algorithm

$$\Delta P = -k_v \Delta V, \tag{2.147}$$

where ΔV is the volume change of the cell and ΔP is the internal pressure due to the volume change. ΔP is uniformly distributed upon the outer layer against volume change. k_v is the penalty parameter. A large k_v enforces volume conservation so that in all of our simulations the volume change is less than 3%. An exception is the deformation of a cell from spherical shape. With the overall surface area fixed, a sphere encloses the maximum possible volume and it is impossible to deform it without volume loss. An analysis of this case is given in Appendix C. Indeed, in that particular case a volume loss of 20-30% is predicted by our model.

2.7 Summary and remarks

In this chapter, we formulated our three-level quasi-static multiscale approach of the RBC membrane and focused on the finite element model in the Level III, including the continuum-based shell element and the master-slave penalty contact algorithm.

Although in this dissertation, we only used the information-passing multiscale algorithm, the concurrent multiscale method may be very useful in simulating several problems for RBC biomechanics. For example, in the tether forming experiments described in Chapter 3, *e.g.,* flow channel stretching, there are some very small points where large deformations occur. It is desirable to employ the concurrent multiscale method to model these small region using the junctional complex model directly while applying the finite element model for the rest of the cell.

Besides the spectrin unfolding, the dissociation of spectrins also plays an important role for the softening behavior of the cytoskeleton, which may be considered in our model in the future.

Currently we modeled the suspension complex as a pinning point. By exploring the molecular structure of the suspension complex, we can build an exact model of it and incorporate it to our multiscale approach.

A more accurate isogeometric shell element (Benson *et al.*, 2010) or the subdivision shell element (Cirak *et al.*, 2000; Feng and Klug, 2006; Ma and Klug, 2008) can be used instead of Hughes-Liu shell element for the red blood cell membrane.

In our master-slave penalty contact algorithm, we break the quadrilateral el-

ement into four triangles. A more accurate way is to find the projection point based on the curved quadrilateral surface directly by solving some cubic nonlinear algebraic equations.

Chapter 2, in part, is a reprint of the material as it appears in 'Multiscale modeling of erythrocyte membranes', *Physical Review E*, **81**: 031904, 2010. Zhangli Peng, Robert J. Asaro and Qiang Zhu, 2010. The dissertation author was the primary investigator and author of this paper.

Chapter 3

Resting Shape and Quasi-static Deformation of Red Blood Cells

In this chapter, we apply our three-level quasi-static multiscale approach described in Chapter 2 to study problems involving mechanical responses of RBC, including the resting shape as well as cell deformations and skeleton-bilayer interactions in three canonical experiments: optical tweezer stretching, micropipette aspiration and flow channel stretching.

3.1 Why does a red blood cell have a biconcave resting shape?

The beautiful biconcave shape of red blood cells (RBCs) is the first of eight mysteries about RBCs proposed by Hoffman (2001) for physiologists to ponder in this millenium. Although this mystery is still not completely understood, it is well accepted that the resting shapes of RBCs are related to the mechanical properties of the composite membrane consisting of the lipid bilayer and the skeleton network. However, the roles played by each of these components are unclear. On the one hand, by washing away the lipid bilayer using non-ionic surfactants, Svoboda *et al.* (1992) showed that the remaining protein skeleton was no longer biconcave. On the other hand, in some diseases (*e.g.* hereditary elliptocytosis) a weakened skeleton network

changes the cell to an elliptical shape. The implication is that both the skeleton and the lipid bilayer contribute to the resting shape.

Accordingly, an important factor is the relaxed (zero shear energy or stress-free) reference state of the protein skeleton. The simplest choice is to use a spherical shape as the reference state. However, it was shown that under this assumption the cell rested at a cup shape (Li *et al.*, 2005). To recover the biconcave shape the elasticity of the skeleton has to be significantly reduced (Li *et al.*, 2005). Although the biconcave shape can be stabilized by using the biconcave shape itself (Zarda *et al.*, 1977) or an oblate ellipsoidal shape (Lim *et al.*, 2002; Khairy *et al.*, 2008) as the relaxed skeleton reference, experiments are needed to explain why red cells have those nonspherical relaxed skeletons.

In the following, we first predict the shape of a lipid vesicle without the cytoskeleton and compare it with existing studies to validate our numerical method. Then using our multiscale approach, we simulate the resting shapes of RBCs and compare the results with predictions made in existing studies.

3.1.1 Lipid bilayer only

We first neglect the effect of the protein skeleton and study the dependence of the lipid vesicle shape upon its internal volume V. By assuming that the spontaneous curvature $C_0 = 0$ as defined in §2.6.9 of Chapter 2, we plot the cell shapes at three different values of V/V_{sphere} in Fig. 3.1 (V_{sphere} is the volume of a sphere with the same surface area as the cell). It is seen that with our model we can accurately duplicate the stomatocyte-oblate-prolate sequence and its dependence upon V obtained by Seifert *et al.* (1991).

We also considered different spontaneous curvatures of the lipid bilayer, the results are consistent with the phase diagram by Seifert *et al.* (1991). Furthermore, the area-difference-elasticity (ADE) theory can be also incorporated in the finite element method framework as shown in Appendix B. But for simplicity, area-difference-elasticity theory is not considered in our current simulations.

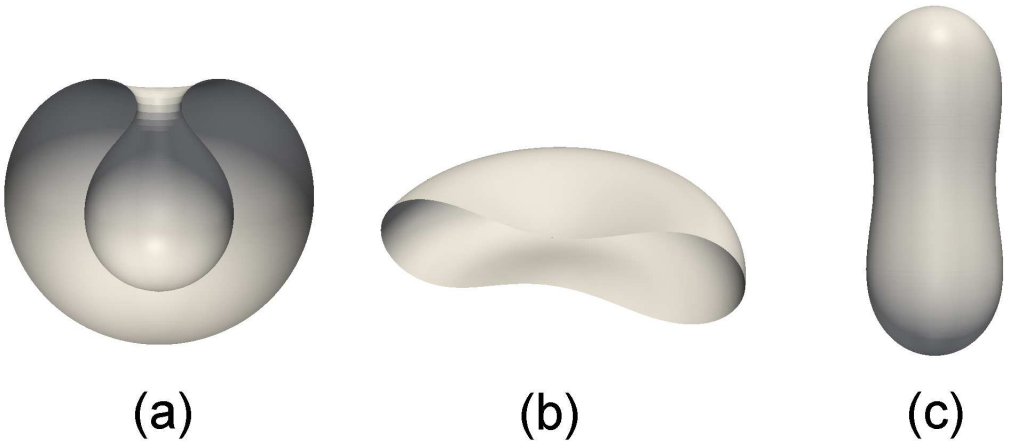

Figure 3.1: Resting shapes of a RBC when the lipid bilayer is considered: (a) stomatocyte (V/V_{sphere}=0.59), (b) oblate (V/V_{sphere}=0.65) and (c) prolate (V/V_{sphere}=0.8).

3.1.2 Lipid bilayer and cytoskeleton

We then take into account the protein skeleton and re-simulate the case with p_f=5.625nm, L_f=6.257nm, $k_c = 8.3 \times 10^{-20} J$, and $C_0 = 0$, where p_f and L_f are the persistence length and contour length of folded domains in spectrins, and k_c is the bilayer bending stiffness. Following Li *et al.* (2005), we start with a spherical shell of radius 3.27 μm (which also serves as the relaxed reference state of the skeleton), and gradually reduce the volume to 65% of its original value. Instead of a biconcave shape, a cup shape is obtained (Fig. 3.2a). After we reduce the shear stiffness of the skeleton by one hundred times, biconcave shape is recovered. This is consistent with the report by Li *et al.* (2005).

To explain the paradox about the shear stiffness of the skeleton, Li *et al.* (2005) proposed that over large time scales the skeleton might be fluidic due to remodeling and possesses a much smaller shear stiffness than that measured under finite deformation rates. This appears to be reasonable, however, it fails to explain why weakened skeleton causes dramatic shape change such as observed in elliptocytosis (at $C_0 = 0$, the biconcave shape is the ground state for $\mu_s \to 0$ at V/V_{sphere}=0.65 as demonstrated in Fig. 3.1b).

Alternatively, we find that with some positive spontaneous curvature the bi-

Figure 3.2: Resting shapes of the RBC when both the lipid bilayer (light color) and the skeleton network (dark color) are considered: (a) cup shape ($c_0 = 0$, $\mu_s = 11$ pN/μm, V/V_{sphere}=0.65), (b) biconcave shape ($c_0 = 2.6$, $\mu_s = 0.4$ pN/μm, V/V_{sphere}=0.65). The gap between lipid bilayer and skeleton is exaggerated.

concave shape can be obtained with a small skeleton shear stiffness. For example, if we assume that the reduced spontaneous curvature $c_0 = 2.6$ (c_0 is the reduced spontaneous curvature defined as $c_0 = C_0 \cdot R_0$ and $R_0 = 3.27\mu$m is the radius of the initial sphere), the biconcave shape is achieved at a skeleton shear stiffness of 0.4 pN/μm as shown in Fig. 3.2b. This is consistent with the behavior of elliptocytosis because the lipid bilayer with such a positive spontaneous curvature tends to be prolate if the shear stiffness of skeleton approaches zero due to the weakened skeleton. In addition, the recent work by Park *et al.* (2009) also showed that when the stiffness of the cytoskeleton is reduced by depletion of ATP, the shape of red blood cells becomes elliptical similar to the shape in elliptocytosis. While the small shear stiffness (0.4 pN/μm) of a normal red cell can be rationalized under the theory of Li *et al.* (2005). Additional evidence can be found in the experimental work of membrane fluctuation by Peterson *et al.* (1992) and the theoretical study by Boal *et al.* (1992), both suggesting that the shear modulus may be considerably smaller than that determined by micropipette experiments ($6 \sim 9$ pN/μm) (Waugh and Evans, 1979).

A complete phase diagram with respect to shear stiffness and spontaneous curvature should be explored further, which is beyond the scope of this dissertation.

Through comparisons with benchmark results, the aforementioned simulations

confirm the validity and accuracy of our models (especially the Level III FEM model). They have also demonstrated that additional studies, both theoretical and experimental, are required to explain the resting shape of RBC.

3.2 Simulations of optical tweezer stretching

In the following we concentrate upon mechanically induced deformations of the cell in three canonical experiments: optical tweezer stretching, micropipette aspiration and flow channel stretching.

In these simulations, we use the initial configuration as the relaxed reference state (shear-free state) of the skeleton and consider the bilayer with a spontaneous curvature $C_0 = 0$ for simplicity. Following Discher *et al.* (1998), two different scenarios are considered. In the first scenario the skeleton has no initial tension inside it (stress-free case with $\bar{T}_0 = 0$). In this case p_f=5.625 nm, L_f=6.257 nm. In the second scenario the skeleton is prestressed with nonzero $\bar{T}_0$. Here we use p_f=11.118 nm, L_f=6.388 nm. Note that all these parameters are from Discher *et al.* (1998). Two different levels of prestress are considered, $T_0 = -15$ pN/μm (following Discher *et al.* (1998)) and $T_0 = -30$ pN/μm (which provides the best comparison with experiments). Unless otherwise specified, for all the following cases we use: $N = 19$, $L_u = 39$ nm, $p_u = 0.8$ nm, $\Delta\Delta x^* = 12.6$ nm, and $F_{1/2} = 12$pN.

We test the model through comparisons with experimental measurements of RBC deformability through optical tweezers. In this setup, an erythrocyte is stretched by two attached beads, whose motions are optically controlled by laser beams. In our model, the initial shape of the cell is biconcave as shown in Fig. 3.3 and is mathematically depicted by Evans and Fung (1972) as,

$$z = \pm 0.5 R_0 \sqrt{1 - \frac{x^2 + y^2}{R_0^2}} \left[C_1 + C_2 \frac{x^2 + y^2}{R_0^2} + C_3 \left(\frac{x^2 + y^2}{R_0^2} \right)^2 \right], \tag{3.1}$$

where $C_1 = 0.21$, $C_2 = 2.03$, $C_3 = -1.12$, and $R_0 = 3.9$ μm. (x, y, z) is a Cartesian coordinate system with its origin located at the centroid of the undeformed cell. As reported by Dao *et al.* (2006), the stretching force is applied by two silica beads, which are attached at the opposite ends of the cell over a small oval region with a

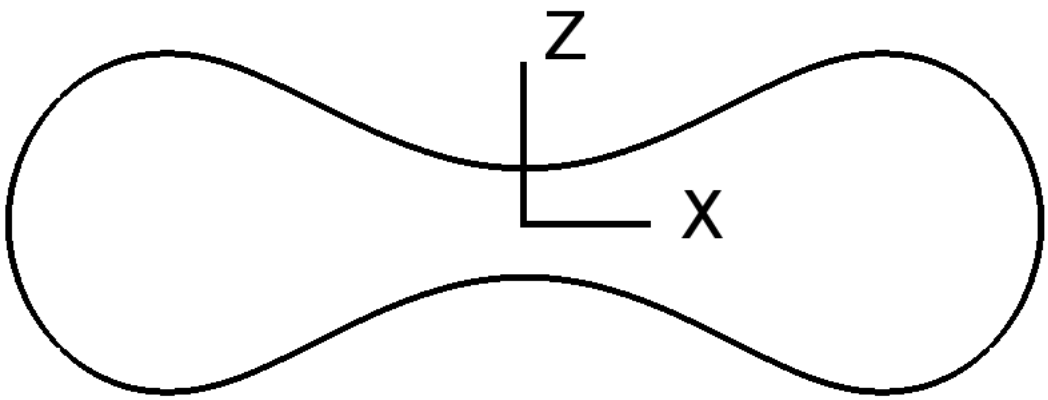

Figure 3.3: The initial shape of the cell described by Eq. 3.1.

diameter of 1∼2 μm (Fig. 3.4). In our simulation, this diameter is chosen to be 1.5 μm.

The force versus displacement curve is shown in Fig. 3.5. As we see, the model predictions match well with the experimental measurements. The prestress cases are softer than the stress-free case because the persistence length is larger. The case with $\bar{T}_0 = -30$ pN/μm is a little bit stiffer than the case with $\bar{T}_0 = -15$ pN/μm. It also provides best comparison with the experiment among the three cases.

3.3 Simulations of micropipette aspiration

Micropipette aspiration is one of the most useful experiments to determine the mechanical properties of cells (Lim *et al.*, 2006). By applying this technique on red blood cells with fluorescence imaging, several important phenomena can be observed, including the relation between aspiraton length and pressure, skeleton density (protein density) variation, vesiculation and necking. In the following, these phenomena are simulated using our multiscale approach and compared with the experiments.

3.3.1 Aspiration length vs. pressure

We simulate the canonical micropipette aspirations and obtain the correlation between the applied pressure and the aspiration length L (*i.e.* the length of the cell

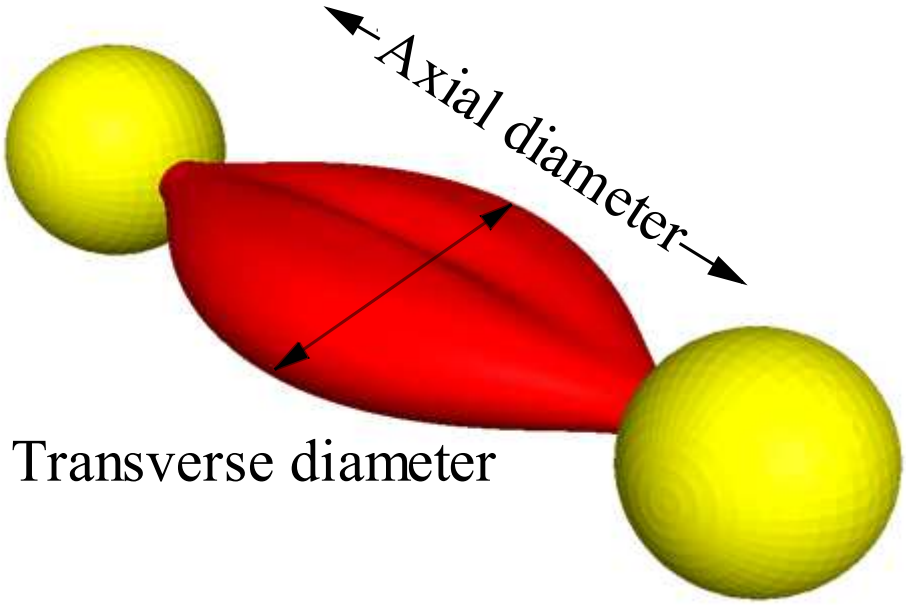

Figure 3.4: Cell deformation stretched by optical tweezers as predicted by our multi-scale model (stress-free case).

sucked into the pipette). In this simulation, a rigid cylindrical surface is employed to represent the pipette. The interaction between the outer layer of the RBC and the pipette is simulated by using a master-slave algorithm similar to the one used to study the bilayer-skeleton interaction, which is presented in Chapter 2. As indicated in experiments by Discher and Mohandas (1996), during the aspiration the membrane is usually separated from the pipette by a small gap of fluid so that the friction between them is insignificant and thus not considered in our model. We further simplify the fluid pressure distribution inside the pipette as a uniform pressure difference ΔP applied on the cap region of the lipid bilayer and a linear distribution along the aspiration length (the pressure difference equals zero at the entrance).

Following Waugh and Evans (1979), we study a flaccid, unswollen cell aspired from the dimple region (Fig. 3.6). The initial shape of the cell is depicted by Eq. (3.1). The cell is aspirated into a pipette with an inner radius R_p of 0.668 μm.

In Fig. 3.7, it is seen that the normalized aspiration length L/R_p depends almost linearly on the two-dimensional pressure defined as $\Delta P R_p/2$. Also plotted in the figure are the experimental measurements by Waugh and Evans (1979) and the results of the coarse-grained model by Discher *et al.* (1998). Good agreements are

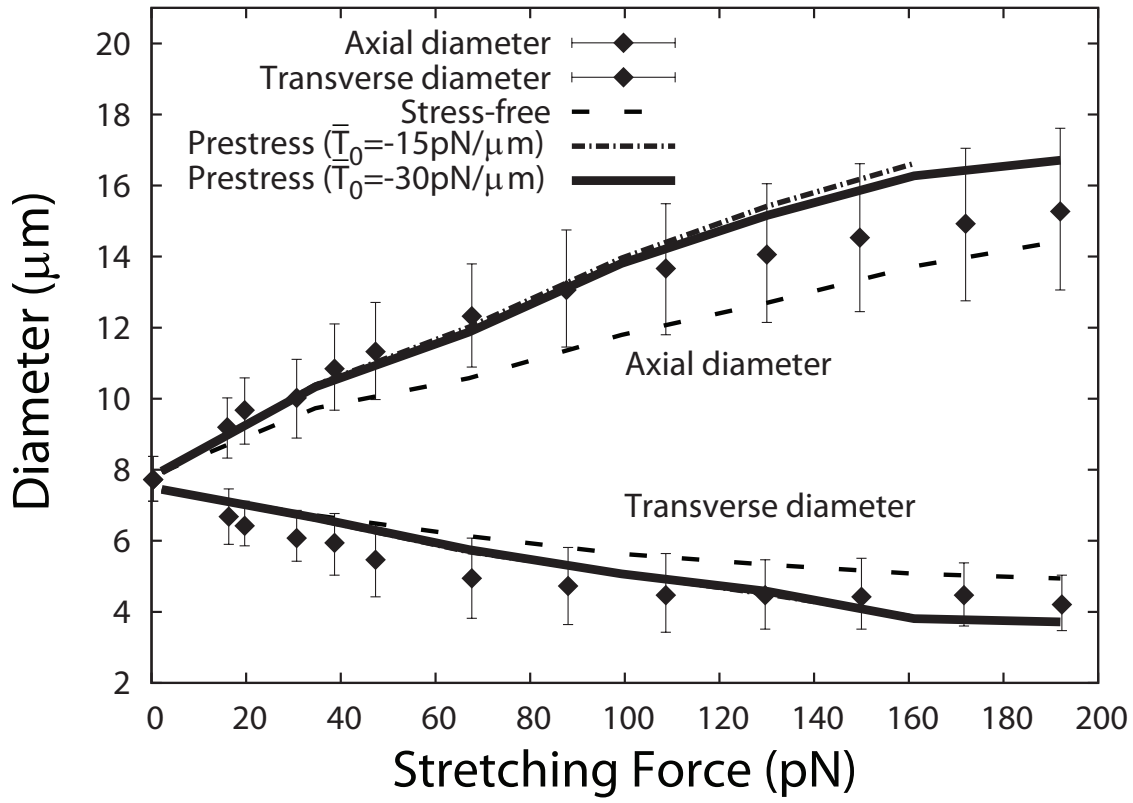

Figure 3.5: Axial and transverse diameters of the cell as functions of the stretching force for the stress-free and the prestress cases as compared with experimental results by Dao *et al.* (2006) (the error bars represent experimental uncertainty).

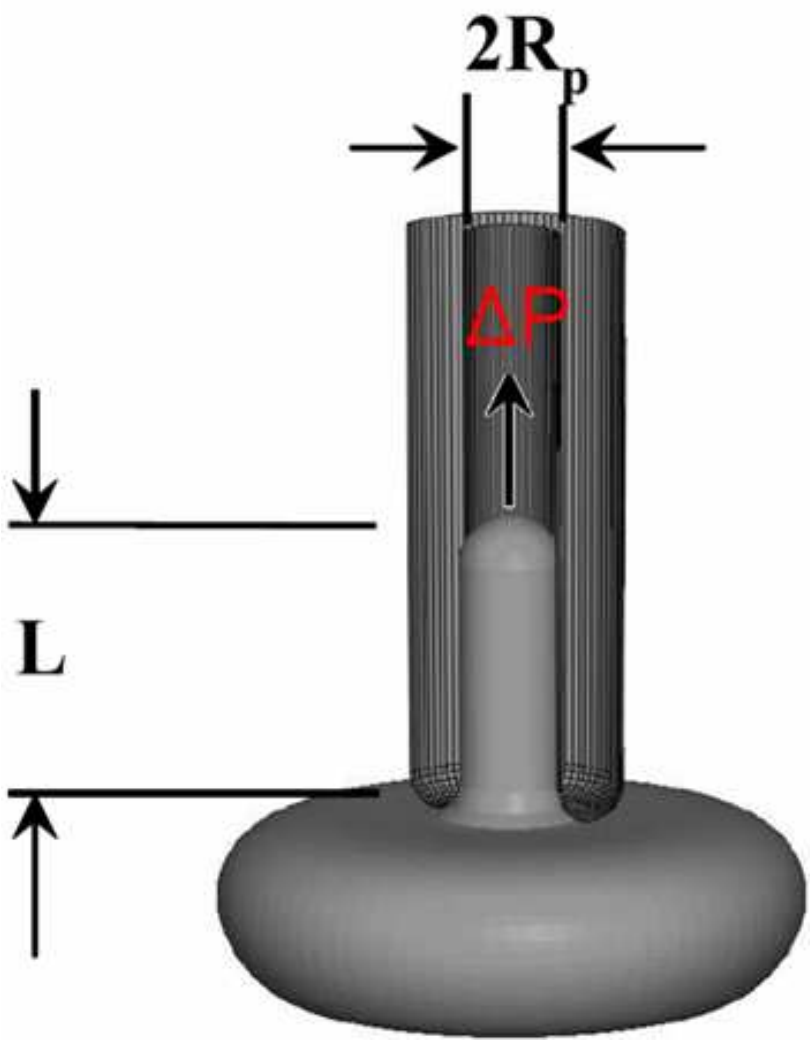

Figure 3.6: Schematic of a micropipette aspiration.

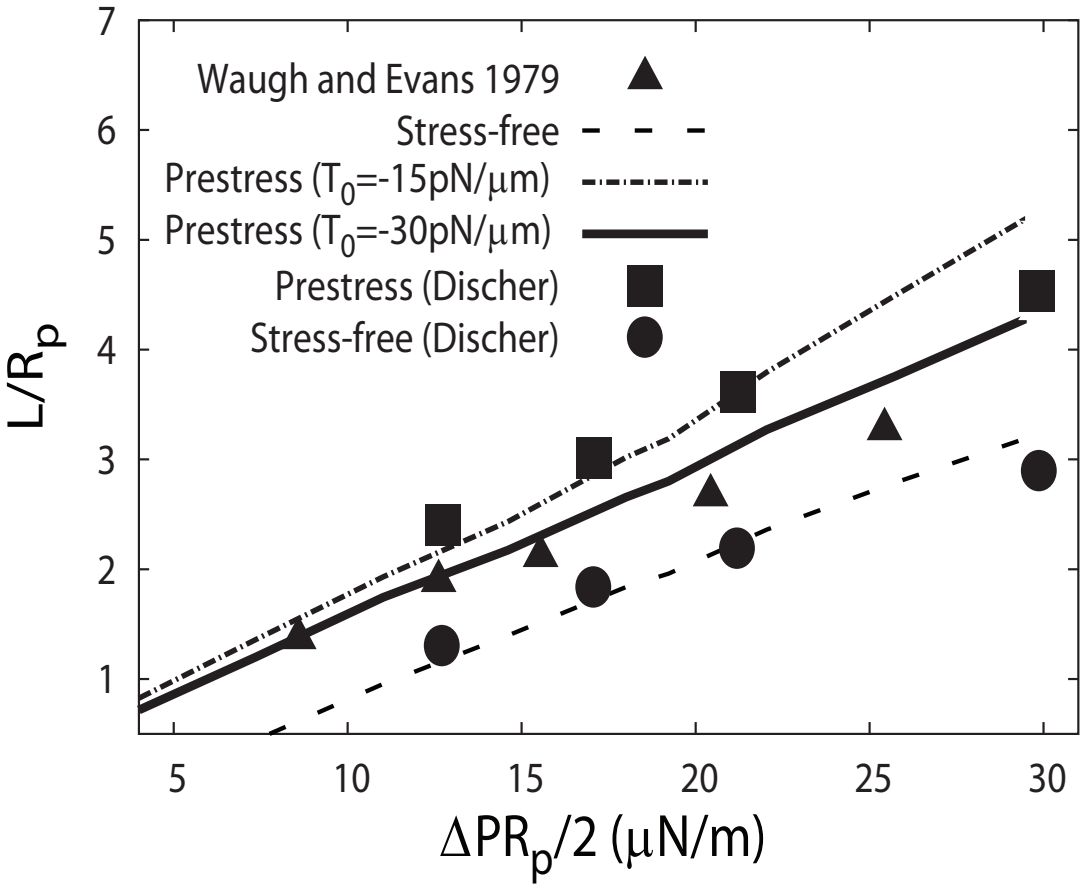

Figure 3.7: The aspiration length as a function of the applied pressure difference ΔP as compared with the experiment by Waugh and Evans (1979) and the coarse-grained model by Discher *et al.* (1998).

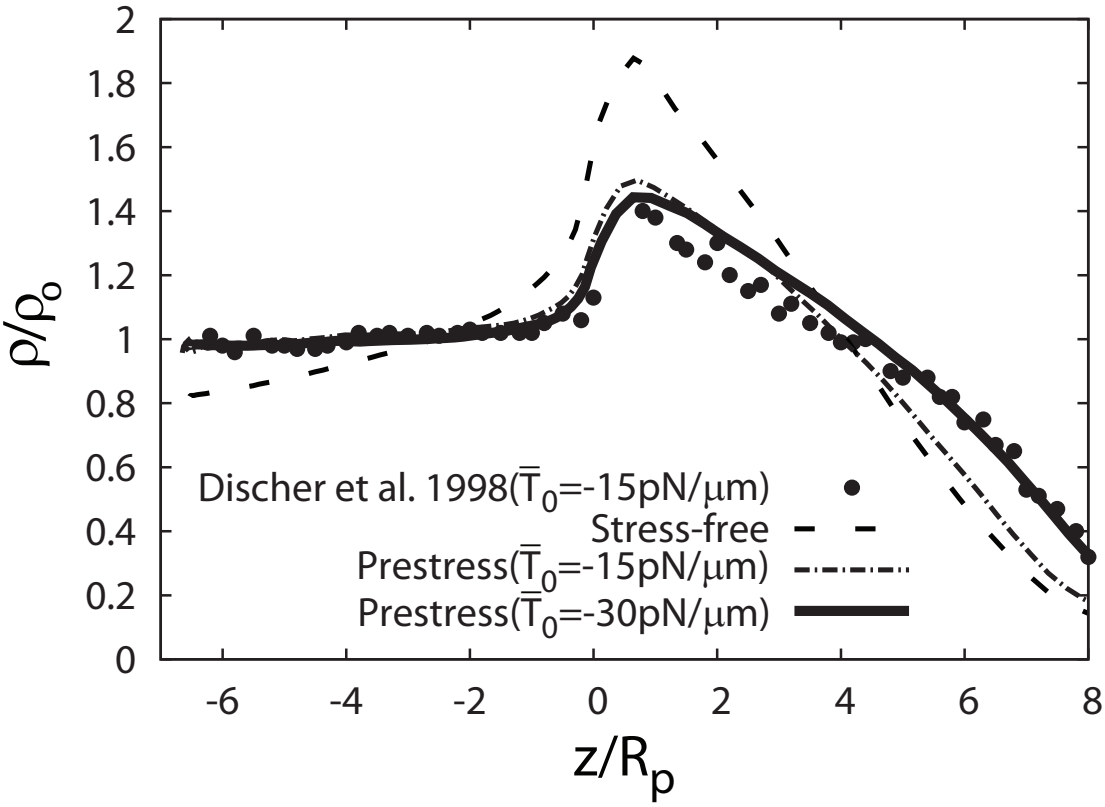

Figure 3.8: The density profile of the protein skeleton as predicted by the FEM model in comparison with the results obtained by using a coarse-grained molecular dynamics model at $L = 8R_p$.

achieved with the coarse-grained model. The prestress case with $T_0 = -30$ pN/μm provides the best agreement with the experiment.

3.3.2 Skeleton density variation

To further test the capacity of our model, we use it to study areal deformation of the skeleton and compare with experimental measurements as well as predictions by the coarse-grained model. The areal variation of the protein skeleton can be denoted as the density ratio ρ/ρ_0, *i.e.* the density of skeleton-attached proteins ρ normalized by its value ρ_0 in the undeformed state. This ratio is related to λ_1 and λ_2 by $\rho/\rho_0 = 1/(\lambda_1\lambda_2)$.

In Fig. 3.8 we plot the density profiles predicted by the current model for stress-free and prestress cases, and compare them with the reported result using the

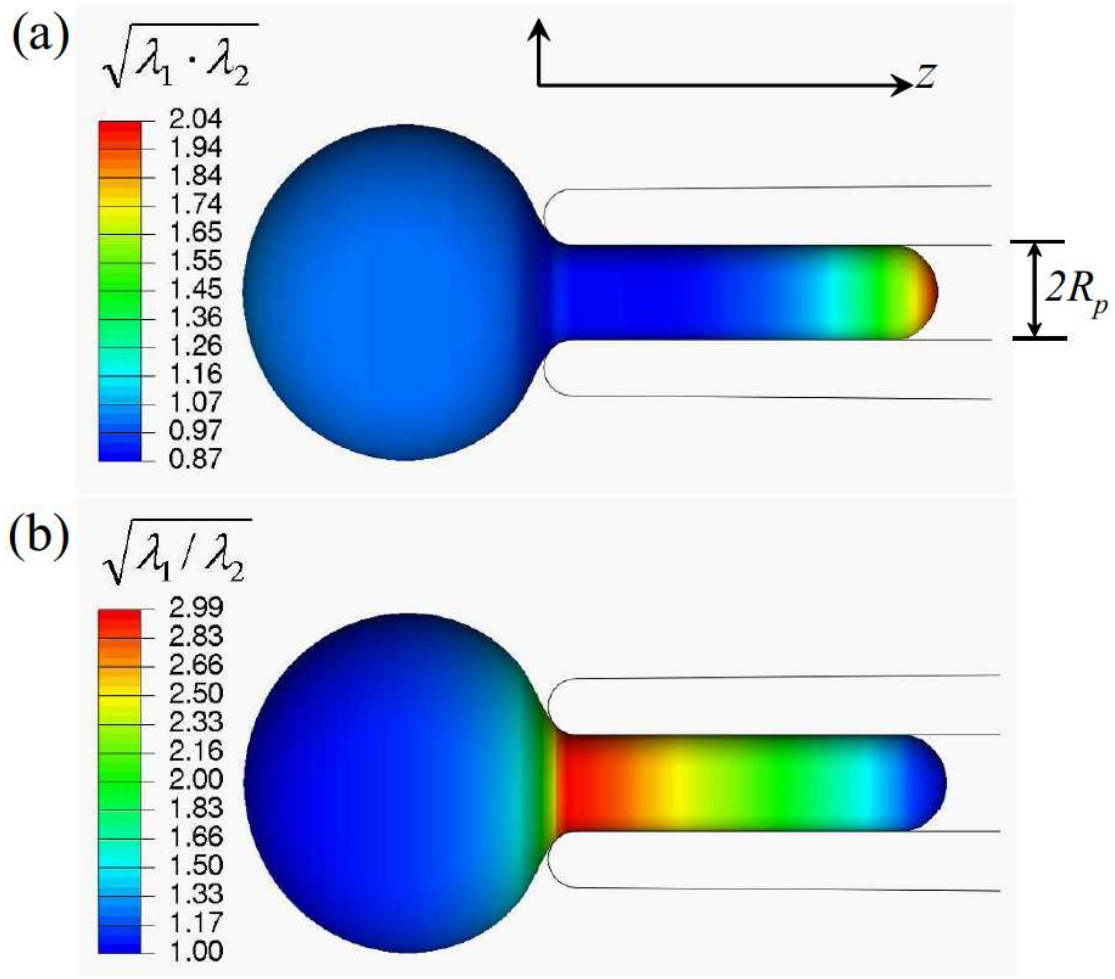

Figure 3.9: (a) Area deformation of the protein skeleton at $L = 8R_p$. (b) Shear deformation of the protein skeleton at $L = 8R_p$.

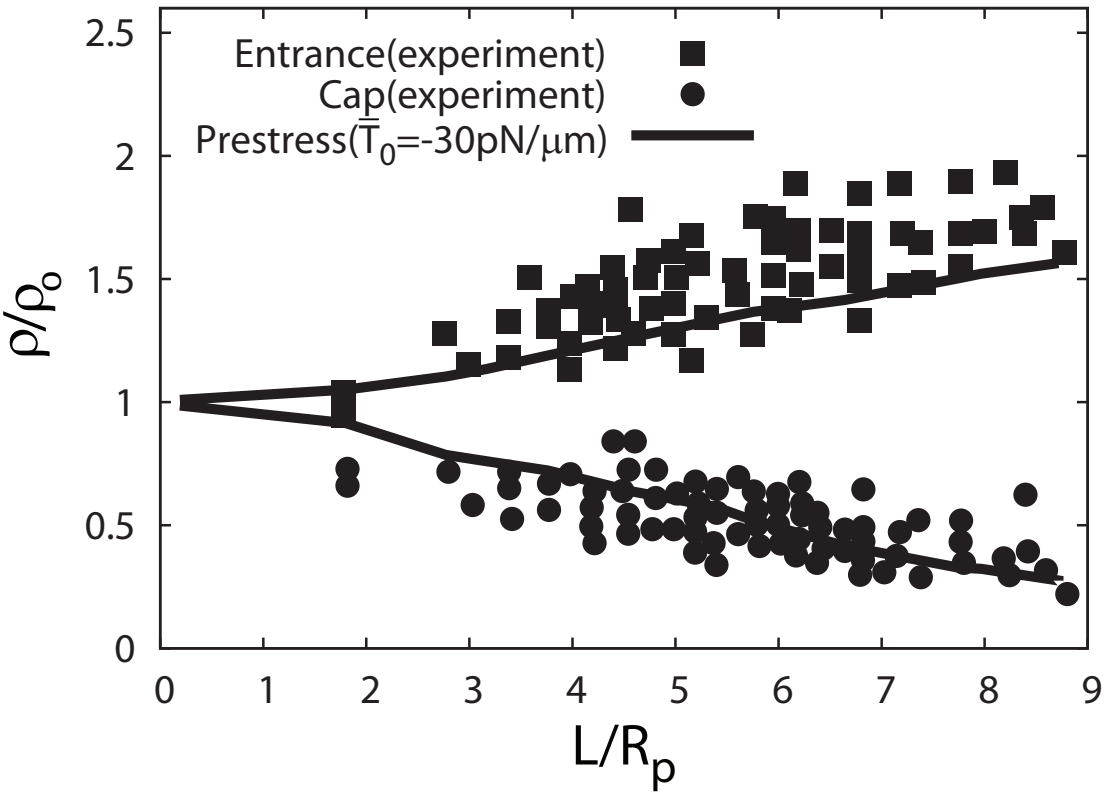

Figure 3.10: The skeleton density predicted by our model with $\bar{T}_0 = -30$ pN/μm compared with experimental data by Dischер *et al.* (1994).

coarse-grained model for prestress case with $\bar{T}_0 = -15$ pN/μm (Discher *et al.*, 1998). In Fig. 3.10 we plot how the skeleton density changes with L/R_p at the cap and the pipette entrance regions predicted by the prestress case with $\bar{T}_0 = -30$ pN/μm, and compare it with experimental data by Discher *et al.* (1994). To match the setup utilized in Discher *et al.* (1998), in this particular simulation at the initial state the cell is slightly swollen and its initial shape is depicted as a sphere with diameter 5.34 μm, while in all other simulations a flaccid biconcave shape as described in Eq. 3.1 is used as the initial shape. The radius of the pipette is 0.668 μm. Based upon the tendency demonstrated in Fig. 3.10, it is clear that our prediction of the density profile is consistent with experimental measurements by Discher *et al.* (1994), *i.e.* the skeleton is expanded near the cap and compressed near the neck.

The area and shear deformation contours of the protein skeleton at $L = 8R_p$ are shown in Fig. 3.9 for the case with $\bar{T}_0 = -15$ pN/μm. We can see the maximum shear deformation happens near the entrance and there is no shear deformation in the tip region.

Fig. 3.10 demonstrates that for the same prestress level ($\bar{T}_0 = -15$ pN/μm), the skeleton density of the cap region predicted by our model is lower than that by the coarse-grained model (Discher *et al.*, 1998). This is partially attributed to the fact that in the coarse-grained model the deformed shape of the cell is artificially assumed (perfect semi-sphere is assumed for the cap), but in our model the deformed shape is directly computed based on continuum mechanics. Although our computed deformed shape is just slightly different from the assumed shape by Discher *et al.* (1998), additional constraints usually make the structure stiffer. The difference is also due to another fact that at $L/R_p = 8$ the number of junctional complexes is relatively small in the cap region where the surface is curved so that the difference between our continuum description and the discretized description in the coarse-grained model may be pronounced. Since in reality there are approximately 33,000 JCs in the cell while 18,434 JCs are considered in the coarse-grained model by Discher *et al.* (1998), the real density profile should be between our result and that of the coarse-grained model.

Fig. 3.8 also shows that the prestress level influences the skeleton density significantly. In fact, the accurate prestress level, even the type of the prestress

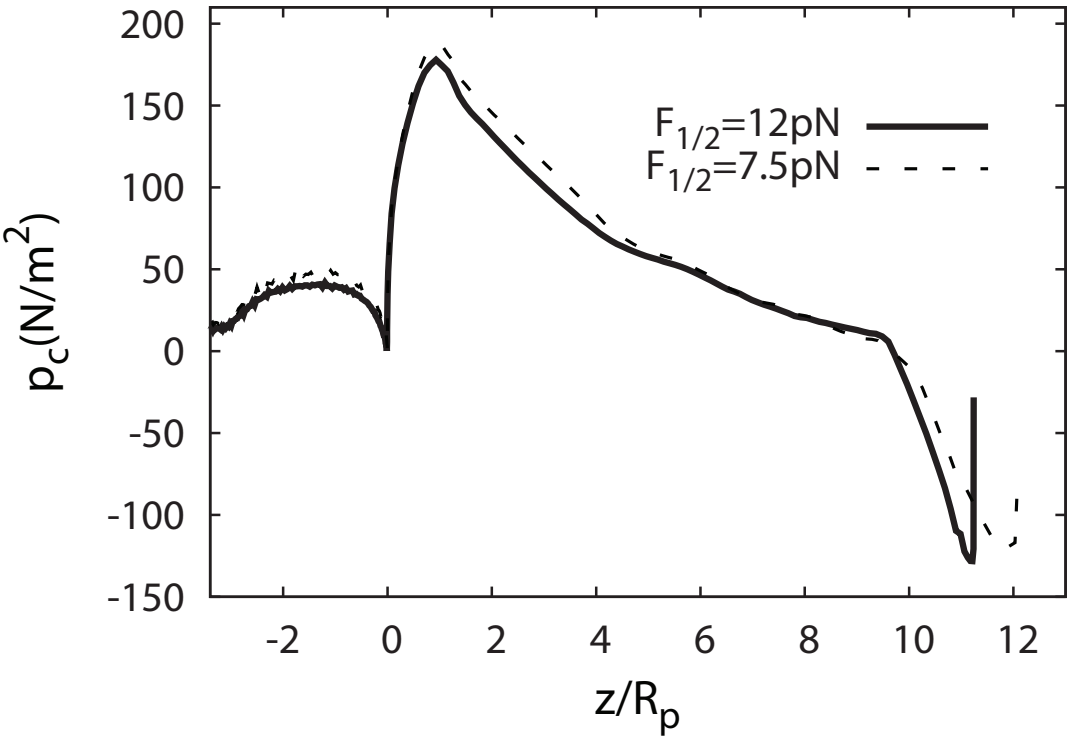

Figure 3.11: Distributions of contact pressure.

(precompression or pretension), is still controversial (Discher *et al.*, 1998; Svoboda *et al.*, 1992; Kozlov and Markin, 1990). In our following simulations we use $\bar{T}_0 = -30$ pN/μm, which matches the experimental data as shown in Fig. 3.10 (and also in Figs. 3.5 and 3.7).

As illustrated in the Appendix C, in this case the initial shape of the cell is spherical and it is thus impossible to simultaneously conserve area and volume. Indeed, if we assume that the cap area is semi-spherical and the part outside of the pipette remains spherical during aspiration, it can be geometrically proven that when the surface area is conserved the volume loss in this case should be 27% as $L = 8R_p$, a value consistent with our numerical simulation.

For all simulations below we use the following parameters: p_f=11.118 nm, L_f=6.388 nm, and $\bar{T}_0 = -30$ pN/μm. Through numerical simulations we have shown that this set of parameters provides consistently good comparisons with experiments in terms of cell deformations induced by micropipettes and optical tweezers, as well as density variations of the protein skeleton during micropipette aspirations.

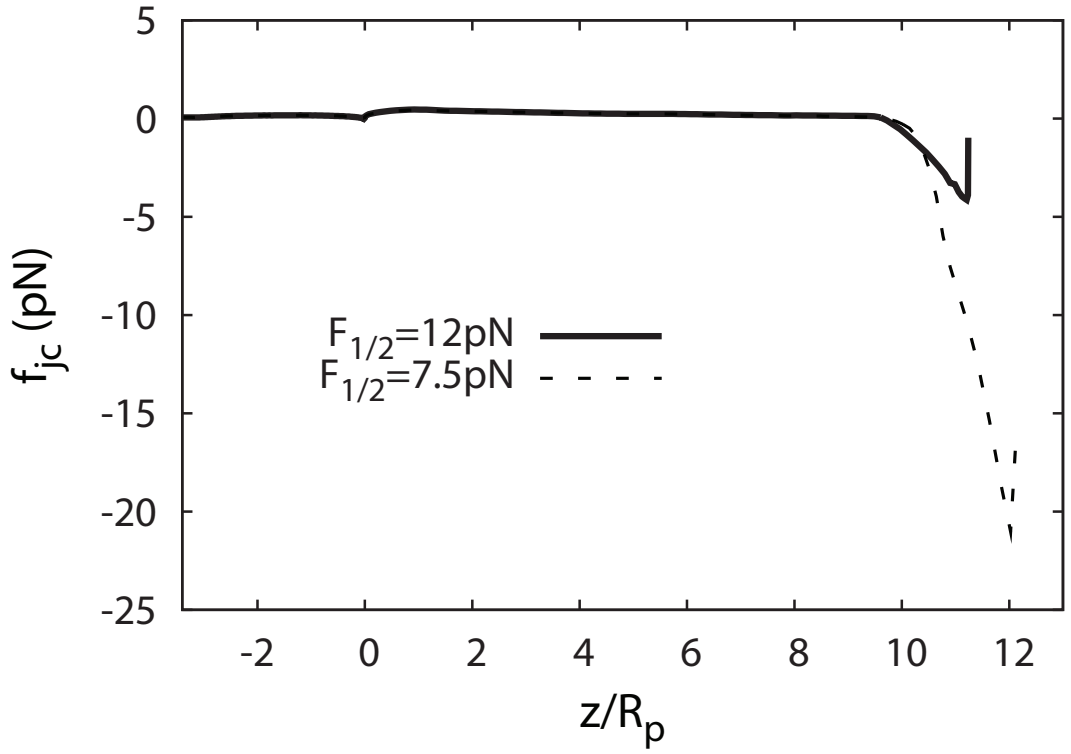

Figure 3.12: Distributions of contact force upon a JC.

3.3.3 Bilayer-skeleton interaction force and the effect of spectrin unfolding

Hereafter we concentrate upon the vertical interaction force (contact force) between the two layers during the micropipette aspiration of a cell from its biconcave state.

Fig. 3.11 displays the distributions of the contact pressure p_c between the two layers during a micropipette aspiration with an applied pressure of 256 pN/μm^2. By definition, a negative contact pressure refers to a scenario in which the two layers are pulled apart (dissociation tendency), and a positive contact force means that the layers are pushed together (adhesion/association tendency). It is seen that positive (association) contact pressure is concentrated close to the entrance, and negative (dissociation) contact pressure exists mostly near the cap. This phenomenon can be explained by considering the local curvature of the inner layer: due to the its own internal tension, the protein skeleton is pulled away from the lipid bilayer at places

where it has a convex shape (Fig. 3.13a) and is pulled towards the lipid bilayer at places where it is concave (Fig. 3.13b).

In our simulation, negative (dissociation) contact pressure with peak value of about -130 pN/μm^2 is recorded in the area close to the cap. To relate the contact pressure p_c to mechanical loading on the molecular structure of the protein skeleton, it is convenient to define a contact force per JC, (*i.e.* the total contact force acting on the area covered by the hexagon formed by the six SCs in a JC) as

$$f_{jc} = \frac{135cm^2}{33000}\frac{\rho_0}{\rho}p_c, \tag{3.2}$$

where ρ and ρ_0 are the current and initial protein densities of the cytoskeleton. In practice, this density ratio is determined as $\rho/\rho_0 = 1/(\lambda_1\lambda_2)$, where λ_1 and λ_2 are principal in-plane stretches of the cytoskeleton. f_{jc} takes into account variations of the density distribution of the pinning points between the protein skeleton and the lipid bilayer. The distribution of f_{jc} along the cell is also plotted in Fig. 3.12. It is seen that near the cap the decreased skeleton density amplifies the concentration of dissociation force.

Sp unfolding may play an important role in determining the skeleton density, and subsequently f_{jc}, near the cap region. Unfolding will unstiffen the skeleton, causing larger area expansion and thus increasing f_{jc} even if p_c remains unchanged. To understand this effect, we recalculate the case above by using a smaller $F_{1/2}$ ($F_{1/2}$ = 7.5 pN), which encourages the occurrence of unfolding. In this case, since the Sp domains will successively unfold under constant external pressure (256 pN/μm^2), the skeleton will deform continuously until structural failures happen, *e.g.* the skeleton-bilayer dissociation. In practice we terminate the simulation when the deformation reaches $L/R_p = 12$. We also note that this unstiffening behavior is only possible under the quasi-static assumption. Any finite deformation rate will introduce finite elasticity and limit the amount of deformation (Zhu and Asaro, 2008). As shown in Fig. 3.12, with $F_{1/2} = 7.5$ (and the same aspiration pressure) the unfolding effect greatly increases the magnitude of f_{jc} near the cap area, which may increase the possibility of vertical skeleton-bilayer dissociation. Consequently, our simulation suggests that $F_{1/2}$ (which is not considered in any other models) is a key parameter in RBC remodeling,

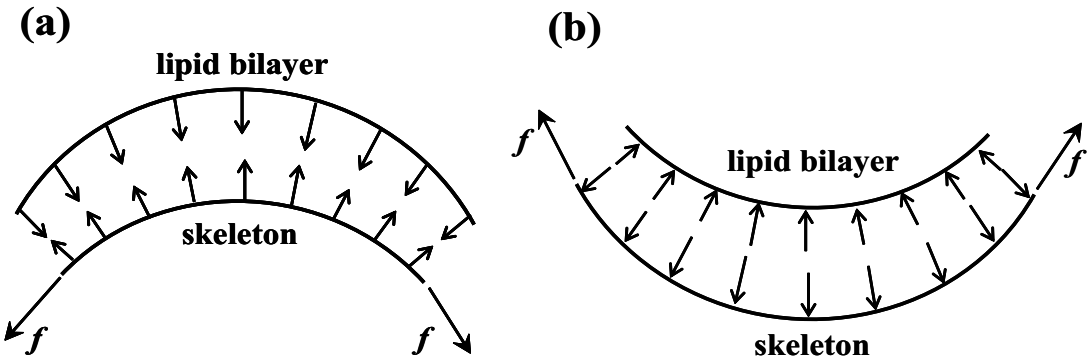

Figure 3.13: To overcome the effect of internal tension f inside the protein skeleton, there must exist (a) negative (dissociation) contact force between the protein skeleton and the lipid bilayer in locations with convex shape, or (b) positive (association) contact force in locations with concave shape.

which deserves dedicated experimental investigation.

3.3.4 Post-dissociation behavior – necking

In the previous section, we studied the interaction force (contact force) between the two layers before the dissociation. Our model is also capable of exploring the subsequently response after skeleton/bilayer dissociation. When the negative pressure in micropipette aspiration is sufficiently high, a vesicle will be separated from the cell. A vesicle is an entity formed by part of the cell membrane is deficient in skeleton proteins such as band 3 (Knowles *et al.*, 1997), suggesting a scenario wherein its formation is caused by the skeleton separating from the lipid bilayer. It was observed in experiments that before a vesicle is created a region of reduced caliber, *i.e.* a neck, was formed in the middle section between the cap and the entrance (Knowles *et al.*, 1997). The location of the neck may appear to be at odds with the fact the skeleton-bilayer dissociation should first occur close to the cap, where the maximum dissociation force occurs.

To shed light on this phenomenon, we simulate the post-dissociation behavior by assuming that the two layers separate when the magnitude of the dissociation force per JC reaches a critical value $\tilde{f}_{jc}$=20 pN for the case with $F_{1/2}$=7.5 pN in the previous section. We note that the choice of $\tilde{f}_{jc}$ does not affect the qualitative simulations that follow. However, further experiments are required to pinpoint its

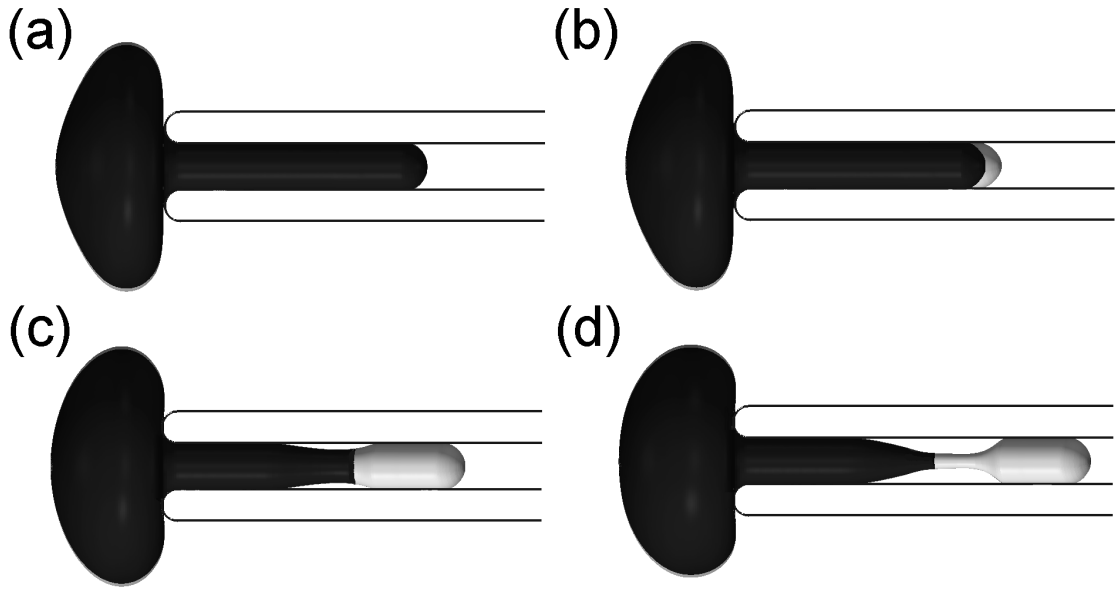

Figure 3.14: FEM simulation of the necking process before vesiculation (lipid bilayer in light color and skeleton in dark color).

exact value. As shown in Fig. 3.14b, the separation is first observed in the cap region, consistent with the distribution of the dissociation force. Subsequently in Fig. 3.14c, when the skeleton network shrinks to certain extent, a separation between the lipid bilayer and the pipette inner surface begins, which eventually leads to formation of a neck (Fig. 3.14d). The tendency for necking is primarily due to two factors: 1) For a cylindrical tether of lipid bilayer, Waugh and Hochmuth (1987) showed that

$$f_0 = 2\pi k_c / R_t, \tag{3.3}$$

where f_0 is the resultant force applied on the tether, R_t is the radius of the cylindrical tether and k_c is the bending stiffness. For the lipid bilayer part without skeleton in Fig. 3.14c, we can also qualitatively apply this relation without considering the negative pressure in radial direction.

$$f_0 = \pi R_p^2 \Delta P = 359pN, \tag{3.4}$$

and $k_c = 0.2pN \cdot \mu m$ so that

$$R_t = 2\pi k_c / f_0 \approx 0.003\mu m. \tag{3.5}$$

It means the lipid bilayer cannot sustain the pressure of $256pN/\mu m$ until it reduces to a tether with $R_t = 0.003\mu m$, which is even smaller than the thickness of the lipid bilayer. It shows the lipid bilayer will neck to a very small tether and then break to form a vesicle; 2) The skeleton at the cap region is significantly expanded before separation. After separation, it tends to contract, generating a large pulling force on the lipid bilayer in the radial direction toward the center of the pipette, which encourages the necking of the bilayer.

We also found that under the aforementioned conditions (*i.e.* external pressure of 256 pN/μm^2 and $F_{1/2}$=7.5 pN) the skeleton/bilayer dissociation occurs before Sp unfolding only if $\tilde{f}_{jc}$ <$\sim$4.0 pN, otherwise the separation occurs after Sp unfolding. Therefore, Sp unfolding may play a critical role in skeleton/bilayer separation. Additional experiments (especially the experiments to determine key parameters such as $\tilde{f}_{jc}$ and $F_{1/2}$) are necessary to illustrate the role of Sp unfolding on skeleton/bilayer separation.

It is necessary to point out that this simulation is qualitative rather than quantitative – to accurately capture the dynamic separation process an accurate evaluation of the damping matrix $\mathbf{C}$ in Chapter 4 is required. This matrix summarizes the effect of the viscosity of the lipid bilayer and the protein skeleton, the friction between these two, and the effects of the surrounding fluid.

3.4 Simulations of flow channel stretching

In this section, we will simulate an experiment called flow channel stretching. Flow channel stretching experiments have been developed to examine the response of cells attached to a substrate to the shear stresses exerted by an incoming flow. In a typical flow channel setup, erythrocytes are allowed to sediment inside a channel consisting of two parallel plates. The substrate is coated with bovine serum albumin (BSA) so that most cells do not adhere to the bottom with large attachment areas.

When external flows are introduced the cells deform while one (in some cases more than one) point remains attached to the substrate. Long membrane strands (tethers) may appear when the fluidic shear surpasses a threshold value ($\sim$1.5 dyn/cm^2, or 0.15 pN/μm^2) (Hochmuth, 1973).

The critical contact force between the lipid bilayer and the protein skeleton that triggers dissociation is determined by numerically duplicating the critical state of a cell in a flow channel before formation of tethers.

The substrate under the red cell is modeled as a rigid body. In this simulation, we focus on the final configuration of the cell deformation, instead of solving the fully-coupled fluid-structure interaction problem and obtaining the fluid loading on the cell as described in Chapter 4, herein we simplify the fluid effect as a uniform distribution of shear force on $-x$ direction acting on the upper surface of the cell ($z > 0$).

In reality the cell attaches to the substrate not at a geometric point, but within a small attachment area. In our model this attachment area is depicted as a circular area on the cell membrane whose diameter D_a is chosen to be within the same range as the diameter of the tether estimated from optical and scanning electron photomicrographs, *i.e.* 0.1-0.2 μm (Hochmuth, 1973) (it is important to notice here that the two are not expected to be exactly the same, since the radius of the tether R_t depends on the applied force f_0 by the relation $R_t = 2\pi k_c/f_0$ (Waugh and Hochmuth, 1987)). We consider that the attachment point is located at the bottom rim of the cell where the cell makes contact with the substrate.

Fig. 3.15 and Fig. 3.16 show the area and shear deformations of the inner layer (the cytoskeleton) with a flow shear stress of 0.15 pN/μm^2 when the diameter of the contact area is 0.2 μm. Fig. 3.17 shows the contact pressure (*i.e.* contact force per unit area) between the two layers. The amount of cell deformation is consistent with experimental observations under similar magnitude of flow shear (see Figs. 1 and 2 in Chien *et al.* (1992)). By definition, a negative contact pressure refers to a scenario in which the two layers are pulled apart (dissociation tendency), and a positive contact force means that the layers are pushed together (adhesion/association tendency). In our simulation, a negative (dissociation) contact pressure with a peak value of about 380 pN/μm^2 is recorded in the area around the attachment area. As shown in Fig. 3.17 due to its own internal tension, the protein skeleton is pulled away from the lipid

Table 3.1: FEM prediction of the critical contact force based upon flow channel experiments.

D_a (μm)	p_c (pN/μm^2)	$-f_{jc}$(pN)	W_0 (pN/μm)
0.10	1813	28.0	63.5
0.13	1185	16.8	41.5
0.16	449	6.2	15.8
0.20	380	4.5	13.3

bilayer at places where it has a convex shape and is pulled towards the lipid bilayer at places where it is concave. Larger local curvature usually leads to greater contact force. For this reason, the diameter of the contact area has a large effect upon the contact force.

For perspective, we compare this contact force with the skeleton-bilayer adhesion energy reported in Hwang and Waugh (1997) ($\sim$60 μJm^{-2}). Following the scenario that during dissociation band 3 is separated from the bilayer, this adhesion energy is related to the energy to pull band 3 out. Taking into account the fact that band 3 is a chain which crosses the bilayer 14 times (Lux, 1989), the subsequent adhesion energy is the energy required to pull all these crossings sequentially out. Assuming that during the process the applied force decreases linearly from the critical contact force to zero as the band 3 is completely out, the adhesion energy W_0 is given as $p_c \times 35$ nm.

The predicted critical contact force and adhesion energy at four different contact areas are shown in Table 3.1.

The interaction force per JC f_{jc} in Table 3.1 is in the same order as the value predicted in the micropipette aspiration simulations. They are consistent. Furthermore, the adhesion energy W_0 predicted in Table 3.1 is consistent with the estimation by Hwang and Waugh (1997).

We also studied the dependence of the critical interaction force on the flow shear stress as shown in Fig. 3.18.

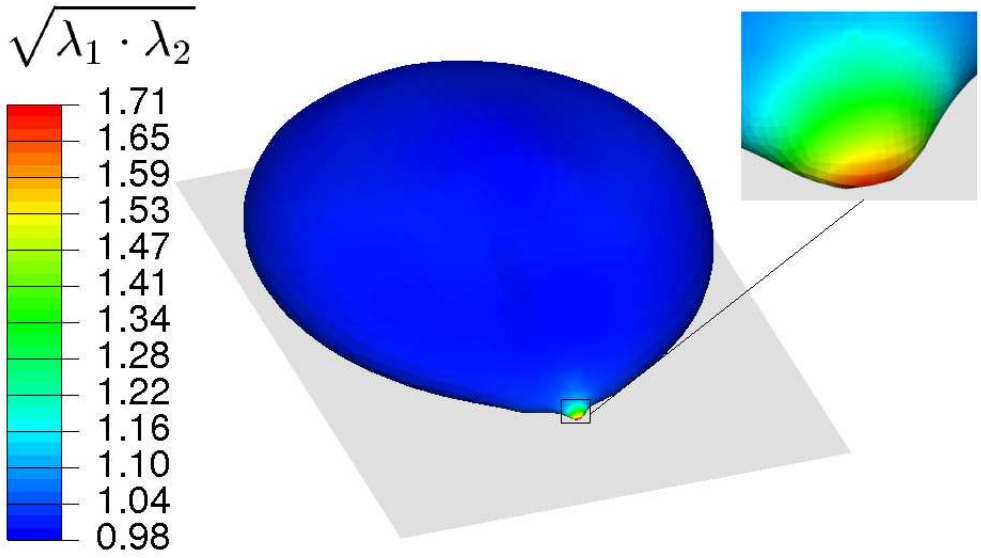

Figure 3.15: Area deformation of the inner layer (the protein skeleton) during a flow channel simulation with the flow shear stress of 0.15 pN/μm^2.

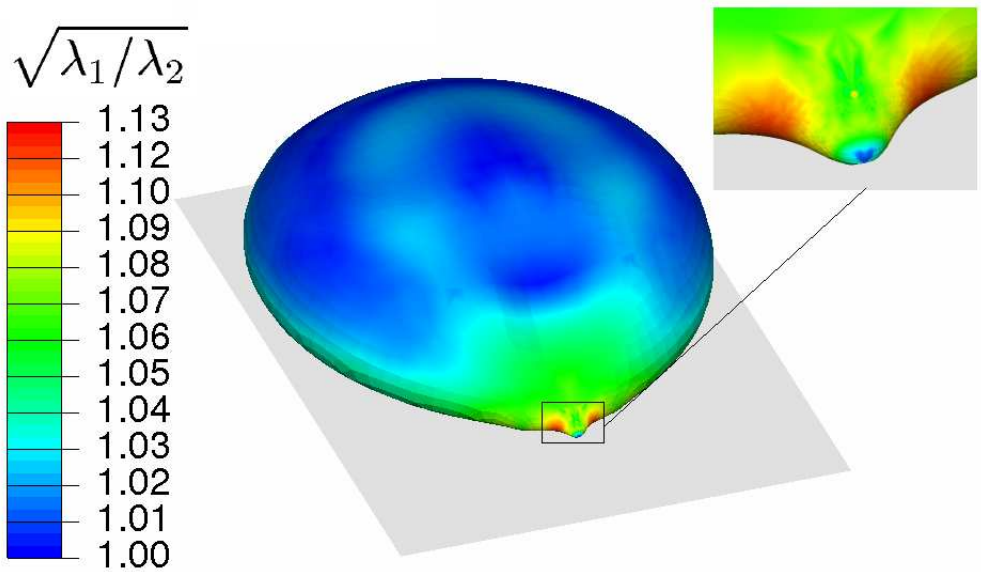

Figure 3.16: Shear deformation of the inner layer (the protein skeleton) during a flow channel simulation with the flow shear stress of 0.15 pN/μm^2.

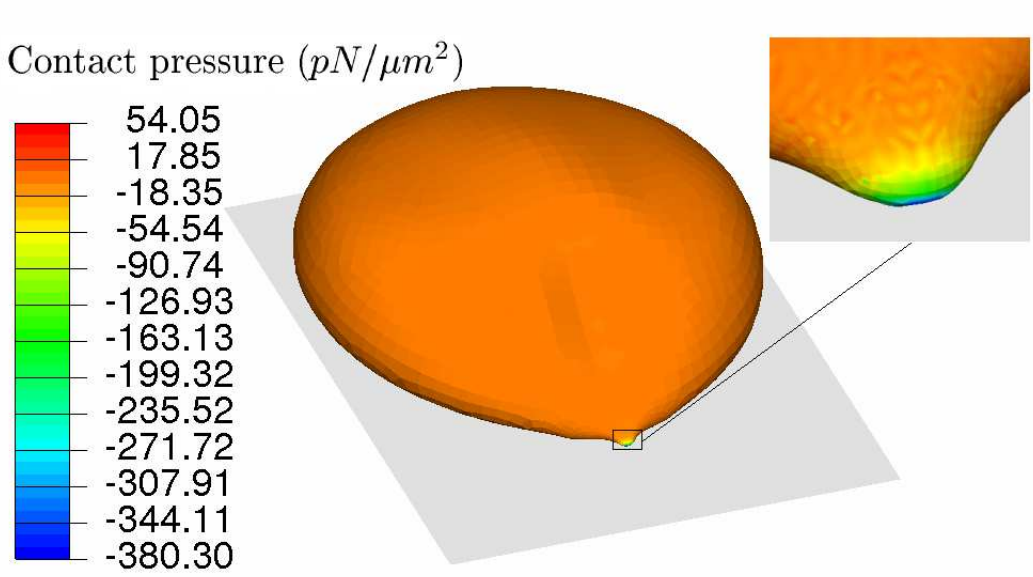

Figure 3.17: Contact pressure of the inner layer (the protein skeleton) during a flow channel simulation with the flow shear stress of 0.15 pN/μm^2.

3.5 Summary and remarks

In this chapter, by using a three-level quasi-static multiscale modeling technique we have quantitatively studied the deformation of the composite erythrocyte membrane prompted by mechanical loads as well as the interactions between the protein skeleton and the lipid bilayer. The primary purpose of this study is to build a framework for understanding erythrocyte mechanics upon which new knowledge from future experiments can be incorporated. Such a model analysis will also help us design new experiments to illustrate the exact mechanism of mechanically-induced membrane morphological changes, and to achieve quantitative predictions of the occurrence of vesiculation and budding of normal or defected erythrocytes. The focus is to quantify the critical dissociation contact force, the amount of normal load between the protein skeleton and the lipid bilayer that may cause dissociation based upon existing data. By numerically duplicating the flow channel experiment, we correlate the critical flow shear that triggers tether formation with the normal detaching force acting on each JC considering the density change of the protein skeleton in the

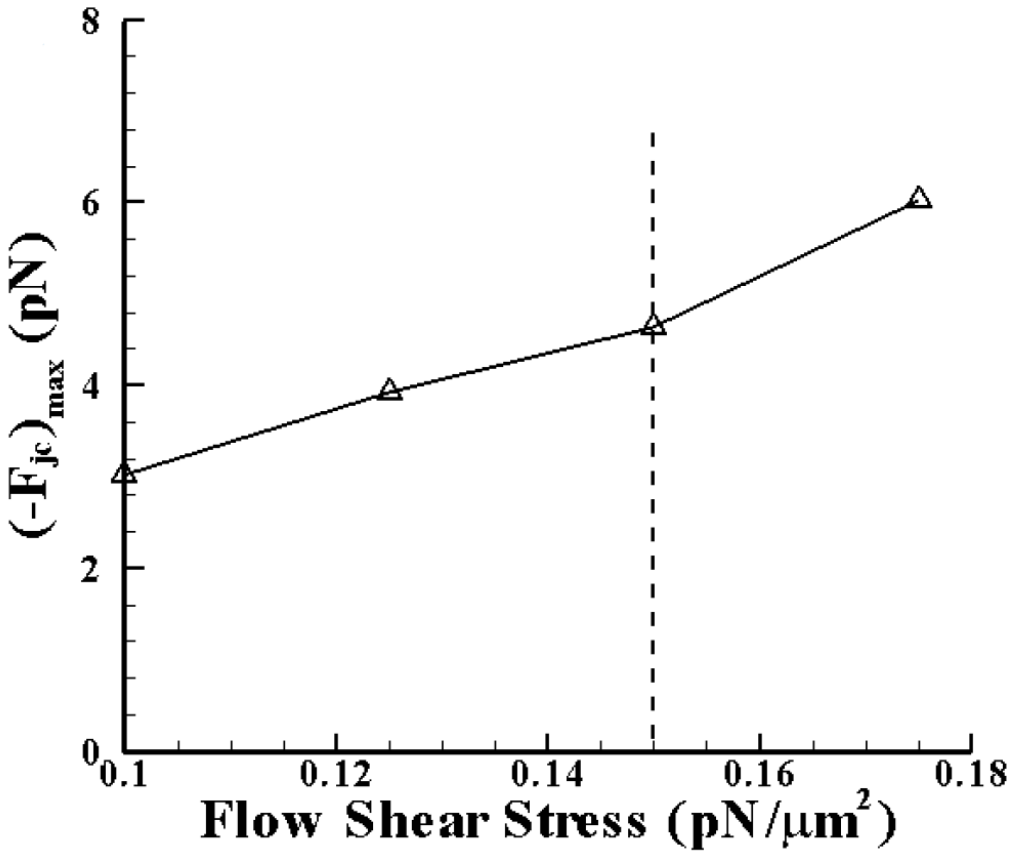

Figure 3.18: The maximum negative contact force per unit JC $-f_{jc}$ as a function of the flow shear stress (the dashed line marks the critical state where tether formation starts).

deformed state. The accurate determination of the normal contact force depends upon the capacity to predict the response of the protein skeleton in large shear and area changing deformations determined by the nonlinear constitutive properties of the protein skeleton, and the curvature of the composite membrane in response to external loads determined by the bending response of the lipid bilayer as well as its interaction with the protein skeleton. To achieve these, we developed a model which takes into account the constitutive properties of the protein skeleton during large deformations (including effects of Sp folding/unfolding) and lateral slide between the protein skeleton and the lipid bilayer.

Compared with existing models of the RBC membrane (Discher *et al.*, 1998; Mukhopadhyay *et al.*, 2002; Svetina *et al.*, 2004), our model has the following characteristics: (1) Our multiscale approach not only delivers accurate predictions of whole-cell response (due to the involvement of the detailed molecular structure and responses at different levels), but also allows us to address physical mechanisms at different length scales and to correlate mechanical loads on the cell with detailed stress distributions within the composite structure. This model has predicted phenomena that had never been found by other models (*e.g.* bifurcation, mode switching, and stress-induced unstiffening due to unfolding) (Zhu *et al.*, 2007; Zhu and Asaro, 2008); (2) our model explicitly incorporates the local interactions between the skeleton and the bilayer, as well as the inter- and intra-molecule interactions inside the skeleton; (3) This model is inherently dynamic and capable of studying time-dependent responses at different length scales, which will be developed in Chapter 4.

The exact molecular mechanism of the skeleton-bilayer uncoupling in physiological conditions remains unresolved. As mentioned earlier, the skeleton-bilayer connectivity is achieved *via* both SC and the protein 4.1/glycophorin C assembly. Therefore, the skeleton-bilayer uncoupling may be attributed to dissociation of multiple inter-protein and protein-to-lipid linkages. For example, there exists a dynamical balance between the ruptured and the reattachment states of the band 3-ankyrin linkage (Anong *et al.*, 2006). Although this balance has been found insensitive to shear deformations (lateral loads), it is likely to be disturbed by vertical loads, which may favor the ruptured state. Vertical load resulting from the negative contact pressure may cause widespread band 3-ankyrin dissociation. This scenario is consistent with

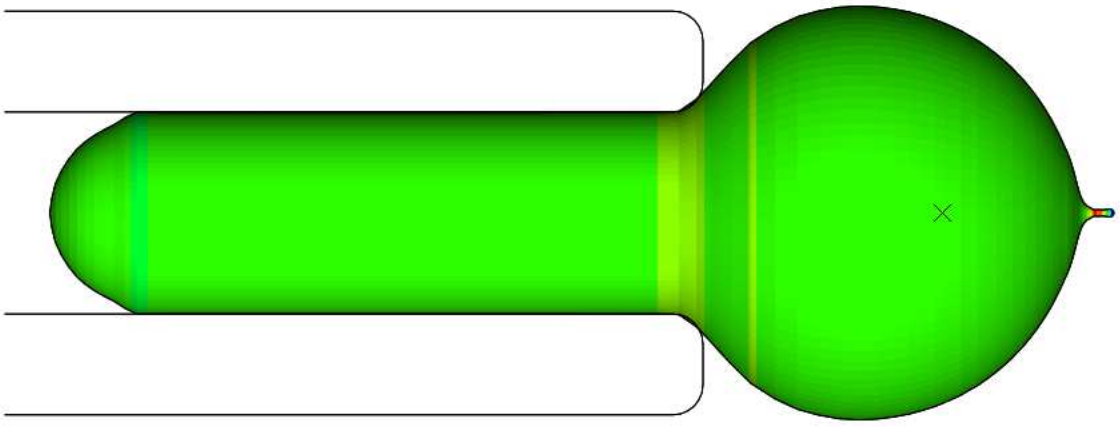

Figure 3.19: Simulation of the tether forming experiment by Hwang and Waugh (1997); Waugh and Bauserman (1995).

a recent experiment (Borghi and Brochard-Wyart., 2007), which indicates that band 3 can be separated from the rest of the protein skeleton rather than the previously-discussed scenario that band 3 is pulled out of the lipid bilayer, suggesting that different physiological mechanisms may be involved in different conditions (*e.g.* deformation rates). It will thus be interesting to examine the dependence of the critical contact force on deformation rates. In addition, the tangential forces between the protein skeleton and the lipid bilayer, which are not considered in the current study due to the quasi-static assumption, may play a significant role if time-dependent responses are included.

It is necessary to indicate that the flow channel simulations suffer from uncertainties about the location and the detailed configuration of the contact area between the cell membrane and the substrate. Moreover, a precise rendition of the fluid-structure interaction is also crucial. The fluid-dynamics problem falls into the low

Reynolds number Stokes/Oseen flow regime, and can be resolved *via* a boundary element approach as described in Chapter 4. Our preliminary results using such a method show that in this configuration the fluid force is indeed concentrated mainly on the upper half of the cell, confirming our assumptions in the current study. We note that there exists another set of experiments in which tether formation was reported. In these experiments the cell is deformed either by the gravitational load from an attached glass bead, or by loads imposed through a cantilever, while it is fixed with a micropipette (Hwang and Waugh, 1997; Waugh and Bauserman, 1995). A predicted shape in a preliminary simulation of this experiment is shown in Fig. 3.19. Tethers were formed as the applied force reaches a critical value ($\sim$50 pN). To numerically duplicate this set of experiments and accurately predict the critical contact force, we also need to resolve a number of uncertainties. For example, in those experiments the erythrocytes were usually pre-swollen in a hypotonic solution and were held by a micropipette. The internal pressure, which significantly affects the cell response, it difficult to specify. In addition, tether formation involves a tiny contact area and subsequently a small number of pinning points. Although our continuous model is adequate in determining the contact pressure between the two layers, in relating this to the exact loading upon each pinning point its accuracy is limited since it only accounts for the average value, not the variations (which could be significant if only a small number of points are involved). A possible solution of this problem is to develop a hybrid model combining a detailed molecular description of the skeleton near the contact area and a continuous model of the skeleton elsewhere.

At the current stage of model development, micropipette aspiration experiments provide a setup that is easier to be duplicated numerically. Experimentally, what is required is a sequence of aspirations using different pipette sizes and deformation rates, from which the exact conditions that lead to vesiculation can be extracted. Fluorescent labels will assist in pinpointing the occurrence of vesiculation, and in determining the exact linkage that may rupture under the load.

Chapter 3, in part, is a reprint of the material as it appears in 'Multiscale modeling of erythrocyte membranes', *Physical Review E*, **81**: 031904, 2010. Zhangli Peng, Robert J. Asaro and Qiang Zhu, 2010. The dissertation author was the primary investigator and author of this paper.

Chapter 4

Dynamic Multiscale Modeling Approach with Fluid-Structure Interaction and Viscoelasticity

In this chapter, we will extend the quasi-static multiscale approach described in Chapter 2 to a dynamic version by incorporating the fluid-structure interaction and the membrane viscoelasticity. The fluid-structure interaction (FSI) problem is solved by coupling a boundary element method of Stokes flow with the finite element model of the membrane (Level III). The membrane viscoelasticity is considered by using a Voigt-Kelvin constitutive model. In addition, the cytoskeleton dynamics is also presented.

4.1 Fluid-bilayer interaction

We consider a red blood cell filled with an interior fluid (cytoplasm, hereafter referred to as fluid 2) and immersed in an exterior fluid (*e.g.* blood plasma, referred to as fluid 1) as illustrated in Fig. 4.1. Ω^f and Ω^b are the volumes occupied by the fluids and the bilayer, respectively. The boundary between the bilayer and the exterior fluid is $\Gamma^{fb,1}$. The boundary between the bilayer and the interior fluid is $\Gamma^{fb,2}$. For a general problem, two types of boundary conditions are specified: Dirichlet boundary Γ^{fD}, and Neumann boundary Γ^{fN}. $\Omega = \Omega^b \cup \Omega^f$ is the entire computational domain, and

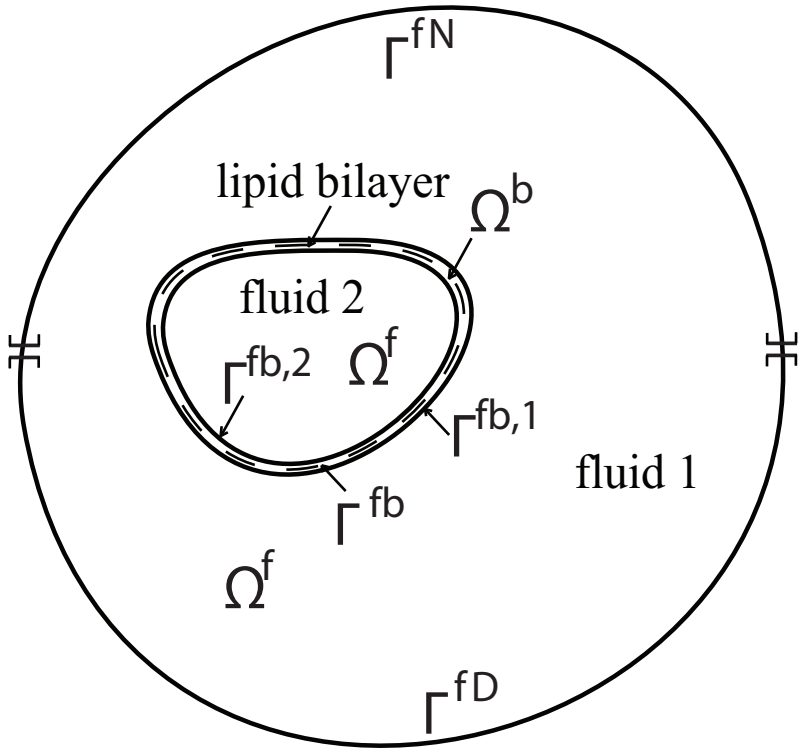

Figure 4.1: Schematic of a red blood cell immersed in two fluids with different viscosites (the cytoskeleton is not drawn, and the dashed line denotes the middle surface of the lipid bilayer).

$\Gamma = \Gamma^{fN} \cup \Gamma^{fD} \cup \Gamma^{fb,1} \cup \Gamma^{fb,2}$ is the entire boundary. Hereafter we use the superscript 'b' to represent the lipid bilayer, 'f' the fluid, and 's' the cytoskeleton. Furthermore, we use bold capital symbols to represent tensors or multi-column matrices, and bold lower-case symbols to represent vectors or single-column matrices.

4.1.1 Governing equations

The dynamic responses of both the lipid bilayer and the fluids are controlled by the conservation of momentum and the conservation of mass. No body force is considered here, and the inertial force is negligible at this length scale. With the updated Lagrangian description, the governing equation of the lipid bilayer is

$$\nabla \cdot \mathbf{\Theta}^b = \mathbf{0}, \tag{4.1}$$

where ∇ is the spatial gradient operator. $\mathbf{\Theta}^b$ is the Cauchy stress tensor inside Ω^b. The constitutive equations of the lipid bilayer from which $\mathbf{\Theta}^b$ is obtained will be presented in §4.3. In Eq. (4.1) and what follows, the single dot denotes the scalar product.

Within the Eulerian description, the Stokes equation of Stokes flow and the continuity equation for interior/exterior Newtonian fluids are expressed as

$$\nabla \cdot \mathbf{\Theta}^f = -\nabla p^f + \eta_l \nabla^2 \mathbf{v}^f = \mathbf{0}, \tag{4.2}$$

$$\nabla \cdot \mathbf{v}^f = 0, \tag{4.3}$$

where $\mathbf{\Theta}^f$ is the Cauchy stress tensor inside the fluids. $\mathbf{v}^f$ is the fluid velocity vector. p^f is the fluid pressure. η_l is the dynamic viscosity of fluid ($l = 1, 2$ stand for the exterior and interior fluids, respectively). For normal *in vivo* red blood cells, $\eta_1 = 1.2$ cP=0.0012 pN/μm^2·s and $\eta_2 = 6$ cP=0.006 pN/μm^2·s (see for example Chien, 1987). $\Lambda = \eta_2/\eta_1$ is the viscosity contrast ratio.

Stokes flow (named after George Gabriel Stokes), also named creeping flow, is a type of fluid flow where advective inertial forces are small compared with viscous

forces. The Reynolds number is low, *i.e.* $Re << 1$, where

$$Re = \frac{\rho^f V L}{\eta}, \tag{4.4}$$

where V is the mean fluid velocity, ρ^f is the fluid density, L is a characteristic linear dimension and η is the dynamic viscosity of the fluid.

The boundary conditions of this fluid-structure interaction problem are given as

$$\mathbf{v}^f = \bar{\mathbf{v}}^{fD} \quad \text{on} \quad \Gamma^{fD}, \tag{4.5}$$

$$\mathbf{t}^f = \bar{\mathbf{t}}^{fN} \quad \text{on} \quad \Gamma^{fN}, \tag{4.6}$$

$$\mathbf{v}^b = \mathbf{v}^f \quad \text{on} \quad \Gamma^{fb,1} \,\text{and}\, \Gamma^{fb,2}, \tag{4.7}$$

$$\mathbf{t}^b = \mathbf{t}^f \quad \text{on} \quad \Gamma^{fb,1}, \tag{4.8}$$

$$\mathbf{t}^b - \boldsymbol{\tau}^{bs} = \mathbf{t}^f \quad \text{on} \quad \Gamma^{fb,2}, \tag{4.9}$$

where $\bar{\mathbf{v}}^{fD}$ is the prescribed velocity vector on Γ^{fD}, and $\bar{\mathbf{t}}^{fN}$ is the prescribed traction vector on Γ^{fN}. $\mathbf{t}^b = \boldsymbol{\Theta}^b \cdot \mathbf{n}$ and $\mathbf{t}^f = \boldsymbol{\Theta}^f \cdot \mathbf{n}$ are the surface tractions of the bilayer and fluid domains (traction is defined as force per unit area on a surface). $\mathbf{n}$ is the normal vector of the boundaries pointing towards fluid 1. $\boldsymbol{\tau}^{bs}$ is the bilayer-skeleton interaction force per unit area applied on the cytoskeleton, which will be presented in §4.2.

In our approach, the lipid bilayer is modeled as a viscoelastic solid with tiny shear stiffness and large area stiffness (since the lipid bilayer is close to a fluid). Equation (4.1), together with the constitutive relations, is solved through a finite element algorithm, which has been formulated in details in §2.6 in Chapter 2. It will briefly be reviewed in (§4.1.2).

A boundary element algorithm is adopted to solve dynamics of both the interior and the exterior fluids. The basic formulations of this method are summarized in §4.1.3.

4.1.2 Variational form of bilayer equations and finite element discretization

As shown in §2.6 in Chapter 2, by using the principle of virtual power (Belytschko *et al.*, 2000), the variational form (weak form) of Eq. (4.1) with its boundary conditions is stated as: finding $\mathbf{u}^b \in V$ such that for $\forall \delta\mathbf{v}^b \in W$,

$$\iiint_{\Omega^b} \nabla\delta\mathbf{v}^b : \boldsymbol{\Theta}^b d\Omega^b = \iint_{\Gamma^{fb,2}} \delta\mathbf{v}^b \cdot \boldsymbol{\tau}^{bs} d\Gamma + \iint_{\Gamma^{fb,1}\cup\Gamma^{fb,2}} \delta\mathbf{v}^b \cdot \mathbf{t}^f d\Gamma, \tag{4.10}$$

where $\mathbf{v}^b = \partial\mathbf{u}^b/\partial t$ is the velocity vector of the lipid bilayer. $V = V(\Omega^b)$ denotes the trial function space for the displacement $\mathbf{u}^b$, and $W = W(\Omega^b)$ the test function space for the momentum equation Eq. (4.1).

Numerically, we employ the FEM to solve Eq. (4.10) by modeling the lipid bilayer as congregations of shell elements. By using the Hughes-Liu shell element representation described in §2.6 in Chapter 2, the lipid bilayer domain Ω^b between the surfaces $\Gamma^{fb,1}$ and $\Gamma^{fb,2}$ is represented by a single middle reference surface Γ^{fb} shown as the dashed line in Fig. 4.1. After finite element discretization, the governing equation (4.1) is re-expressed as $6N_{\text{FE}}$ (N_{FE} is the number of nodes in finite elements) algebraic equations symbolically expressed as

$$\mathbf{f}^b_{\text{FE}} = \mathbf{f}^{bs}_{\text{FE}} + \mathbf{f}^{fb}_{\text{FE}}, \tag{4.11}$$

$$\mathbf{m}^b_{\text{FE}} = \mathbf{m}^{bs}_{\text{FE}} + \mathbf{m}^{fb}_{\text{FE}}, \tag{4.12}$$

where $\mathbf{f}^b_{\text{FE}}$ is the global nodal vector of internal force related to material constitutive equations of the lipid bilayer, $\mathbf{f}^{bs}_{\text{FE}}$ is the global nodal vector of external force from the bilayer-skeleton interaction, and $\mathbf{f}^{fb}_{\text{FE}}$ is the global nodal vector of fluid-bilayer interaction force on the surface Γ^{fb}. $\mathbf{m}^b_{\text{FE}}$ is the global nodal vector of internal moment of the lipid bilayer, $\mathbf{m}^{bs}_{\text{FE}}$ is the global nodal vector of external moment from the bilayer-skeleton interaction, and $\mathbf{m}^{fb}_{\text{FE}}$ is the global nodal vector of fluid-bilayer interaction moment on the surface Γ^{fb}. All these vectors have the dimension of $3N_{\text{FE}}$. Detailed forms of these vectors can be found in §2.6 in Chapter 2.

4.1.3 Boundary integral representation for fluid equations and boundary element discretization

By using the Lorentz reciprocal theorem (Pozrikidis, 1992), Eqns. (4.2) and (4.3) can be described by a boundary integral representation. First, we write the velocity field around the lipid bilayer as

$$\mathbf{v}^f = \bar{\mathbf{v}}^f + \mathbf{v}^{f\prime}, \tag{4.13}$$

where $\bar{\mathbf{v}}^f$ is the undisturbed flow in the absence of the cell, and $\mathbf{v}^{f\prime}$ is the disturbance flow due to the cell.

Then we focus on the volume occupied by fluid 1, which is enclosed by boundaries Γ^{fN}, Γ^{fD} and $\Gamma^{fb,1}$. For a point $\mathbf{x}_0$ lying in this volume, the disturbance velocity is written as

$$\begin{aligned}\mathbf{v}^{f\prime}(\mathbf{x}_0) = &-\frac{1}{8\pi\eta_1}\iint_{\Gamma^{fD}\cup\Gamma^{fN}\cup\Gamma^{fb,1}} \mathbf{G}(\mathbf{x}_0,\mathbf{x})\cdot\mathbf{t}^f(\mathbf{x})d\Gamma(\mathbf{x}) \\ &+\frac{1}{8\pi}\iint_{\Gamma^{fD}\cup\Gamma^{fN}\cup\Gamma^{fb,1}} \mathbf{v}^{f\prime}(\mathbf{x})\cdot\mathbf{T}(\mathbf{x},\mathbf{x}_0)\cdot\mathbf{n}(\mathbf{x})d\Gamma(\mathbf{x}),\end{aligned} \tag{4.14}$$

where η_1 is the viscosity of fluid 1. $\mathbf{t}^f$ is the traction on the surface. The first right-hand term is the single-layer potential, which represents the contribution from the distribution of point forces associated with the Green's function for velocity. The second term is the double-layer potential, which represents contributions from point sources and point force dipoles. $\mathbf{G}$ contains the free-space Green's function for velocity G_{ij} expressed as

$$G_{ij}(\mathbf{x}_0,\mathbf{x}) = \frac{\delta_{ij}}{|\mathbf{x}-\mathbf{x}_0|} + \frac{(x_i - x_{0_i})(x_j - x_{0_j})}{|\mathbf{x}-\mathbf{x}_0|^3}, \tag{4.15}$$

where δ_{ij} is Kronecker's delta. $\mathbf{T}$ is the Green's function for stress. Its components are

$$T_{ijk}(\mathbf{x}_0,\mathbf{x}) = -6\frac{(x_i - x_{0_i})(x_j - x_{0_j})(x_k - x_{0_k})}{|\mathbf{x}-\mathbf{x}_0|^5}. \tag{4.16}$$

We assume that the fluid Neumann boundary Γ^{fN} is sufficiently far from the cell so that $\mathbf{v}^{f\prime}$ vanishes at Γ^{fN}, and $\mathbf{v}^f = \bar{\mathbf{v}}^{fD} = \mathbf{0}$ on the fluid Dirichlet boundary

Γ^{fD}. Following Pozrikidis (2005b), we apply the reciprocal theorem over the cell volume twice and then obtain an integral representation for the exterior flow of fluid 1 as

$$\mathbf{v}^f(\mathbf{x}_0) = \bar{\mathbf{v}}^f(\mathbf{x}_0) - \frac{1}{8\pi\eta_1}\Big[\iint_{\Gamma^{fb}} \mathbf{G}(\mathbf{x}_0,\mathbf{x})\cdot\Delta\mathbf{t}^f(\mathbf{x})d\Gamma(\mathbf{x}) + \iint_{\Gamma^{fN}} \mathbf{G}(\mathbf{x}_0,\mathbf{x})\cdot\bar{\mathbf{t}}^f(\mathbf{x})d\Gamma(\mathbf{x}) + \iint_{\Gamma^{fD}} \mathbf{G}(\mathbf{x}_0,\mathbf{x})\cdot\mathbf{t}^f(\mathbf{x})d\Gamma(\mathbf{x})\Big] + \frac{1-\Lambda}{8\pi}\iint_{\Gamma^{fb}} \mathbf{v}^f(\mathbf{x})\cdot\mathbf{T}(\mathbf{x},\mathbf{x}_0)\cdot\mathbf{n}(\mathbf{x})d\Gamma(\mathbf{x}), \tag{4.17}$$

where $\bar{\mathbf{v}}^f(\mathbf{x}_0)$ is the prescribed undisturbed velocity field. η_1 is the viscosity of the exterior fluid, and $\Lambda = \eta_2/\eta_1$. $\Delta\mathbf{t}^f = \mathbf{t}^{f,1} - \mathbf{t}^{f,2}$ is the discontinuity in the interfacial surface traction, where $\mathbf{t}^{f,1}$ is the traction in the outside surface $\Gamma^{fb,1}$ of the interface, and $\mathbf{t}^{f,2}$ is the traction in the inside surface $\Gamma^{fb,2}$ of the interface.

When $\mathbf{x}_0$ is located on the interface Γ^{fb}, the boundary integral equation becomes

$$\mathbf{v}^f(\mathbf{x}_0) = \frac{2}{1+\Lambda}\bar{\mathbf{v}}^f(\mathbf{x}_0) - \frac{1}{4\pi\eta_1(\Lambda+1)}\Big[\iint_{\Gamma^{fb}} \mathbf{G}(\mathbf{x}_0,\mathbf{x})\cdot\Delta\mathbf{t}^f(\mathbf{x})d\Gamma(\mathbf{x}) + \iint_{\Gamma^{fN}} \mathbf{G}(\mathbf{x}_0,\mathbf{x})\cdot\bar{\mathbf{t}}^f(\mathbf{x})d\Gamma(\mathbf{x}) + \iint_{\Gamma^{fD}} \mathbf{G}(\mathbf{x}_0,\mathbf{x})\cdot\mathbf{t}^f(\mathbf{x})d\Gamma(\mathbf{x})\Big] + \frac{1-\Lambda}{4\pi(1+\Lambda)}\fint\!\!\!\iint_{\Gamma^{fb}} \mathbf{v}^f(\mathbf{x})\cdot\mathbf{T}(\mathbf{x},\mathbf{x}_0)\cdot\mathbf{n}(\mathbf{x})d\Gamma(\mathbf{x}), \tag{4.18}$$

where $\fint\!\!\!\iint$ denotes the principal value integration.

Similarly, when $\mathbf{x}_0$ is located on the Dirichlet boundary Γ^{fD} ($\mathbf{v}^f = \bar{\mathbf{v}}^{fD} = \mathbf{0}$), the boundary integral equation becomes

$$\bar{\mathbf{v}}^f(\mathbf{x}_0) - \frac{1}{8\pi\eta_1}\Big[\iint_{\Gamma^{fb}} \mathbf{G}(\mathbf{x}_0,\mathbf{x})\cdot\Delta\mathbf{t}^f(\mathbf{x})d\Gamma(\mathbf{x}) + \iint_{\Gamma^{fN}} \mathbf{G}(\mathbf{x}_0,\mathbf{x})\cdot\bar{\mathbf{t}}^f(\mathbf{x})d\Gamma(\mathbf{x}) + \iint_{\Gamma^{fD}} \mathbf{G}(\mathbf{x}_0,\mathbf{x})\cdot\mathbf{t}^f(\mathbf{x})d\Gamma(\mathbf{x})\Big] = \mathbf{0}. \tag{4.19}$$

Numerically, we apply the boundary element method (BEM) to discretize the boundary integral equations (Eqns. (4.18) and (4.19)). The collocation method is employed. A constant four-node quadrilateral element is developed. We discretize the boundaries Γ^{fb}, Γ^{fD}, and Γ^{fN} into N_{BE}^{fb}, N_{BE}^{fD}, and N_{BE}^{fN} elements, respectively. The

single-layer potential kernel with a weak $1/r$ ($r = |\mathbf{x} - \mathbf{x}_0|$) singularity is integrated by segmenting the quadrilateral into flat triangles and the integration is performed analytically in a polar coordinate system. The weak $1/r$ singularity in the double-layer potential kernel is removed by using the relation

$$\iint_{\Gamma^{fb}} \mathbf{v}^f(\mathbf{x})\cdot\mathbf{T}(\mathbf{x},\mathbf{x}_0)\cdot\mathbf{n}(\mathbf{x})d\Gamma(\mathbf{x}) = \iint_{\Gamma^{fb}} [\mathbf{v}^f(\mathbf{x})-\mathbf{v}^f(\mathbf{x_0})]\cdot\mathbf{T}(\mathbf{x},\mathbf{x}_0)\cdot\mathbf{n}(\mathbf{x})d\Gamma(\mathbf{x})+4\pi\mathbf{v}^f(\mathbf{x}_0). \tag{4.20}$$

Applying the boundary integral equation at the collocation points of boundary Γ^{fb}, and after discretization of Eq. (4.18), we get $3N_{\mathrm{BE}}^{fb}$ algebra equations, which is written symbolically in matrix form as

$$\mathbf{v}_{\mathrm{BE}}^{fb} = \bar{\mathbf{v}}_{\mathrm{BE}}^{fb} - \mathbf{S}^{fb,fb}\mathbf{q}_{\mathrm{BE}}^{fb} - \mathbf{S}^{fb,fD}\mathbf{q}_{\mathrm{BE}}^{fD} - \mathbf{S}^{fb,fN}\mathbf{q}_{\mathrm{BE}}^{fN} + \mathbf{D}^{fb,fb}\mathbf{v}_{\mathrm{BE}}^{fb}, \tag{4.21}$$

where $\mathbf{v}_{\mathrm{BE}}^{fb}$ is the global vector including velocities at all collocation points on Γ^{fb} (*i.e.* its dimension is $3N_{\mathrm{BE}}^{fb}$). $\bar{\mathbf{v}}_{\mathrm{BE}}^{fb}$ is the global vector of undisturbed velocities. $\mathbf{q}_{\mathrm{BE}}^{fb}$, $\mathbf{q}_{\mathrm{BE}}^{fD}$, $\mathbf{q}_{\mathrm{BE}}^{fN}$ are the global surface traction vectors on Γ^{fb}, Γ^{fD}, and Γ^{fN}. $\mathbf{S}^{fb,fb}$, $\mathbf{S}^{fb,fD}$, $\mathbf{S}^{fb,fN}$ are the single-layer potential coefficient matrices on the interface Γ^{fb} by itself, the surface Γ^{fD}, and the surface Γ^{fN} respectively. $\mathbf{D}^{fb,fb}$ is the double-layer potential coefficient matrix on the interface Γ^{fb} by itself. The matrix vector multiplication $\mathbf{D}^{fb,fb}\mathbf{v}_{\mathrm{BE}}^{fb}$ is achieved by using Eq. (4.20).

Next, we apply the boundary integral equation Eq. (4.19) at the collocation points on boundary Γ^{fD}. Applying the no-slip and no-penetration boundary conditions on Γ^{fD}, we get

$$\bar{\mathbf{v}}_{\mathrm{BE}}^{fD} - \mathbf{S}^{fD,fb}\mathbf{q}_{\mathrm{BE}}^{fb} - \mathbf{S}^{fD,fD}\mathbf{q}_{\mathrm{BE}}^{fD} - \mathbf{S}^{fD,fN}\mathbf{q}_{\mathrm{BE}}^{fN} = \mathbf{0}, \tag{4.22}$$

where $\bar{\mathbf{v}}_{\mathrm{BE}}^{fD}$ is the global vector of velocities at every collocation point on Γ^{fD} with dimension $3N_{\mathrm{BE}}^{fD}$.

Solving Eq. (4.22) for $\mathbf{q}_{\mathrm{BE}}^{fD}$, we get

$$\mathbf{q}_{\mathrm{BE}}^{fD} = (\mathbf{S}^{fD,fD})^{-1}\left[\bar{\mathbf{v}}_{\mathrm{BE}}^{fD} - \mathbf{S}^{fD,fb}\mathbf{q}_{\mathrm{BE}}^{fb} - \mathbf{S}^{fD,fN}\mathbf{q}_{\mathrm{BE}}^{fN}\right]. \tag{4.23}$$

Solving Eq. (4.21) for $\mathbf{v}_{\mathrm{BE}}^{fb}$, we get

$$\mathbf{v}_{\mathrm{BE}}^{fb} = (\mathbf{I} - \mathbf{D}^{fb,fb})^{-1} \left[\bar{\mathbf{v}}_{\mathrm{BE}}^{fb} - \mathbf{S}^{fb,fb}\mathbf{q}_{\mathrm{BE}}^{fb} - \mathbf{S}^{fb,fD}\mathbf{q}_{\mathrm{BE}}^{fD} - \mathbf{S}^{fb,fN}\mathbf{q}_{\mathrm{BE}}^{fN} \right], \tag{4.24}$$

where $\mathbf{I}$ is an identity matrix. For numerical efficiency, the solution of Eq. (4.24) is obtained by using successive substitutions instead of direct matrix inversion $(\mathbf{I} - \mathbf{D}^{fb,fb})^{-1}$ (Pozrikidis, 1992).

Now the interfacial velocity $\mathbf{v}_{\mathrm{BE}}^{fb}$ is expressed in terms of $\mathbf{q}_{\mathrm{BE}}^{fD}$ (obtained from Eq. (4.23)), $\mathbf{q}_{\mathrm{BE}}^{fN}$ (prescribed), and $\mathbf{q}_{\mathrm{BE}}^{fb}$ (transferred from finite elements of the lipid bilayer, which is discussed in §4.1.4).

In the special case when $\Lambda = 1$ (*i.e.* the viscosities of the interior and the exterior fluids are identical), the computation is much simplified since Eq. (4.24) is reduced to

$$\mathbf{v}_{\mathrm{BE}}^{fb} = \bar{\mathbf{v}}_{\mathrm{BE}}^{fb} - \mathbf{S}^{fb,fb}\mathbf{q}_{\mathrm{BE}}^{fb} - \mathbf{S}^{fb,fD}\mathbf{q}_{\mathrm{BE}}^{fD} - \mathbf{S}^{fb,fN}\mathbf{q}_{\mathrm{BE}}^{fN}. \tag{4.25}$$

If the fluid domain is a free space without any Neumann and Dirichlet boundaries, *e.g.*, a red blood cell in shear flow as studied in this paper, Eq. (4.24) can be simplified as

$$\mathbf{v}_{\mathrm{BE}}^{fb} = (\mathbf{I} - \mathbf{D}^{fb,fb})^{-1} \left[\bar{\mathbf{v}}_{\mathrm{BE}}^{fb} - \mathbf{S}^{fb,fb}\mathbf{q}_{\mathrm{BE}}^{fb} \right]. \tag{4.26}$$

Many problems can be simplified by using proper Green's functions as well. For example, the problem of a file of periodic RBCs in a cylindrical tube with axisymmetric configuration can be greatly simplified by using a Green's function representing a periodic array of point force rings inside a circular cylinder (Pozrikidis, 1992), which is used in our simulations.

4.1.4 Coupling finite element and boundary element methods

According to the boundary conditions (Eqns. (4.7), (4.8) and (4.9)), the lipid bilayer and the fluid share the same velocity and balance the tractions on the interface. To achieve this, numerically we employ a staggered algorithm to couple FEM and BEM (Walter *et al.*, 2010).

For the constant quadrilateral elements in BEM, four nodes are shared with the

quadrilateral shell element derived in §4.1.2. In axisymmetric cases, the axisymmetric Hughes-Liu shell elements (Hughes and Liu, 1981b) are coupled with the axisymmetric boundary elements with the special Green's function mentioned in §4.1.3 by sharing two nodes.

Furthermore, it is necessary to relate the global nodal force and moment vectors $\mathbf{f}_{\mathrm{FE}}^{fb}$ and $\mathbf{m}_{\mathrm{FE}}^{fb}$ of finite elements to the surface traction vector $\mathbf{q}_{\mathrm{BE}}^{fb}$ in boundary elements. Walter *et al.* (2010) employed iso-parametric elements for both FEM and BEM, and related the nodal force $\mathbf{f}_{\mathrm{FE}}^{fb}$ of membrane elements in FEM with the nodal traction $\mathbf{q}_{\mathrm{BE}}^{fb}$ of BEM by solving a linear equation expressed as

$$\mathbf{M}\mathbf{q}_{\mathrm{BE}}^{fb} = \mathbf{f}_{\mathrm{FE}}^{fb}, \tag{4.27}$$

where the square matrix $\mathbf{M}$ has a similar structure as the consistent mass matrix in FEM. However, for the continuum-based shell element described in §4.1.2, there are also rotational degrees of freedom at the nodes. If iso-parametric elements are used for both FEM and BEM, the system will be over-determined, *i.e.* there will be $3N_{\mathrm{FE}}$ unknowns ($\mathbf{q}_{\mathrm{BE}}^{fb}$) but $6N_{\mathrm{FE}}$ equations ($\mathbf{f}_{\mathrm{FE}}^{fb}$ and $\mathbf{m}_{\mathrm{FE}}^{fb}$). In addition, it is very expensive to solve this equation even if a sparse solver is employed. To deal with this problem, in our coupling algorithm we use constant value elements in BEM. Instead of solving Eq. (4.27), we employ a lumping technique for both the translational and rotational degrees of freedom. This method is similar to the mass lumping technique in the finite element method with explicit time integration (Belytschko *et al.*, 2000), and greatly reduces the computational cost. Detailed description of the algorithm is provided as follows.

We consider a node 'a' with nodal force $\mathbf{f}^{(a)}$ and moment $\mathbf{m}^{(a)}$, which is connected with n elements with indexes $i = 1, ..., n$. To conserve the linear momentum, we distribute finite element nodal forces $\mathbf{f}^{(a)}$ to the connected neighboring elements as surface tractions based on the weights of element areas, *i.e.* $\bar{\mathbf{q}}_i^{(a)} = \mathbf{f}^{(a)}/A^{(a)}$, where $\bar{\mathbf{q}}_i^{(a)}$ is the surface traction on element i from node 'a' due to its nodal force, and $A^{(a)}$ is the area sum of connected elements on node 'a'.

To conserve the angular momentum, we distribute the nodal moments to the neighboring elements as force couples. Let $\mathbf{r}_i$ denote the relative position vector from

the node 'a' to the collocation point (the centroid) of the element i, the moment $\mathbf{m}_i^{(a)}$ assigned to element i as

$$\mathbf{m}_i^{(a)} = (\mathbf{R}_i)^2 \cdot \mathbf{W}^{-1} \cdot \mathbf{m}^{(a)}, \tag{4.28}$$

where

$$\mathbf{R}_i = \begin{bmatrix} 0 & -\hat{r}_{i,3} & \hat{r}_{i,2} \\ \hat{r}_{i,3} & 0 & -\hat{r}_{i,1} \\ -\hat{r}_{i,2} & \hat{r}_{i,1} & 0 \end{bmatrix},$$

$$\hat{\mathbf{r}}_i = \mathbf{r}_i - \frac{1}{n-1} \sum_{j=1(j\neq i)}^{n} \mathbf{r}_j,$$

and

$$\mathbf{W} = \sum_{i=1}^{n} (\mathbf{R}_i)^2,$$

where $\hat{r}_{i,1}$, $\hat{r}_{i,2}$, and $\hat{r}_{i,3}$ are the three components of the vector $\hat{\mathbf{r}}_i$.

We note that $\sum_{i=1}^{n} \mathbf{m}_i^{(a)} = \mathbf{m}^{(a)}$ and $\mathbf{m}_i^{(a)} \cdot \hat{\mathbf{r}}_i = 0$, *i.e.* $\mathbf{m}_i^{(a)}$ is perpendicular to $\hat{\mathbf{r}}_i$, which guarantees the existence of an equivalent force couple for $\mathbf{m}_i^{(a)}$ associated with position vector $\hat{\mathbf{r}}_i$. This equivalent force couple is obtained by applying a force $\mathbf{f}_i^{(a)\prime} = \mathbf{R}_i \cdot \mathbf{W}^{-1} \cdot \mathbf{m}^{(a)}$ at the center of this element while applying opposite sign forces $-\mathbf{f}_i^{(a)\prime}/(n-1)$ with zero net resultant at the centers of other connected elements. The corresponding surface traction is

$$\mathbf{q}_{ij}^{(a)\prime} = \begin{cases} \mathbf{f}_i^{(a)\prime}/A_j^{(a)} & \text{if } i = j \\ -\frac{1}{n-1}\mathbf{f}_i^{(a)\prime}/A_j^{(a)} & \text{if } i \neq j \end{cases}, \tag{4.29}$$

where $A_j^{(a)}$ is the area of element j connected to node 'a'.

The total surface traction on an element is obtained by summing the contributions from the nodal force and moment of all its neighboring nodes.

Applying Eq. (4.24), the velocity at the element collocation point can be obtained. We relate the nodal velocity $\mathbf{v}^{(a)}$ to the velocity at the element collocation point $\mathbf{v}_i$ by

$$\mathbf{v}^{(a)} = \frac{1}{A^{(a)}} \sum_{i=1}^{n} \mathbf{v}_i A_i^{(a)}. \tag{4.30}$$

The continuum-based shell element used here stems from the Reisser-Mindlin

shell theory (see Belytschko *et al.* 2000). In this approach, the fiber is not necessary to be perpendicular to the shell reference surface, and it can rotate locally. The local fiber rotation is determined by the nodal moments as follows.

Let $\mathbf{q}_{\mathrm{BE}}^{fb\prime}$ denote the global surface traction vector attributed to the nodal moments. We express the global velocity vector $\mathbf{v}_{\mathrm{BE}}^{fb\prime}$ at the element collocation point due to $\mathbf{q}_{\mathrm{BE}}^{fb\prime}$ as

$$\mathbf{v}_{\mathrm{BE}}^{fb\prime} = (\mathbf{I} - \mathbf{D}^{fb,fb})^{-1}\mathbf{S}^{fb,fb}\mathbf{q}_{\mathrm{BE}}^{fb\prime}. \tag{4.31}$$

If node 'a' rotates locally as a rigid body with a local angular velocity $\boldsymbol{\omega}^{(a)}$, then the velocity at the collocation point of connected elements can be written as

$$\mathbf{v}_i' - \mathbf{v}^{(a)\prime} = \boldsymbol{\omega}^{(a)} \times \mathbf{r}_i = \begin{bmatrix} 0 & -\omega_3^{(a)} & \omega_2^{(a)} \\ \omega_3^{(a)} & 0 & -\omega_1^{(a)} \\ -\omega_2^{(a)} & \omega_1^{(a)} & 0 \end{bmatrix} \cdot \mathbf{r}_i \tag{4.32}$$

where

$$\mathbf{v}^{(a)\prime} = \frac{1}{A^{(a)}} \sum_{i=1}^{n} \mathbf{v}_i' A_i^{(a)} \tag{4.33}$$

There are $3n$ equations but 3 unknowns ($\omega_1^{(a)}, \omega_2^{(a)}, \omega_3^{(a)}$, the three components of the angular velocity vector at node 'a'). A least square method is used to solve these equations for $\boldsymbol{\omega}^{(a)}$.

After the nodal velocities and the local angular velocities are obtained, at each time step we need to update both the locations of the nodes and the orientations of the shell elements at the nodes (*i.e.* the 'fiber orientation' mentioned in Hughes and Liu (1981a)). The nodal coordinates are updated using the explicit Euler method. Then the fiber direction of node 'a', $\mathbf{x}'^{(a)}$ (a unit direction vector), is updated first by averaging the normals of connected elements based on the updated coordinates, then by applying the local rotation $\boldsymbol{\omega}^{(a)}$ using Hughes-Winget's formula as

$$\mathbf{x}'^{(a)} = \boldsymbol{\Phi}^{(a)}\mathbf{x}'^{(a)}, \tag{4.34}$$

where

$$\boldsymbol{\Phi}^{(a)} = \left(\mathbf{I} - \frac{1}{2}\boldsymbol{\Omega}^{(a)}\right)^{-1} \left(\mathbf{I} + \frac{1}{2}\boldsymbol{\Omega}^{(a)}\right), \tag{4.35}$$

$$\mathbf{\Omega}^{(a)} = \begin{bmatrix} 0 & -\omega_3^{(a)}\Delta t & \omega_2^{(a)}\Delta t \\ \omega_3^{(a)}\Delta t & 0 & -\omega_1^{(a)}\Delta t \\ -\omega_2^{(a)}\Delta t & \omega_1^{(a)}\Delta t & 0 \end{bmatrix}. \tag{4.36}$$

Δt is the time step. For the axisymmetric case, a similar coupling algorithm is developed as the above three dimensional case. Finally, the procedure of the staggered coupling algorithm is summarized as:

1. Generate the FE and BE meshes based on the geometry;
2. Assemble the matrix $\mathbf{S}^{fD,fD}$ from boundary Γ^{fD} in Eq. (4.23). Invert it and store it;
3. Calculate the internal forces and moments of the shell elements based on the deformation and the constitutive laws, and subtract external forces and moments (*e.g.* from the skeleton-bilayer interaction) to obtain the fluid-structure interaction forces and moments on the interface;
4. Project the interaction forces and moments to surface tractions on the boundary elements using the lumping technique;
5. Apply Eq. (4.22) to obtain the velocities of the collocation points of the boundary elements. If $\Lambda \neq 1$, the method of successive substitutions is needed to solve the equations;
6. Project the velocities of BE collocation points to FE nodal velocities and calculate the local nodal angular velocities;
7. March coordinates with FE nodal velocities and update the fiber directions;
8. Return to step (c) and repeat the calculation for the new configuration.

4.2 Cytoskeleton dynamics

The motion of the cytoskeleton is determined through its constitutive equations, its elastic interaction with the lipid bilayer, its viscous friction with the lipid bilayer *via* the transmembrane proteins, and its hydrodynamic interaction with the

lipid bilayer *via* the cytoplasm. Hereby we only consider the hydrodynamic loads upon the cytoskeleton, whereas its influence on the surrounding flow field is not considered. Due to the proximity of the cytoskeleton to the lipid bilayer, it is reasonable to assume that the cytoplasm near the lipid bilayer, in which the cytoskeleton is immersed, moves at the same speed as the lipid bilayer. In that sense, the interaction between the cytoskeleton and the cytoplasm can be merged with the cytoskeleton's interaction with the lipid bilayer. The balance of internal forces and external forces of the cytoskeleton leads to $\boldsymbol{\tau}^{bs} + \mathbf{t}_s = \mathbf{0}$, where $\boldsymbol{\tau}^{bs}$ is the total interaction force per unit area between the lipid bilayer and the cytoskeleton (applied on the skeleton), and $\mathbf{t}^s$ is the internal force per unit area of the cytoskeleton due to its internal stress $\boldsymbol{\Theta}^s$. $\mathbf{t}^s$ is calculated using the finite element method, whereas $\boldsymbol{\Theta}^s$ is presented in §4.3.

For convenience we also use the shell element formulation presented in §4.1.2 to model the cytoskeleton. One Gaussian integration point is used in the thickness direction so that the shell elements are actually reduced into membrane elements without bending stiffness. Thus the rotational degrees of freedom of the shell elements do not need to be considered for the cytoskeleton. Numerically, $\mathbf{t}^s$ is calculated at the nodes *via* dividing the nodal forces by the nodal areas.

After $\mathbf{t}^s$ and $\boldsymbol{\tau}^{bs}$ are obtained, the velocity of the cytoskeleton is calculated as follows. A local Cartesian system is defined so that z is in the normal direction of the cytoskeleton surface, x and y are tangential to the surface. The skeleton velocity, $\mathbf{v}^s = [v_x^s \;\; v_y^s \;\; v_z^s]^T$, is obtained as

$$v_x^s = \frac{\tau_x^{bs}}{c_f + c_{xy}} + v_x^b, \tag{4.37}$$

$$v_y^s = \frac{\tau_y^{bs}}{c_f + c_{xy}} + v_y^b, \tag{4.38}$$

$$v_z^s = v_z^b, \tag{4.39}$$

where $\mathbf{v}^b = [v_x^b \;\; v_y^b \;\; v_z^b]^T$ is the velocity vector of the lipid bilayer. c_f is the viscous friction coefficient between the lipid bilayer and the cytoskeleton, which will be formulated in §4.2.1. c_{xy} and c_z are tangential and vertical hydrodynamic drag coefficients, which will be formulated in §4.2.2. Strictly speaking, c_f is applied in front of the relative velocity between the skeleton and the lipid bilayer, whereas c_{xy} should

be applied in front of the relative velocity between the skeleton and the cytoplasm. However, in the vicinity of the lipid bilayer these two are close to each other owing to the no-slip condition. For this reason in the current study we do not distinguish them. Eq. (4.39) enforces the normal no-penetration condition between the lipid bilayer and the cytoskeleton. Numerically, $\mathbf{v}^s$ is calculated at the node 'a' of the cytoskeleton mesh, while $\mathbf{v}^b$ is calculated at the projection point of node 'a' on the lipid bilayer mesh in the master-slave contact algorithm (Malone and Johnson, 1994; Peng *et al.*, 2010). Note that although τ_z^{bs} is not shown in Eqns 4.37, 4.38 and 4.39, it can be obtained using $\boldsymbol{\tau}^{bs} = -\mathbf{t}_s$. τ_z^{bs} includes both the elastic interaction and the normal hydrodynamic interaction forces between the lipid bilayer and the cytoskeleton.

After the velocity of the cytoskeleton is obtained, the coordinates of the cytoskeleton are updated using explicit time integration (*e.g.* explicit Euler method).

4.2.1 Viscous friction between the lipid bilayer and the cytoskeleton due to the mobilities of transmembrane proteins

By applying the Stokes-Einstein relation, the drag force on a protein anchored in the lipid bilayer is given as

$$f = -\frac{v}{b_T} = -\frac{k_B T v}{D_T}, \tag{4.40}$$

where v is the translational velocity of the protein. The minus sign refers to the fact that the drag force is in the opposite direction of the velocity. D_T is the translational diffusivity of the protein. b_T is the translational mobility of the protein. $k_B = 1.38 \times 10^{-23}$ JK^{-1} is the Boltzmann constant and T is the absolute temperature. The translational diffusivities of band 3 and glycophorin C in the lipid bilayer are measured experimentally as 0.0014$\sim$0.022 μm^2/s (normal intact RBCs) (Kodippili *et al.*, 2009) and 4.0 μm^2/s (Kapitza *et al.*, 1984), respectively. For ghost RBCs, the band 3 diffusivity becomes 0.53μm^2/s (Tomishige, 1998). In this study we use the upper bound (0.022 μm^2/s) of the band 3 diffusivity of normal intact RBCs. Thus the drag forces on a band 3 and a glycophorin C are $f_B = -0.194$ pN·s/μm·v and

$f_G = -0.001$ pN·s/μm·v, respectively.

In our problem, the translational velocity v of the proteins is equal to the relative tangential velocity between the lipid bilayer and the cytoskeleton. Considering 33,000 JCs with three band 3 (since the band 3's are shared by neighboring JCs) and six glycophorin C per JC in a total area of 135 μm^2 (the surface area of a normal human red blood cell) with a normal human temperature $T = 310$ K. The friction coefficient between the lipid bilayer and the cytoskeleton per unit area is then calculated as

$$c_f = -\frac{\rho}{\rho_0}\frac{(f_B/v + 2f_G/v) \times 3 \times 33000}{135\mu\text{m}^2} = \frac{\rho}{\rho_0} \cdot 144 \text{ pN} \cdot \text{s}/\mu\text{m}^3, \tag{4.41}$$

where ρ and ρ_0 are the current and initial protein densities of the cytoskeleton. The protein density is defined as the number of proteins per unit area. The factor ρ/ρ_0 is associated with cytoskeleton deformation and its effect upon the density of skeleton-bilayer pinning points (*i.e.* transmembrane proteins). This ratio also represents the density of skeleton-attached proteins, whose variations are experimentally measurable (see for example Discher *et al.*, 1994). In practice, this density ratio is determined as $\rho/\rho_0 = 1/(\lambda_1\lambda_2)$, where λ_1 and λ_2 are principal in-plane stretches of the cytoskeleton. In our model, λ_1 and λ_2 are readily determined through FEM simulations of the inner layer (Peng *et al.*, 2010).

4.2.2 Hydrodynamic drag on the cytoskeleton

Although the cytoskeleton is a porous network with three-dimensional structure, for computational efficiency when considering its interaction with the surrounding fluid we simplify it as a planar triangular network (*i.e.* only the Sps are considered). The overall drag is calculated as the summation of drag forces on each individual Sp, and the hydrodynamic interactions between Sps are not considered. Specifically, we consider each Sp as a cylindrical bar with length l and radius r immersed in infinite Stokes flow as shown in Fig. 4.2a.

Hereby the drag coefficients are defined as

$$f_\perp = -c_\perp v_\perp \tag{4.42}$$

$$f_\parallel = -c_\parallel v_\parallel, \tag{4.43}$$

where $f_\perp$ is the transverse drag (*i.e.* the drag perpendicular to the cylinder axis), $f_\parallel$ is the longitudinal drag (the drag parallel to the cylinder axis), $v_\perp$ is the transverse velocity component, and $v_\parallel$ is the longitudinal velocity component as shown in Fig. 4.2b. If $\epsilon = \frac{r}{l} << 1$, then

$$c_\perp = \frac{4\pi\eta_2 l}{\ln(\frac{l}{r}) + \frac{1}{2}} \left[1 + \mathrm{O}(\epsilon^2)\right], \tag{4.44}$$

$$c_\parallel = \frac{2\pi\eta_2 l}{\ln(\frac{l}{r})} \left[1 + \mathrm{O}(\epsilon^2)\right], \tag{4.45}$$

where $\eta_2 = 6$ cP=0.006 pN/μm^2·s is the viscosity of the interior cytoplasm solution. Note that for $\epsilon << 1$, $c_\perp \sim 2c_\parallel$. For a Sp tetramer (*i.e.* two Sp dimers linked by head-to-head connection), the length is $l = 75$ nm and the radius is around $r = 1$ nm. Thus the drag coefficients are estimated as $c_\perp = 1.174 \times 10^{-3}$ pN·s/μm and $c_\parallel = 0.655 \times 10^{-3}$ pN·s/μm.

We now consider a perfect triangle as shown in Fig. 4.3 with length l on each side located inside the xy plane moving in a Stokes flow with a velocity $\mathbf{v} = [v_x, 0, v_z]$. The y direction is chosen to be in the triangle plane and perpendicular to the moving direction, and z direction is chosen to be the normal direction to the triangle. We assume that the total drag on this triangle equals the sum of the drags on the three edges.

A simple calculation shows that the in-plane drag $f_{\Delta,x}$ of the triangle is isotropic (independent of the orientation of the triangle), and no lateral force (force in the y direction) is generated. The drags are calculated as

$$f_{\Delta,x} = -\frac{3}{2}(c_\perp + c_\parallel)v_x = -(2.74 \times 10^{-3}\mathrm{pN}/\mu\mathrm{m} \cdot s)v_x, \tag{4.46}$$

$$f_{\Delta,y} = 0, \tag{4.47}$$

$$f_{\Delta,z} = -3c_\perp v_z = -(3.52 \times 10^{-3}\mathrm{pN}/\mu\mathrm{m} \cdot \mathrm{s})v_z. \tag{4.48}$$

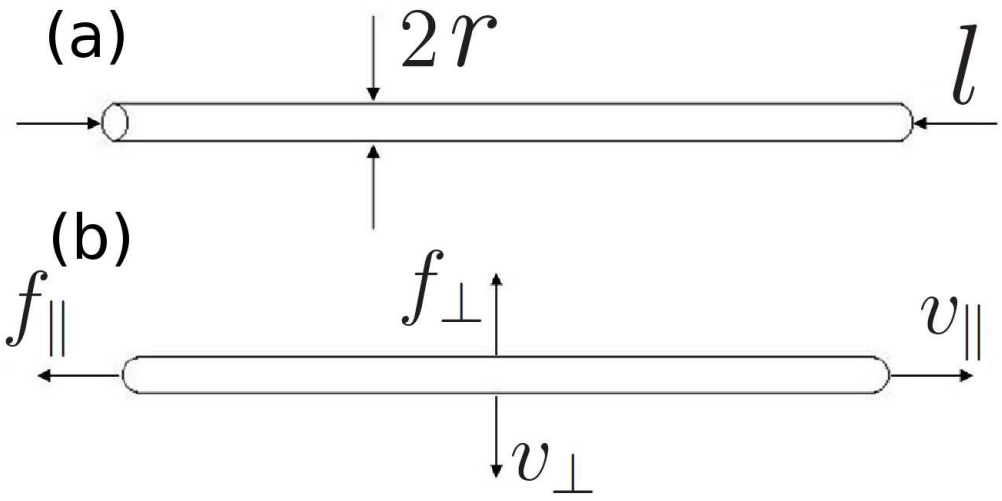

Figure 4.2: (a) Geometry of the slender cylinder. (b) Drags and velocities of the slender cylinder.

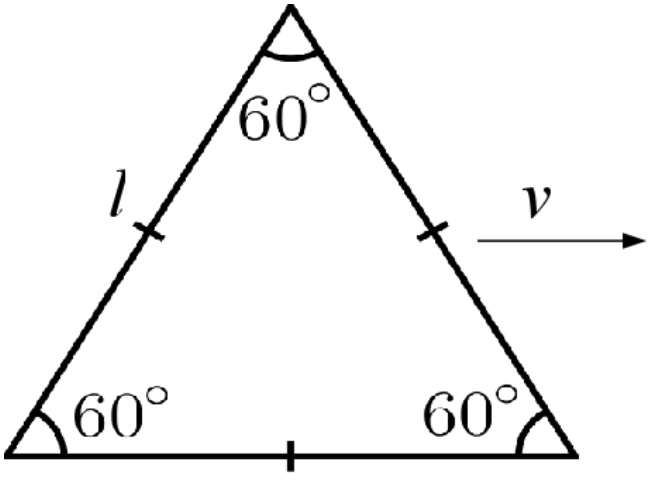

Figure 4.3: Drag coefficients of a moving perfect triangle.

For a cytoskeleton network with a total area of $135\mu\text{m}^2$, there are 33,000 actin protofilaments. Each protofilament is in connection with six Sp tetramers, whereas each tetramer is connected with two protofilaments. Based on this, there should be 33,000 independent triangles (as the one described above) in the network. Therefore the tangential drag force of the network per unit area is

$$c_{xy} = -\frac{\rho}{\rho_0} \cdot 33000/135\mu\text{m}^2 f_{\Delta,x}/v_x = \frac{\rho}{\rho_0} \cdot 0.67\text{pN} \cdot \text{s}/\mu\text{m}^3,$$

and the normal drag force of the network per unit area is

$$c_z = -\frac{\rho}{\rho_0} \cdot 33000/135\mu\text{m}^2 f_{\Delta,z}/v_z = \frac{\rho}{\rho_0} \cdot 0.86\text{pN} \cdot \text{s}/\mu\text{m}^3.$$

These hydrodynamic drags are included in $\boldsymbol{\tau}^{bs}$ and transferred to the lipid bilayer through the boundary condition (Eq. (4.9)). Note that $c_f >> c_{xy}$, *i.e.* the bilayer-skeleton viscous friction is much larger than the hydrodynamic drag in the tangential direction. Strictly, the wall effect of the lipid bilayer on the motion of spectrins should be considered. In practice, however, since the hydrodynamic drag is much smaller than the bilayer-skeleton viscous friction, the current approach is sufficiently accurate.

4.3 Membrane viscoelasticity

The viscoelasticity of the bilayer-skeleton system is essential for its ability to maintain structural stability under large dynamic loads. The viscosity stems from the following sources: (a) the viscosity of the lipid bilayer, (b) the viscosity of the cytoskeleton, (c) the skeleton-bilayer viscous friction due to the mobility of the transmembrane proteins (band 3 and glycophorin C) within the lipid bilayer and the bilayer-skeleton hydrodynamic drags, and (d) the viscosity of the surrounding flow. Effects (c) and (d) have been considered in §4.2.1 and §4.2.2, respectively.

4.3.1 Voigt-Kelvin model

Evans and Hochmuth (1976) applied a generalized Voigt-Kelvin stress-strain relation to simulate the viscoelastic response of the membrane. Puig-De-Morales-Marinkovic *et al.* (2007) found that the viscoelastic property of the RBC membrane followed a power law. Fractional order models were used by Craiem and Magin (2010) to study the viscoelasticity of RBCs. Lubarda (2010) presented a rate-type constitutive theory of elastic and viscoelastic response of an erythrocyte membrane for arbitrary isotropic strain energy functions. For simplicity, we use the generalized Voigt-Kelvin stress-strain relation by Evans and Hochmuth (1976), which is written as

$$\Theta_1 h = \bar{T} + \frac{\mu_i}{2\lambda_1^2\lambda_2^2}(\lambda_1^2 - \lambda_2^2) + 2\nu_i \frac{1}{\lambda_1}\frac{D\lambda_1}{Dt}, \tag{4.49}$$

$$\Theta_2 h = \bar{T} + \frac{\mu_i}{2\lambda_1^2\lambda_2^2}(\lambda_2^2 - \lambda_1^2) + 2\nu_i \frac{1}{\lambda_2}\frac{D\lambda_2}{Dt}, \tag{4.50}$$

where D/Dt is the material derivative with respect to time t. ν_i is the surface viscosity. μ_i is the surface shear stiffness ($i = b, s$ stands for the lipid bilayer or the cytoskeleton, respectively). $\bar{T}$ is the isotropic tension. For the cytoskeleton, μ_s and $\bar{T}$ are calculated based on the molecular-detailed model of the junctional complex, and the exact formulations are presented in Peng *et al.* (2010). For the lipid bilayer, $\bar{T} = K_b(\lambda_1\lambda_2 - 1)$, where $K_b = 5 \times 10^5 pN/\mu m$ is the bilayer area stiffness. λ_1 and λ_2 are principal stretches. Since the lipid bilayer is a fluid and its shear modulus is nearly zero, for numerical stability we choose a small but nonzero value as $\mu_b = 10^{-3}\mu_s$. h is the thickness of the bilayer (2.2 nm) or the cytoskeleton (2 nm). The discrepancy between the bilayer thickness used herein and its actual value (4-5 nm) is attributed to the fact that in our study the bilayer is simplified as a continuous (but anisotropic) shell without considering its detailed molecular architecture. The detailed explanations of the bilayer and skeleton thicknesses used here can be found in Peng *et al.* (2010). Θ_1 and Θ_2 are principal stresses.

The viscosity for the lipid bilayer is given as $\nu_b = 10^{-9}$ Pa·m·s (Otter and Shkulipa, 2007). Since the total membrane viscosity is measured as 5×10^{-8} Pa·m·s (Tran-Son-Tay *et al.*, 1984), which is 50 times higher than the lipid bilayer viscosity, it is reasonable to assume that the membrane viscosity is mainly attributed to the

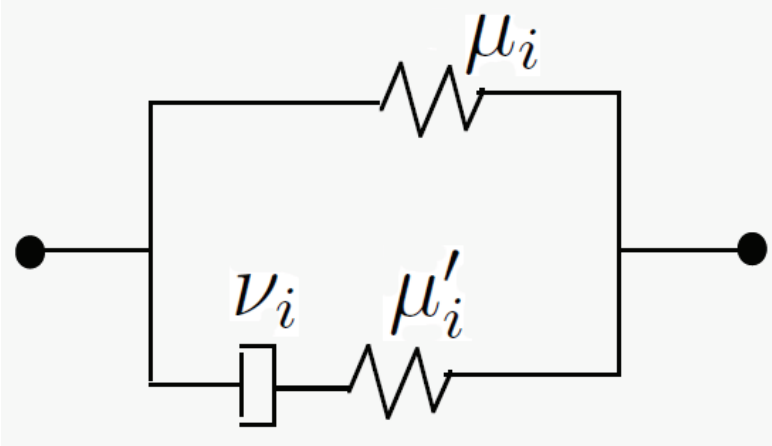

Figure 4.4: An approximation of the Voigt-Kelvin model.

viscosity of the cytoskeleton. Thus we assign the viscosity of the cytoskeleton as $\nu_s = 5 \times 10^{-8}$ Pa·m·s.

4.3.2 Numerical implementation

Through numerical tests it was shown that for our modeling approach described in the previous sections, a direct numerical implementation of the Voigt-Kelvin stress-strain relation as described in Eqns. 4.49 and 4.50 is not very stable. Following the numerical implementation of the viscous foam (material type 62) in the commercial package LS-DYNA (Hallquist, 1998), similarly we add an elastic term with a shear stiffness $\mu_i' = 100\mu_i$ in series with the viscous term (ν_i) to approximate the generalized Voigt-Kelvin model of Evans and Hochmuth (1976) and prevent timestep problems as shown in Fig. 4.4. It is noteworthy that if $\mu_i' = \infty$, this formulation is exactly the same as the generalized Voigt-Kelvin model of Evans and Hochmuth (1976). The numerical implementation of this viscoelastic model with finite strains can be found in Hallquist (1998) and Holzapfel (2000).

4.4 Summary and remarks

In this chapter, we coupled the finite element method (FEM) and the boundary element method (BEM) to solve the fluid-structure interaction (FSI) problem of red

blood cells immersed in Stokes flow. The fluid problem of Stokes flow is solved using BEM based on the work by Pozrikidis (1992), while the membrane is modeled using the multiscale model described in Chapter 2. Furthermore, we employed a Voigt-Kelvin constitutive model to consider the membrane viscoelasticity and described the cytoskeleton dynamics based on protein mobility and hydrodynamic drags.

Zienkiewicz *et al.* (1977) claimed that coupling FEM and BEM is a 'Marriage a la mode: the best of both worlds'. Our numerical experiments show that our algorithm of coupling FEM and BEM is fast, robust and accurate for the fluid-structure interaction (FSI) problem of red blood cells.

First, the boundary element method reduces the 3D fluid problem to a 2D problem and significantly decreases the number of elements. For a 3D single red blood cell immersed in shear flow, usually it only takes 5 hours to simulate a motion period using a single CPU. For an axisymmetric problem of red blood cells immersed in tube flow, it only takes half an hour. But, as well known, the computational cost of the BEM scales with N^2, where N is the number of the degrees of freedom. If multiple red blood cells are considered, we may need fast boundary element methods to speed up this algorithm, *e.g.,* using the fast multipole boundary element method (Liu, 2009).

Secondly, this coupling algorithm is also very robust. It employs explicit time integration. No equation solver is needed, even a linear solver, so that the troublesome convergence problem for implicit calculations is avoided. In addition, since the boundary elements are only located on a surface or a line, there is no domain element distortion.

Finally, due to the analytical Green's function used in boundary element methods, this algorithm is also very accurate.

However, the Stokes problem solved by the BEM is only valid in the small length scale. If the inertial effect must be considered in some cases, other methods for fluid problem may be needed, *e.g.,* the Immersed Boundary Method (IBM) (see for example, Shoele and Zhu (2010), Eggleton and Popel (1998), Bagchi (2007), Zhang *et al.* (2008), Le (2010)).

As mentioned before, experiments (Puig-De-Morales-Marinkovic *et al.*, 2007) showed that the viscoelastic property of the RBC membrane followed a power law

so that fractional order models may be more appropriate to study the viscoelasticity of RBCs (Craiem and Magin, 2010). Fractional order models can be also easily incorporated in the finite element method framework.

Chapter 4, in part, has been submitted for publication of the material as it may appear in 'Molecular-detailed modeling of erythrocytes in Stokes flow', *Journal of Fluid Mechanics*, 2011. Zhangli Peng, Robert J. Asaro and Qiang Zhu, 2011. The dissertation author was the primary investigator and author of this paper.

Chapter 5

Red Blood Cells in Tube Flow and Shear Flow

In this chapter, we will simulate the red blood cells in tube (capillary) flow and shear flow. They are closely related to the *in vivo* physiological conditions.

As shown in Fig. 5.1, when the diameter of the blood vessel is as small as the red blood cell, it can be considered a capillary flow case. When the blood vessel is very large, *e.g.,* an artery, then the flow around the cell is approximately of a linear profile as shown in Fig. 5.1. In this case, it can be idealized as a simple shear flow. In the following, we first validate our numerical method of fluid-structure interaction by simulating some benchmark problems and comparing the results with existing studies. Then we will use our multiscale approach to study the RBC behaviors in tube flow and shear flow.

5.1 Model validations

The fluid-structure interaction model is validated by simulating three canonical cases: 1) RBCs passing through a cylindrical tube 2) a spherical capsule in shear flow 3) a RBC in shear flow with low shear rates. The predictions are then compared with benchmark results from previous studies. To be consistent with these existing studies, in this validation work we consider a reduced version of our model, in which the cell membrane is modeled as a single-layer structure (*i.e.* the detailed bilayer-skeleton

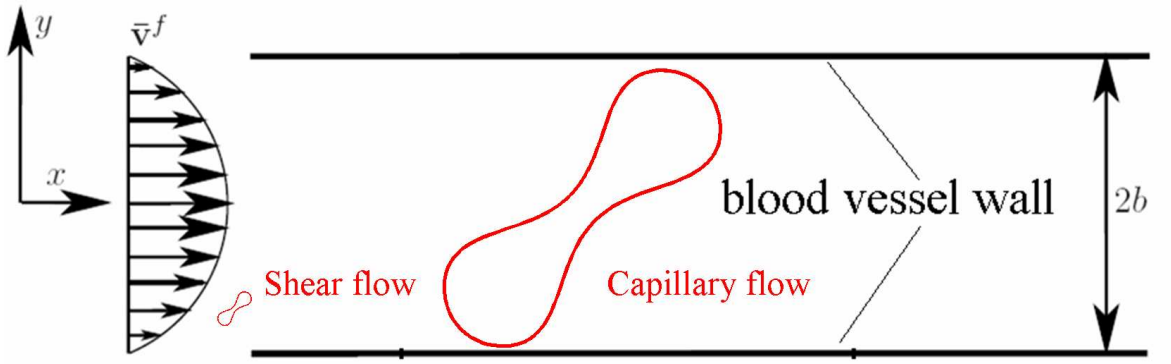

Figure 5.1: Capillary flow and shear flow.

architecture is not specified) with uniform mechanical properties. Furthermore, the mechanical parameters and the constitutive relations are kept the same as those in the corresponding previous studies to be compared with.

5.1.1 Red blood cells in tube flow

First, we simulate a file of RBCs passing through a cylindrical tube (which resembles cell motion inside capillaries), and compare our results with the predictions by Pozrikidis (2005a). As shown in Fig. 5.2(a), the problem is considered to be axisymmetric with respect to the x axis (the centerline of the tube). y represents the distance measured from the centerline towards the boundary of the tube. As discussed in §4.1.3, in axisymmetric cases the Green function is spatially periodic so that the method is capable of simulating an infinite sequence of cells without additional computational effort. The cell membrane is modeled as a Skalak material defined as

$$\Theta_1 h = \frac{K}{2}\lambda_1\lambda_2(\lambda_1^2\lambda_2^2 - 1) + \frac{\mu}{2}\frac{\lambda_1}{\lambda_2}(\lambda_1^2 - 1), \tag{5.1}$$

$$\Theta_2 h = \frac{K}{2}\lambda_1\lambda_2(\lambda_1^2\lambda_2^2 - 1) + \frac{\mu}{2}\frac{\lambda_2}{\lambda_1}(\lambda_2^2 - 1), \tag{5.2}$$

where μ is the membrane shear modulus and K is the membrane area modulus.

We use $L/a = 3.0$, $b/a = 1.0$, $G = 0.5$, where L is the space between periodic cells (see Fig. 5.2a), $a = (3V/4\pi)^{1/3} \approx 2.82\mu m$ is the equivalent cell radius ($V \approx$

$98\mu m^3$ is the cell volume), and b is the tube radius. The undisturbed velocity profile $\bar{\mathbf{v}}^f$ is a parabolic function of y with the maximum speed is reached at $y = 0$. $G = \eta U_m/\mu$ is the reduced flow rate, where U_m is the maximum undisturbed flow velocity and $\eta = \eta_1 = \eta_2 = 1.2$cP=0.0012 pN/$\mu$m^2·s is the fluid viscosity. We use the same moduli as in Pozrikidis (2005a), *i.e.*, $\mu = 4.2pN/\mu m$, $\eta U_m/K = 200$, and bending stiffness $\kappa_c = 1.8 \times 10^{-19}J$. The predicted shape of the RBCs is shown in Fig. 5.2a, which is graphically indistinguishable from that obtained in Pozrikidis (2005a) (see Fig. 8 in that paper). The distributions of membrane tensions in both the meridional and azimuthal directions along the arc length s are shown in Fig. 5.2b, which again demonstrate consistency with the study of Pozrikidis (2005). The arc length s is measured from the front point as shown in Fig. 5.2a. s_t is the total arc length from the front point to the trailing point. The tensions are normalized by ηU_m.

Furthermore, a time sequence of RBC shapes at different time points are shown in Fig. 5.3, in which $G = 0.5$ and other parameters are the same. These predicted shapes are consistent with the results by Pozrikidis (2005a).

5.1.2 A spherical capsule in shear flow

Secondly, we simulate the motion of a spherical capsule in a simple shear flow with undisturbed velocity ky in the horizontal direction, where k is the shear rate and the center of the cell lies at $y = 0$ (see Fig. 5.4). In this simulation, both the mechanical parameters ($G = \eta ka/\mu = 0.20$, where a is the equivalent radius and μ is the shear modulus of the membrane, and $\Lambda = 1$) and the constitutive law of the capsule with an energy function of a neo-Hookean form are taken from Ramanujan and Pozrikidis (1998). This constitutive law, as well as its related surface strain invariants, was originally derived by Barthès-Biesel and Rallison (1981). As shown in Fig. 5.5 and Fig. 5.6, our results, in this case for the inclination angle θ_{xy} of the maximum dimension with respect to the x axis in the xy plane (the mid-plane) and the Taylor deformation parameter $D_{xy} = (A - B)/(A + B)$ (A, B are the maximum and minimum dimensions in xy plane; see Fig. 5.4 for definitions of θ_{xy}, A, and B) match well with the reported data in Ramanujan and Pozrikidis (1998). In practice, to calculate A and B we adopt the approach suggested by Ramanujan and Pozrikidis

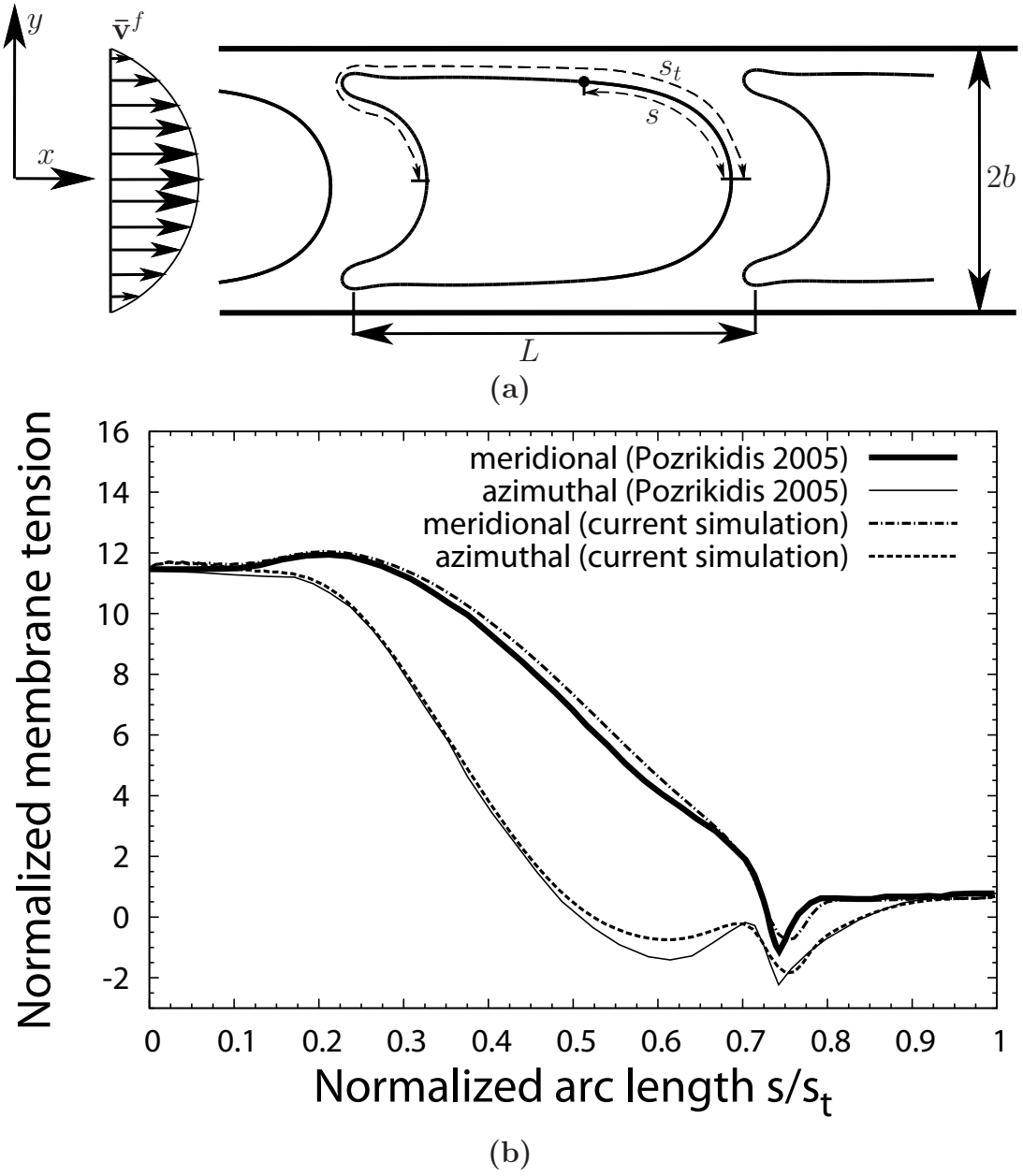

Figure 5.2: (a) The shape of RBCs passing through a cylindrical tube driven by flow. (b) Distributions of membrane tensions in meridional and azimuthal directions along the arc length s (compared with Pozrikidis (2005)). The tensions are normalized by ηU_m.

Figure 5.3: Time evolution of RBC shapes at different time points (from top to bottom t=0, 1.2, 5.2, 18).

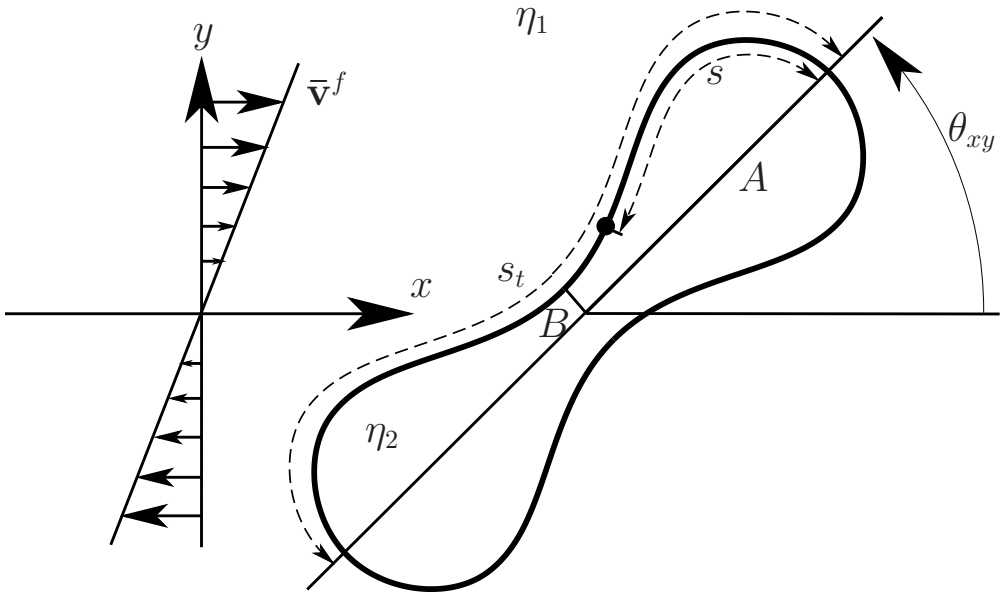

Figure 5.4: Schematic of a RBC (or capsule) in simple shear flow.

(1998). The basic procedure is: a) calculate the inertia tensor of the cell or the capsule; b) calculate the dimensions of an equivalent triaxial ellipsoid with the same inertia tensor; c) calculate A and B of this ellipsoid, and use these to find D_{xy} of the cell.

5.1.3 Tumbling of a red blood cell in shear flow

Finally, we simulate the tumbling motion of a RBC in a shear flow by incorporating both bending stiffness and area stiffness of its membrane, and compare our results with those in Pozrikidis (2003b). The constitutive law used here is the same as in Pozrikidis (2003b), which is similar to the one for capsules in Ramanujan and Pozrikidis (1998) but with an extra area stiffness term. The reduced shear rate $G = 0.1$, the bending stiffness $k_c = 1.8 \times 10^{-19}$J, the shear modulus $\mu = 3pN/\mu m$, and the normalized area stiffness $K/\eta_1 ka$=200, where K is the area stiffness. Following Pozrikidis (2003b), we use $\Lambda = 5$ ($\eta_2 = 0.006$ pN/μm^2·s). Fig. 5.7 shows snapshots of the cell motion/deformation as well as the cell profiles in the xy plane. These results are very close to the predictions by Pozrikidis (2003) (see Fig. 4a in that paper). The corresponding time evolution of the inclination angle is plotted in Fig. 5.8, which agrees well with Pozrikidis (2003b).

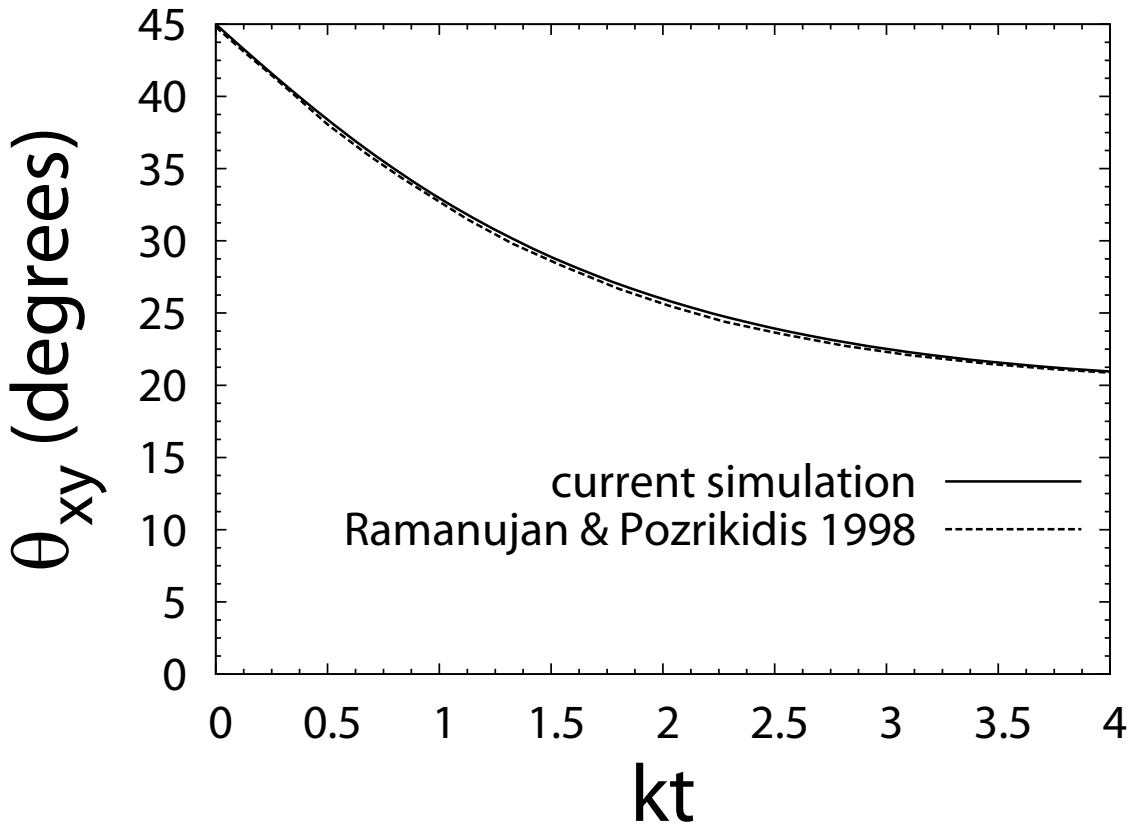

Figure 5.5: The inclination angle.

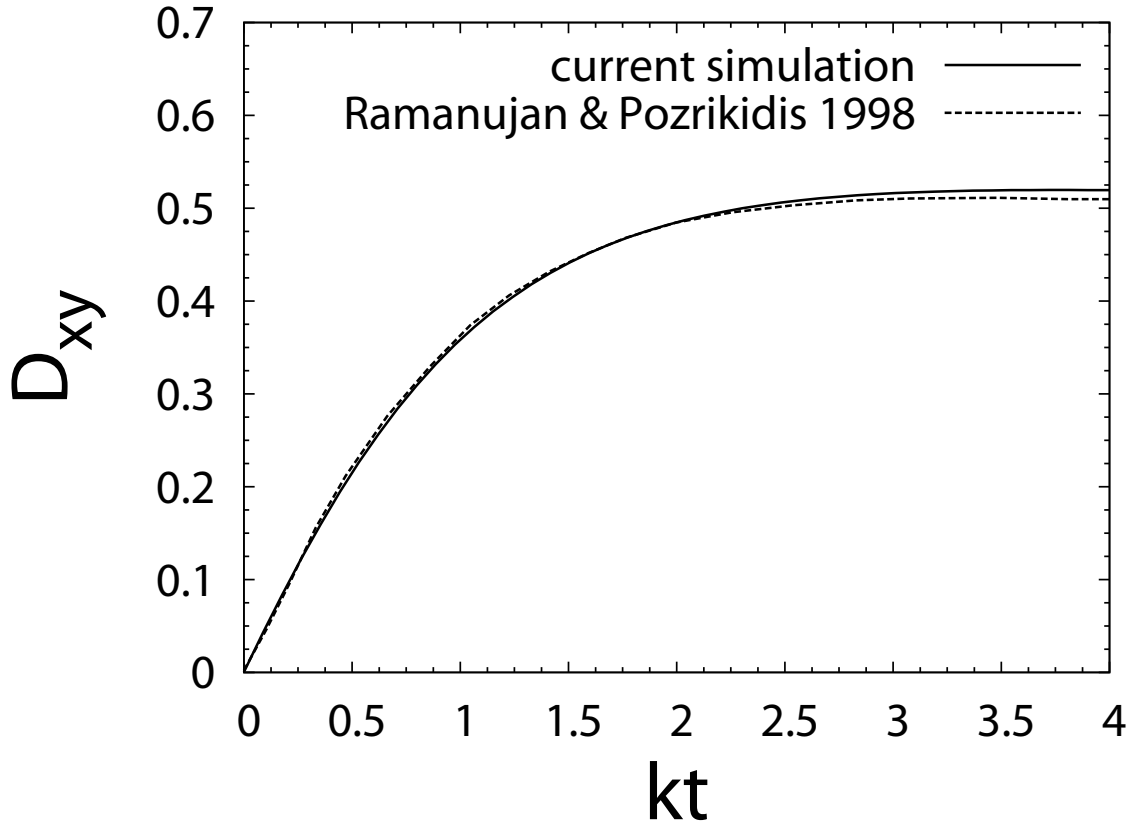

Figure 5.6: The Taylor deformation parameter as functions of time.

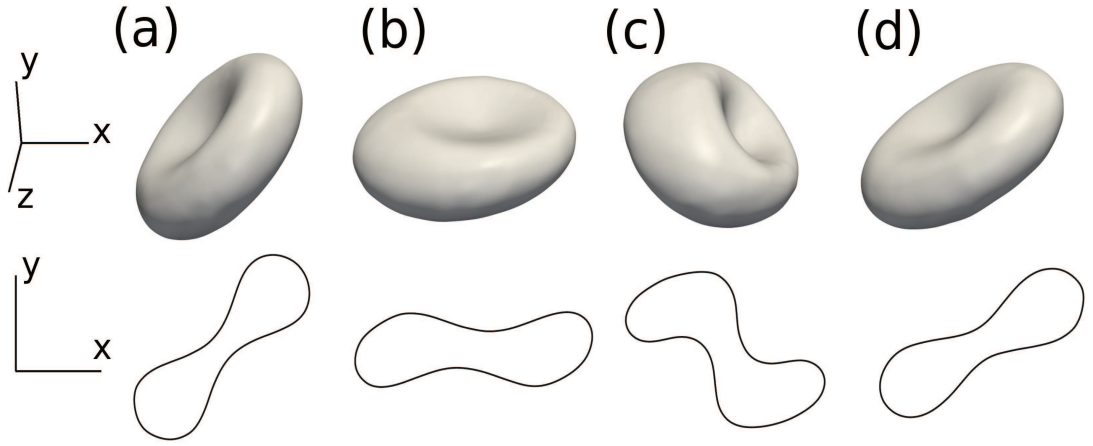

Figure 5.7: Cell shapes (top) and profiles in the xy plane (bottom) at (a) kt=0, (b) kt=4, (c) kt=8.15, and (d) kt=11.80.

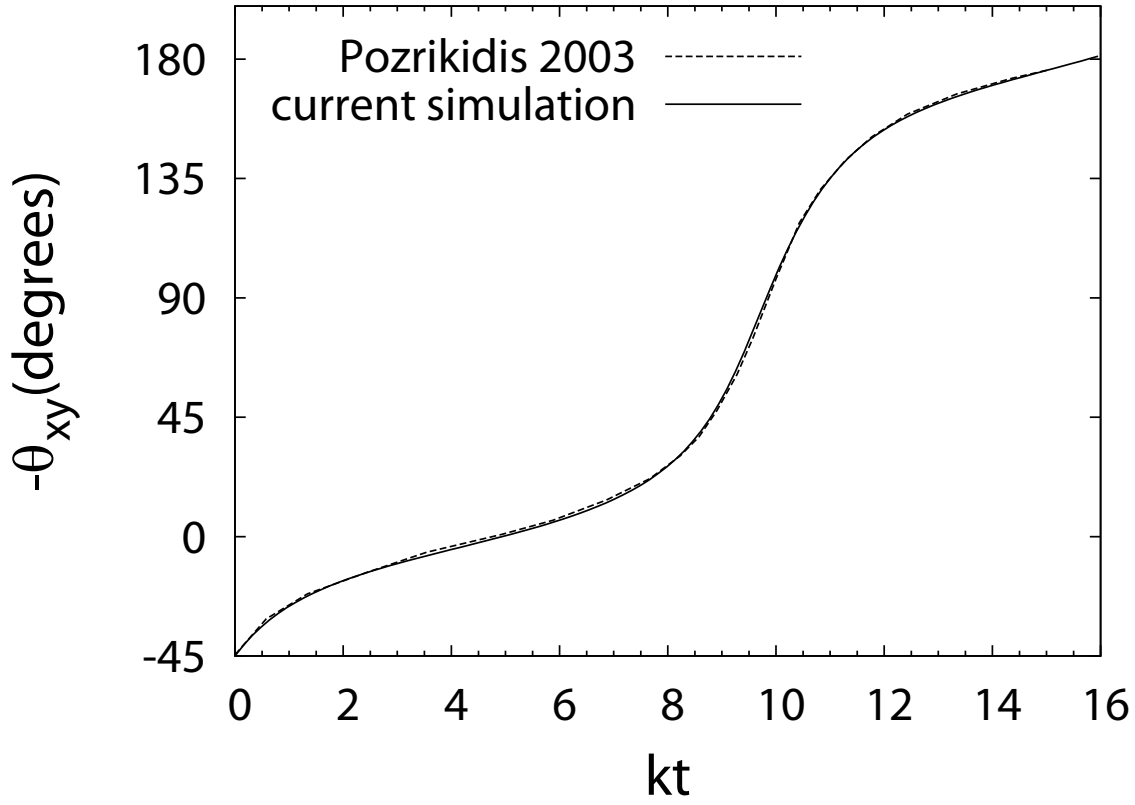

Figure 5.8: Evolution of the inclination angle θ_{xy} during the tumbling motion of a RBC. The result is compared with the prediction by Pozrikidis (2003b).

The multiscale model of the membrane has been validated extensively in Chapter 3.

In the following we apply the fluid-structure coupled multiscale model to examine the deformation of the cytoskeleton (which is related to the mechanical loads inside it), and the interaction forces between the lipid bilayer and the skeleton in both tangential and normal (*i.e.* vertical with respect to the lipid bilayer) directions in the aforementioned scenarios associated with Stokes flows (inside a tube and a shear flow). Specifically, we will study the area deformation and the shear deformation of the skeleton. Herein the areal change of the skeleton is directly related to the protein density in the membrane, and is thus experimentally measurable through fluorescent marking (Discher *et al.*, 1994). Large skeleton deformations may trigger structural remodeling such as Sp unfolding or dissociation of the head-to-head connection between Sp dimers (Li *et al.*, 2007) (which causes a phase transition of the skeleton). Both the area deformation and the shear deformation contribute to the internal tension inside the skeleton, which, together with the local curvature of the membrane determines the normal interaction force between the bilayer and the skeleton (Peng *et al.*, 2010). In quasi-static cases there is tiny tangential force between the bilayer and the skeleton owing to the near-fluidic nature of the bilayer. In dynamic cases, whenever there is sliding motion between the two there will be tangential force, which is determined by the sliding speed and the mobilities of the transmembrane proteins as discussed before. Sufficiently large bilayer-skeleton interaction forces can lead to dissociation between the two, causing physiologically important phenomena such a budding, vesiculation, or tether formation. Systematic experiments are required to explore that exact conditions for these to happen. On the other hand, state-of-the-art experimental techniques are not able to resolve the distribution of mechanical loads inside a cell. In this sense, the multiscale numerical capacity developed in this study provides a complementary measure to predict the mechanical loads inside the cell, enabling quantitative prediction of mechanically induced structural remodeling.

5.2 Skeleton density variation and bilayer-skeleton interaction forces of red blood cells in tube flow

Using our multiscale model, we herein predict the protein density of the skeleton and the interaction force between the lipid bilayer and the skeleton (Fig. 5.9) in RBC membranes in a tube flow. For flow conditions, we use the same parameters as in §5.1, *e.g.,* $L/a = 3.0$, $b/a = 1.0$, $G = 0.5$, and $a = 2.82\mu m$. The parameters of the cytoskeleton, including the persistence lengths of folded and unfolded domains in Sp, the contour lengths of the folded and unfolded domains, the difference between the activation length of the unfolding process and that of the refolding process, and the force corresponding to the state when half of the domains are unfolded, are obtained from Peng *et al.* (2010). Lac and Barthès-Biesel (2005) and Lefebvre and Barthès-Biesel (2007) showed that the membrane prestress plays an important role for RBC motions in both tube flow and shear flow. To match the skeleton density variation recorded in micropipette aspirations, the prestress of the cytoskeleton is set to be $\bar{T}_0 = \bar{T}|_{\lambda_1=1,\lambda_2=1} = -30\text{pN}/\mu\text{m}$ (Peng *et al.*, 2010). The spontaneous curvature of the bilayer is assumed to be 0, *i.e.* in its unloaded state a piece of lipid bilayer remains flat. Since in this particular case we only focus on the final steady configuration, the membrane viscosity, the bilayer-skeleton friction, and the plasma viscosity contrast are irrelevant.

5.2.1 Skeleton density variation

Fig. 5.9 shows the distribution of the density ratio along the arc length s. It is seen that the skeleton is expanded ($\rho/\rho_0 < 1$) at the head region (the head of the bullet shape) and the trailing region (the bottom) , whereas it is compressed ($\rho/\rho_0 > 1$) at the side of the cell that is almost parallel to the tube wall ($0.3 < s < 0.6$). A slight variation of the density ratio occurs at the edge formed between the bottom and the side ($s \sim 0.7$). The increase of protein density near the wall ($0.3 < s < 0.6$) as shown in Fig. 5.9 might help facilitating the biochemical interaction between the RBC cytoskeleton and the endothelial cells on the vessel wall. Indeed, it has been showed

that RBCs can release nitric oxide (NO) (Kleinbongard *et al.*, 2009) to dilate the blood vessel and improve blood perfusion, as well as adenosine triphosphate (ATP) to regulate blood pressure (Wan *et al.*, 2008).

5.2.2 Normal bilayer-skeleton interaction force

The normal interaction force between the lipid bilayer and the skeleton is also plotted in Fig. 5.9. No tangential force exists since the sliding between the lipid bilayer and the cytoskeleton has been already finished before this final steady configuration. The quantity we show is the interaction force applied on one junctional complex (JC), which is obtained as the product between the interaction force per unit area $\boldsymbol{\tau}^{bs}$ and the area of one JC after the deformation of the skeleton in that particular location as

$$\mathbf{f}_{jc} = \frac{135cm^2}{33000}\frac{\rho_0}{\rho}\boldsymbol{\tau}^{bs}. \tag{5.3}$$

This force is negative when $0 < s < 0.8$ (a negative normal interaction force refers to the scenario when the skeleton and bilayer tend to separate from each other (dissociation tendency)). The maximum negative interaction force occurs at the trailing edge of the bullet shape. For $0.8 < s < 1$, this force is positive, *i.e.* the skeleton and bilayer are pushed towards each other (association tendency).

A noteworthy phenomenon is that in tube flow (capillary flow) both the protein density variation and the bilayer-skeleton interaction forces are much lower than those during the micropipette aspiration experiments. During micropipette aspirations, the maximum interaction force per JC (*i.e.* the force that induces bilayer-skeleton separation) is 5$\sim$20 pN as shown in Peng *et al.* (2010), whereas in capillary flow the value is less than 0.3 pN. This may help explain the structural stability and durability of RBCs when they pass through the capillaries.

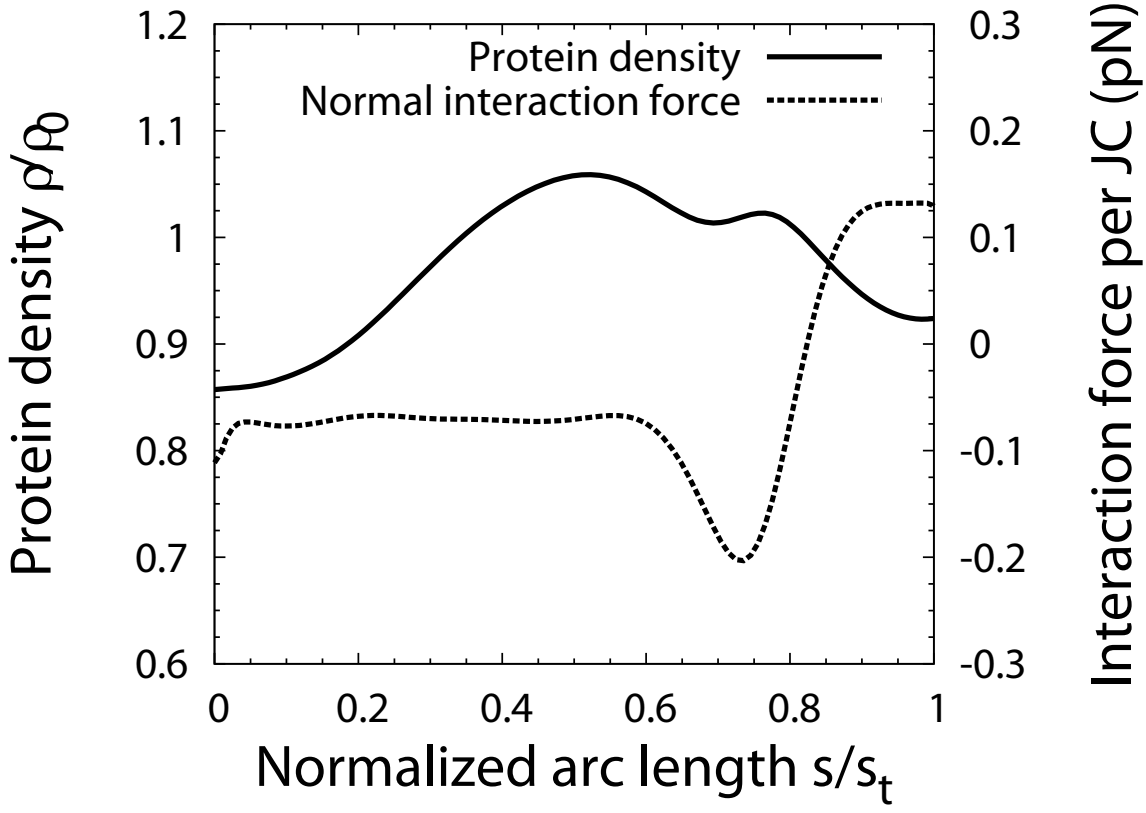

Figure 5.9: The protein density ratio ρ/ρ_0 and the normal interaction force acting on each JC when RBCs pass through a cylindrical tube.

5.3 Tank-treading motion of a red blood cell in shear flow

In §5.1, we discussed the tumbling motion of RBC in shear flow. When the shear rate is sufficiently large, however, these cells may demonstrate a new type of response called tank-treading motion, in which a RBC deforms to an ellipsoidal shape and the membrane circulates around while the inclination angle remains almost unchanged.

To simulate this tank-treading response, we use the same parameters as in §5.2. The viscosity of the internal fluid $\eta_2 = 6cP$=0.006 pN/μm^2·s.

5.3.1 Tank-treading frequency

In Fig. 5.10, we compare the predicted tank-treading frequency (defined as the inverse of the period for a point on the membrane to complete one circle around the cell) with the experimental measurements by Fischer *et al.* (1978). We show the relations between shear rate and tank-treading frequency with external fluid viscosities 13 cP, 31 cP, and 59 cP. It is seen that the tank-treading frequency increases linearly with the shear rate. Furthermore, our results demonstrate an increase in the ratio of tank-treading frequency to shear rate when the external fluid viscosity is increased. These features are consistent with experiments by Tran-Son-Tay (1983) and Fischer (2007), and the numerical results by Dodson and Dimitrakopoulos (2010). If the membrane viscosities are neglected ($\nu_b = \nu_s = 0$), then the frequency is overestimated as shown in Fig. 5.10. This is consistent with the result by Fedosov *et al.* (2010a).

5.3.2 Swinging motion

Our simulations also demonstrate swinging motions of the cell, referring to variations of the inclination angle θ_{xy} and the cell shape (characterized by the Taylor deformation parameter D_{xy}) over time. The time histories of θ_{xy} and D_{xy} at shear rates of 270/s and 1640/s are shown in Fig. 5.11 and Fig. 5.12, respectively. For the shear rate of 270/s, the time period of swinging motion is found to be 0.08 s,

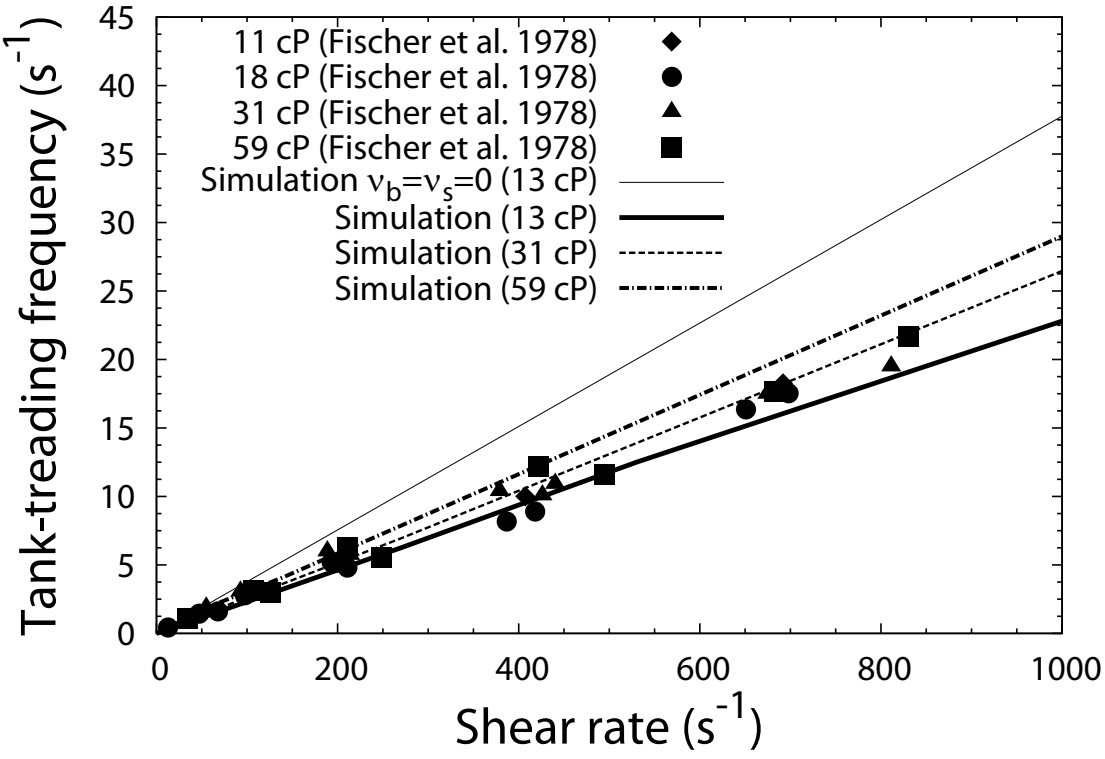

Figure 5.10: The tank-treading frequency as a function of the shear rate for different blood plasma viscosities and membrane viscosities. The results are compared with experimental measurements by Fischer *et al.* (1978).

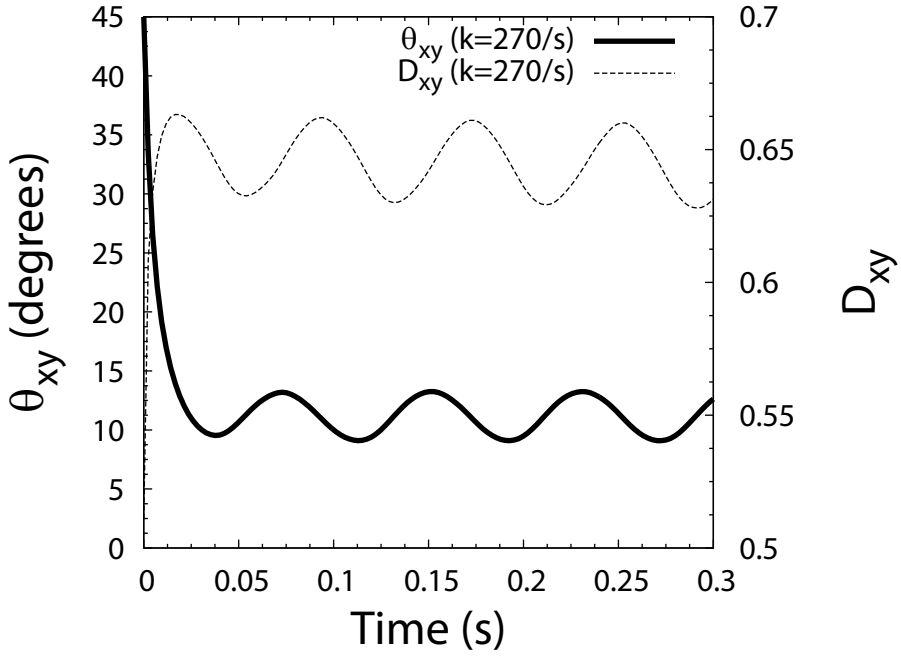

Figure 5.11: Time histories of θ_{xy} and D_{xy} during swinging motions. k=270/s, η_1 = 13cP.

which is half of the time period of the tank-treading motion (0.16 s) (Fig. 5.10). This is consistent with the conclusions by Ramanujan and Pozrikidis (1998) and Fedosov *et al.* (2010a).

5.3.3 Skeleton density variation

In the following simulations we consider two typical *in vivo* shear rates, 270/s and 1640/s. 270/s is considered as the average shear rate, and 1640/s is considered as the peak shear rate in human body (Stroeva *et al.*, 2007) or in an artificial heart (Hochareon, 2003; Deutsch *et al.*, 2006). Our results show that for both shear rates, the areal dilation and protein density variation of the cytoskeleton are less than 1% everywhere if the friction coefficients derived in §4.2 are used. This is in contradiction with simulation results by Dodson and Dimitrakopoulos (2010), in which measurable cytoskeleton areal dilation was predicted. The primary cause of this discrepancy is the inclusion of dissipation effects. Specifically, in the model by Dodson and Dimitrakopoulos (2010), neither the bilayer-skeleton friction nor the membrane viscosity are considered. In our simulations, the areal dilation remains very small even if the

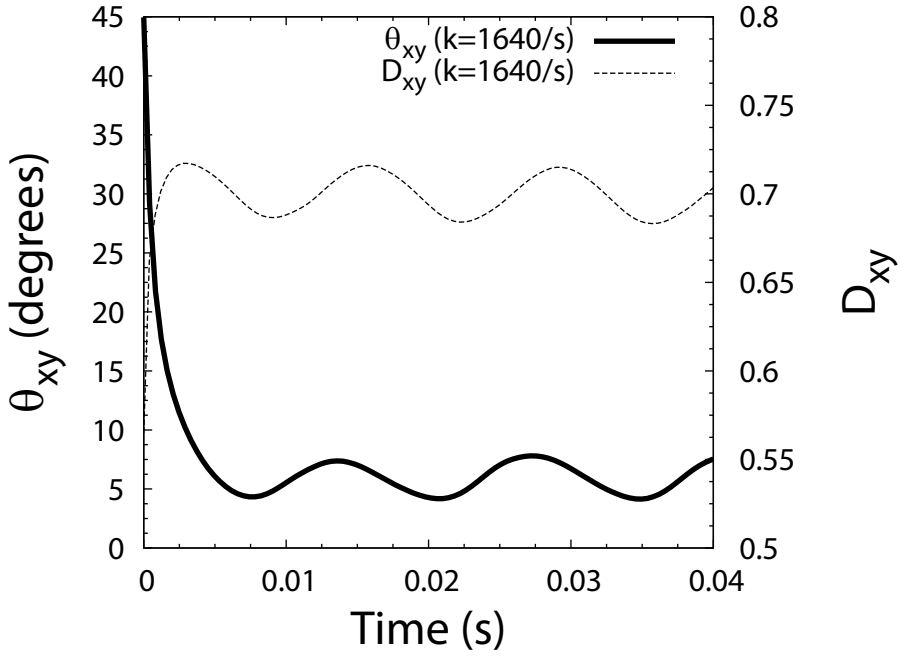

Figure 5.12: Time histories of θ_{xy} and D_{xy} during swinging motions. k=1640/s, $\eta_1 = 13$cP.

band 3 diffusivity of ghost RBCs ($0.53\mu\text{m}^2$/s, which is 24 times larger than intact RBCs and measured by Tomishige (1998)) is used. Significant cytoskeleton areal dilation does not appear until we reduce the friction coefficient of intact RBCs by 1000 times. Therefore, our simulations confirm the prediction by Fischer (1992) that the tank-treading motion is too fast to allow significant bilayer-skeleton slip.

5.3.4 Distributions of shear ratio and interaction forces

Contours of the shear ratio $\sqrt{\lambda_1/\lambda_2}$ as well as the tangential and normal interaction forces between the lipid bilayer and the cytoskeleton are shown in Fig. 5.13. The shear rate is 270/s, and the external fluid viscosity $\eta_1 = 13$ cP. The corresponding vector field of the tangential interaction forces (the interaction forces on the lipid bilayer) is shown in Fig. 5.14. The corresponding contours for shear rate 1640/s are shown in Fig. 5.16. Incidently, the cell shapes shown in Fig. 5.13 and Fig. 5.16 match well with the experimental pictures as shown in Fig. 4.4.2 in Pozrikidis (2003a).

The results show that in both cases the minimum shear ratios happen at the tips of the cell and their values are close to 1. The maximum shear ratio is 1.589 for

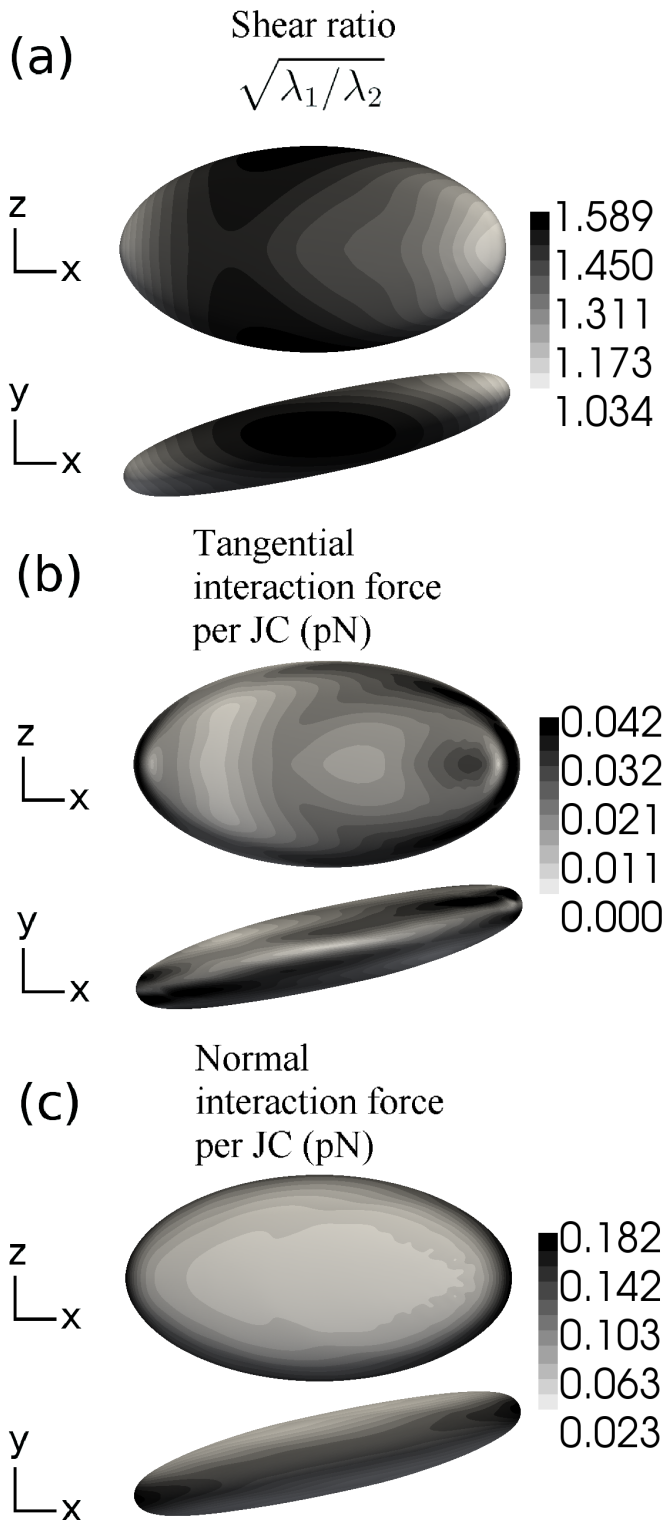

Figure 5.13: Contours (top view and side view) of (a) the shear ratio $\sqrt{\lambda_1/\lambda_2}$, (b) magnitude contour of the tangential interaction force per JC, (c) magnitude contour of the normal interaction force per JC. k=270/s, η_1 = 13cP. Contours are shown at the instant when D_{xy} reaches the maximum value.

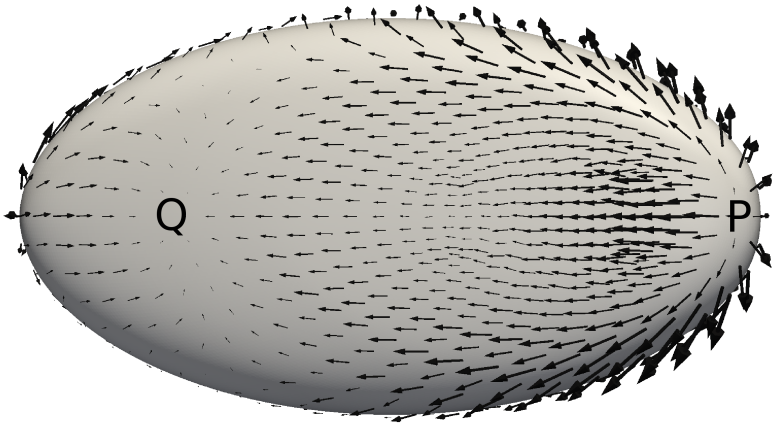

Figure 5.14: Vector field of the tangential interaction force applied on the lipid bilayer, k=270/s, $\eta_1 = 13$cP. It is shown at the time when D_{xy} reaches the maximum value.

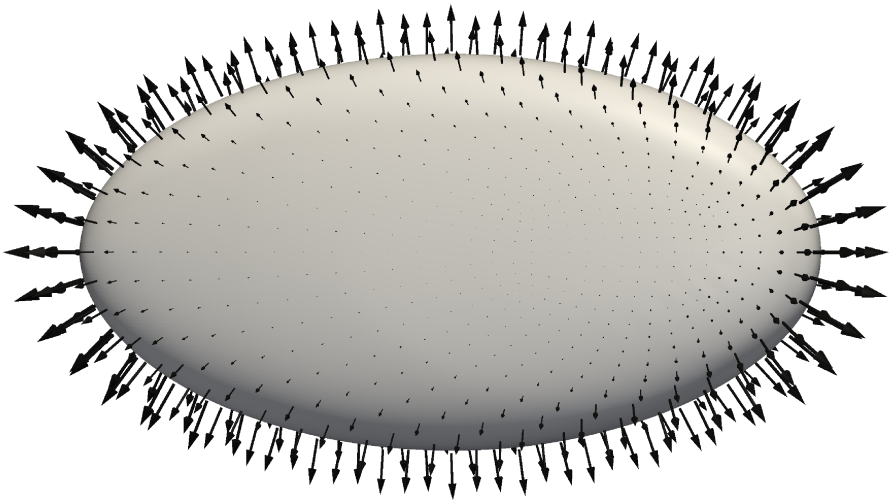

Figure 5.15: Vector field of the normal interaction force applied on the lipid bilayer, k=270/s, $\eta_1 = 13$cP. It is shown at the time when D_{xy} reaches the maximum value.

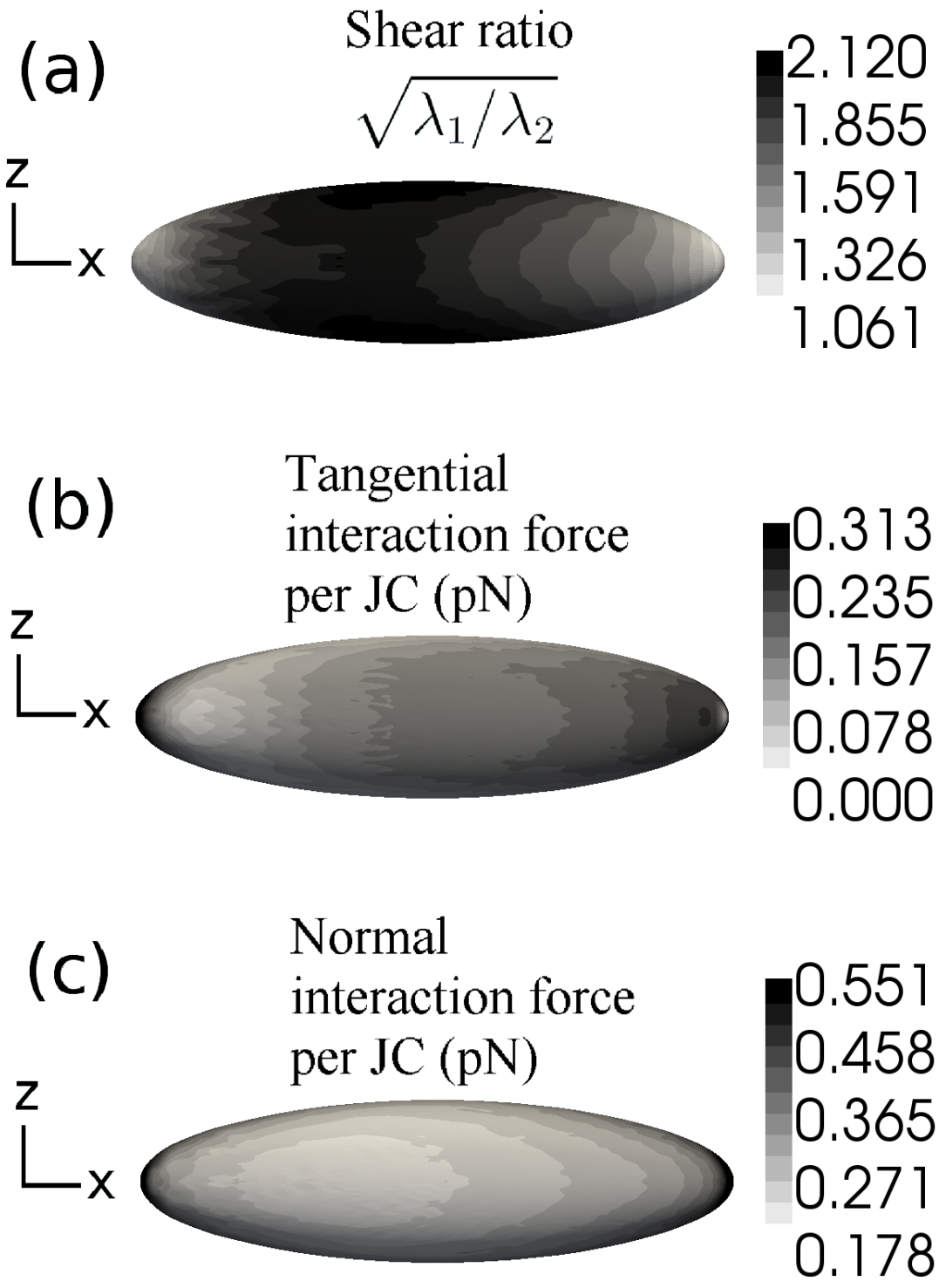

Figure 5.16: Contours (top view) (a) the shear ratio $\sqrt{\lambda_1/\lambda_2}$, (b) magnitude contour of the tangential interaction force per JC, (c) magnitude contour of the normal interaction force per JC. k=1640/s, $\eta_1 = 13$cP. Contours are shown at the time when D_{xy} reaches the maximum value.

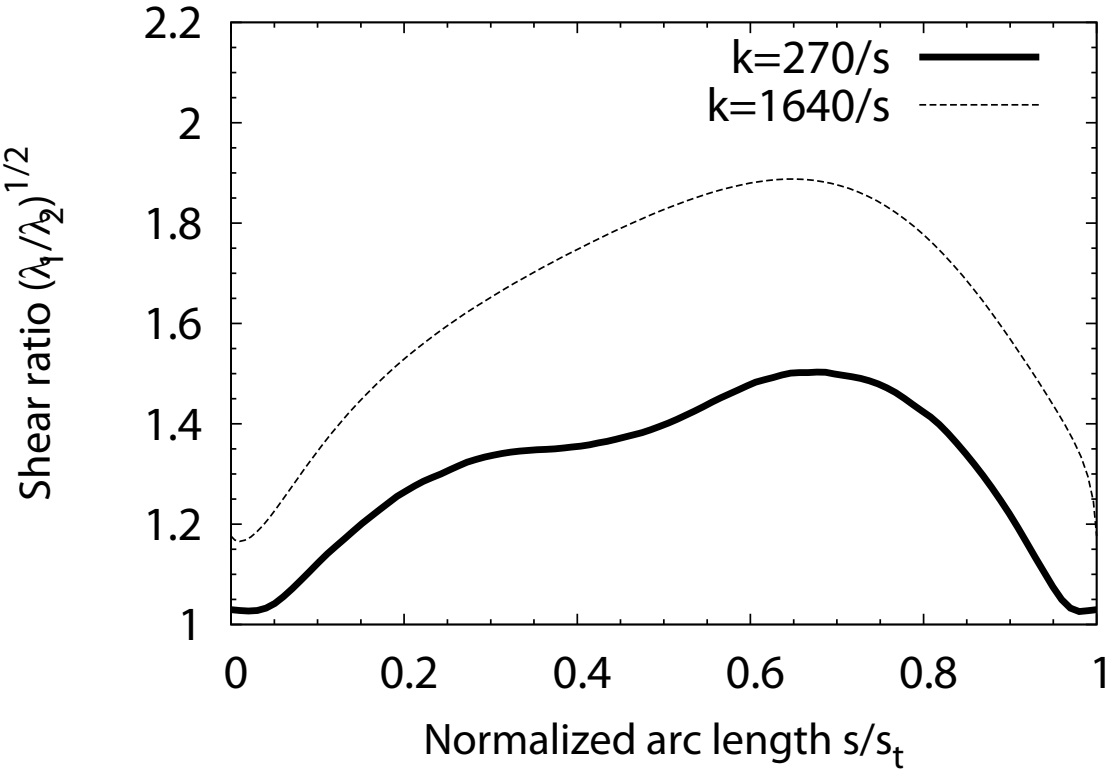

Figure 5.17: Shear ratio in the cross section by xy plane (shown at the time when D_{xy} reaches the maximum value).

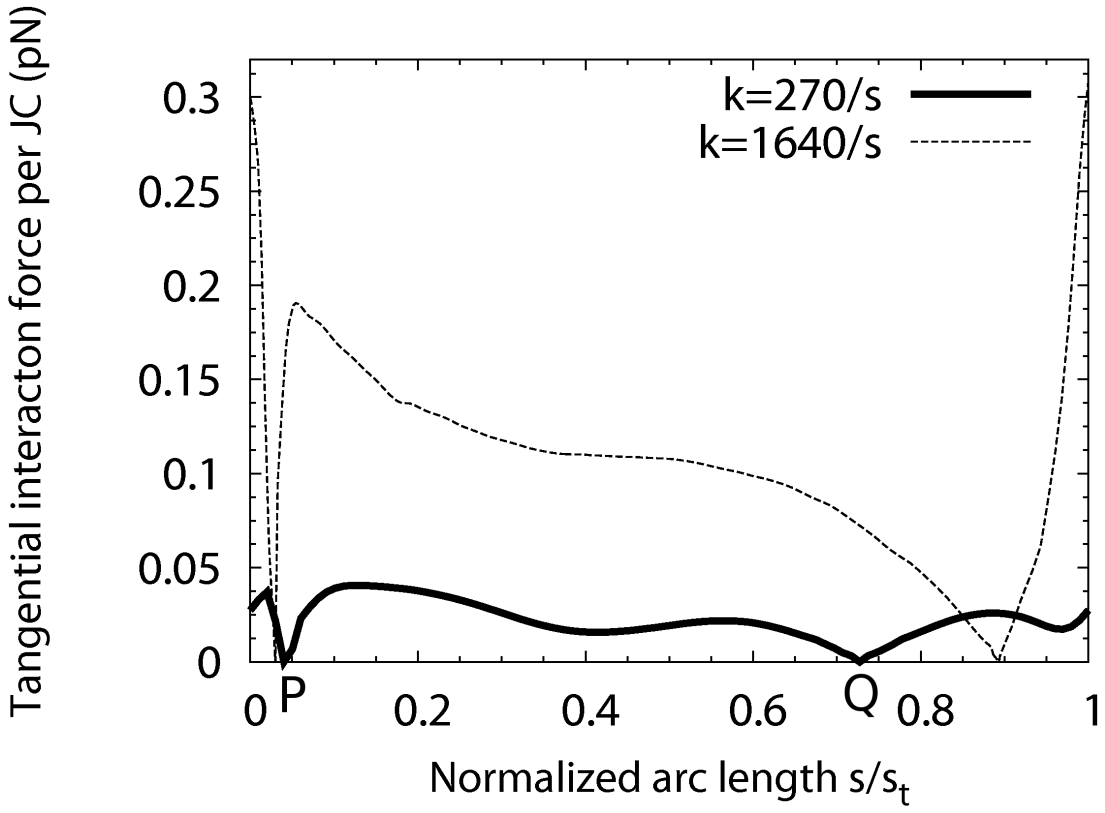

Figure 5.18: Tangential interaction force per JC in the cross section by xy plane (shown at the time when D_{xy} reaches the maximum value).

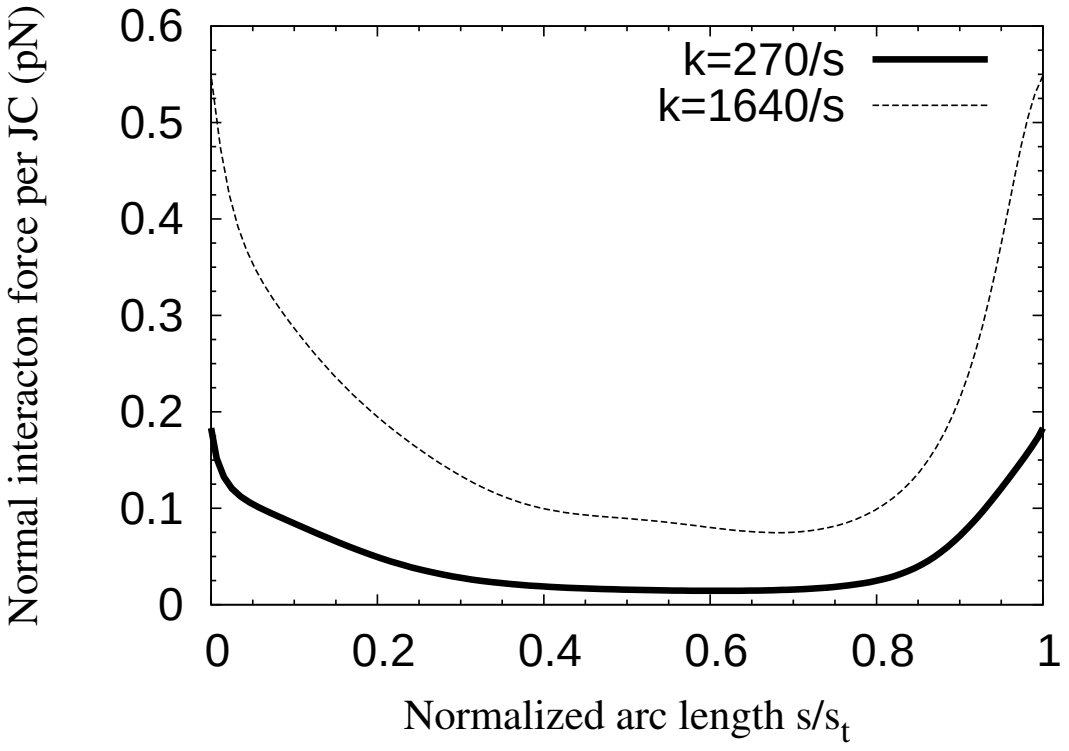

Figure 5.19: Normal interaction force per JC in the cross section by xy plane (shown at the time when D_{xy} reaches the maximum value).

shear rate 270/s and 2.120 for shear rate 1640/s, occurring near the middle region of the cell but off from the center plane (the xy plane).

For the tangential interaction force, the maximum values occur at the tips of the cell (0.042 pN per JC for shear rate 270/s and 0.313 pN per JC for shear rate 1640/s). In the top view of the vector field (Fig. 5.14) it is seen that there are points (P & Q) where the tangential interaction force changes direction. In Fig. 5.14, the bilayer-skeleton interaction force on the lipid bilayer instead of on the skeleton is shown for clarity.

For normal interaction forces, the maximum value again occurs at the tips of the cell (0.182pN per JC for shear rate 270/s and 0.551pN per JC for shear rate 1640/s). Since we consider pre-compression of the cytoskeleton with prestress $\bar{T}_0 = -30pN/\mu m$ Peng *et al.* (2010), the cytoskeleton pushes the lipid bilayer outwards. The normal interaction forces mainly depend on the prestress and the curvature of

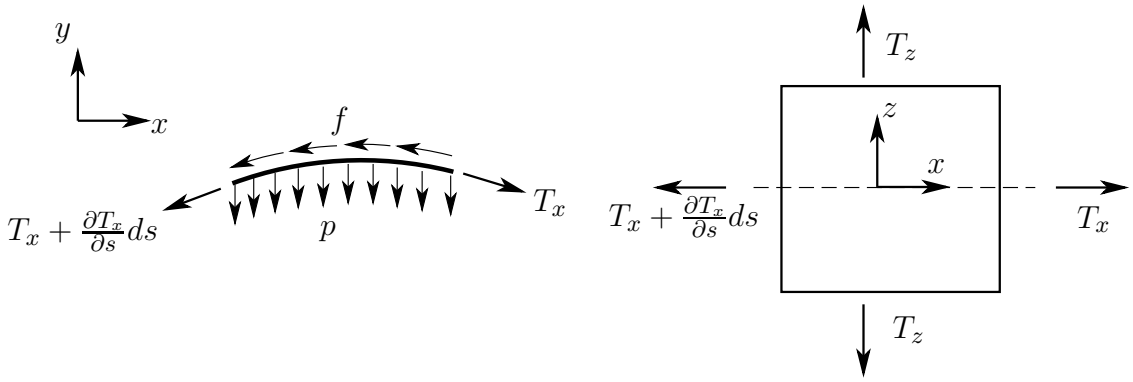

Figure 5.20: The equilibrium of an infinitely small element of the cytoskeleton at the center line (cross section by xy plane).

the shape. The top view of the vector field is shown in Fig. 5.15.

The distributions of the shear ratio and interaction forces along the cell profile within the xy plane are shown in Figs. 5.17, 5.18 and 5.19 for shear rates 270/s, and 1640/s.

To better understand the distributions of the tangential and normal interaction forces, we consider an infinitely small element of the cytoskeleton along the center line (the xy cross section) as shown in Fig. 5.20. The equilibriums of the cytoskeleton (a membrane without bending stiffness) in the tangential direction and the normal direction (the Laplace's law) lead to

$$\frac{\partial T_x}{\partial s} + f^{bs} = 0, \tag{5.4}$$

$$\frac{T_x}{r_x} + \frac{T_z}{r_z} - p^{bs} = 0, \tag{5.5}$$

where $T_x = \Theta_x h$ and $T_z = \Theta_z h$. r_x and r_z are the radii of the curvatures in x and z directions, respectively. f^{bs} is the friction force per unit area (the component of $\boldsymbol{\tau}^{bs}$ in the tangential direction) and p^{bs} is the normal interaction force per unit area (the component of $\boldsymbol{\tau}^{bs}$ in the normal direction).

There is almost no area change ($\lambda_1\lambda_2 \approx 1$) in the cytoskeleton so that the mean stress due to area change is extremely small ($\bar{T} \approx \bar{T}_0$) and the shear ratio $\gamma = \sqrt{\lambda_1/\lambda_2} \approx \lambda_1$. $\bar{T}_0 = -30pN/\mu m$ is the prestress. If we ignore the cytoskeleton

viscosity temporarily ($\nu_s = 0$), T_x and T_z can be written as

$$T_x = \bar{T}_0 + \frac{\mu_s}{2}(\gamma^2 - 1/\gamma^2), \tag{5.6}$$

$$T_z = \bar{T}_0 - \frac{\mu_s}{2}(\gamma^2 - 1/\gamma^2), \tag{5.7}$$

as shown in Eqns. (4.49) and (4.50). Therefore Eq. (5.4) can be re-expressed as

$$f^{bs} = -\frac{\partial T_x}{\partial s} = -\frac{\partial T_x}{\partial \gamma}\frac{\partial \gamma}{\partial s} = -\frac{\mu_s}{2}\left(2\gamma + \frac{2}{\gamma^3}\right)\frac{\partial \gamma}{\partial s}. \tag{5.8}$$

Eq. (5.8) relates the friction force f^{bs} to the derivative of γ with respect to the arch length s. This relation is demonstrated in Figs. 5.17 and 5.18. Indeed, it can be shown that there are two points where the derivative of γ with respect to the arch length s equals to zero in Fig. 5.17, corresponding to two points (P & Q) in Fig. 5.18 where the tangential force equals zero. The drifts of the two points in arc length positions from Fig. 5.17 to Fig.5.18 are caused by the cytoskeleton viscosity ($\nu_s \neq 0$).

For normal interaction forces, if we ignore the cytoskeleton viscosity temporarily ($\nu_s = 0$), Eq. (5.5) can be rewritten as

$$\bar{T}_0\left(\frac{1}{r_x} + \frac{1}{r_z}\right) + T_s\left(\frac{1}{r_x} - \frac{1}{r_z}\right) - p^{bs} = 0. \tag{5.9}$$

This relation explains characteristics of Fig. 5.19. At the convex tips the curvatures ($1/r_x$ and $1/r_z$) are significantly larger than those in other places on the surface and T_s is very small due to small shear ($\gamma \approx 1$), therefore the maximum normal interaction force p^{bs} happens in the tips.

5.3.5 Effect of the skeleton reference shape

Although the cell shapes predicted in Fig. 5.13 and Fig. 5.16 match well with the experiments, our simulations show significant swinging motions, while there is no significant swinging motion based on the experimental pictures by Fischer *et al.* (1978) and Fig. 1.6b by T.M. Fischer (Pozrikidis, 2003a). A possible cause of this discrepancy is the choice of the reference configuration of the cytoskeleton, *i.e.* the configuration with zero shear deformation. In our simulations, we chose the biconcave

shape as the reference configuration, but existing studies (*e.g.* Lim *et al.* (2002)) suggest that the actual reference configuration may be between the biconcave shape and the spherical shape. By deflating a spherical cell into a biconcave shape first as we did in our previous work (Peng *et al.*, 2010), we simulate the tank-treading motion of this red blood cell with a spherical shape as its reference configuration. It is found that in this scenario there is almost no swinging motion. This confirms the work by Tsubota and Wada (2010). On the other hand, the reference shape may not be a perfect sphere for *in vivo* red blood cells. According to the experiment by Fischer (2004), red blood cells have shape memory. This implies that the reference shape of the cell is not perfectly spherical (otherwise all points on the membrane will be indistinguishable so that there will be no shape memory. Thus, our results provide indirect evidence that the reference configuration is between the biconcave shape and the spherical shape.

5.4 Summary and remarks

In this chapter, we applied the dynamic multiscale model described in Chapter 4 to study red blood cells in tube flow and shear flow.

The vital difference between our model and the existing models is the incorporation of a multiscale structural model to describe the mechanical response of the cell membrane, which enables predictions of not only highly accurate RBC responses to external loads, but also the physical mechanisms involved in the dynamic response of a cell at different temporal and spatial levels. The multiscale simulations illustrated novel (and potentially important) phenomena in membrane mechanics that had never been discovered using other models.

Among the important phenomena that have been analyzed are the remodeling of skeleton density and the development of both positive (tensile) and negative (compressive) forces that act between the lipid bilayer and the attached skeleton. For example, in our previous investigations the development of negative contact forces between the skeleton and the lipid bilayer, coupled to protein density changes, was related to the phenomena of membrane necking and vesiculation during RBC aspiration into a micropipette (Peng *et al.*, 2010). During aspiration, however, large

variations in skeleton density are typically forecast as, in fact, found experimentally. Density variations are easily in the range $0.2 < \rho/\rho_0 < 1.4$. Accompanying this is the development of negative contact force (per JC) as large as ∼-20 pN. In contrast, we show here that within tube flow and shear flow RBCs undergo quite modest protein density variations as illustrated in the example simulation results shown in Fig. 5.9 where $0.85 < \rho/\rho_0 < 1.07$. Likewise the local contact forces per JC are also modest. The implication is that micropipette aspirations may exaggerate the mechanical loading on RBC and the subsequent mechanical responses in most *in vivo* conditions (*e.g.* inside capillaries or blood vessels).

On the other hand, RBCs may sustain much larger loads and deformations inside spleen, where blood flows from the red-pulp cords (ends of small arterioles) to the venous sinuses and merges back into the venous system (Mebius and Kraal, 2004). The venous sinuses are made of parallel series of endothelial cells with slits between them. Normal RBCs can pass through these slits, while aging, defected, or infected RBCs may be stuck there, where they are phagocytosed by macrophages. Furthermore, the contractility of the stress fibers in the endothelial cells can control the opening of these slits and assist the retention of RBCs in the spleen. Further studies are necessary to illustrate these processes.

Chapter 5, in part, has been submitted for publication of the material as it may appear in 'Molecular-detailed modeling of erythrocytes in Stokes flow', *Journal of Fluid Mechanics*, 2011. Zhangli Peng, Robert J. Asaro and Qiang Zhu, 2011. The dissertation author was the primary investigator and author of this paper.

Chapter 6

Summary and Future Directions

6.1 Summary

The research described in this dissertation focused on multiscale modeling of a red blood cell and its fluid-structure interaction. The main purpose of this study is to explore the structure-function relationships of red blood cells.

The main novel contributions of this work are summarized as follows.

- We developed a three-level multiscale modeling approach of the red blood cell membrane. It includes the spectrin model (Level I), the junctional complex model (Level II) and the complete cell finite element model (Level III). Compared with existing models of the RBC membrane (Discher *et al.*, 1998; Mukhopadhyay *et al.*, 2002; Svetina *et al.*, 2004), our model has the following characteristics: (1) Our multiscale approach not only delivers accurate predictions of whole-cell response (due to the involvement of the detailed molecular structure and responses at different levels), but also allows us to address physical mechanisms at different length scales and to correlate mechanical loads on the cell with detailed stress distributions within the composite structure. This model has predicted phenomena that had never been found by other models (*e.g.* bifurcation, mode switching, and stress-induced unstiffening due to unfolding) (Zhu *et al.*, 2007; Zhu and Asaro, 2008); (2) Our model explicitly incorporates the local interactions between the skeleton and the bilayer, as well as the inter- and intra-molecule interactions inside the skeleton; (3) This model is inherently

dynamic and capable of studying time-dependent responses at different length scales as presented in Chapter 4.

- We formulated a master-slave penalty contact algorithm for the interaction between the lipid bilayer and the cytoskeleton, and the interaction between the lipid bilayer and some rigid surfaces, *e.g.,* the micropipette inner surface. This algorithm makes it possible to study the bilayer-skeleton interaction force in the molecular level.

- We predicted the resting shape of red blood cells using our multiscale model. We found that the biconcave shape of healthy RBCs and the elliptical shape of diseased RBCs (elliptocytosis) can be explained if the lipid bilayer has a positive spontaneous curvature while the skeleton possesses a small shear stiffness.

- We found that the predicted complete cell deformations for quasi-static experiments match well with the micropipette aspiration, optical tweezer stretching and flow channel stretching, especially for the skeleton under a prestress $\bar{T}_0 = -30pN/\mu m$.

- We predicted the protein density variation in the micropipette aspiration. The results match well with the micropipette aspiration experiment with the fluorescence imaging and the existing molecular model by Discher *et al.* (1998).

- We calculated the bilayer-skeleton interaction forces of RBCs in the molecular level for the micropipette aspiration. We found that the spectrin unfolding may significantly increase this interaction force, which may lead to the bilayer-skeleton separation and vesiculation.

- We simulated and explained the necking phenomenon in the micropipette aspiration, and provided some information which cannot be observed in the experiments, which may guide the experiments in the future.

- We predicted the critical bilayer-skeleton interaction force in the molecular level which causes the bilayer-skeleton separatio by simulating the flow channel

stretching experiment, and got consistent results with the adhesion energy theory by Hochmuth and Marcus (2002) and the experimental data by Hochmuth (1973).

- We developed an efficient, robust and accurate fluid-structure interaction algorithm in the cell length scale by coupling the multiscale approach of the membrane with a boundary element method of the surrounding Stokes flow.

- We incorporated the membrane viscoelasticity into the multiscale approach by using a Voigt-Kelvin constitutive model. Furthermore, we employed a special numerical algorithm to stabilize the implementation of this constitutive model.

- We formulated the friction between the lipid bilayer and the cytoskeleton based on the mobilities of transmembrane proteins and calculated the hydrodynamic drags on the cytoskeleton. We found that the bilayer-skeleton friction is much larger than the hydrodynamic drag on the cytoskeleton.

- We investigated the skeleton density variation and the bilayer-skeleton interaction force of red blood cells in tube flow. We found that the skeleton density is large near the vessel wall, which may facilitate the biochemical interaction between the RBC cytoskeleton and endothelial cells. We found the maximum bilayer-skeleton interaction force happens in the trailing edge of RBCs, where the potential vesiculation may happen. The skeleton density and the bilayer-skeleton interaction force we predicted are much smaller than those in micropipette experiments. It may help explain why red blood cells are stable and durable in microcirculation.

- We predicted the tank-treading frequency of a red blood cell in shear flow, which is consistent with existing experiments. We found there is a linear dependence of the tank-treading frequency on the extracellular fluid viscosity, which matches well with the existing numerical studies and experiments. In addition, we found that the membrane viscosity plays a vital role in determining the tank-treading frequency.

- We showed that the skeleton density of the red blood cell almost doesn't change

in tank-treading motion due to the significant bilayer-skeleton friction. It is consistent with the analysis by Fischer (1992), but contradicts with the numerical results by Dodson and Dimitrakopoulos (2010).

- We studied the swinging motion of a red blood cell in shear flow, and found consistent swinging frequency with the existing studies.

- We predicted the distributions of shear deformation, the bilayer-skeleton interaction forces of a RBC in the tank-treading motion, and explained these distributions by a simple analytical derivation.

- We investigated the effect of the cytoskeleton reference shape on the tank-treading motion, and found that the cytoskeleton reference shape is close to a spherical shape by comparing predicted cell shapes with experimental images.

6.2 Future Directions

There are still many open questions and ongoing research for the red blood cell (RBC), *e.g.*, the deformability of diseased RBCs and the inhomogeneity of the membrane. Several aspects of our numerical methods can be polished as well. In the following, we list several future directions.

- A concurrent multiscale model can be developed for problems with some singular points, *e.g.* the flow channel stretching. In these singular points, such as the attachment point in the flow channel stretching experiments, the deformation and stress are very large, and the continuum model is not very appropriate. To make the simulations more accurate, our molecular models (Level I and Level II) can be employed in these small regions, while the continuum model (Level III) can be used for the rest of the cell.

- Besides the spectrin unfolding, the head-to-head dissociation of spectrins also plays an important role for the unstiffening behavior of the cytoskeleton, which may be considered in our model in the future.

- Currently we modeled the suspension complex as a pinning point. By exploring the molecular structure of the suspension complex, we can build an exact model of it and incorporate it to our multiscale approach.

- For the resting shape problem, a full phase diagram with parameters of skeleton stiffness and bilayer spontaneous curve can be explored. In addition, the area-difference-elasticity (ADE) theory can be incorporated in the finite element method as shown in Appendix B. Furthermore, some experiments revealed that the RBC membrane may be inhomogeneous, *i.e.,* the membrane stiffness of the dimple region may be different from the membrane stiffness of the rim region. This membrane inhomogeneity may also contribute to the biconcave shape of the cell, which can be considered by using our multiscale modeling approach.

- Both the optical tweezer stretching and micropipette aspiration experiments were also used to study the dynamic behaviors of the red blood cell based the relaxation and creep. Our dynamic multiscale modeling approach can be used directly to simulate these time-dependent experiments. In addition, sophisticated constitutive laws, *e.g.,* the fractional order constitutive model, can be incorporated in our framework to fit the RBC dynamic responses.

- The dynamic multiscale model in Chapter 4 can be used to study the flow channel stretching experiment. The accuracy of the predictions may be significantly improved.

- Instead of the Hughes-Liu shell element, the isogeometric Kirchhoff-Love shell element (Benson *et al.*, 2010) can be used in our approach to make the FEM/BEM coupling algorithm more elegant, because the rotational degrees of freedom do not exist for the isogeometric Kirchhoff-Love shell element.

- The fast boundary element methods, *e.g.,* the fast multipole BEM (Liu, 2009) and the pre-corrected FFT BEM, can be used to accelerate the FEM/BEM coupling algorithm for large scale simulations of multiple red blood cells.

- The dynamic multiscale modeling approach can be employed to study how the

spleen filters out the old and diseased red blood cells. RBCs may sustain much large loads and deformations inside spleen, where blood flows from the red-pulp cords (ends of small arterioles) to the venous sinuses and merges back into the venous system (Mebius and Kraal, 2004). The venous sinuses are made of parallel series of endothelial cells with slits between them. Normal RBCs can pass through these slits, while aging, defected, or infected RBCs may be stuck there, where they are phagocytosed by macrophages. Furthermore, the contractility of the stress fibers in the endothelial cells can control the opening of these slits and assist the retention of RBCs in the spleen. Further studies are necessary to illustrate these processes.

- The deformability of the diseased red blood cells can be investigated further using our multiscale modeling approach, including the membrane protein defects in some hereditary RBC diseases, the sickle cell disease and the malaria (Fedosov *et al.*, 2010b).

- In the aspect of cellular mechanics, the red blood cell is a simple model system for other cells, because it has no nucleus and is well characterized. The multiscale modeling approach and microhydrodynamics we used for RBCs can be extended to study other cells, *e.g.*, white blood cells, yeast cells, endothelial cells and cancer cells. However, these cells are usually more complicated due to the nucleus and the 3D cytoskeleton.

- In terms of the fluid-structure interaction (FSI), RBCs 'swim' passively in the blood flow. The approach we developed for studying the FSI of RBCs by coupling finite element and boundary element methods can be also applied in bacteria swimming in a straightforward way.

Appendix A

Occurrence of Negative Area Stiffness

During the course of our simulations, we noted the occurrence of what appears to be a negative area stiffness. To illustrate its existence associated with domain unfolding, we apply a simplified model and idealize the protein skeleton as a two-dimensional mesh consisting of triangular units located within the (X, Y) plane (Dao *et al.*, 2006). Each unit contains three Sp tetramers, whose configurations are represented by the vectors $\mathbf{a} = (a_X, a_Y)$, $\mathbf{b} = (b_X, b_Y)$, and $\mathbf{c} = (c_X, c_Y)$. The stress inside the network is then given as

$$\sigma_{ij} = \frac{1}{2A}\{\frac{F(a)}{a}a_i a_j + \frac{F(b)}{b}b_i b_j + \frac{F(c)}{c}c_i c_j\} - \frac{C}{A^2}\delta_{ij}, \quad i, j = X, Y \tag{A.1}$$

where $a \equiv |\mathbf{a}|$, $b \equiv |\mathbf{b}|$, and $c \equiv |\mathbf{c}|$. A is the area occupied by the unit. F is the function determining the tension inside $\mathbf{a}$, $\mathbf{b}$, and $\mathbf{c}$. C is the steric coefficient (same as the one in Eq. 2.36). The resulting pressure inside the protein skeleton P_s is obtained as the trace of σ_{ij} divided by -2. We have

$$P_s = -\frac{1}{4A}\{aF(a) + bF(b) + cF(c)\} + \frac{C}{A^2}, \tag{A.2}$$

In order for P_s to be zero at the natural state $a = b = c = a_0$ and $A = A_0$, the constant C has to be $C = \frac{3}{4}A_0 a_0 F(a_0)$.

As an example, we consider an equibiaxial deformation in which the Sp tetramers

are stretched by the same amount. For illustration, we assume that until the occurrence of unfolding the tension F can be described by the worm-like-chain (WLC) model $F = \frac{k_B T}{p}\{\frac{1}{4(1-x')^2} - \frac{1}{4} + x'\}$, where p is the persistence length, $x' = a/L$ (L is the contour length). Based upon our previous study (Zhu and Asaro, 2008), we assume that unfolding occurs at $x' = x'_c = 0.85$ and the post-unfolding behavior can be approximated as $F = c_0 + c_1(x' - x'_c)^{1/2}$. As an example, we choose $c_0 = 6.1$ pN and $c_1 = 3$ pN/m$^{1/2}$. Following Dao *et al.* (2006), we choose $a_0 = 87$ nm and $L = 238$ nm. We thus obtain a modified strain-stretch relation. By studying the pressure as a function of $A/A_0 - 1$, it is found that corresponding to the occurrence of unfolding, the dependence of the pressure on A changes its direction at $A/A_0 \sim 4.5$. This clearly indicates the existence of negative area stiffness.

Appendix B

Area-Differece-Elasticity Theory of the Lipid Bilayer

For the lipid bilayer, the free bending energy functional $F_{pm}[S]$ is given as (Lim *et al.*, 2008)

$$F_{pm}[S] = F_{sc}[S] + F_{ad}[S] + F_g[S], \tag{B.1}$$

where $F_g[S]$ is Gaussian-curvature term, which is irrelevant (topological invariant) according to Gauss-Bonnet theorem.

$$F_{sc}[S] = \frac{\kappa_c}{2} \oint_S dA \left[2H - C_0\right]^2, \tag{B.2}$$

$$F_{ad}[S] = \frac{\pi\bar{\kappa}}{2D_0^2 A_0}(\Delta A[S] - \Delta A_0)^2, \tag{B.3}$$

where

$$H = (C_1 + C_2)/2, \tag{B.4}$$

is the mean curvature.

$$\Delta A[S] = 2D_0 \oint_S dA\, H, \tag{B.5}$$

is the area difference of the two leaflets. ΔA_0 is the initial area difference of the two leaflets. κ_c and $\bar{\kappa}$ are the regular bending stiffness and area-difference bending stiffness, and $\alpha_b = \bar{\kappa}/\kappa_c$. D_0 is the distance between the midpoints of the two leaflets.

Variation of $F_{pm}[S]$ can be written as

$$\delta F_{pm}[S] = \delta F_{sc}[S] + \delta F_{ad}[S], \tag{B.6}$$

where

$$\delta F_{sc}[S] = -2\kappa_c C_0 \oint_S dA\, H + 2\kappa_c \oint_S dA\, H^2, \tag{B.7}$$

and

$$\delta F_{ad}[S] = 2\kappa_c \frac{\pi \alpha_b}{D_0^2 A_0} (\Delta A[S] - \Delta A_0) \oint_S dA\, H. \tag{B.8}$$

Combine Eq. B.7 and Eq. B.8, it gives

$$\delta F_{pm}[S] = 2\kappa_c \oint_S dA\, H^2 - 2\kappa_c C_0^{eff} \oint_S dA, \tag{B.9}$$

where

$$C_0^{eff}[S] = C_0 - \frac{\pi \alpha_b}{D_0^2 A_0} (\Delta A[S] - \Delta A_0). \tag{B.10}$$

This means, the area difference elasticity (ADE) term can be corporated in the spontaneous curvature model by replacing C_0 by $C_0^{eff}[S]$, but it should be noticed that $C_0^{eff}[S]$ is a functional of S while C_0 is constant.

The deformation gradient tensor $\mathbf{F}$, defined as

$$\mathbf{F} = \begin{bmatrix} F_{11} & F_{12} & F_{13} \\ F_{21} & F_{22} & F_{23} \\ F_{31} & F_{32} & F_{33} \end{bmatrix} = \hat{\mathbf{F}}\tilde{\mathbf{F}}, \tag{B.11}$$

where $\hat{\mathbf{F}}$ is the deformation gradient caused by external loading and $\tilde{\mathbf{F}}$ is the initial deformation gradient caused by the spontaneous curvature $C_0^{eff}[S]$.

In finite element method, the area difference elasticity (ADE) term can be incorporated by calculating

$$\Delta A[S] = \sum_{e=1}^{n_e} \left(A_e^+ - A_e^- \right) = \sum_{e=1}^{n_e} \left[(J_e^+ - J_e^-) A_e^0 \right], \tag{B.12}$$

where A_e^+ and A_e^- are the areas at top and botttom surfaces and J_e^+ and J_e^- are the Jacobians at top and botttom surfaces.

Appendix C

Analysis of Two Stages in the Micropipette Aspiration

Under large negative pressure, the aspiration process can be divided into two stages as shown in Fig. C.1. In Stage I, the cell part outside the pipette is flaccid. In Stage II, it becomes spherical. In Stage I, the relation between aspiration length and pressure mainly depends on the elastic properties of the membrane, i.e. the shear stiffness. In Stage II, this relation mainly depends on the compressibility of the volume and the compressibility of the lipid bilayer (surface area). In an extreme case, if the volume and the surface area of the cell is completely conserved, the cell can sustain infinitely large negative pressure in Stage II, since any increase of the aspiration length in Stage II will either increase surface area or decrease volume.

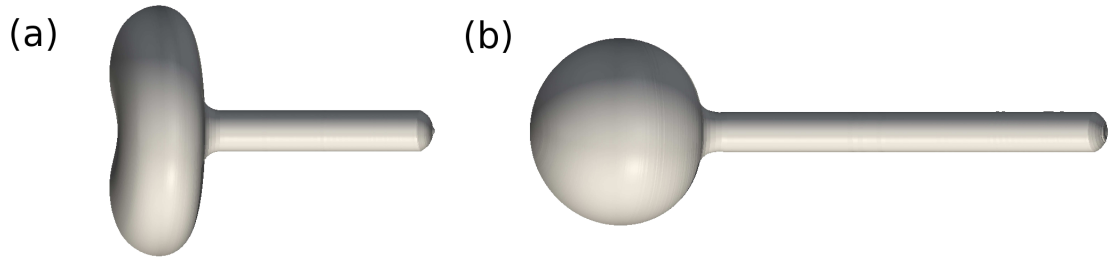

Figure C.1: (a) Stage I. (b) Stage II.

Critical transition point between Stage I and II

The critical condition between Stage I and Stage II is that the volume V and surface area A in Stage II should be equal to the initial volume V_0 and A_0. For a cylindrical pipette, this condition leads to two equations as

$$A = \underbrace{2\pi R_p^2}_{\text{semi-sphere at cap } A_p} + \underbrace{(L - Rp) \cdot 2\pi R_p}_{\text{cylindrical part}} + \underbrace{\left[4\pi R_s^2 - 2\pi(R_s^2 - R_s\sqrt{R_s^2 - R_p^2})\right]}_{\text{sphere outside pipette } A_s} = A_0 C_a \tag{C.1}$$

$$V = \underbrace{\frac{2}{3}\pi R_p^3}_{\text{semi-sphere at cap}} + \underbrace{(L - Rp) \cdot \pi R_p^2}_{\text{cylindrical part}} + \underbrace{\left[\frac{4}{3}\pi R_s^3 - \pi(R_s h^2 - \frac{1}{3}h^3)\right]}_{\text{sphere outside pipette}} = V_0 C_v \tag{C.2}$$

where L is the aspiration length, R_s is the radius of the cell part outside the pipette. For example, if the pipette radius $R_p = 0.59\mu m$. $A_0 = 129.2\mu m^2$ and $V_0 = 88.0\mu m^3$ are the initial area and volume of a cell with diameter $7.65\mu m$. C_v and C_a are the ratios of volume and surface area change. $C_v = 1.0, C_a = 1.0$ at this critical condition because of incompressibility. $h = R_s - \sqrt{R_s^2 - R_p^2}$ is the height of the overlap part of outside sphere and the inner cylinder.

Notice that only two unknowns L and R_s in Eqns.C.1 and C.2, so that they can be solved together. Then we get $L = 11.8997\mu m$, $R_s = 2.6189\mu m$ at this critical transition point. They are consistent with the experiments.

Deformation in Stage II

After the critical transition point, the volume of the cell will decrease when the cell continues to deform in Stage II. Since the area change is less than 1% under pressure of 1000 mm H_2O (Evans and Waugh, 1977), we neglect the area change, *i.e.* $C_a = 1.0$. The volume change can be calculated as Evans and Waugh (1977)

$$\frac{V_0 - V}{V_0} = 1.0 - C_v = \frac{4R_w\bar{T}}{\beta C_i}\left(\frac{A_p/2R_p + A_s/2R_s}{A_p + A_s}\right) \tag{C.3}$$

where $R_w = 0.6$ is the fraction of total cell volume that is water, $\beta = RT$ is the gas constant ($R = 8.314471 JK^{-1}mol^{-1}$) times absolute temperature $T = 300K$.

$C_i \approx 0.003 \sim 0.3 \times 10^3 mol/m^3$ is the molar concentrations of solute, $\bar{T} = \frac{\Delta P R_p}{2(1-R_p/R_s)}$ is the isotropic tension in the membrane.

Notice that since C_v becomes another unknown in Stage II, there are three unknowns (C_v,L and R_s) in Equations C.1,C.2 and C.3, they can be solved together. For pressure of 550 mm H_2O and molar concentration of $C_i = 0.004 \times 10^3 mol/m^3$, we get $L = 14.2003 \mu m$, which is consistent with experiment. We get $R_s = 2.4650 \mu m$, which is a little bit smaller than the diameter of $5.7 \mu m$ ($R_s = 2.85 \mu m$) measured in experiment, and $C_v = 0.89$, which is consistent with the experimental result by Engstrom and Meiselman (1996).

Bibliography

M. Abkarian, M. Faivre, and A. Viallat. Swinging of red blood cells under shear flow. *Phys. Rev. Lett.*, 98:188302, 2007.

M. Abkarian, M. Faivre, R. Horton, K. Smistrup, C. Best-Popescu, and H. Stone. Cellular-scale hydrodynamics. *Biomed. Mater.*, 3:034011, 2008.

X. An, Y. Takakuwa, W. Nunomura, S. Manno, and N. Mohandasr. Modulation of erythrocyte membrane mechanical function by protein 4.1 phosphorylation. *J. Biol. Chem.*, 271:7581007587, 1996.

X. An, M.C. Lecomte, J.A. Chasis, N. Mohandas, and W. Gratzer. Shear-response of the spectrin dimer-tetramer equilibrium in the red blood cell membrane. *J. Bio. Chem.*, 277:31796–31800, 2002.

W. A. Anong, T. L. Weis, and P. S. Low. Rate of rupture and reattachment of the band 3-ankyrin bridge on the human erythrocyte membrane. *J. Biol. Chem.*, 281: 2360–2236, 2006.

R. J. Asaro and V. Lubarda. *Mechanics of Solids and Materials*. Cambridge Univ Press, New York, NY., 2006.

P. Bagchi. Mesoscale simulation of blood flow in small vessels. *Biophys. J.*, 92: 1858–1877, 2007.

D. Barthès-Biesel. Motion of spherical microcapsule freely suspended in a linear shear flow. *J. Fluid Mech.*, 100:831–853, 1980.

D. Barthès-Biesel and J.M. Rallison. The time-dependent deformation of a capsule freely suspended in a linear shear flow. *J. Fluid Mech.*, 113:251–267, 1981.

T. Belytschko, W. Liu, and B. Moran. *Nonlinear Finite Elements for Continua and Structures*. John Wiley, New York, 2000.

G. Benavides, G. Squadrito, R. Mills, H. Patel, T. Isbell, R. Patel, V. Darley-Usmar, J. Doeller, and D. Kraus. Hydrogen sulfide mediates the vasoactivity of garlic. *Proc. Natl. Acad. Sci. USA*, 104:17977–17982, 2007.

V. Bennett and P. J. Stenbuck. The membrane attachment protein for spectrin is associated with band 3 in human rbc membranes. *Nature*, 280:468–473, 1979.

D.J. Benson, Y. Bazilevs, M.-C. Hsu, and T. J. R. Hughes. A large-deformation rotation-free isogeometric shell. *Comput. Meths. Appl. Mech. Engr.*, 2010.

A. A. Berk and R. M. Hochmuth. Lateral mobility of integral proteins in red blood cell tethers. *Biophys. J.*, 61:9–18, 1992.

L. Bo and R. E. Waugh. Determination of bilayer membrane bending stiffness by tether formation from giant, thin-walled vesicles. *Biophys. J.*, 55:509–517, 1989.

D.H. Boal. Computer simulation of a model network for the erythrocyte cytoskeleton. *Biophys. J.*, 67:521–529, 1994.

D.H. Boal, U. Seifert, and A. Zilker. Dual network model for red blood cell membranes. *Phys. Rev. Lett.*, 69:3405–3408, 1992.

N. Borghi and F. Brochard-Wyart. Tether extrusion from red blood cells: Integral proteins unbinding from cytoskeleton. *Biophys. J.*, 93:1369–1379, 2007.

L. J. Bruce, R. Beckmann, M. L. Ribeiro, L. L. Peters, J. A. Chasis, J. Delaunay, N. Mohandas, D. J. Anstee, and M. J. Tanner. A band 3-based macrocomplex of integral and peripheral proteins in the rbc membrane. *Blood*, 101:4180–4188, 2003.

J. Butler, N. Mohandas, and R. E. Waugh. Integral protein linkage and the bilayer-skeletal separation energy in red blood cells. *Biophy. J.*, 95:1826–1836, 2008.

S. H. Chang and P. S. Low. Regulation of the glycophorin c-protein 4.1 membrane-to-skeleton bridge and evaluation of its contribution to erythrocyte membrane stability. *J. Biol. Chem.*, 276:22223–22230, 2001.

S. Chien. Red cell deformability and its relevance to blood flow. *Ann. Rev. Physiol.*, 49:177–192, 1987.

S. Chien, L. A. Sung, M. M.L. Lee, and R. Skalak. Red cell membrane elasticity as determined by flow channel technique. *Biorheology*, 29:467–478, 1992.

F. Cirak, M. Ortiz, and P. Schröder. Subdivision surfaces: a new paradigm for thin-shell finite-element analysis. *Int. J. Num. Meths. Engr.*, 47:2039–2072, 2000.

C. M. Cohen, J. M. Tyler, and D. Branton. Spectrin-actin associations studied by electron microscopy of shadowed preparations. *Cell*, 21:875–883, 1980.

D. Craiem and R. Magin. Fractional order models of viscoelasticity as an alternative in the analysis of red blood cell (rbc) membrane mechanics. *Physical Biology*, 7: 013001, 2010.

M. Dao, C. T. Lim, and S. Suresh. Mechanics of the human red blood cell deformed by optical tweezers. *J. Mech. Phys. Solids*, 51:2259–2280, 2003.

M. Dao, J. Li, and S. Suresh. Molecularly based analysis of deformation of spectrin network and human erythocyte. *Mater. Sci. Engr.*, C26:1232–1244, 2006.

T.M. DeSilva, K-C Peng, K.D. Speicher, and D.W. Speicher. Analysis of human red cell spectrin tetramer (head-to-head) assembly using complementary univalent peptides. *Biochemistry*, 31:10872–10878, 1992.

S. Deutsch, J. M. Tarbell, K. B. Manning, G. Rosenberg, and A. A. Fontaine. Experimental fluid mechanics of pulsatile artificial blood pumps. *Annu. Rev. Fluid Mech.*, 38:65–86, 2006.

D. Diesen, D. Hess, and J. Stamler. Hypoxic vasodilation by red blood cells: evidence for an s-nitrosothiol-based signal. *Circulation Research*, 103:545–553, 2008.

M. Diez-Silva, M. Dao, J. Han, C.T. Lim, and S. Suresh. Shape and biomechanical characteristics of human red blood cells in health and disease. *MRS BULLETIN*, 35:382–388, 2010.

D. Discher, C. Dong, J. Fredberg, F. Guilak, D. Ingber, P. Janmey, R. Kamm, G. W. Schmid-Schönbein, and S. Weinbaum. Biomechanics: Cell research and applications for the next decade. *Annals of biomedical engineering*, 37:847–859, 2009.

D. E. Discher and N. Mohandas. Kinematics of red cell aspiration by fluorescence-imaged microdeformation. *Biophys. J.*, 71:1680–1694, 1996.

D. E. Discher, N. Mohandas, and E. A. Evans. Molecular maps of red cell deformation: hidden elasticity and in situ connectivity. *Science*, 266:1032–1035, 1994.

D. E. Discher, D. H. Boal, and S. K. Boey. Simulations of the erythrocyte cytoskeleton at large deformation. *Biophys. J.*, 75:1584–1597, 1998.

W. R. Dodson and P. Dimitrakopoulos. Tank-treading of erythrocytes in strong shear flows via a nonstiff cytoskeleton-based continuum computational modeling. *Biophys. J.*, 99:2906–2916, 2010.

C. D. Eggleton and A. S. Popel. Large deformation of red blood cell ghosts in a simple shear flow. *Phys. Fluids*, 10:1834–1845, 1998.

K. G. Engstrom and H.J. Meiselman. Effects of pressure on red blood cell geometry during micropipette aspiration. *Cytometry*, 23:22–27, 1996.

E. Evans and R. Hochmuth. Membrane viscoelasticity. *Biophys. J.*, 16:1–11, 1976.

E. A. Evans and Y. C. Fung. Improved measurements of the erythrocyte geometry. *Microvasc. Res.*, 4:335–347, 1972.

E.A. Evans and R. Skalak. *Mechanics and thermodynamics of biomembranes*. CRC Press, Boca Raton, FL, 1980.

E.A. Evans and R. Waugh. Osmotic correction to elastic area compressibility measurements on red cell membrane. *Biophys. J.*, 20:307–313, 1977.

D. A. Fedosov, B. Caswell, and G. E. Karniadakis. A multiscale red blood cell model with accurate mechanics, rheology, and dynamics. *Biophys. J.*, 98:2215–2225, 2010a.

D. A. Fedosov, B. Caswell, S. Suresh, and G. E. Karniadakis. Quantifying the biophysical characteristics of plasmodium-falciparum-parasitized red blood cells in microcirculation. *Proc. Natl. Acad. Sci. USA.*, 2010b. In press.

F. Feng and W. S. Klug. Finite element modeling of lipid bilayer membranes. *J. Comput. Phys.*, 220:394–408, 2006.

T. Fischer. Tank-tread frequency of the red cell membrane: dependence on the viscosity of the suspending medium. *Biophys. J.*, 93:2553–2561, 2007.

T.M. Fischer. Is the surface area of the red cell membrane skeleton locally conserved. *Biophys. J.*, 61:298–305, 1992.

T.M. Fischer. Shape memory of human red blood cells. *Biophys. J.*, 86:3304–3313, 2004.

T.M. Fischer, M. Stöhr-Liesen, and H. Schmid-Schönbein. The red cell as a fluid droplet: tank tread-like motion of the human erythrocyte membrane in shear flow. *Science*, 202:894–896, 1978.

J. Fish. *Multiscale Methods: Bridging the Scales in Science and Engineering*. Oxford Press, 2010.

Y.C. Fung. *Biomechanics: mechanical properties of living tissues*. Springer-Verlag, New York, 1993. 2nd edition.

J. Hallquist. *LS-DYNA Theoretical Manual*. Livermore Software Technology Corporation, Livermore, California, 1998.

D. Halpern and T. W. Secomb. The squeezing of red blood cells through parallel-sided channels with near-minimal widths. *J. Fluid Mech.*, 244:307–322, 1992.

W. Helfrich. Elastic properties of lipid bilayers: Theory and possible experiment. *Z. Naturforsch.*, C28:693–703, 1973.

S. Henon. A new determination of the shear modulus of the human erythrocyte membrane using optical tweezers. *Biophys. J.*, 76:1145–1151, 1999.

P. Hochareon. *Development of particle imaging velocimetry (PIV) for wall shear stress estimation within a 50cc Penn State Artificial Heart Ventricular Chamber*. PhD thesis, The Pennsylvania State University, University Park, PA, 2003.

R. Hochmuth and W. D. Marcus. Membrane tethers formed from blood cells with available area and determination of their adhesion energy. *Biophys. J.*, 82:2964–2969, 2002.

R. M. Hochmuth. Measurement of the elastic modulus for red blood cell membrane using a fluid mechanical technique. *Biophys. J.*, 13:747–762, 1973.

J. Hoffman. Questions for red blood cell physiologists to ponder in this millenium. *Blood Cells Mol. Dis.*, 27:57–61, 2001.

G.A. Holzapfel. *Nonlinear Solid Mechanics: A Continuum Approach for Engineering*. Wiley, New York, 2000.

T. J. R. Hughes and W. K. Liu. Non-linear finite-element analysis of shells 1. 3-dimensional shells. *Comput. Meths. Appl. Mech. Engr.*, 26:331–362, 1981a.

T. J. R. Hughes and W. K. Liu. Non-linear finite-element analysis of shells 1. 2-dimensional shells. *Comput. Meths. Appl. Mech. Engr.*, 27:167–181, 1981b.

T.J.R. Hughes and J. Winget. Finite rotation effects in numerical integration of rate constitutive equations arising in large deformation analysis. *Int. J. Num. Meths. Engr.*, 15:1862–1867, 1980.

W. C. Hwang and R. E. Waugh. Energy of dissociation of lipid bilayer from the membrane skeleton of red blood cells. *Biophys. J.*, 72:2669–2678, 1997.

P. Jarolim, J. Palek, and D. Amato. Deletion in erythrocyte band-3 gene in malaria-resistant southeast-asian ovalocytosis. *Proc. Natl. Acad. Sci. USA*, 88:11022–11026, 1991.

A. W.L. Jay. Viscoelastic properties of the human red blood cell membrane i: Deformation, volume loss, and rupture of red cells in micropipettes. *Biophys. J.*, 13: 1166–1182, 1973.

A. W.L. Jay and P. B. Canham. Viscoelastic properties of the human red blood cell membrane ii: Area and volume of individual red cells entering a micropipette. *Biophys. J.*, 17:169–178, 1973.

N. Jiang, N. Tan, B. Ho, and J. Ding. Respiratory protein-generated reactive oxygen species as an antimicrobial strategy. *Nature Immunology*, 8:1114–1122, 2007.

D. Kabaso, R. Shlomovitz, T. Auth, V. Lew, and N. Gov. Curling and local shape changes of red blood cell membranes driven by cytoskeletal reorganization. *Biophys. J.*, 99:808–816, 2010.

H. Kapitza, D. Rüppel, H. Galla, and E. Sackmann. Lateral diffusion of lipids and glycophorin in solid phosphatidylcholine bilayers. the role of structural defects. *Biophys. J.*, 45:577–587, 1984.

S. Keller and R. Skalak. Motion of a tank-treading ellipsoidal particle in a shear flow. *J. Fluid Mech.*, 120:27–47, 1982.

S. Kessler, R. Finken, and U. Seifert. Swinging and tumbling of elastic capsules in shear flow. *J. Fluid Mech.*, 605:207–226, 2004.

K. Khairy, J. Foo, and J. Howard. Shapes of red blood cells: Comparison of 3d confocal images with the bilayer-couple model. *Celluar and Molecular Bioengr.*, 1: 173–181, 2008.

P. Kleinbongard, R. Schulz, T. Rassaf, T. Lauer, A. Dejam, T. Jax, I. Kumara, P. Gharini, S. Kabanova, B. Özüyaman, H. Schnürch, A. Gödecke, A. Weber, M. Robenek, H. Robenek, W. Bloch, P. Rösen, and M. Kelm. Red blood cells express a functional endothelial nitric oxide synthase. *Blood*, 107:2943–2951, 2009.

D. W. Knowles, L. Tilley, N. Mohandas, and J. A. Chasis. Erythrocyte membrane vesiculation: Model for the molecular mechanism of protein sorting. *Proc. Natl. Acad. Sci. USA*, 94:12969–12974, 1997.

G. Kodippili, J. Spector, C. Sullivan, F. Kuypers, R. Labotka, P. Gallagher, K. Ritchie, and P. Low. Imaging of the diffusion of single band 3 molecules on normal and mutant erythrocytes. *Blood*, 113:6237–6245, 2009.

M.M. Kozlov and V.S. Markin. *Contemporary Problems of Biomechanics*, volume 11. CRC Press, 1990.

E. Lac and D. Barthès-Biesel. Deformation of a capsule in simple shear flow: effect of membrane prestress. *Phys. Fluids*, 17:072105, 2005.

E. Lac, D. Barthès-Biesel, N. A. Pelekasis, and J. Tsamopoulos. Spherical capsules in three-dimensional unbounded stokes flows: effect of the membrane constitutive law and onset of buckling. *J. Fluid Mech.*, 516:303–334, 2004.

P. Langevin. On the theory of brownian motion. *C. R. Acad. Sci. (Paris)*, 146: 530–533, 1908.

R. Law, P. Carl, S. Harper, P. Dalhaimer, D. W. Speicher, and D. E. Discher. Cooperativity in forced unfolding of tandem spectrin repeats. *Biophy. J.*, 84:533–544, 2003.

D. Le. Subdivision elements for large deformation of liquid capsules enclosed by thin shells. *Comput. Meths. Appl. Mech. Engr.*, 199:2622–2632, 2010.

G. Lee, K. Abdi, Y. Jiang, P. Michaely, V. Bennett, and P. E. Marszalek. Nanospring behaviour of ankyrin repeats. *Nature*, 440:246–249, 2006.

J.C.M. Lee and D.E. Discher. Deformation-enhanced fluctuations in the red cell skeleton with theoretical relations to elasticity, connectivity, and spectrin unfolding. *Biophys. J.*, 81:3178–3192, 2001.

Y. Lefebvre and D. Barthès-Biesel. Motion of a capsule in a cylindrical tube: effect of membrane pre-stress. *J. Fluid Mech.*, 589:157–181, 2007.

J. Li, M. Dao, C. T. Lim, and S. Suresh. Spectrin-level modeling of the cytoskeleton and optical tweezers stretching of the erythrocyte. *Biophys. J.*, 88:3707–3719, 2005.

J. Li, G. Lykotrafitis, M. Dao, and S. Suresh. Cytoskeletal dynamics of human erythrocyte. *Proc. Natl. Acad. Sci. USA*, 104:4937–4942, 2007.

C.T. Lim, E.H. Zhou, and S.T. Quek. Mechanical models for living cells - a review. *Journal of Biomechanics*, 39:195–216, 2006.

G. Lim, M. Wortis, and R. Mukhopadhyay. Stomatocytecdiscocytecechinocyte sequence of the human red blood cell: Evidence for the bilayer-couple hypothesis from membrane mechanics. *Proc. Natl. Acad. Sci. USA*, 99:16766–16769, 2002.

G. Lim, M. Wortis, and R. Mukhopadhyay. *Soft Matter series*, volume 4, chapter Red blood cell shapes and shape transformations: newtonian mechanics of a composite membrane. Wiley-VCH, Weinheim, 2008.

L.C. Lin and F.L Brown. Dynamic simulations of membranes with cytoskeletal interactions. *Phys. Rev. E*, 72:011910, 2005.

S. Liu, J. Palek, and J. Prchal. Defective spectrin dimer association in hereditary elliptocytosis. *Proc. Natl. Acad. Sci. USA*, 79:2072–2076, 1983.

S. Liu, S. Zhai, J. Palek, D. Golan, D. Amato, K. Hassan, G. Nurse, D. Babona, T. Coetzer, P. Jarolim, and *et al.* Molecular defect of the band 3 protein in southeast asian ovalocytosis. *N. Engl. J. Med.*, 323:1530–1538, 1990.

S. Liu, J. Palek, S. Yi, P. Nichols, L. Derick, S. Chiou, D. Amato, J. Corbett, M. Cho, and D. Golan. Molecular basis of altered red blood cell membrane properties in southeast asian ovalocytosis: role of the mutant band 3 protein in band 3 oligomerization and retention by the membrane skeleton. *Blood*, 86:349–358, 1995.

Y.J. Liu. *Fast Multipole Boundary Element Method*. Cambridge University Press, 2009.

V. Lubarda. Rate theory of elasticity and viscoelasticity for an erythrocyte membrane. *J. Mech. Mater. Struct.*, 2010. In press.

S. E. Lux. Cloning and characterization of band 3, the human erythrocyte anion-exchange protein (ae1). *Proc. Natl. Acad. Sci. USA*, 86:9089–9093, 1989.

L. Ma and W. S. Klug. Viscous regularization and r-adaptive remeshing for finite element analysis of lipid membrane mechanics. *J. Comput. Phys.*, 227:5816–5835, 2008.

J.G. Malone and N.L. Johnson. A parallel finite-element contact/impact algorithm for nonlinear explicit transient analysis 1. the search algorithm and contact mechanics. *Int. J. Num. Meths. Engr.*, 37:559–590, 1994.

G. Marcelli, K. H. Parker, and C. P. Winlove. Thermal fluctuations of red blood cell membrane via a constant-area particle-dynamics model. *Biophys. J.*, 89:2473–2480, 2005.

J. McWhirter, H. Noguchi, and G. Gompper. Flow-induced clustering and alignment of vesicles and red blood cells in microcapillaries. *Proc. Natl. Acad. Sci. USA*, 106: 6039–6043, 2009.

R.E. Mebius and G. Kraal. Structure and function of the spleen. *Nature Reviews Immunology*, 5:606–616, 2004.

N. Mohandas and P.G. Gallagher. Red cell membrane: past, present, and future. *Blood*, 112:3939–3948, 2008.

N. E. Mohandas and E. Evans. Mechanical properties of the red cell membrane in relation to molecular structure and genetic defects. *Annu. Rev. Biophys. Biomol. Struct.*, 23:787–818, 1994.

R. Mukhopadhyay, G. H.W. Lim, and M. Wortis. Echinocyte shapes: Bending, stretching, and shear determine spicule shape and spacing. *Biophys. J.*, 82:1756–1772, 2002.

H. Noguchi and G. Gompper. Shape transitions of fluid vesicles and red blood cells in capillary flows. *Proc. Natl. Acad. Sci. USA*, 102:14159–14164, 2005.

W.K. Otter and S.A. Shkulipa. Intermonolayer friction and surface shear viscosity of lipid bilayer membranes. *Biophys. J.*, 93:423–433, 2007.

J. Palek and S. Lambert. Genetics of the red-cell membrane skeleton. *Seminars in Hemotology*, 27:290–332, 1990.

J. Palek and S. Lambert. Cellular molecular-biology of rbc membrane. 4. clinical expression and laboratory detection of red-blood-cell membrane-protein mutations. *Seminars in Hemotology*, 30:249–283, 1993.

S. Paramore and G.A. Voth. Examining the influence of linkers and tertiary structure in the forced unfolding of multiple-repeat spectrin molecules. *Biophys. J.*, 91:3436–3445, 2006.

Y. Park, C.A. Best, T. Auth, N.S. Gov, S.A. Safran, G. Popescu, S. Suresh, and M.S. Feld. Metabolic remodeling of the human red blood cell membrane. *Proc. Natl. Acad. Sci. USA*, 107:1289–1294, 2009.

Z. Peng, X. Yuan, and S. Dong. Tensegrity torus. *Spatial Structures*, 13:60–64, 2007.

Z. Peng, R. J. Asaro, and Q. Zhu. Multiscale simulation of erythrocyte membranes. *Physical Review E*, 81(031904), 2010.

M.A. Peterson, H. Strey, and E. Sackmann. Theoretical and phase contrast microscopic eigenmode analysis of erythrocyte flicker : amplitudes. *J. Phys. II (France)*, 2:1273–1285, 1992.

C. Pozrikidis. The axisymmetric deformation of a red blood cell in uniaxial straining flow. *J. Fluid Mech.*, 216:231–254, 1990.

C. Pozrikidis. *Boundary Integral and Singularity Methods for Linearized Viscous Flow*. Cambridge University Press, 1992.

C. Pozrikidis. Effect of membrane bending stiffness on the deformation of capsules in simple shear flow. *J. Fluid Mech.*, 440:269–291, 2001.

C. Pozrikidis. *Modeling and Simulation of Capsules and Biological Cells*. Boca Raton: Chapman & Hall/CRC, 2003a.

C. Pozrikidis. Numerical simulation of the flow-induced deformation of red blood cells. *Ann. Biomed. Engr.*, 31:1194–1205, 2003b.

C. Pozrikidis. Axisymmetric motion of a file of red blood cells through capillaries. *Phys. Fluids*, 17:031503, 2005a.

C. Pozrikidis. Numerical simulation of cell motion in tube flow. *Annals of Biomedical Engineering*, 33:165–178, 2005b.

C. Pozrikidis. *Computational Hydrodynamics of Capsules and Biological Cells*. Taylor & Francis, 2010.

A. R. Pries and T. W. Secomb. Blood flow in microvascular networks. In R. F. Tuma, W. N. Durán, and K. Ley, editors, *Handbook of Physiology: Microcirculation*, pages 3–36. Academic Press, Elsevier, San Diego, 2008.

M. Puig-De-Morales-Marinkovic, K. T. Turner, J. P. Butler, J. J. Fredberg, and S. Suresh. Viscoelasticity of the human red blood cell. *Am. J. Physiol. - Cell Physiol.*, 293:C597–C605, 2007.

S. Ramanujan and C. Pozrikidis. Deformation of liquid capsules enclosed by elastic membranes in simple shear flow: Large deformations and the effect of capsule viscosity. *J. Fluid Mech.*, 361:117–143, 1998.

M. E. Reid, Y. Takakuwa, J. Conboy, G. Tchernia, and N. Mohandas. Glycophorin c content of human erythrocyte membrane is regulated by protein 4.1. *Blood*, 75: 2229–2234, 1990.

M. Rief, M. Gautel, F. Oesterhelt, J. M. Fernandez, and H. E. Gaub. Reversible unfolding of individual titin immunoglobulin domains by afm. *Science*, 276:1109–1112, 1997.

M. Rief, J. Pascual, M. Saraste, and H.E. Gaub. Single molecule force spectroscopy of spectrin repeats: low unfolding forces in helix bundles. *J. Mol. Biol.*, 286:553–561, 1999.

V. Sarabia, J. Casey, and R. Reithmeier. Molecular characterization of the band-3 protein from southeast-asian ovalocytes. *J. Biol. Chem.*, 268:10676–10680, 1993.

P. Savvides, O. Shalev, K. John, and S. Lux. Combined spectrin and ankyrin deficiency is common in autosomal-dominant hereditary spherocytosis. *Blood*, 82: 2953–2960, 1993.

T.W. Secomb, R. Skalak, N. Ozkaya, and J.F. Gross. Flow of axisymmetric red blood cells in narrow capillaries. *J. Fluid Mech.*, 163:405–423, 1986.

U. Seifert. Configurations of fluid membranes and vesicles. *Advances in physics*, 46: 13–138, 1997.

U. Seifert, K. Berndl, and R. Lipowsky. Shape transformations of vesicles: Phase diagram for spontaneous-curvature and bilayer-coupling models. *Physical Review A*, 44:1182–1202, 1991.

K. Shoele and Q. Zhu. Flow-induced vibrations of a deformable ring. *Journal of Fluid Mechanics*, 650:343–362, 2010.

R.E. Skelton and M.C. de Oliveira. *Tensegrity Systems*. Springer, New York, 2009.

J.M. Skotheim and T.W. Secomb. Red blood cells and other nonspherical capsules in shear flow: oscillatory dynamics and the tank-treading-to-tumbling transition. *Phys. Rev. Lett.*, 98:078301, 2007.

J. Sleep, D. Wilson, R. Simmons, and W. Gratzer. Elasticity of the red cell membrane and its relation to hemolytic disorders: an optical tweezers study. *Biophys. J.*, 77: 3085–3095, 1999.

P. Stroeva, P. Hoskinsb, and W. Eassona. Distribution of wall shear rate throughout the arterial tree: A case study. *Atherosclerosis*, 191:276–280, 2007.

L.A. Sung and C. Vera. Protofilament and hexagon: a three-dimensional mechanical model for the junctional complex in the rbc membrane skeleton. *Ann. Biomed. Eng.*, 31:1314–1326, 2003.

S. Svetina, P. Ziherl D. Kuzman R. E. Waugh, and B. Zêkŝ. The cooperative role of membrane skeleton and bilayer in the mechanical behaviour of red blood cells. *Bioelectrochemistry*, 62:107–113, 2004.

K. Svoboda, C.F. Schmidt, D. Branton, and S.M. Block. Conformation and elasticity of the isolated red blood cell membrane. *Biophys. J.*, 63:784–793, 1992.

M. Tomishige. Regulation mechanism of the lateral diffusion of band 3 in erythrocyte membranes by the membrane skeleton. *The Journal of Cell Biology*, 142:989–1000, 1998.

R. Tran-Son-Tay. *A study of the tank-treading motion of red blood cells in shear flow.* PhD thesis, Washington University, St. Louis, MO, 1983.

R. Tran-Son-Tay, S. Sutera, and P. Rao. Determination of red blood cell membrane viscosity from rheoscopic observations of tank-treading motion. *Biophys. J.*, 46: 65–72, 1984.

K. Tsubota and S. Wada. Effect of the natural state of an elastic cellular membrane on tank-treading and tumbling motions of a single red blood cell. *Physical Review E*, 81:011910, 2010.

P. Ulker, L. Sati, C. Celik-Ozenci, H. Meiselman, and O. Baskurt. Mechanical stimulation of nitric oxide synthesizing mechanisms in erythrocytes. *Biorheology*, 46: 121–132, 2009.

C. Vera, R. Skelton, F. Bossens, and L.A. Sung. 3-d nanomechanics of an erythrocyte junctional complex in equibiaxial and anisotropic deformations. *Ann. Biomed. Eng.*, 33:1387–1404, 2005.

J. Walter, A.-V. Salsac, D. Barthès-Biesel, and P. Le Tallec. Coupling of finite element and boundary integral methods for a capsule in a stokes flow. *International Journal for Numerical Methods in Engineering*, 83:829–850, 2010.

J. Wan, W. D. Ristenpart, and H. A. Stone. Dynamics of shear-induced atp release from red blood cells. *Proc. Natl. Acad. Sci. USA*, 105:16432–16437, 2008.

N. Wang, K. Naruse, D. Stamenovic, J. Fredberg, S. Mijailovich, I. Tolic-Norrelykke, T. Polte, R. Mannix, and D. E. Ingber. Mechanical behavior in living cells consistent with the tensegrity model. *Proc. Natl. Acad. Sci. USA*, 98:7765–7770, 1997.

Y. C. Wang and R.S Lakes. Composites with inclusions of negative bulk modulus: Extreme damping and negative possion's ratio. *Journal of Composite Materials*, 39:1645–1657, 2004.

R. Waugh. Effects of abnormal cytoskeletal structure on erythrocyte-membrane mechanical properties. *Cell Motility and the Cytoskeleton*, 3:609–622, 1983.

R. Waugh and P. Agre. Reductions of erythrocyte-membrane viscoelastic coefficients reflect spectrin deficiencies in hereditary spherocytosis. *J. Clin. Invest.*, 81:133–141, 1988.

R. Waugh and E. Evans. Thermoelasticity of red blood cell membrane. *Biophys. J.*, 26:115–131, 1979.

R.E. Waugh and R. G. Bauserman. Physical measurements of bilayer-skeletal separation forces. *Annals Biomed. Engr.*, 23:308–321, 1995.

R.E. Waugh and R.M. Hochmuth. Mechanical equilibrium of thick, hollow, liquid membrane cylinders. *Biophys. J.*, 52:391–400, 1987.

J.H. Weiner. *Statistical Mechanics of Elasticity.* Dover,Mineola, NY, 1983.

X. Yuan, Z. Peng, S. Dong, and B. Zhao. A new tensegrity module - 'torus'. *Advances in Structural Engineering*, 11:243–251, 2008.

P. R. Zarda, S. Chien, and R. Skalak. Elastic deformations of red blood cells. *J. Biomechanics*, 10:211–221, 1977.

J. Zhang, P.C. Johnson, and A.S. Popel. Red blood cell aggregation and dissociation in shear flows simulated by lattice boltzmann method. *J. Biomech.*, 41:47–55, 2008.

H. Zhao, A.H.G. Isfahani, L.N. Olson, and J.B. Freund. A spectral boundary integral method for flowing blood cells. *J. Comp. Phys.*, 229:3726–3744, 2010.

H. Zhou and C. Pozrikidis. Deformation of capsules with incompressible interfaces in simple shear flow. *J. Fluid Mech.*, 283:175–200, 1990.

Q. Zhu and R. Asaro. Spectrin folding vs. unfolding reactions and rbc membrane stiffness. *Biophy. J.*, 94:2529–2545, 2008.

Q. Zhu, C. Vera, R. Asaro, P. Sche, and L. A. Sung. A hybrid model for erythrocyte membrane: a single unit of protein network coupled with lipid bilayer. *Biophys. J.*, 93:386–400, 2007.

C. Zienkiewicz, D. Kelly, and P. Bettess. Marriage a la mode: The best of both worlds - finite elements and boundary integrals. In *International Symposium on Innovative Numerical Analysis in Applied Engineering Science, Versailles, France*, pages 19–26, 1977.